Ultrastructure of Dentine Carious Lesions

by

Alexander Zavgorodniy

The thesis submitted in fulfillment of the requirements for the degree of

Doctor of Philosophy

Supervisor: Prof. Michael V. Swain
Co-supervisor: Dr. Ramin Rohanizadeh

Biomaterials Science Research Unit, Faculty of Dentistry, the University of Sydney

November 2008

Declaration

Candidate's Certificate

This is to certify that the work presented in this thesis was carried out by the candidate in the Discipline of Biomaterials Science, Faculty of Dentistry, the University of Sydney and has not been submitted to any other university or institution for a higher degree. This work contains no material written or published by any other person except where due reference has been made.

Alexander Zavgorodniy
Sydney, November 2008

Acknowledgements

I wish to express my deep sense of gratitude to Prof. Michael Swain from the Faculty of Dentistry, the University of Sydney, for his inspiring guidance, constant encouragement and support of my research work. I thank him very much for giving me the freedom to explore the realms of science and for sharing his wide knowledge and expertise. I very much appreciate the working environment he provides to the group members, thereby leading to a highly productive atmosphere, where everyone understands their responsibilities and acts accordingly. I am deeply grateful to him for his support in times of difficulties, solving many problems and motivating me to progress ahead. In spite of his busy schedule, he has always made himself available whenever I approached him and I sincerely thank him for being open and supportive to my suggestions. I am very grateful that he let me present the results of my research at conferences, workshops and meetings.

Also I would like to express my deepest gratitude to Dr. Ramin Rohanizadeh from the Faculty of Farmacy, the University of Sydney for his continuous guidance throughout my research work and my sincere thanks for every discussion that I had with him, the confidence he had shown and the vast amount of patience he has had when reviewing and correcting my papers during the preparation of the manuscripts for submission to various journals.

My thanks also to Prof. Neil Hunter from the Institute of Dental Research, Westmead Hospital and A/Prof. Hans Zoellner from the Faculty of Dentistry, the University of Sydney for their interest in my research and useful discussions. I would like to extend my thanks to all colleagues at the Faculty of Dentistry, the University of Sydney for helping to create a pleasant and inspiring working atmosphere and

especially Mr. Ken Tyler for his ongoing assistance with the equipment in the Biomaterials Laboratory and Mrs. Rebecca Granger and Mrs. Tracey Bowerman for all their valuable information support during my research project.

I wish to thank Mrs. Ellie Kable from the Electron Microscope Unit, the University of Sydney for giving me the opportunity to work in the Electron Microscope Unit and making all the facilities available for my research work. I wish to thank Mr. Adam Sikorski, Ms. Emine Korkmaz, Ms. Anne Simpson and Mr. Tony Romeo from the Electron Microscope Unit, the University of Sydney, for their valuable guidance in specimens preparation for observation in transmission and scanning electron microscopes. It is a great pleasure to thank Mr. Shaun Bulcock from the Electron Microscope Unit, the University of Sydney for his valuable constant support of my research and for training me to use TEMs. I wish to thank Dr. Ian Kaplin from the Electron Microscope Unit, the University of Sydney for training me to use SEMs. It is a great pleasure to thank Dr. Julie Cairney from the Electron Microscope Unit, the University of Sydney and Dr. Sergey Rubanov from Bio21 Institute, the University of Melbourne, for training me to use dual-beam FIB/SEM systems. I wish to thank Dr. Renee Whan from the Electron Microscope Unit, the University of Sydney for training me to use light microscopes. The excellent technical assistance from the Electron Microscope Unit, the University of Sydney throughout my research is gratefully appreciated. I wish to thank A/Prof. Brendan Kennedy from the School of Chemistry, the University of Sydney for training me to use Rietica software and his guidance with Le Bail refinement.

I gratefully acknowledge the financial support from Sydney Dental Hospital in the form of scholarship and especially Mr. Graeme Angus and A/Prof. Sameer Bhole for their keen interest and their support of my research. Partial support in the form of a

travel grant to present my work at the 4th International Symposium on Apatite and Correlative Biomaterials (Manila, Philippines) from Sydney Dental Hospital is acknowledged. Partial support in the form of grants from the Australian Dental Research Foundation (ADRF) and the Australian Dental Industry Association (ADIA) is also acknowledged.

This thesis could not have been completed without constant encouragement and support to go ahead, especially during difficult times, from my dearest friend Mr. Ernest Randall, M.B.E.

Finally, I express my thanks to all my family and friends for their support, friendship and love during the whole period of this work. Especially I would like to thank my parents, Ludmila & Victor and my sister Marina and her family, who always supported me and kept me motivated to finish my thesis.

Alexander Zavgorodniy
Sydney, November 2008

Abstract

Objectives

Today dental caries is a widespread disease affecting most of the world's population. Once caries becomes established it becomes a chronic disease and if not treated often the consequences are loss of teeth. Current restorative procedures include mechanical removal of caries and replacement of the affected part of the tooth with dental materials such as resins or metals with inorganic-base cements as glues. Although dental restorative composite materials technology has succeeded in creating highly specialized, high performance materials, it is still far from being able to replicate the elegance of biological composites, such as enamel and dentine. Therefore dental restorative procedures are generally temporary with a lifespan of only few years before the restorative material or supporting tooth structure fails. The prerequisite for producing such biomimetic materials with properties close to natural biological composites is to understand the influence of the ultrastructural properties of dental hard tissue minerals, such as size, lattice parameters and preferred orientation of enamel and dentine nanocrystallites on the overall mechanical properties. Therefore a systematic investigation of tooth structures is needed to understand this correlation.

Although at present the operative radical intervention and removal of all carious affected dentine is widely accepted, an alternative, cariologist view of dentinal caries treatment, has started to emerge. It has been suggested that the progress of caries front can be halted and that the softened dentine can be remineralized if the cariogenic environment is removed. Further progress in this area requires that an ultrastructural analysis of the dentine carious layers and the mechanisms behind the

conversion of the untreated dentine carious lesion from an active and closed lesion environment into one that is open and arrested be undertaken.

The purpose of the present study was: (1) to test the hypothesis that the crystal structure and texture of the enamel and dentine mineral phases varies in a location dependent manner; (2) to test the hypothesis that dentinal microbranches play an important role in the progress of caries through dentine and that the size of the dentine crystallites varies in different dentine carious zones; (3) to test the hypothesis that caries-induced intratubular dentine formation is biologically regulated as a response to caries challenge, while the presence of previously reported Mg-substituted β-TCP phase is purely the result of 'dissolution and precipitation' mechanism in acidic pH environment; (4) to test the hypothesis that softened and arrested carious lesions have distinctly different ultrastructure, which in turn can explain the reported increase of hardness and mineral density at the cavity floor of arrested carious dentine lesions.

Materials and Methods

Human molar non-carious teeth were extracted for orthodontic reasons and human molar carious affected teeth were extracted due to severe occlusal carious lesions with no prior history of restoration. All the specimens were collected for this study according to the protocols approved by the Ethics Review Committee of Sydney South West Area Health Service and by the Human Research Ethics Committee of the University of Sydney.

The specimens were chemically fixed, sectioned and areas of interest were determined with the aid of optical and scanning electron microscopes, and a dental explorer (probe). Electron transparent ultrathin sections of dentine and enamel were prepared using diamond knife and ion-beam thinning techniques. Conventional, high

resolution and scanning transmission electron microscopy, electron diffraction, energy-dispersive X-ray spectroscopy and X-ray microdiffraction analytical techniques were used to investigate the ultrastructure of the inorganic phase of carious and sound dental structures. The XRD data was refined using Rietveld - Le Bail algorithm.

Summary of outcomes and conclusions

1. The thickness of sound dentine apatite crystallites was found to decrease towards the DEJ, while the thickness of the enamel apatite crystallites increased from the DEJ towards the outer layers. It was demonstrated that enamel exhibited an increase of preferred orientation in 002 lattice planes from the DEJ towards the outer layers. Texture was also detected in 102 lattice planes. The texture effect in 002 planes at the scales of less than 1 μm was also demonstrated in dentine. The values of the non-uniform microstrain in the dentine and enamel crystallites were low but a correlation between the width of the dentine and enamel crystals and microstrain was observed. The variation of lattice parameters as a function of the position within the thickness of dentine and enamel was confirmed.

   The increased preferred orientation and width of the enamel crystallites towards the outer surfaces of tooth confirmed the hypothesis that such structure maybe evolutionary designed to resist wear, while the observed interprismatic cleavages may serve the purpose of resisting fracture. The variation of crystal sizes through the thickness of dentine towards the DEJ fits with the hypothesis that the outer 200 μm layer of dentine functions as a cushion, which allows enamel and dentine to work together. The correlation

between the position within dentine and enamel layers and the variation of lattice parameters was explained in termes of variation of chemical composition of the tooth mineral phase.

2. Intertubular dentine crystallites in caries induced transparent zone were 53% smaller in length and 12% smaller in width than those in sound intertubular dentine. Intertubular dentine crystallites within the demineralized zone were 65% smaller in length and 32% smaller in width than those in sound intertubular dentine. The intratubular mineral crystals deposited within the lumens of the tubules in carious transparent zone were an apatite phase, nanometer size (<10 nm), plate-shaped, and chemically similar to intertubular dentine. Ultrastrastructural observations of the intertubular dentine in the carious transparent zone demonstrated partial demineralization of the intertubular dentine through the dissolution of microbranches and exposure of the intertubular transparent dentine to acids.

   The study suggested that a 'dissolution and precipitation' mechanism is important in understanding the process of formation of intratubular dentine within the transparent zone induced by caries attack. The observed partial demineralization of intertubular dentine in transparent zone is discussed in terms of dissolution of tubule microbranches and exposure of intertubular dentine to acids.

3. The majority of the intratubular dentine crystals deposited within the lumens of the tubules in the carious transparent zone were needle- and plate-like apatite. Highly orientated apatite crystallites in intratubular dentine suggested a bio-regulated mineralization process in the formation of intratubular dentine. Minor presence of Mg-substituted β-TCP (whitlockite) crystals was observed

in caries-induced intratubular dentine. The polycrystalline nature of the Mg-substituted β-TCP crystals observed suggested that the formation of this mineral was purely due to the mechanism of dissolution of intertubular dentine followed by the precipitation of Mg-substituted β-TCP crystals within the tubule lumens under acidic conditions and in the presence of Mg. The presence of whitlockite and therefore the conditions that favor its formation may have a crucial role in caries decay. Direct observation of the Mg-substituted β-TCP crystallites partly forming carious induced intratubular dentine coupled with volume diffusion mechanism and in conjunction with layer-spiral growth theory allowed the calculation of the growth kinetics of Mg β-TCP crystals. Rapid formation of Mg β-TCP crystallites in the caries transparent zone was also demonstrated.

The study suggests that a regulated biomineralization process occurs during the formation of the apatite mineral phase of the intratubular dentine in caries transparent layer, whereas Mg β-TCP crystals, which were observed in the intratubular dentine, were presumably formed purely via 'dissolution/precipitation' mechanism. The study demonstrated the importance of 'dissolution/precipitation' process and the growth kinetics of Mg-substituted β-TCP crystals in understanding the process of formation of calcium-phosphate crystallites in carious intratubular dentine.

4. Within the arrested layer of dentinal carious lesions, the density of mineral content was higher than that of active carious lesions. The remineralization of carious dentine associated with the arrested carious lesions was due to the precipitation of apatite mineral. No preferred orientation of the apatite crystallites was observed, which may suggest that the process of

mineralization of the arrested carious layer of dentine was primarily not biologically controlled. No degradation of the collagen matrix in active carious lesions was detected, while the observed degradation of the collagen matrix near cavity floor was due to a longer exposure to acidic challenge associated with caries and therefore activation of host metalloproteinases in low pH conditions in demineralized dentine.

The arrested layer of dentinal caries was found to have a denser mineral content over that of the inner layers of carious lesions. This observation confirmed the hypothesis that the reported increase of hardness in arrested carious lesions in comparison with active carious lesions was due to the increased densities of mineral deposits at the cavity floor.

In summary, the present work provides some evidence that the formation of the apatite phase of carious induced intratubular dentine can be attributed to the extracellular dentine matrix proteins secreted by odontoblasts or odontoblast-like cells during early stages of caries attack followed by a rapid formation of Mg substituted β-TCP phase, which has a non-biological origin. These findings have important implications to the restorative dentistry since β-TCP mineral phase is unstable at neutral pH and consequently bonding to such substrate is unreliable in the long term. Further ultrastructural investigations, which include specific protein staining, will give further insight into the fascinating world of biomineralization and are expected to be beneficial for the development of dental restorative materials, which better mimic the structure, composition and mechanical properties of dentine.

It is anticipated that the outcomes of the present work will assist further studies on the ultrastructure of sound and carious dentine especially on the location

and activity of MMPs and TIMPs in carious affected dentine by means of immunohistochemical examination and colloidal gold immunochemistry. Such experiments can provide specific information of the role of these proteins in the degradation of the organic matrix in carious dentine. These studies are crucial for the development of a less invasive dental restorative procedure and remineralization of carious affected dental structures.

The location-dependent variation of dentine and enamel ultrastructure gives us an important insight on how dentine and enamel work together for many years in harsh environment of oral cavity. However, the identification of the underlying correlations between the ultrastructural composition of dentine and enamel and the mechanical properties of these biological mineral composites has to await future experiments.

Table of Contents

List of Figures

List of Tables

Publications and scientific meeting presentations arising from this research

Journal publications:

1. **Zavgorodniy A.V.**, Rohanizadeh R., Swain M.V. Ultrastructure of Dentine Carious Lesions. Archives of Oral Biology 2008;53(2):124-32.
2. **Zavgorodniy A.V.**, Rohanizadeh R., Bulcock S., Swain M.V. Ultrastructural Observations and Growth of Occluding Crystals in Carious Dentine. Acta Biomaterialia 2008;4(5):1427-39.
3. **Zavgorodniy A.V.**, Rohanizadeh R., Swain M.V. Ultrastructure of Arrested Carious Dentine Lesions. Journal of Dentistry, In Review.
4. Xue J., **Zavgorodniy A.V.**, Kennedy B.J., Li W., Swain M.V. X-ray Microdiffraction and TEM Characterization of Human Dentine and Enamel. Biomaterials, In Review.

Book Chapter:

Portions of the paper '**Zavgorodniy A.V.**, Rohanizadeh R., Swain M.V. Ultrastructure of Dentine Carious Lesions. Archives of Oral Biology 2008;53(2):124-32' will be published in:

Lehman R.A. How to Prepare for the DAT. Dental Admissions Test. Hauppauge, NY: Barron's Education Publishing Company; 2009.

Scientific meetings

International Meetings:

Zavgorodniy A.V., Rohanizadeh R., Bulcock S., Swain M.V. Ultrastructural Observations and Growth of Occluding Crystals in Carious Dentine. The 4th International Symposium on Apatite and Correlative Biomaterials (ISACB). Manila, Philippines; 2008. Oral Presentation.

Xue J., **Zavgorodniy A.V.**, Wei L., Swain M.V. Integrated TEM and X-Ray Microdiffraction of Human Tooth Crystallographic Structure and Ultrastructure. The 4th International Symposium on Apatite and Correlative Biomaterials (ISACB). Manila, Philippines; 2008. Poster Presentation.

Zavgorodniy A.V., Rohanizadeh R., Bulcock S., Swain M.V. Ultrastructure and Growth Kinetics of Inorganic Phase of the Caries-Induced Intratubular Dentine. 20th Australian Conference on Microscopy & Microanalysis / 4th Congress of the International Union of Microbeam Analysis Societies (ACMM-20 & IUMAS-IV). Perth, Western Australia; 2008. Poster Presentation.

Zavgorodniy A.V., Rohanizadeh R., Swain M.V. Ultrastructure of Dentine Carious Zones. 47th Annual Meeting of the Australian and New Zealand Division of the International Association for Dental Research (IADR). Barossa Valley, South Australia; 2007. Poster Presentation.

National Meetings:

Zavgorodniy A.V., Rohanizadeh R., Swain M.V. Ultrastructure of Dentine Carious Lesions. Oral Health Services Clinical Forum. Sydney, New South Wales; 2008. Oral Presentation.

Zavgorodniy A.V., Rohanizadeh R., Swain M.V. Ultrastructural Investigation of Caries Dentine Zones. Germany Innovations & Technology Conference. Sydney, New South Wales; 2007. First Prize Student Poster Presentation Winner.

Zavgorodniy A.V., Rohanizadeh R., Swain M.V. TEM Ultrastructural Observations of Caries Modified Dentine. Australian Research Network for Advanced Materials (ARNAM) Annual Workshop. Kioloa, New South Wales; 2007. Poster Presentation.

Zavgorodniy A.V., Rohanizadeh R., Swain M.V. A Transmission Electron Microscopy Study of Ultrastructural Changes in Caries-Induced Dentine. 17th Annual Conference Australasian Society for Biomaterials. Melbourne, Victoria; 2007. The Best Poster Presentation Winner.

Chapter I. Introduction

1.1 Significance

Teeth are hard, bone-like structures in the mouth, anchored into sockets in the upper and lower jawbones and project through the lining tissue of the jaw into the mouth. Teeth functions are, (i) to tear, scrape and chew food; (ii) some vertebrates, carnivores in particular, also use teeth for hunting and defence. While the geometry of teeth can be generally linked with food's elastic modulus and toughness [1], the size of teeth can only be partially explained by the variation of the mechanical properties of foods and not fully understood at present.

The importance of teeth can be derived from the evidence that mammals and other vertebrates, whose dental function is sufficiently impaired, die and the functionality of the dentition (essentially affected by wear) significantly contributes to the factors limiting lifespan of mammals in the wild [2].

Teeth and the mouth cavity have very efficient self-cleaning mechanisms for natural diets, which was evolved as a self-protection mechanism against bacteria invasion and vulnerability to the infection around the roots of the teeth or a break through the teeth material itself. Humans, however, domesticated both plants and animals in order to have an uninterruptible and fully controlled food supply and that's when for the first time humans encountered tooth decay (dental caries). The onset of a significant presence of dental caries started with the high consumption of cultivated grain products about 10000 BC [3-5]. The nutritional content of these foods comes from starches that are bound in seeds into relatively insoluble granules of micrometer size [6]. During cooking procedures starch is solubilised and breaks into very small

fragmented granules [7], which cannot easily be cleared from the mouth. Enzymes (amylases) in saliva break starch into sugars [8] and bacteria living in the mouth convert those sugars into acid [9]. Once acidity drops below a certain level (< pH 5.5) teeth start to dissolve and decay sets in [10]. The major effect on dental caries is associated with one particular sugar, sucrose, which is a major part of modern refined diet. Sucrose forms an exceptionally adhesive layer to the teeth surfaces, much stronger than other sugars [11] and that's when the self-cleaning mechanism of the oral cavity fails. Even though sucrose is not uncommon because it serves as a transport medium for energy [12, 13] but it is never concentrated and cells rapidly convert sucrose into other types of sugars, e.g. for building cell walls. Also most natural diets do not contain sugars in the form of sucrose but when they do, the concentration of sucrose is very low. In fact even most of the fruit-eating birds do not have the corresponding enzyme, sucrase (α-glucosidase), to break sucrose [14] and they develop diarrhoea if they consume it in concentrated quantities [15].

Today dental caries is a widespread disease affecting most of the world population [16]. It is an infectious communicable disease [17] (although it is an exception amongst the general concept of a transmittable, infectious disease, which is discussed in more detail elsewhere [18]). Once caries sets in it becomes a chronic disease [19] and if not treated often the consequences are loss of teeth [20] and spread of bacteria throughout the body via blood circulation [21].

Current restorative procedures include mechanical removal of caries and replacement of the affected part of the tooth with dental materials such as resins or metals with inorganic-base cements as glues. During this restorative procedure the unaffected part of the tooth is also excavated to prepare a larger surface for mechanical bonding of the repair material to the tooth structure [22]. Different thermal

expansion and contraction behaviour between tooth structures and repair materials, which are caused by the differences in terms of chemical composition and crystal structure, prevent perfect adhesion and therefore such restorative procedures are always only temporary with a lifespan of only few years before the restorative material or supporting tooth structure fails. From this perspective a new generation of synthetic restorative materials are needed resembling the ultrastructure and mechanical properties of normal enamel and dentine.

Though at present the operative radical intervention and removal of all carious affected dentine is widely accepted, an alternative, cariologist view of dentinal caries treatment, has started to emerge. It has been suggested that the progress of caries front can be halted and that the softened dentine can be remineralized if the cariogenic environment is removed [23]. This treatment alternative to the radical intervention procedures is very attractive and triggered various clinical studies with a reportedly positive outcome [24, 25] but the rationale behind the ultraconservative dentinal caries treatment is by no means clear cut. Further progress in this area requires that an ultrastructural analysis of the dentine carious layers and the mechanisms behind the conversion of the untreated dentine carious lesion from an active and closed lesion environment into one that is open and arrested be undertaken. The ultrastructural analysis of the untreated carious lesions may help transform the treatment philosophy of dentine carious lesions and to enable the less invasive restorative procedures to make their way into dental surgeries around the world.

1.2 Aims

The present work was set up with the following aims:

1. To investigate the ultrastructure of the inorganic phase of sound coronal dentine and enamel using transmission electron microscopy and X-ray microdiffraction techniques.
2. To investigate the ultrastructural changes within the different zones of carious dentine and compare those changes with sound dentine using scanning and transmission electron microscopy and electron diffraction analytical methods.
3. To investigate the ultrastructure and chemical content of the inorganic phase of the caries-induced intratubular dentine using transmission electron microscopy, electron diffraction analytical methods and energy-dispersive X-ray spectroscopy.
4. To investigate the ultrastructure of the dentine arrested carious lesions using transmission electron microscopy and electron diffraction techniques.

1.3 Outline of the thesis

Chapter 2 focuses on the introduction of terms, which are widely used in the presented work. The extent of this chapter is limited to the scope of this thesis and provides the necessary background related to the histology of dentine, literature review, which outlines the results to date related to the organic and inorganic phases of dentine, dentinogenesis, dentine structure, consequences of caries attack on dentine and defence mechanisms of the body to arrest caries attack. Brief, yet informative introduction into the structure of enamel is also part of this chapter.

Chapter 3 describes the methodology used in this work, namely transmission and scanning electron microscopy, and micro X-ray diffraction. Specimen preparation techniques used in this work are also part of this chapter.

Ultrastructure of sound unaffected teeth and particularly the ultrastructure of the mineral phase of teeth structure are of a great importance to dental applications and biomaterial science, which leads to the development of new more effective restorative materials with a better match to tooth structures. The results of the ultrastructure of the mineral phase of teeth structures investigated are presented in Chapter 4, which further contributes not only to our general understanding of the structure of teeth and how teeth function but are also important to further advance development of dental restorative materials. The observations presented in this chapter were instrumental to reveal the difference on the ultrastructural level between normal and carious affected dentine.

The recently developed new approach called 'minimum intervention' has been introduced for cavity preparation prior to restoration of carious lesions in order to preserve tooth structure. This approach suggests that caries do not always need to be removed completely from the deeper portions of the cavity [26]. However, how much of the caries affected structure needs to be removed and where to stop is currently not settled [27]. From this perspective, it is important to investigate the ultrastructure of the inorganic phase of various layers of caries affected dentine and the results of this work are presented in Chapter 5.

The phenomena of the defence mechanisms of the body to protect pulp from the bacterial invasion, toxins and acids during caries attack also needs to be recognised in restorative dental applications. In Chapter 6 we investigate the ultrastructure of the caries induced intratubular dentine and demonstrate that tubules

occluding material is not just a single homogenous phase and that the bonding and lifespan of the restorative material directly depends on the mineral phase, which participates in the adhesion.

Chapter 7 is focused on the phenomena of the ultrastructure of the arrested caries dentine, which provides clues on the remineralization potential of caries affected dentine and the development of the treatments to preserve the organic dentine matrix followed by remineralization of dentine.

Chapter 8 draws together all the aspects of the above chapters and summarises the outcomes as well as identifies opportunities for future research in this area.

1.4 References

1. Lucas P.W., Prinz J.F., Agrawal K.R., Bruce I.C. Food physics and oral physiology. Food Quality and Preference 2002;13(4):203-13.
2. DeGusta D., Everett M.A., Milton K. Natural Selection on Molar Size in Wild Population of Howler Monkeys (Alouatta palliata). The Royal Society Proceedings: Biological Sciences 2003;270(Supplement: Biology Letters):S15-S17.
3. Beckett S., Lovell N.C. Dental Disease Evidence for Agricultural Intensification in the Nubian C-Group. International Journal of Osteoarchaeology 1994;4:223-40.
4. Lucacs J.R. Dental Paleopathology and Agricultural Intensification in South Asia: New Evidence from Bronze Age Harappa. American Journal of Physical Anthropology 1992;87(2):133-50.
5. Martin D.L., Armelagos G.J., Goodman A.H., van Gerven D.P. The Effects of Socioeconomic Change in Prehistoric Africa: Sudanese Nubia as a Case Study. In: Cohen M.N., Armelagos G.J., editors. Paleopathology at the Origins of Agriculture. New York: Academic Press; 1984. p. 193-214.
6. Bain J.M., Mercer F.V. Subcellular organisation of the cotyledons in germinating seeds and seedlings of Pisum arvense L. Australian Journal of Biological Sciences 1966;19:69-84.
7. Mizukami H., Takeda Y., Hizukuri S. The structure of the hot-water soluble components in the starch granules of new Japanese rice cultivars. Carbohydrate Polymers 1999;38(4):329-36.
8. Juge N., Nøhr J., Le Gal-Coëffet M.-F., Kramhøft B., Furniss C.S.M., Planchot V., et al. The activity of barley alpha-amylase on starch granules is enhanced by fusion of a starch binding domain from Aspergillus niger glucoamylase. Biochimica et Biophysica Acta (BBA) 2006;1764:275-84.

9. Stookey J.K. The effect of saliva on dental caries. The Journal of the American Dental Association 2008;139(Supp 2):11S-17S.
10. Dawes C. What Is the Critical pH and Why Does a Tooth Dissolve in Acid. Journal of the Canadian Dental Association 2003;69(11):722-24.
11. Cury J.A., Rebelo M.A.B., Del Bel Cury A.A., Derbyshire M.T.V.C., Tabchoury C.P.M. Biochemical Composition and Cariogenicity of Dental Plaque Formed in the Presence of Sucrose or Glucose and Fructose. Caries Research 2000;34(6):491-97.
12. Neuhaus H.E. Transport of primary metabolites across the plant vacuolar membrane. FEBS Letters 2007;581(12):2223-26.
13. Yazaki K. Transporters of secondary metabolites Current Opinion in Plant Biology 2005;8(3):301-07.
14. Sinnott M.L. Catalytic mechanism of enzymic glycosyl transfer. Chemical Reviews 1990;90(7):1171-202.
15. Malcarney H.L., del Rio C.M., Apanius V. Sucrose Intolerance in Birds: Simple Nonlethal Diagnostic Methods and Consequences for Assimilation of Complex Carbonhydrates. The Auk 1994;111(1):170-77.
16. Petersen P.E., Bourgeois D., Ogawa H., Estupinan-Day S., Ndiaye C. The global burden of oral diseases and risks to oral health. Bulletin of the World Health Organization 2005;83:661-69.
17. Bryers J.D., Ratner B.D. Biomaterials Approaches to Combating Oral Biofilms and Dental Disease. BMC Oral Health 2006;6(Supp 1):S1-S15.
18. Fejerskov O., . Changing Paradigms in Concepts on Dental Caries: Consequences for Oral Health Care. Caries Research 2004;38(3):182-91.
19. Krol D.M., Nedley M.P. Dental Caries: State of the Science for the Most Common Chronic Disease of Childhood. Advances in Pediatrics 2007;54(1):215-39.
20. Broadbent J.M., Thomson W.M., Poulton R. Progression of Dental Caries and Tooth Loss between the Third and Fourth Decades of Life: A Birth Cohort Study. Caries Research 2006;40(6):459-65.
21. Meurman J.H., Sanz M., Janket S.-J. Oral Infection and Vascular Disease. Vascular Disease Prevention 2007;4(4):260-67.
22. Silva N.R.F.A., Carvalho R.M., Pegoraro L.F., Tay F.R., Thompson V.P. Evaluation of a Self-limiting Concept in Dentinal Caries Removal. Journal of Dental Research 2006;85(3):282-86.
23. Bjørndal L. The Caries Process and Its Effect on the Pulp: The Science Is Changing and So Is Our Understanding. Journal of Endodontics 2008;34(7 (Supp. 1)):S2-S5.
24. Mertz-Fairhurst E.J., Curtis J.W. Jr., Ergle J.W., Rueggeberg F.A., Adair S.M., . Ultraconservative and Cariostatic Sealed Restorations: Results at Year 10. Journal of the American Dental Association 1998;129(1): 55-66.
25. Frencken J.E., Songpaisan Y., P. P, Pilot T. An atrauamatic treatment (ART) technique; evaluation after one year. International Dental Journal 1994;44:460-64.
26. McComb D. Systematic review of conservative operative caries management strategies. Journal of Dental Education 2001;65(10):1154-61.
27. Kidd E.A. How 'clean' must a cavity be before restoration? Caries Research 2004;38(3):305-13.

Chapter II. Literature review

2.1 Tooth structure

Mature human tooth is divided macroscopically into crown, neck and a root (Figure 2.1). Enamel, dentine and cementum are mineralized components of a tooth, pulp is a non-mineralized tissue.

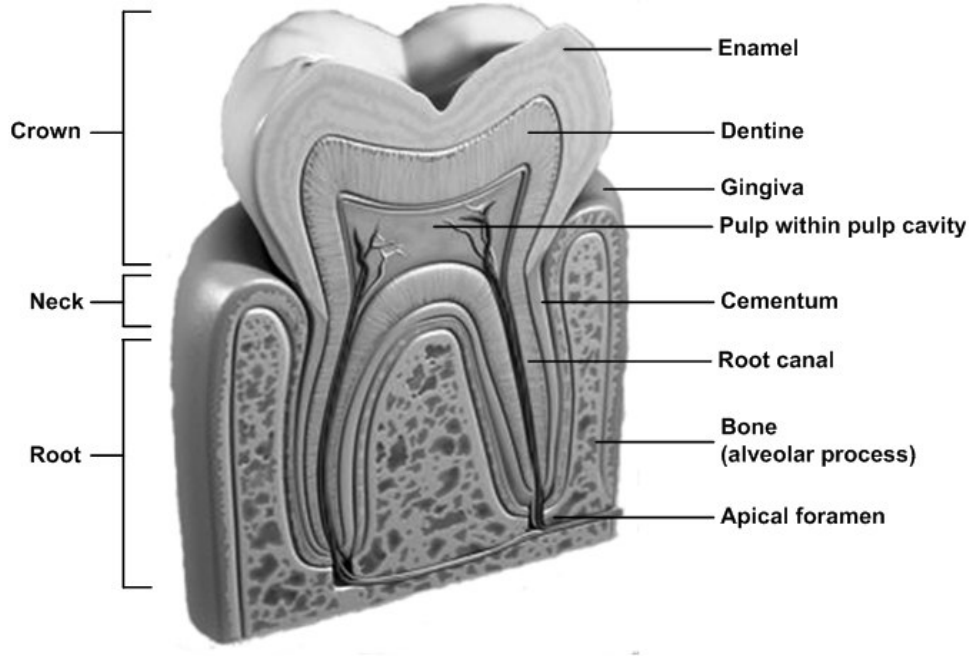

Figure 2.1 Macroscopic structure of a mature human tooth (after [1]).

The crown is covered by enamel (Figure 2.1), which is hard, acellular, avascular and the most mineralized tissue found in the body. It consists of 96% of biological apatite crystallites and the rest of the matrix components are water 3.6% and proteins 0.4% (by weight) (Table 2.1).

The root is covered by cementum (Figure 2.1), which is 50% mineralized with biological apatite crystals and it has a collagen organic matrix.

Below enamel and cementum is a dentine layer (Figure 2.1), which forms the bulk of the tooth. It is 70% mineralized with biological carbon rich hydroxyapatite

crystals and organic material of the dentine is mainly fibrous collagen type I and comprises 20% of the matrix, while the remaining 10% is water (Table 2.1). Mineralized dentine together with the pulp tissue forms the dentine-pulp complex, which is responsible for the formation and maintenance of the tooth [2]

Table 2.1. Major constituents of enamel and dentine.

Phase	Enamel		Dentine	
	Weight (%)	Volume (%)	Weight (%)	Volume (%)
Mineral	96	87 - 91	70	48
Organic	0.4	2	20	29
Water	3.6	7 - 11	10	23

2.2 Brief introduction into the enamel structure

Enamel is designed to masticate nutrients placed in the oral cavity and its mechanical behaviour, structure and composition can be derived from this specialised function [3]. Enamel differs markedly from dentine and bone in that that mature enamel contains only a minute but operationally significant amount of organic materials and water (Table 2.1). It lacks collagen and any microscopical tubular or canalicular structure. Also its porosity is of a different order and structure from that of bone [4-6].

The major component of mature enamel is carbonated hydroxyapatite (Table 2.1) and it is the hardest vertebrate structure of the human body. Enamel is composed of extremely long (at least 100 μm) [7] and narrow crystals (Figure 2.2), packed into parallel arrays, called enamel prisms (rods) (Figure 2.3) of 4-5 μm in diameter [8].

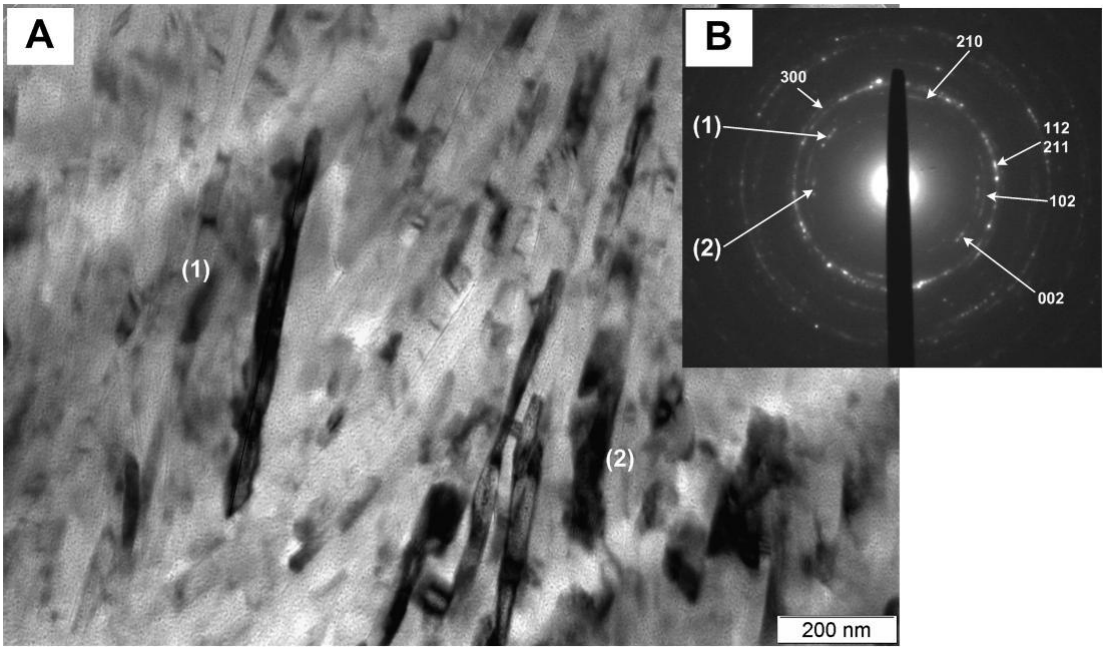

Figure 2.2 TEM bright-field image of enamel crystallites (A) forming prisms (1) and (2) at the interprismatic junction and the corresponding SAED pattern (B) with indexing confirming the apatite mineral phase with preferred orientation in c-direction of the crystallites. Arrows point to 002 reflections of the prisms (1) and (2).

They form a 3D structure that neither branch nor merge but run from the DEJ to the outer surface of the tooth and form intricate interwoven patterns [9]. Organic sheaths surround individual prisms of approximately 0.1–0.2 μm wide (Figure 2.3). They are composed of the O-linked glycosylated protein, ameloblastin [10]. Post-secretion, ameloblastin is proteolytically cleaved and accumulates in these interprismatic sheaths. Prisms are domains of highly ordered bundles of nano-size biological crystallites [11] (Figure 2.2). Each crystallite is associated with the protein enamelin, which fragments remain attached to individual crystallite surfaces after normal post-secretory cleavage [3]. Each enamel crystallite is surrounded by a hydration shell of clustered water. Clustered water exists at two structural levels: prism sheaths and hydration shells. Clustered water uniquely differs from the bulk water in both its physical and chemical attributes [12]. Clustered water exhibits long-range order and is

capable of forming an infinite hydrogen-bonded network, with localised, supramolecular aggregates or clusters [13].

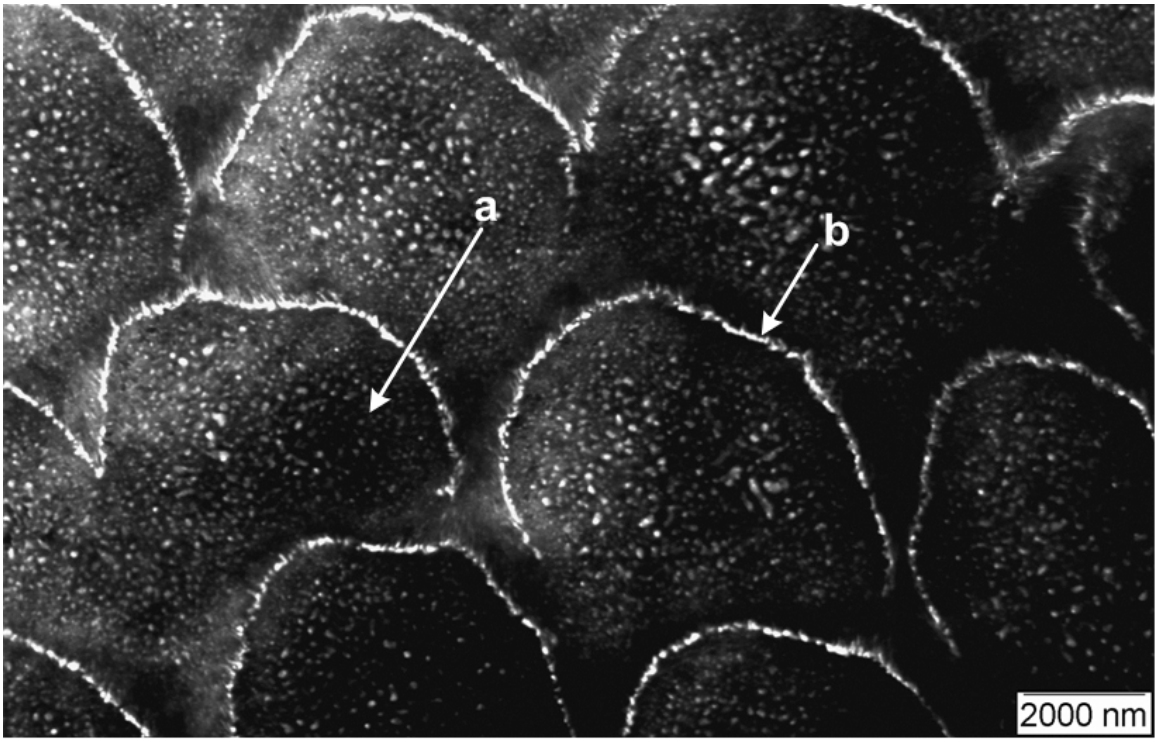

Figure 2.3 TEM bright-field image of human enamel prisms (a) and interprismatic sheaths (b).

This high degree structural organisation of enamel strongly suggests that extracellular enamel matrix proteins secreted by ameloblasts during early stages of amelogenesis must regulate this organisation. The organic matrix of forming tooth enamel consists of two main categories of proteins, the amelogenin (AMEL) and non-amelogenins, namely ameloblastin (AMBN), enamelin (ENAM) [14] and a matrix metalloproteinase, enamelysin (MMP-20) [15]. The importance of these proteins in enamel formation in mammals has been demonstrated through recent animal studies. AMEL knockout mice [16] and transgenic mice expressing mutated forms of AMEL [17-19] exhibited major structural defects that affected overall enamel thickness and prism structure. AMBN gene knockout and ENAM point mutations studies demonstrated that these proteins are essential in development of the enamel layer itself [20, 21]. MMP-

20 null mice exhibit a severely abnormal tooth phenotype, with an altered prism pattern and hypoplastic enamel that delaminates from dentine [22, 23]. A serine proteinase ESMP1 (kallikrein 4) has also been identified in enamel during the maturation stage and it is believed to be responsible for almost complete breakdown of enamel proteins [24].

AMEL accumulate in the forming enamel layer while AMBN and ENAM are present extracellularly in smaller amounts due to a very short half-life and therefore does not accumulate [25]. Both AMEL and non-amelogenin proteins, which form enamel matrix are believed to regulate biomineralization and structuring of the enamel mineral phase and eventually are almost completely removed through the process of the extracellular enzymatic degradation [26]. This allows enamel to achieve an extremely high mineral density through a maturation process associated with ameloblast modulation [26] much higher than that found in collagen-based calcified structures such as dentine.

Ameloblasts are responsible for producing of the organic matrix of forming enamel and they exhibit an extensive Golgi apparatus, which occupies much of the supranuclear compartment [27, 28]. The secretory granules of the cells are directed towards two spatially distinct secretory sites on an apical extension called Tome's process where they release proteins to build up interprism and prism enamel [29]. The secretory granules that accumulate at these sites constitute a morphologically and cytochemically heterogeneous population [30]. Presently it is inconclusive whether the characteristic spatial distributions of the AMEL and AMBN is the result of a distinctive intracellular routing or represent differences in their extracellular activity [31].

The extracellular distribution of AMEL and non-amelogenins has been linked with their function. AMEL is found throughout the forming enamel with the lowest levels present at the enamel growth sites [25, 32]. AMEL form supramolecular aggregates in the form of nano-spheres, which are densely packed within the gaps between the biological apatite crystals throughout the forming enamel layer [33]. It is believed that the individual protein molecules forming the nano-spheres inhibit the growth of crystals in width and length by attaching their hydrophilic C-terminal portions to the faces of the growing crystals [34].

Opposite to AMEL, AMBN and ENAM accumulate at the enamel growing sites, where apatite crystals actively elongate and only fragments of these proteins were found deeper within enamel layer [25, 35, 36]. The concentration of AMBN at the enamel growth sites and a lack of formation of an enamel layer when the corresponding gene is switched off suggest its role in crystal elongation although how this protein accumulates at the growth sites and how it exerts a regulatory effect on the growth of apatite crystals is unknown.

2.3 Dentine-pulp complex

Dentine is the mineralized connective tissue that constitutes the bulk of the tooth. Dentine is a mesenchymal tissue and as such based on a collagenous matrix reinforced by apatite crystallites. It is intimately related to the dental pulp with which it shares the same embryological origin from dental papilla. Dentine forms the hard tissue portion of the dentine-pulp complex, whereas the dental pulp is the living, soft connective tissue that retains the vitality of dentine [37]. Dentine contains multiple closely packed dentinal tubules surrounded by a cuff of highly mineralized peritubular dentine and collagen based intertubular dentine between them (Figure 2.4). It is still

unclear whether peritubular dentine is also a collagen based structure but based on the effect of piezoelectricity of collagen fibrils and applying piezoresponse force microscopy (PFM) technique the hypothesis that peritubular dentine is a non-collagenous material was put forward [38] and therefore makes peritubular dentine the only known exception among mineralized tissues that derive from the mesenchyme [38]. Dentinal tubules contain dentinal fluid and the cytoplasmic processes of the cells that formed dentine, the odontoblasts, are located. Human pre-odontoblasts originate from neural crests and migrate from the central part of the mesenchymal or embryonic pulp towards the periphery of the pulp. Pre-odontoblasts are actively dividing cells with the fixed number of mitoses. The final mitotic division is followed by the differentiation of two specific groups of cells. The outermost cells, which are in contact with the basement membrane, differentiate into post-mitotic polarizing odontoblasts, while the daughter cells, located some distance from the basement membrane, are included into the Höhl's layer and serve as replacement cells in case of odontoblast alterations. The fully differentiated human odontoblast is a polarized columnar cell, approximately 50 μm tall. It has non-secretory proximal (basal) and secretory distal (apical) ends. The nucleus is located at the proximal pole of the cell body, mitochondria and organelles associated with protein synthesis (rough endoplasmic reticulum (REP) complex and well developed Golgi apparatus) are found distally. Odontoblasts are connected extensively with each other and with a subodontoblastic layer by desmosomes and gap junctions. The odontoblastic processes and the soma are separated by a terminal web of microfilaments. Normally vital odontoblasts remain throughout life on the dentine's pulpal surface along the predentine border [39].

Under the odontoblasts layer there is a cell-free zone (the zone of Weil), which followed by a deeper layer, which has high cell density (a cell-rich zone). The pulp

core, in which the cell density is again reduced, consists of connective tissue, major blood vessels and nerves. The unity of dentine-pulp is responsible for dentine formation and protection of the tooth.

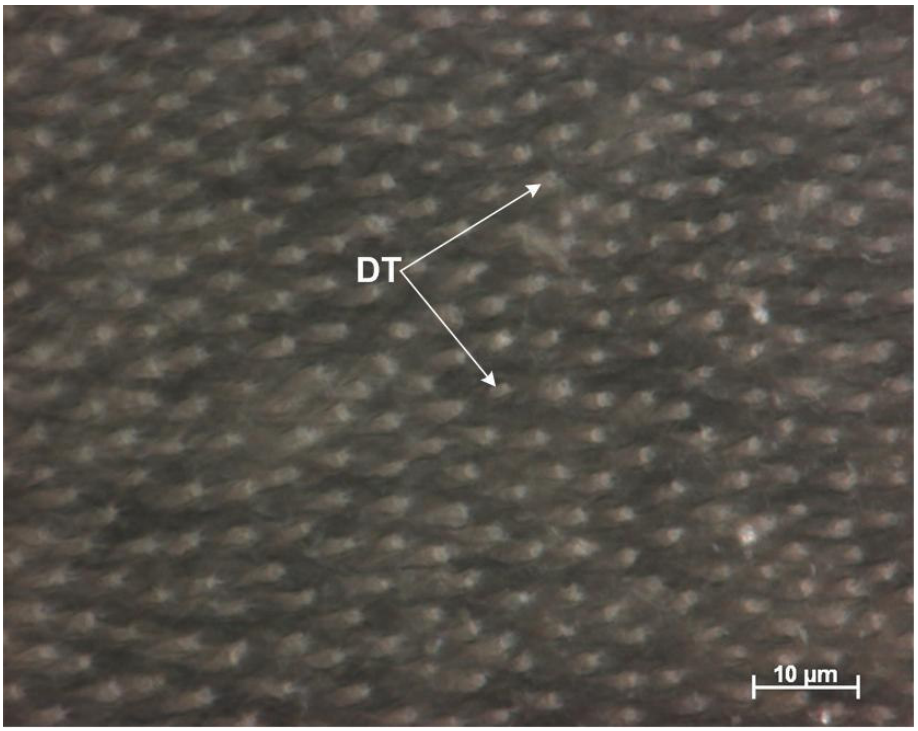

Figure 2.4 Optical image of dentinal tubules (DT) in the middle crown dentine. Average diameter of the tubules was 1.5 µm. The dark contrast material between the tubules was intertubular dentine.

2.4 Dentine-enamel junction (DEJ)

Dentine-enamel junction (DEJ) is the common surface (Figure 2.5), from which ameloblasts and odontoblasts move oppositely during odontogenesis. For many years hard and brittle enamel has to function in the oral cavity together with dentine, which is a much softer and tougher material, where these materials are subjected to a cyclic mechanical loading, thermal and hydration stresses. Opposite to some other mammalian species, in humans the load from the enamel cap is distributed into the bulk of dentine during mastication without fracture [40]. Instead, the continuous cycle loading of a human tooth during mastication results in a fatigue damage, which is

associated with pathology or extensive wear and therefore elastic properties of enamel and dentine are more important for the human teeth than the fracture properties of these materials. The importance of DEJ as an interface binding dentine and enamel together has long been recognized [41] and intensively studied. However, still the views on the ultrastructure of DEJ remains unsettled. It was demonstrated that early enamel apatite crystals are formed in intimate association with dentine crystals located at the terminal ends of dentine collagen fibrils and that the enamel and dentine domains are continuous with the co-localisation of apatite crystallites extending from the calcified collagen fibrils to enamel sheaths [42]. Other studies however, demonstrated no inter-domain continuity with the existence of protein-rich continuum between enamel and dentine [43, 44].

It was demonstrated that the dentine zone of 200 – 300 μm adjacent to DEJ has a compression elastic modulus (stiffness) of 1 – 12 GPa measured on fully hydrated teeth by means of non-contact laser-speckle interferometer (ESPI) [45]. This value is significantly lower than the value of stiffness measured with resonant ultrasound spectroscopy (RUS) for a hydrated bulk crown dentine of 24.4 GPa (isotropic symmetry model) [46], by an atom force microscope (AFM) of fully hydrated dentine specimens, 22.8 – 24.5 GPa [47] or measured with a nano-indenter in air (exposure to air was minimized to prevent drying), 24.8 GPa [48]. Mechanical deformation and the in-plain strain distribution mapping of tooth slices by the Moiré fringe interferometry technique demonstrated that most strain was concentrated in this softer 200 μm dentine layer adjacent to the DEJ and it was suggested that this zone functions as a cushion, which allows enamel and dentine work together [49]. By means of high-resolution Moiré fringe technique it was demonstrated that this zone of dentine is subjected to high strain levels during hydration/dehydration cycles and that

maximum peaks of the stiffness exist at buccal and lingual sides of a tooth [50], which not only confirmed the results of the finite element analysis that the stress on the cusp tip is transferred downwards along the buccal and lingual sides of enamel to the cervical margin and then through the DEJ to the root dentine [51, 52] but also suggested that stress is transferred through buccal and lingual sides of enamel into the coronal dentine through mid-way between the cusp tip and the cervical margin on to root dentine.

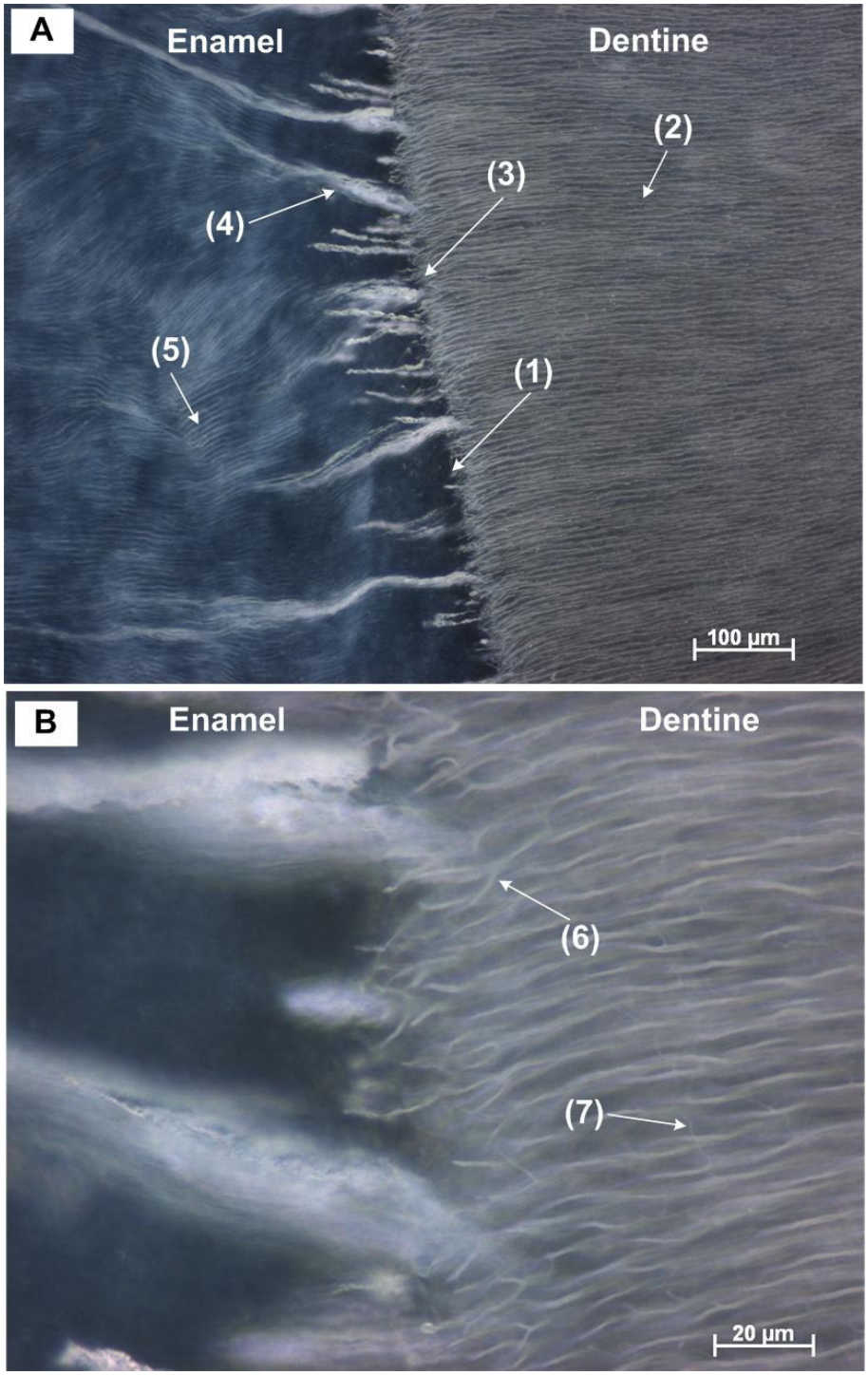

Figure 2.5 Dark field optical image of enamel, DEJ, mantle and circumpulpal dentine. A. The DEJ interface (1) separated enamel and dentine. The dentinal tubules were light contrast lines (2) representing microscopic channels, which radiated outward through the whole thickness of the dentine from the pulp to the exterior cementum or enamel border, DEJ on this image. The darker contrast material between the tubules was intertubular dentine. The lighter contrast material of approximately 30 µm adjacent to DEJ (3) was mantle dentine. The light contrast thick lines protruding from DEJ into the thickness of enamel (4) were tufts. Thin light contrast lines visible in enamel (5) were enamel rods of approximately 5 µm in diameter. B. Demonstrates magnified image of the DEJ and dentine. Y-shaped dentinal tubules terminal branches (6) were clearly visible at the DEJ. Lateral microbranches were visible throughout the thickness of the circumpulpal dentine (7).

2.5 Dentinogenesis and biomineralization

Predentine is the unmineralized layer with the constant 15–20 μm thickness followed by metadentine layer 0.5 to 2.5 μm thick and mineralized dentine on one side and odontoblasts on the other side. Dentine mineralization sharply occurs at the metadentine mineralization front [37, 53, 54]. At the onset of dentine formation odontoblasts synthesize and secrete type I collagen, proteoglycans and other significant constituents to the predentine layer. In predentine collagen molecule fibers aggregate with their long axes in parallel into fibrils, which further arrange into bundles, possibly with the help of proteoglycans [55, 56]. Following synthesis of the dentine organic matrix, a formation of an inorganic phase at the mineralization front occurs. Calcium ions $\left(Ca^{2+}\right)$ are transported to the mineralization front by a transcellular route. This route includes a Ca^{2+} - activated ATPase, which in conjunction with Na^{+}/Ca^{2+} - exchangers, calcium channels and intracellular calcium binding proteins, maintain a fine calcium ion homeostasis in odontoblasts [57-61]. Highly phosphorylated dentine phosphoprotein, phospholipids and possibly other pool of proteoglycans are added to the mineralization front where they act as mineral nucleators and induce apatite formation. They bind to the collagen fiber surface and enhance the ability of the fibres to bind calcium ions and therefore mineral deposition [62, 63]. Alkaline phosphatase, which non-specifically cleaves phosphate ions from compounds, was associated with matrix mineralization and it was shown to increase at the mineralization front where crystal growth is occurring [64]. In addition stromelysins of matrix metalloproteinases may further control proteoglycan turnover [65]. Primary dentine matrix is synthesized at a rate of approximately 4 μm per day during tooth development [37, 54]. This increase in thickness occurs to the detriment of the pulp. The

rate of dentine deposition decreases at the end of the root formation. The tooth volume consists primarily of primary dentine, which outlines the pulp chamber and therefore it is referred as circumpulpal dentine. At the outermost layer of the primary dentine, subjacent to the DEJ, there is a zone of approximately 30 μm called mantle dentine (Figure 2.6). This layer was formed as the result of the very first mineralization activity of the newly differentiated odontoblasts. It exhibits extensive peripheral branching and has a slightly different composition than circumpulpal primary dentine [37, 54].

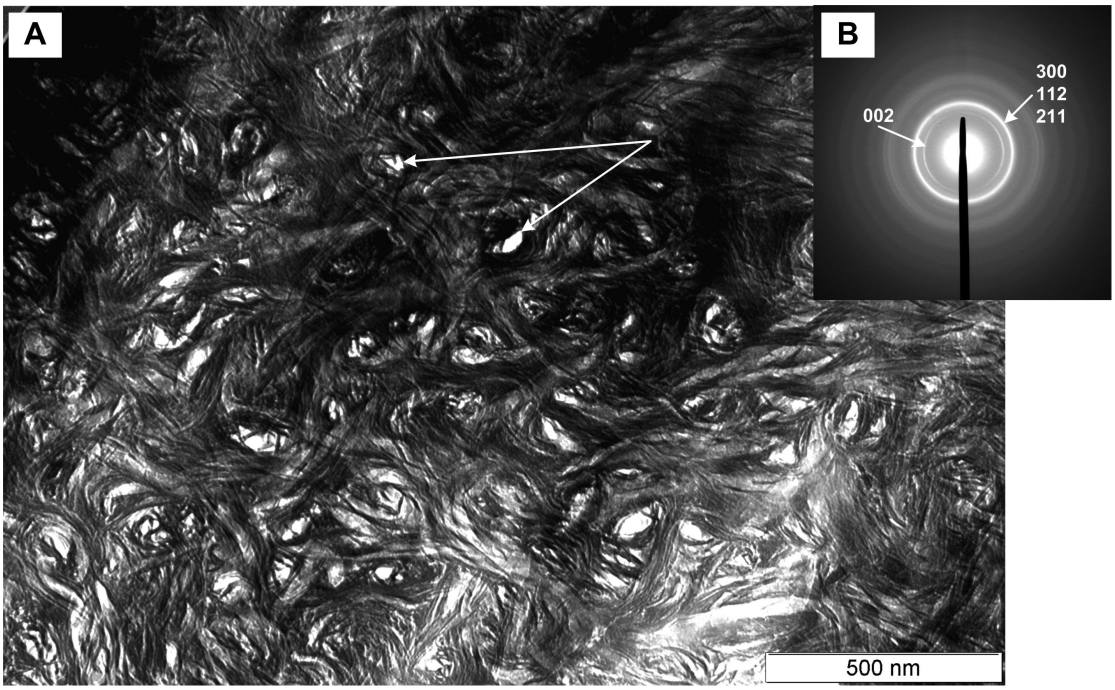

Figure 2.6 TEM bright-field image of mantle dentine at 4 μm below DEJ (A). Arrows indicate bending of crystallites around the voids. Indexing of the corresponding SAED pattern (B) confirms the presence of apatite and a highly polycrystalline structure at the characteristic scale of 1 μm.

The characteristic feature of the physiological dentine matrix is its tubular pattern [54] (Figures 2.4 and 2.5). Dentinal tubules extend from the odontoblastic layer to the dentine-enamel junction (DEJ). Dentinal tubules form around the pre-existing odontoblastic processes and the diameter of the tubules is only slightly larger than the diameter of the odontoblastic processes. The space between the odontoblastic process

membrane and the dentinal tubule wall is called the periprocessal space and its thickness is 0.2 – 0.4 μm. The extent of odontoblastic processes into dentinal tubules of the mature teeth is unclear at the present time. Initially the odontoblastic processes fill the entire length of dentinal tubules but in mature dentine, due to centripetal retraction, the odontoblastic processes extend only into inner ¼ of tubules length [66]. Conversely, it was reported that the odontoblastic processes continuously present through the entire length of dentinal tubules, including all the branches in mature dentine [67]. In addition to odontoblastic processes, tubules contain dentinal fluid, a complex mixture of proteins such as albumin, transferrin, tenascin and proteoglycans [37, 54]. Furthermore, dentinal fluid calcium and sodium concentrations have been shown to be higher in injured teeth compared to intact ones, indicating an active transportation system between the matrix and the tubules [68]. Loosely aggregated collagen fibre bundles have also been detected in the dentinal tubules [69]. Whether the hypermineralized type of dentine detected inside the dentinal tubules (intratubular dentine) is the result of odontoblast activity or purely the result of physicochemical reactions within dentine minerals is presently unknown [54]. However, the intratubular dentine formation inside the tubules may ultimately obliterate the tubules and reduce the permeability of the dentine, which has, in turn, a positive impact on pulp vitality [54]. Following primary dentinogenesis, odontoblasts continue to deposit a physiological, secondary dentine around the pulp at a slow rate leading eventually to the reduced size of the pulp chamber. Secondary dentine is commonly formed in erupted, functionally occlusal, non-carious, permanent teeth. Odontoblasts deposit secondary dentine in those areas of the pulpal wall, which are subjacent to the functionally loaded enamel surface [70]. Structurally secondary dentine resembles

primary dentine and also have a tubular pattern, which is however, less regular than that of the primary dentine [37, 54].

2.5.1 Tertiary dentine

As a response to various external stimuli, such as dental caries, attrition and trauma, tertiary dentine is synthesized. If the injury is severe and causes odontoblast cell death, odontoblast-like cells synthesize specific reparative dentine just beneath the site of injury to protect pulp tissue [37, 54, 71-74]. Unlike physiological dentine, the morphology of the reparative dentine varies greatly and is often irregular, with cellular inclusions. Furthermore, the tubular pattern of the reparative dentine varies from a discontinuous to an atubular nature and thus the reparative dentine matrix permeability is reduced and diffusion of noxious agents from the tubules is prevented [75]. However, if injury to the tooth is mild and primary odontoblasts survive, they are stimulated to synthesize reactionary dentine, which resembles primary dentine matrix and has a tubular pattern [75].

2.6 Organic matrix of dentine

The dentine organic matrix primarily consists of fibrous collagens and non-collagen proteins (NCP) such as phosphoproteins, proteoglycans, phospholipids etc. The matrix provides the framework for biomineralization.

2.6.1 Collagen

Collagens (Table 2.2) comprise 90% of the dentine matrix [76]. Collagens form a family of proteins and each type has its own characteristic amino acid sequence. Each collagen molecule consists of three individual polypeptides known as α-chains. Each

α-chain has a left-handed helical secondary structure around its axis. By means of X-ray diffraction technique it was identified that three α-chains are coiled around each other into a right-handed superhelix called a triple helix structure, also known as Madras helix [77]. Using topographical enumeration technique it was demonstrated that in order to form a triple helix structure each individual chain contains glycine in the every third amino acid position [78]. This triple-helical conformation is unique to collagen. Application of the immunochistochemical technique revealed that collagen type I is the principal collagen of the dentinal matrix [79, 80]. By means of the variety of different techniques such as CM-cellulose chromatography, ultracentrifugation, light scattering, gel filtration and gel electrophoresis it was identified that type I collagen is composed of two identical α1(I) chains and one α2(I) chain [81]. In situ hybridization technique allowed to demonstrate that pro-α2(I) mRNA is expressed by mature human odontoblasts [82], while the other collagen chain pro-α1(I) mRNA has not been studied in fully developed human odontoblasts. Type I collagen is synthesized as a larger procollagen, which contains extensions at both N- and C-terminal ends, called the aminoterminal and carboxyterminal propeptides, which prevent premature collagen aggregation into fibrils [83]. After procollagen is secreted from cells, extracellular modification takes place and propeptides are removed by specific proteinases and mature collagen molecules aggregate into a fibrous matrix [84, 85], which then serves as a scaffold for inter- and intrafibrillar mineral deposition [86].

Type I trimer is a collagen consisting of three α1(I) chains. Using densitometry method to scan gels after electrophoresis it was demonstrated that type I trimer is synthesised by odontoblasts actively forming mineralized dentine in rodent teeth [87] and applying gel electrophoresis technique type I trimer was identified in bovine teeth [88]. The occurrences of type I trimer in the human teeth is unknown.

Type III collagen, a homopolymer of three α1(III) chains, was identified by means of gel electrophoresis technique as a conspicuous constituent of pulp tissue, where it comprises approximately half of the collagen matrix [89, 90]. Using immunohistochemical technique the evidence that calcified tissues are also able to express type III collagen was produced and it was shown that mature and intact human odontoblasts secrete type III collagen after tooth development [91]. Using immunostaining technique type III procollagen was observed to be transiently located in human predentine during matrix formation but not in mineralized dentine [92]. The role of type III collagen in normal physiological dentine mineralization is unknown. Transmission immunoelectron microscopy revealed that type III collagen is a constituent of the abnormal dental matrix such as in dentinogenesis imperfecta patients [93]. Also using immunochistochemical localization technique type III collagen has been detected in reparative dentine of carious human teeth [91, 94].

Additionally using immunochemical staining technique other collagens were detected in the organic matrix of human dentine, i.e. expression of type V collagen was observed in the predentine of mature human teeth but not in dentine [80] and type VI collagen was detected both in predentine and dentine of intact teeth [92] and in the teeth of dentinogenesis imperfecta patients [93].

Table 2.2 Collagen (90%) in the dentine biological matrix.

Collagen	Structure	Role
Type I collagen	$\left[\alpha 1(\mathrm{I})\right]_2 \alpha 2(\mathrm{I})$	Scaffold
Type I trimer	$\left[\alpha 1(\mathrm{I})\right]_3$	Elasticity of the structure
Types III, V, VI	Minor collagens 1 – 3 %	Pathologic dentine

2.6.2 Phosphorylated proteins

Phosphorylated proteins identified in dentine (Table 2.3) are small molecules containing integrin-binding tri-peptide Arg-Gly-Asp (RGD) cell adhesion sites and therefore these proteins are known as Small Integrin-Binding Ligand N-linked Glycoprotein (SIBLING) family [95, 96]. It should be noted however, that technically osteopontin (OPN) may not be always N-glycosylated [97]. These proteins also share other common features such as the presence of relatively large amounts of sialic acid and phosphate [98].

Dentine phosphophoryn (DPP) [99], dentine sialoprotein (DSP) [100, 101] and dentine glycoprotein (DGP) [102], also known as DSP-PG, are dentine sialophosphoprotein (DSPP) gene products and highly phosphorylated proteins that accounts for 50% of all non-collagenous dentinal proteins [103]. DPP was identified in human dentine using thin layer chromatography technique [104]. Using light microscope radioautography technique it was demonstrated that DPP is deposited directly at the advancing mineralization front of dentine [105]. DPP covalently cross-linked to type I collagen and induces the mineralization of the collagen in calcium phosphate solutions, therefore plays crucial role in calcification of dentine [106, 107], which was directly confirmed when DSPP-null mice developed dentine defects in the absence of other symptoms [108]. The role of DSP on dentine mineralization, which accounts for 5 to 8% of the dentine matrix, is not clear at the present time [109] but using transgenic mice overexpressing DSP the increased hardness of enamel was demonstrated and it was concluded that DSP may contribute to structural properties of the innermost layer of enamel close to DEJ that is formed during the initial stages of amelogenesis when DSP is naturally expressed [110]. DGP was recently characterized [111] but its role has not yet been elucidated.

Dentine matrix protein 1 (DMP1), also known as AG1, was identified by cDNA cloning using a rat odontoblast mRNA library [112]. DMP1 is a very acidic phosphoprotein and contains a large number of acidic domains, which implies it as also a key participant in regulating dentine matrix mineralization [112, 113]. The importance of DMP1 for dentine was demonstrated by knockout experiments in mice and by mutation studies in humans: DMP1 null mice showed profound defects in the mineralization dentine such as hypomineralization of dentine, increased width of predentine layer, enlarged pulp [114] and mutations in the Dmp1 gene resulted in autosomal-recessive hypophosphatemic rickets in humans [115]. Like DSPP, DMP1 is present in the ECM of dentine as (i) an NH_2- terminal (37 kDa) fragment, (ii) a $COOH$-terminal (57 kDa) fragment [116], and (iii) a proteoglycan form known as DMP1-PG of the NH_2 - terminal fragment [117]. These three forms, different in structure, may be distributed differently among individual compartments of tooth and may have different functions in dentinogenesis.

Bone acidic glycoprotein (BAG-75), phosphorylated glycoprotein, was isolated from dentine using SDS-PAGE and Western immunoblots techniques [98]. Biological significance of BAG-75 though unclear at the present time but based on the gold immunolabelling technique it was demonstrated *in vivo* and *in vitro* that BAG-75 self-associates into large spherical aggregate structures composed of a meshwork of 10 nm diameter fibrils, which as identified by X-ray microanalysis, sequester large amounts of phosphate ions and therefore it was proposed that macromolecular complexes of BAG-75 may function as extracellular electronegative barriers restricting local diffusion of phosphorus ions and therefore facilitating nucleation of apatite [118].

Bone sialoprotein (BSP) is a highly glycosylated and sulphated phosphoprotein was identified in dentine using competitive enzyme immunoassays technique [119]. Based on the finding of the ability of BSP to bind to collagen [120], hydroxyapatite [121] and to cell membrane receptors [122] it was proposed that BSP mediates interactions between the matrix and cells. It was also proposed that BSP acts as a nucleator for the formation of the initial apatite crystals [123] and at later stages as this mineral grows on the collagen matrix it acts as an inhibitor in directing the growth of the crystals [121].

Osteopontin (OPN) in dentine was demonstrated biochemically [119]. Using in situ hybridization [124, 125] and Western immunoblots [98, 125] techniques it was concluded that odontoblasts do not express OPN at the early stages of dentine formation, however direct observations using immunochemistry techniques demonstrated OPN over the Golgi region at the beginning of mantle dentine mineralization [126]. OPN may be associated with the odontoblastic process serving as a link between matrix and cell membrane. OPN null mice also demonstrated that OPN may be a major inhibitory factor of mineralization [127].

Matrix extracellular phosphoglycoprotein (MEPE), also often referred as OF45 has been recently demonstrated in dental tissue, in odontoblasts, using reverse-transcription polymerase chain reaction (RT-PCR) amplification and characterization of a partial mouse cDNA [128]. Using immunochemistry techniques it was demonstrated that MEPE is mechanically responsive and has a distinct role in the response of osteocytes to mechanical loading but what that role is, is at present unknown.

Table 2.3 Phosphorylated proteins identified in dentine.

Phosphorylated proteins (SIBLING)	Role
DPP, DSP, DGP	Promotion of mineralisation
DMP1	Promotion of mineralisation
BAG-75	Promotion of mineral nucleation
BSP	Promotes mineral nucleation but acts as a crystal growth inhibitor
OPN	Inhibitor of mineralisation
MEPE	Unknown

2.6.3 Non-phosphorylated proteins

Non-phosphorylated proteins identified in dentine are summarised in Table 2.4. Matrix Gla protein (MGP) was first isolated from bovine bone matrix [129] and characterized as it contained calcium-binding γ-carboxyglutamic acid (Gla) residues and three phosphoserines [130]. MGP has high affinity to calcium and HAP through the interaction with Gla residue, which implies that MGP is an effective mineralization inhibitor. This hypothesis was reinforced when it was demonstrated that MGP-null mice exhibited abnormal calcification of cartilages, aortic walls and valves [131] but the role of MGP of dentine mineralization is unknown at present.

Osteocalcin, also known as bone Gla protein, has been observed in rodent dentine [132] but the biochemical study reported no osteocalcin present in human and bovine dentine [133], which was confirmed by immunolabelling in intertubular dentine of human forming teeth [134]. Also it was demonstrated that bovine odontoblasts were immunonegative to osteocalcin [133]. Conversely, applying immunochistochemistry technique on human dentine revealed osteocalcin presence in odontoblasts and through the entire length of the odontoblastic processes as well as within enamel

matrix at the DEJ [134]. Although its role in biomineralization of the dentine organic matrix is unclear at present, osteocalcin-null mice demonstrated increased mineralization in bones [135]. These observations were also supported by *in vitro* studies demonstrated that osteocalcin is an effective inhibitor of HAP growth [136].

Osteonectine is expressed by odontoblasts but as was demonstrated in human [134] and bovine [137, 138] dentine, it was only restricted to the unmineralized predentine for the intertubular dentine. Conversely, using reverse transcription polymerase chain reaction (RT-PCR) technique osteonectine was also demonstrated in human peritubular dentine and that the odontoblast cell process membrane interacted locally with osteonectine [134]. It was therefore proposed that since the cellular processes of osteonectine-producing odontoblasts are in contact with external stimuli, e.g. cariogenic bacteria products, osteonectine stimulates peritubular dentinogenesis, which may result in tubules obliteration under pathological conditions.

Table 2.4. Non-phosphorilated proteins found in dentine.

Non-phosphorylated proteins	Role
Matrix GLA protein	Inhibitor of mineralisation
Osteocalcin	Inhibitor of mineralisation
Osteonectine	Unknown

2.6.4 Proteoglycans

Proteoglycans (PGs) constituent another portion of non-collagenous components of dentine (Table 2.5). Using autoradigraphic technique it was shown that the odontoblasts synthesise two distinct pools of PGs: one in the proximal part of the predentine, which then diffuse through the predentine layer and another one near the predentine-dentine interface [139]. Applying techniques based on collagenase digestion

and anion-exchange chromatography the presence of condroitin sulfate (CS) PGs in dentine was demonstrated [140]. Binding studies have suggested that CS is capable of binding five time more calcium than dermatan sulfate (DS) PGs at a calcium concentration similar to that of serum [141]. Using histochemical technique it was demonstrated that intact DS proteoglycans can inhibit mineralization [142], which suggests that the presence of DS PGs within predentine may act as inhibitors of mineralization. This also implies that the degradation of DS PGs in predentine near the mineralization front may be a necessary step before mineral deposition. Conversely, the presence of highly sulfated CS PGs within the predentine-dentine interface may have a role of the control of mineralization perhaps as ion exchangers [143]. Using liquid chromatography technique traces of keratan sulfate (KS) were also detected in dentine [144].

Table 2.5 Proteoglycans and glycosamino-glycans constituents of the dentine biological matrix.

Proteoglycans and glycosamino-glycans	Role
CS/DS containing SLPRs: decorin-biglycan	Role in the inhibition or promotion of mineralisation is unknown
KS containing SLRPs: lumican, fibromodulin, osteoadherin	Collagen fibrillogenesis

The exact role of PG populations in either inhibiting, promoting or guiding the biomineralization process is inconclusive at the present time.

2.6.5 Growth factors

Dentine biological matrix also contains several growth factors and cytokines (Table 2.6) with various biological effects onto dentinogenesis events [145]. Since mature human dentine does not undergo remodelling like bone does, it is likely that growth

factors sequestered in the dentine matrix may mediate the cellular responses during tissue repair processes [145]. The transforming growth factor-β (TGF-β) superfamily consists of numerous structurally related secreted proteins including TGF-β, bone morphogenetic proteins (BMPs), activins and inhibins [146-148]. They play an essential role in the development and maintenance of the adult tissue homeostasis. In the dentine-pulp complex TGF-β or BMP are believed to regulate both tooth development and the response to external irritation [75, 149, 150]. Three forms of TGF-β were identified in mammals: TGF-β1, TGF-β2 and TGF-β3 but only TGF-β1 was detected in human dentine [151, 152]. TGF-β1 released from dentine matrix has target receptors both in odontoblasts and pulp tissue, which indicates that signalling pathways in the cells respond to the TGF-β [153]. TGF-β1 was associated with reactions in response to the dental injury by regulating tertiary dentine formation [75]. Depending on the degree of injury TGF-β1 either stimulates pulpal cell proliferation and differentiation [154, 155] or has an effect on the odontoblasts and pulpal cell secretory activity [155, 156]. Upon which cell responds to TGF-β1, reactionary (odontoblast cells) or reparative (odontoblast-like cells) dentine is formed to protect pulp vitality against external irritants [75]. The effect of TGF-β on type I collagen synthesis in calcified tissue repair is not clear at present. Although TGF-β may induce type I collagen synthesis in several tissues, in osteoblasts collagen synthesis is affected by the state of cell differentiation and in mature osteoblasts TGF-β1 has no effect on collagen synthesis [157]. Animal studies with osteoblast-like cells indicate that TGF-β1 had no effect on type I collagen synthesis [158]. However, TGF-β may stimulate type I collagen in young cells, which have recently differentiated [155, 157].

2.6.6 Bone morphogenetic proteins

Bone morphogenetic proteins (BMPs) induce bone and cartilage formation [159, 160] however, unidentified BMP was also been purified from human dentine [161], their role in dentine formation is unknown. 15 types of BMPs were identified [146, 162-167], of which BMP-2 and BMP-4 form a subgroup. It was demonstrated that BMP-2 expressed by both functional odontoblasts and human adult pulp tissue [149, 168, 169]. BMPs have some role in repair processes in mature teeth since it was shown that BMP-2 induced reparative dentine formation [150].

Table 2.6 Growth factors in dentine-pulp complex.

	Growth Factors
Dentine	TGF-β1 BMP activity EGF FGF-2 IGF-I IGF-II PDGF-AB P1GF VEGF
Odontoblasts	TGF-β1 BMP-2 IL-8
Pulp	BMP-2 BMP-4 BMP-6 OP-1 HGF IGF-II IL-1 IL-2 IL-6 IL-8 NGF VEGF

2.6.7 Matrix metalloproteinases and tissue inhibitors of metalloproteinases

Matrix metalloproteinases (MMPs) family includes 28 secreted or transmembrane enzymes collectively capable of processing and degrading various extracellular matrix (ECM) proteins. MMPs are counteracted by the tissue inhibitors of metalloproteinases (TIMPs), which inhibit MMP activity and therefore control MMP-mediated ECM breakdown [170]. It was demonstrated that matrix metalloproteinases (MMPs) are implicated in epithelio–mesenchymal interactions during the initial stages of odontogenesis [171]. MMPs and TIMPs identified in dentine are summarized in Table 2.7.

MMP-1 (collagenase-1) was detected in gingival fibroblasts capable of disrupting ECM collagen [172]. MMP-1 represents the stable active enzyme [172, 173].

Active MMP-1 hydrolyzes type I collagen into N-terminal ¾, and the C-terminal ¼ fragments. However, it hydrolyzes type III collagen 10-fold faster than type I collagen [172].

MMP-2 (gelatinase-A, 72 kDa type IV collagenase) is produced by osteoblasts and odontoblasts [174, 175]. MMP-2 has also been identified in sound [176] and in carious [177] human dentine. MMP-2 preferentially cleaves gelatin and type IV collagen, but also types V and VII collagens, fibronectin [178, 179] and type X collagen [180]. MMP-2 is also able to cleave soluble, triple helical type I collagen at the typical Gly-Ile / Leu sites, producing the ¾ and ¼ fragments [181]. The catalytic and hemopexin domains of MMP-2, but not the fibronectin domain, are responsible for collagenolysis [182]. MMP-2 also degrades cartilage proteoglycan and elastin [183], IL 1β [184] decorin [185] and laminin-5 [186]. MMP-2 exists in the ECM bound to type I and type IV collagen molecules, gelatin and laminin. MMP-2 binds to type I collagen through the fibronectin domain, which stabilizes it from autolysis, thereby controlling its activity [187, 188]. On the other hand, latent MMP-2 is one of the few MMPs so far known to localize to the cell membrane for proteolytic activation [189].

MMP-20 (enamelysin) is mostly expressed by odontoblasts in mature tissues and also to a smaller extent in pulp tissue [190, 191]. During tooth development MMP-20 localizes to ameloblasts, odontoblasts, enamel and to a lesser extent to dentine [192-195]. It was demonstrated that MMP-20 was found to be expressed in oral squamous cell carcinoma (SCC) cells *in vitro* [196] but to date they are the only cells outside the tooth forming cells that have been shown to express MMP-20. In MMP-20 knock-out mice, an amelogenesis imperfecta phenotype was seen, but the circumpulpal dentine seemed apparently unaffected [23]. Also MMP-20 knock-out mice studies revealed hypomineralized mantle dentine and it was suggested that the mineralization of

mantle dentine is postponed rather than completely arrested in the absence of MMP-20 [197].

Table 2.7 Dentine matrix metallo-proteinases.

Metallo-proteinases	Structure	Role
MMP - 1	Collagenase	Native collagen cut into ¼ - ¾
MMP – 2 & 9	Gelatinase A & B	Degradation of collagen peptides
MMP - 3	Stromelysin 1	Proteoglycans
MMP - 20	Enamelysin	Amelogenin expressed by odontoblasts
MT1 - MMP	Activation of proforms	
TIMP – 1 & 3	Forming complexes with MMPs	Inhibition of MMPs

2.6.8 Other organic components of dentine matrix

Other molecules found in dentine ECM are summarised in Table 2.8. Applying immunohistochemistry technique it was demonstrated that amelogenin migrated through dentine and then incorporated into odontoblast processes and pulp cells through the internalization process [198]. Therefore it was suggested that MMP-20, which was located within odontoblasts, acted as a degradation agent of amelogenin following the internalization. Conversely, it was shown that amelogenin, expressed either by all exons (A+4) or by all exons except exon 4 (A-4), was actually synthesized by odontoblasts and it was isolated from bovine [199] and rat [200] dentine. It was demonstrated that A+4 and A-4 acted as a differentiation factor [200] and a chondrocyte-inducing agent (CIA) [199].

Lipids comprise of less than 2% of the dentine organic matrix. The lipid content in predentine was found to be higher than in dentine. Lipids are essential part of cell membrane components and therefore when lipid material is extracted from dentine after demineralization it may contain a mixture of cellular and extracellular

components, even though most of it was obtained from the acellular part of dentine. Lipids may not be actually associated with the mineral in the *in vivo* situation but artifactually associated during the release of extracted species and therefore special care should be taken in determining of the specific role of lipids extracted from dentine [201]. Using gene engineered mice with phospholipids (namely sphingolipids) deficiency (Fabry disease) it was demonstrated that metadentine was substantially widened [202]. These observations provided some evidence that lipid alterations influence the area where the mineralization process is initiated. The widening of the metadentine zone suggested that this process was delayed.

Table 2.8 Other organic components of dentine matrix.

Group	Molecule	Structure	Role
Serine-proteinases	Cathepsins		Degradation
Other enzymes	Alkaline phosphatase		Phosphate release
Proteins expressed in ameloblasts	Amelogenin 5 – 7 kDa	Spliced forms of A+4 & A-4	Chondrogenic including agent - signalling
Serum-derived proteins	αHS_2 – glicoprotein Albumin Lipoproteins: HDL & LDL	Polyacidic stretches	Inhibition of the complement – mediated attack
Lipids	Phospholipids	Membrane phospholipids. Extracellular mineral associated phospholipids	Initial nucleation and crystal growth

The diverse range of molecules found in dentine poses numerous questions in terms of their functional relationships. Their precise locations within pulp-dentine complex are still limited even though it is crucial in elucidating of their functions. The interactions between these molecules may be fundamental in their function during dentinogenesis and homeostasis but our appreciation of such interactions has only just started to unfold.

2.7 Inorganic phase of dentine

Dentine is a composite material of organic ECM, mainly type 1 collagen, and inorganic phase, carbon rich calcium deficient biological hydroxyapatite (HAP) mineral particles, which are closely packed and arranged with their c-axes parallel with the collagen fibrils and incorporated into them. HAP is a hydrated form of calcium phosphate with a chemical formula $Ca_5(PO_4)_3(OH)$ but usually presented its structural formula, $Ca_{10}(PO_4)_6(OH)_2$ (Figure 2.7), to denote that the HAP crystal unit cell comprises two molecules of HAP with stochiometric $Ca/P \approx 1.67$ and weight $Ca/P \approx 2.2$ ratios.

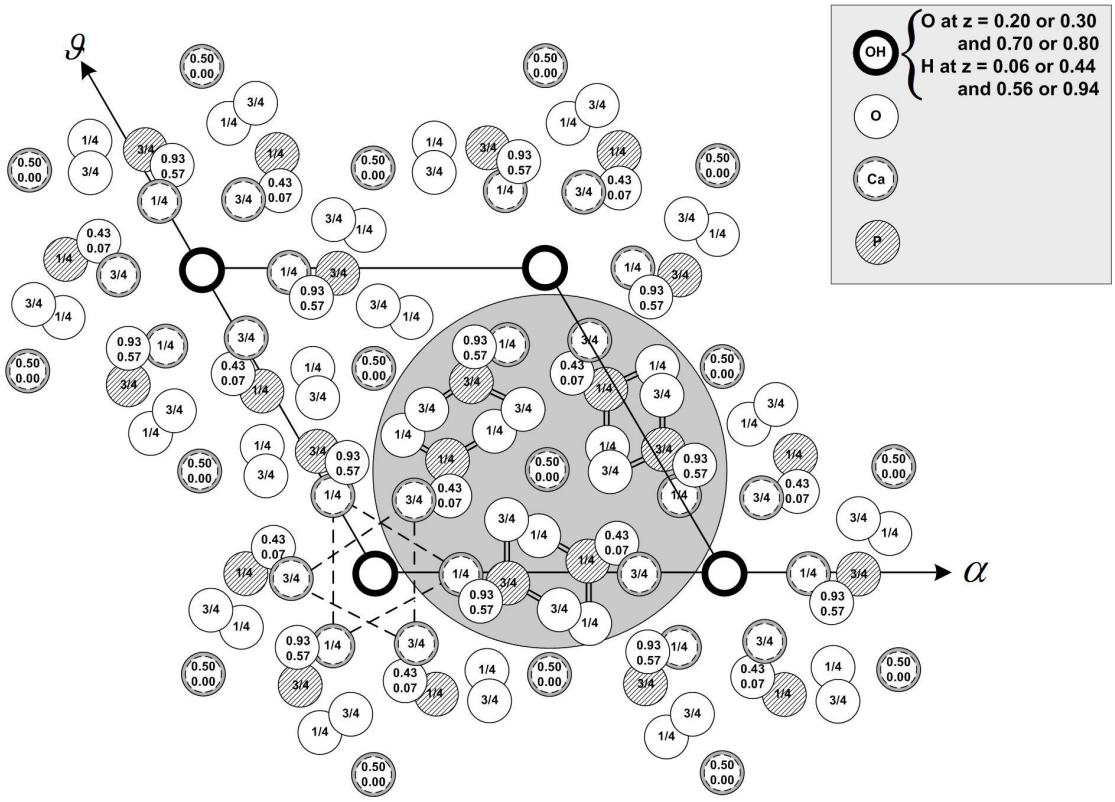

Figure 2.7 Crystal structure of hydroxyapatite projected on the X-Y plane. Pozner's cluster (C_0) is encircled (After [203, 204]).

HAP crystallises into hexagonal crystal lattice with space group $P6_3/m$ ($N_0 176$) [205] (Figure 2.8), characterised by six-fold c-axis perpendicular to three equivalent a-axes at angles 120° to each other. Applying X-ray and neutron diffraction techniques HAP crystal structure was determined [203]. HAP unit-cell contains $10Ca$, $6PO_4$ and $2OH$ closely packed together (Figure 2.7). Calcium atoms are identified as either Ca(1) or Ca(2) depending on their environment in the HAP unit cell. There are two Ca atoms, which occupy Ca(1) positions at levels z = 0 and two at z = ½ . Other six Ca atoms occupy Ca(2) positions. Three of these atoms are located at z = ¼ and the other three at z = ¾ surrounding the OH ions located at the corners of the unit cell. Six PO_4 tetrahedral are arranged in sets of three at levels z = ¼ and z = ¾ . The network of PO_4 groups provides the skeletal framework of the apatite and gives the apatite structure stability.

The intensity-enhanced dynamic light scattering technique allowed to demonstrate the presence of amorphous calcium phosphate (ACP) clusters in simulated body fluid from 0.7 – 1.0 nm in size [206], which was in the perfect agreement with the proposed nucleation and growth of HAP crystallites in physiological conditions from ACP precursors, also known as Posner's clusters, with structural formular of $Ca_9(PO_4)_6$ [204]. These observations were also in agreement with high-resolution TEM studies of HAP crystal structure, which demonstrated the lowest level of HAP hierarchical structure [207], nanoparticles, with dimensions close to 1 nm [208]. Applying atomic force microscopy (AFM) *in situ* the growth of HAP a-faces, $\{10\bar{1}0\}$ (Figure 2.8), in physiological conditions was observed. It was demonstrated that the growth of HAP a-face occurs by step flow with heights of 0.8 nm and 1.6 nm [209], which means that neither volume nor surface diffusion mechanisms of crystal growth

were rate-determining. Also using microscopic Raman spectroscopy technique it was demonstrated that the newly grown layer had a poorer crystallinity than the seed crystal [209]. Applying AFM *in situ* the step kinetics coefficient was measured for HAP crystallites a-face growth in physiological conditions and the value reported was $\beta = 0.4 \times 10^{-4} \frac{cm}{s}$ [210]. This value was in the order of 100 times lower than of other inorganic crystals but comparable with the values reported for protein [211] and viral [212] crystals and therefore the probability of the incorporation of a growth unit into HAP bulk crystal is low and there are similarities with the growth mechanisms of protein crystals, which grow by a macromolecule unit, which has anisotropy in shape and binding sites and HAP. There are two types of Posner's clusters, right- and left-handed chiral clusters: the first one is that centering at the Ca(1) site at z = 0 level, namely C_0 (encircled on Figure 2.7), and the other one is centered at the Ca(1) site at the z = ½ level, namely C_{50} [206]. Deficiency in calcium does not affect the chirality of clusters because chirality arises not only from calcium but also from phosphate arrangements. Hexagonal packing of Posner's clusters automatically leads to a framework of HAP structure. These findings strongly support HAP growth mechanism in physiological conditions by the incorporation process of growth units (Posner's clusters) into bulk crystal with the surface conversion of the ACP phase into HAP with chirality selection and orientation arrangement of Posner's clusters during the incorporation of clusters into the HAP lattice.

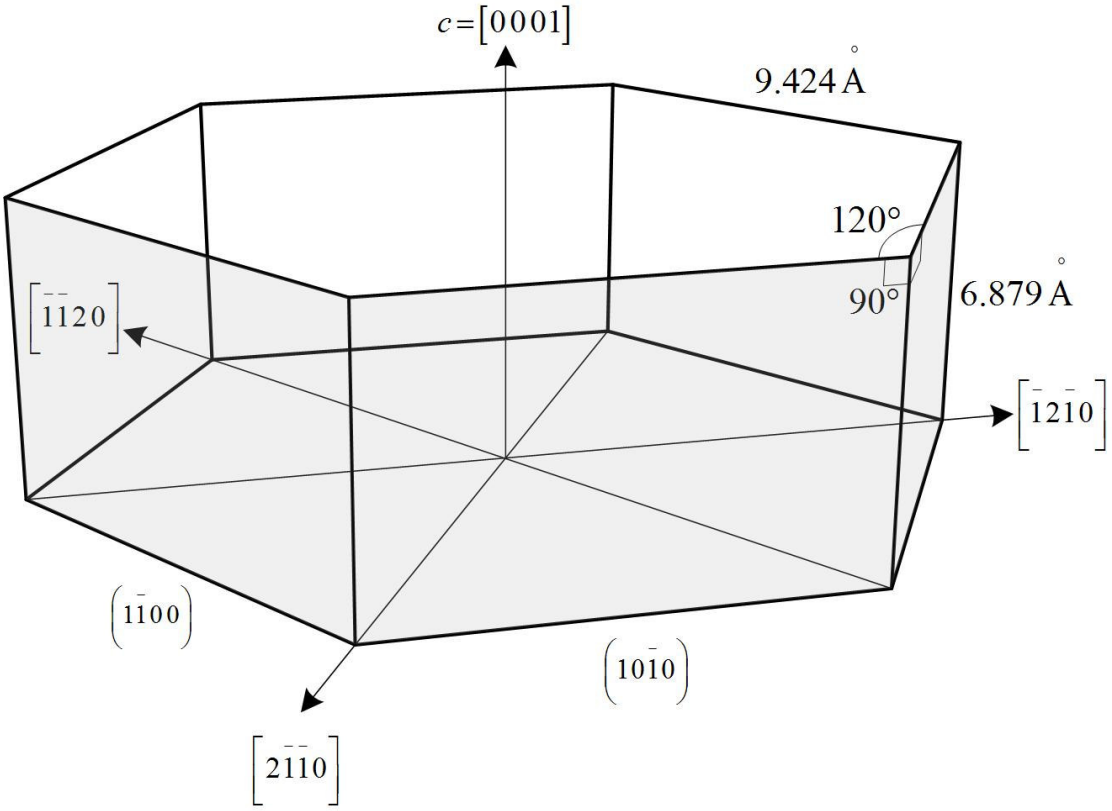

Figure 2.8 Schematic representation of HAP crystal unit cell. The drawing demonstrates hexagonal symmetry, some crystallographic directions, planes and cell unit parameters of HAP.

Applying the ultrasonic technique on dentine the elastic modulus of inorganic phase of dentine was measured and the value reported was 114 GPa, organic phase was 12 GPa and therefore it was demonstrated that the elastic modulus of biological HAP was about 9.5 times higher than collagen [213]. The pliant collagen matrix is reinforced by stiff mineral particles and as a composite, the brittleness of the mineral is compensated by the pliancy of the matrix. The development of the micro-mechanics cell theory of a dentine composite, which included peritubular and collagen-impregnated intertubular dentine, which in turn was treated as a porous phase saturated with water, allowed to predict the elastic properties of macroscopically significant volumes of dentine with the great accuracy [214].

Among other properties of HAP it is worth to mention that even though HAP is a non-magnetic material but due to a magnetic anisotropy in its crystal unit cell it is

susceptible to magnetic field and it was demonstrated that HAP crystals align with c-direction perpendicular to the applied magnetic field [215], which implies a possibility of a controlled arrangement of HAP crystallites during the mineralization process.

2.8 Carious dentine

Social dentistry studies demonstrated that dental caries is the most common tooth destructing condition and still, in the 21st century, continues to affect most of the world's population, rich or poor, old or young [216]. It is the bacterial disease in which through the process of fermentation of sugars oral bacteria produce acids [217], such as lactate, acetate, propionate and butyrate as was identified by means of gas chromatography technique. Limited amount of isobutyrate, valerate, isovalerate, caproate and isocaproate acids were also detected [218]. These acids dissolve the inorganic phase of tooth, biological apatite crystallites. The most common scenario is that dental caries first affect enamel and then affect dentine [218, 219] causing the condition called carious dentine. Applying optical and electron microscopy as well as hydrophobicity technique it was demonstrated that the adhesion strength of various strains of cariogenic bacteria to HAP surfaces depends on medium calcium concentrations that bind the functional groups of the bacteria to HAP. The adhesion of the bacteria to HAP was favoured by high calcium concentrations and therefore it was proposed that lactic acid formation during caries attack generates conditions favourable for further bacterial adhesion [220]. Many types of resident bacteria found to be sufficiently acidogenic to be cariogenic, such as Streptococcus mutans [221], lactobacilli (especially Lactobacillus acidophilus) as well as non-mutans streptococci such as S. sanguis, mitis and milleri and the bacteria that were neither streptococci nor lactobacilli, such as strains of actinomyces and bifidobacteria are considered

important in the formation of dental caries [219, 222]. However, for deep dentine caries many other species of bacteria, facultative and obligate anaerobes, have been detected at higher rates than for surface caries. Conversely, the rate of S. mutans for example, was demonstrated to be lower than in surface caries [223, 224]. The role of many species in the formation of deep caries has not been clarified, however, by working together, they play crucial role in the formation of deep caries [218]. As a consequence of an acidic environment the collagenous matrix of dentine is demineralized, which leads to a caries lesion. However, bacterial acids are not able to hydrolyze fibrous collagens and there is no evidence that bacterial enzymes are associated with caries development by degrading the organic matrix of dentine. *In vitro* experiments demonstrated that caries-related bacteria can readily demineralize the matrix but fail to degrade the dentine organic matrix [225, 226]. It was suggested then that host enzymes, matrix metalloproteinases, degrade the dentine matrix during or after demineralization by bacterial acids [177, 227]. Such host proteases, either from odontoblasts, odontoblast-like cells or pulp tissue may be responsible for collagen matrix destruction and in combination with additional hydrolytic enzymes such as lactate dehydrogenase (LDH) and glycoproteases may catalyse dentine connective tissue degradation in caries progression. In physiological conditions proteolytic enzymes may in turn model calcified matrix [68].

Histologically carious dentine is described in terms of specific altered layers – outer carious dentine layer and inner (affected) carious dentine layer with or without an underlying deeper layer of unaffected normal dentine (Figure 2.9) [228]. Each carious layer is further divided into more specific zones [229].

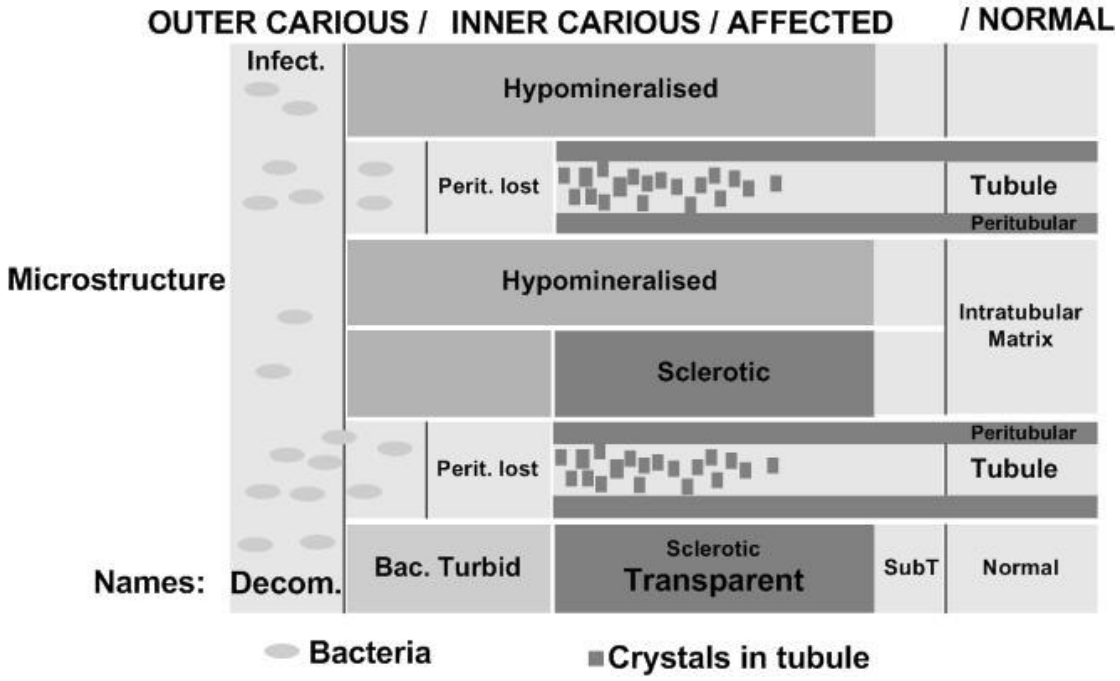

Figure 2.9 Diagram of carious dentine zones. (After [228]).

The outer carious dentine layer lost most of its mineral content in the intertubular dentine, peritubular dentine is lost completely and the organic structure is decomposed. Bacteria colonized this layer of carious dentine so this layer is also known as an infected layer. The inner layer of carious dentine consists of turbid, transparent and subtransparent zones. Although intertubular dentine in the turbid zone is mostly demineralized, the crossbanded structure of collagen matrix remains unaffected. Peritubular dentine is lost. In transparent dentine the tubule lumens are partially filled with mineral, tubules retain peritubular dentine, intertubular dentine is partially demineralized. The mineral levels of intertubular dentine in the subtransparent zone differ from normal dentine, the tubule lumen is not filled with mineral and peritubular dentine remains unaffected.

Only macroscopic studies have been performed so far to characterize various layers of human carious dentine [228, 230, 231], while the underlying ultrastructure of layers of carious dentine remains controversial and unknown.

2.9 References

1. Morelli C., Russi R. Anatomical 3D Models. http://www.turbosquid.com/FullPreview/Index.cfm/ID/300142 2006.
2. Nanci A. Ten Cate's Oral Histology: Development, Structure and Function. 7th ed. St Louis: Mosby; 2008.
3. He L.H., Swain M.V. Understanding the mechanical behaviour of human enamel from its structural and compositional characteristics. Journal of the Mechanical Behavior of Biomedical Materials 2008;1(1):18-29.
4. Smit T.H., Huyghe J.M., Cowin S.C. Estimation of the poroelastic parameters of cortical bone. Journal of Biomechanics 2002;35(6):829-35.
5. Maung N.L., Wohland T., Hsu C.-Y.S. Enamel diffusion modulated by Er:YAG laser: (Part 1)—FRAP. Journal of Dentistry, 2007;35(10):787-93.
6. Maung N.L., Wohland T., Hsu C.-Y.S. Enamel diffusion modulated by Er:YAG laser: (Part 2). Organic matrix. Journal of Dentistry 2007;35(10):794-99.
7. Daculsi G., Menanteau J., Kerebel L. M., Mitre D. Length and shape of enamel crystals Calcified Tissue International 1984;36(1):550-55.
8. Macho G.A., Jiang Y., Spears I.R. Enamel microstructure - a truly three dimensional structure. Journal of Human Evolution 2003;45(1):81-90.
9. Warshawsky H. Organization of crystals in enamel. Anatomical Record 1989;224:242-62.
10. Fincham A.G., Moradian-Oldak J., Simmer J.P. The structural biology of the developing dental enamel matrix. Journal of Structural Biology 1999;126(3):270-99.
11. Poole D.F.G., Brooks A.W., . The arrangement of crystallites in enamel prisms. Archives of Oral Biology 1961;5(1):14-26.
12. Wiggins P.M. Water in complex environments such as living systems. Physica A: Statistical Mechanics and its Applications 2002;314(1-4):485-91.
13. Cameron I.L., Kanal K.M., Keener C.R., Fullerton G.D. A mechanistic view of the non-ideal osmotic and motional behavior of intracellular water. Cell Biology International 1997;21(2):99-113.
14. Hu J.C., Yamakoshi Y., Yamakoshi F., Krebsbach P.H., Simmer J.P. Proteomics and genetics of dental enamel. Cells Tissues Organs 2005;181:219-31.
15. Bartlett J.D., Ryu O.H., Xue J., Simmer J.P., Margolis H.C. Enamelysin mRNA Displays a Developmental Defined Pattern of Expression and Encodes a Protein which Degrades Amelogenin. Connective Tissue Research 1998;39(1-3):101-09.
16. Gibson C.W., Yuan Z.A., Hall B., Longenecker G., Chen E.H., Thyagarajan T., et al. Amelogenin-deficient mice display an amelogenesis imperfecta phenotype. Journal of Biological Chemistry 2001;276:31871–75.

17. Dunglas C., Septier D., Paine M.L., Zhu D.H., Snead M.L., Goldberg M. Ultrastructure of forming enamel inmouse bearing a transgene that disrupts the amelogenin self-assembly domains. Calcified Tissue International 2002;71:155-66.
18. Paine M.L., White S.N., Luo W., Fong H., Sarikaya M., Snead M.L. Regulated gene expression dictates enamel structure and tooth function. Matrix Biology 2001;20(273-292).
19. Paine M.L., Luo W., Zhu D.H., Bringas Jr. P., Snead M.L. Functional domains for amelogenin revealed by compound genetic defects. Journal of Bone and Mineral Research 2003;18:466-72.
20. Fukumoto S., Kiba T., Hall B., Iehara N., Nakamura T., Longenecker G., et al. Ameloblastin is a cell adhesion molecule required for maintaining the differentiation state of ameloblasts. Journal of Cell Biology 2004;167:973-83.
21. Masuya H., Shimizu K., Sezutsu H., Sakuraba Y., Nagano J., Shimizu A., et al. Enamelin (Enam) is essential for amelogenesis: ENU-induced mouse mutants as models for different clinical subtypes of human amelogenesis imperfecta (AI). Human Molecular Genetics 2005;14(575-583).
22. Beniash E., Skobe Z., Bartlett J.D. Formation of the dentino-enamel interface in enamelysin (MMP-20) deficient mouse incisors. European journal of Oral Sciences 2006;114(Suppl 1):24-29.
23. Caterina J.J., Skobe Z., Shi J., Ding Y., Simmer J.P., Birkedal-Hansen H., et al. Enamelysin (Matrix Metalloproteinase 20)-deficient Mice Display an Amelogenesis Imperfecta Phenotype. Journal of Biological Chemistry 2002;277(51):49598–604.
24. Hu J.C., Sun X., Zhang C., Liu S., Bartlett J.D., Simmer J.P. Enamelysin and kallikrein-4 mRNA expression in developing mouse molars. European journal of Oral Sciences 2002;110(4):307-15.
25. Nanci A., Zalzal S., Lavoie P., Kunikata M., Chen W.-Y., Krebsbach P.H., et al. Comparative immunochemical analyses of the developmental expression and distribution of ameloblastin and amelogenin in rat incisors. Journal of Histochemistry and Cytochemistry 1998;46:911-34.
26. Smith C.E. Cellular and chemical events during enamel maturation. Critical Reviews in Oral Biology and Medicine 1998;9:128-61.
27. Nanci A., Zalzal S., Kan F.W.K. High-resolution scanning electron microscopy of rat incisor ameloblasts. Scanning Microscopy 1993;7:165-75.
28. Smith C.E., Nanci A. Overview of morphological changes in enamel organ cells associated with major events in amelogenesis. International Journal of Developmental Biology 1995;39:153-61.
29. Nanci A., Warshawsky H. Characterization of putative secretory sites on ameloblasts of the rat incisor. American Journal of Anatomy 1984;171:163-89.
30. Nanci A., Smith C.E. Development and calcification of enamel. Boca Raton CRC Press; 1992.
31. Zalzal S., Smith C.E., Nanci A. Ameloblastin and amelogenin share a common secretory pathway and are co-secreted during enamel formation. Matrix Biology 2008.
32. Nanci A., Hashimoto J., Zalzal S., Smith C.E. Transient accumulation of proteins at interrod and rod enamel growth sites. Advances in Dental Research 1996;10:135-49.
33. Moradian-Oldak J. Amelogenins: assembly, processing and control of crystal morphology. Matrix Biology 2001;20:293-305.

34. Moradian-Oldak J., Bouropoulos N., Wang L., Gharakhanian N. Analysis of self-assembly and apatite binding properties of amelogenin proteins lacking the hydrophilic C-terminal. Matrix Biology 2002;21:197-205.
35. Dohi N., Murakami C., Tanabe T., Yamakoshi Y., Fukae M., Yamamoto Y., et al. Immunocytochemical and immunochemical study of enamelins, using antibodies against porcine 89-kDa enamelin and its N-terminal synthetic peptide, in porcine tooth germs. Cell and Tissue Research 1998;293:313-25.
36. Uchida T., Murakami C., Dohi N., Wakida K., Satoda T., Takahashi O. Synthesis, secretion, degradation and fate of ameloblastin during the matrix formation stage of the rat incisor as shown by immunocytochemistry and immunochemistry using region-specific antibodies. Journal of Histochemistry and Cytochemistry 1997;45:1329-40.
37. Linde A., Goldberg M. Dentinogenesis. Critical Reviews in Oral Biology and Medicine 1993;4(5):679-728.
38. Habelitz S., Rodriguez B.J., Marshall S.J., Marshall G.W., Kalinin S.V., Gruverman A., et al. Peritubular Dentin Lacks Piezoelectricity. Journal of Dental Research 2007;86(9):908-11.
39. Arana-Chavez V.E., Massa L.F. Odontoblasts: the cells forming and maintaining dentine. The International Journal of Biochemistry & Cell Biology 2004;36(8):1367-73.
40. Osborn J.W. Dentine hardness and incisor wear in the beaver (Castor fiber). Acta Anatomica 1969;72:123-32.
41. Tylman S.D. The dentino-enamel junction. Journal of Dental Research 1928;8:615-22.
42. Arsenault A., Robinson B. The dentino-enamel junction: a structural and microanalytical study of early mineralization. Calcified Tissue International 1989;45(2):111-21.
43. Bodier-Houllé P., Steuer P., Meyer J.M., Bigeard L., Cuisinier F.J.G. High-resolution electron-microscopic study of the relationship between human enamel and dentin crystals at the dentinoenamel junction. Cell and Tissue Research 2000;301(3):389-95.
44. Gallagher R., Demos S., Balooch M., Marshall G. Jr., Marshall S. Optical spectroscopy and imaging of the dentin–enamel junction in human third molars. Journal of Biomedical Materials Research Part A 2003;64(2):372-77.
45. Zaslansky P., Friesem A.A., Weiner S. Structure and mechanical properties of the soft zone separating bulk dentin and enamel in crowns of human teeth: Insight into tooth function. Journal of Structural Biology 2006;153(2):188-99.
46. Kinney J. H., Gladden J. R., Marshall G. W., Marshall S. J., So J. H., Maynard J. D. Resonant ultrasound spectroscopy measurements of the elastic constants of human dentin. Journal of Biomechanics 2004;37(4):437-41.
47. Habelitz S., Marshall G.W., Balooch M., Marshall S.J. Nanoindentation and storage of teeth. Journal of Biomechanics 2002;35(7):995-98.
48. Fong H., Sarikaya M., White S.N., Snead M.L. Nano-mechanical properties profiles across dentin–enamel junction of human incisor teeth. Materials Science and Engineering: C 2000;7(2):119-28.
49. Wang R. Z., Weiner S. Strain–structure relations in human teeth using Moiré fringes. Journal of Biomechanics 1997;31(2):135-41.
50. Wood J.D., Wang R., Weiner S., Pashley D.H. Mapping of tooth deformation caused by moisture change using Moiré interferometry. Dental Materials 2003;19(3):159-66.

51. Yettram A.L., Wright K.W.J., Pickard H.M. Finite element stress analysis of the crowns of normal and restored teeth. Journal of Dental Research 1976;55(6):1004-11.
52. Goel V.K., Khera S.C., Ralston J.L., Chang KH. Stresses at the dentinoenamel junction of human teeth—A finite element investigation. Journal of Prosthetic Dentistry 1991;66(4):451-59.
53. Jontell M., Linde A. Non-collagenous proteins of predentin from dentinogenically active bovine teeth. Biochemical Journal 1983;214(3):769-76.
54. Torneck C.D. Dentin-Pulp Complex. In: Ten Cate A.R., editor. Oral Histology: Development, Structure and Function. 4th ed. St Louis: Mosby; 1994. p. 169-217.
55. Boskey A.L. Noncollagenous matrix proteins and their role in mineralization. Bone and Mineral 1989;6(2):111-23.
56. Jones S.J., Boyde A. Ultrastructure of dentin and dentinogenesis. In: Linde A., editor. Dentin and Dentinogenesis. Boca Raton: CRC Press; 2000. p. 81-134.
57. Granström G., Linde A. ATP-dependent uptake of Ca2+ by a microsomal fraction from rat incisor odontoblasts. Calcified Tissue International 1981;33(1):125-28.
58. Granström G. Further evidence of an intravesicular Ca2+- pump in odontoblasts from rat incisors. Archives of Oral Biology 1984;29(8):599-606.
59. Carafoli E. Intracellular calcium homeostasis. Annual Review of Biochemistry 1987;56:395-433.
60. Lundgren T., Linde A. Na+/Ca2+ antiports in membranes of rat incisor odontoblasts. Journal of Oral Pathology 1988;17(9-10):560-63.
61. Magloire H., Joffre A., Azerad J., Lawson D.E. Localization of 28 kDa calbindin in human odontoblasts. Cell and Tissue Research 1988;254(2):341-46.
62. Stetler-Stevenson W.G., Veis A. Type I collagen shows a specific binding affinity for bovine dentin phosphophoryn. Calcified Tissue International 1986;38(3):135-41.
63. Goldberg M., Boskey A.L. Lipids and biomineralizations. Progress in Histochemistry and Cytochemistry 1996;31(2):1-187.
64. Ten Cate A.R. Hard tissue formation and destruction. In: Ten Cate A.R., editor. Oral Histology.Development, Structure and Function. 4th ed. St. Louis: Mosby; 1994. p. 111-19.
65. Hall R., Septier D., Embery G., Goldberg M. Stromelysin-1 (MMP-3) in forming enamel and predentin in rat incisor-coordinated distribution with proteoglycans suggests a functional role. Histochemical Journal 1999;31(12):761-70.
66. Goracci G., Mori G., Baldi M. Terminal end of the human odontoblastic process: study using SEM and confocal microscopy. Clinical Oral Investigations 1999;3(3):126-32.
67. Grötz K.A., Duschner H., Reichert T.E., de Aguiar E.G., Götz H., Wagner W. Histomography of the odontoblast processes at the dentino-enamel junction of permanent healthy human teeth in the confocal laser scanning microscope. Clinical Oral Investigations 1998;2(1):21-25.
68. Larmas M. Odontoblast function seen as the response of dentinal tissue to dental caries. Advances in Dental Research 2001;15(1):68-71.

69. Dai X.F., Ten Cate A.R., Limeback H. The extent and distribution of intratubular collagen fibrils in human dentine. Archives of Oral Biology 1991;36(10):775-78.
70. Phillipas G., Applebaum E. Age factors in secondary dentin formation. Journal of Dental Research 1966;45(3):778-89.
71. Cox C.F., White K.C., Ramus D.L., Farmer J.B., Snuggs H.M. Reparative dentin: factors affecting its deposition. Quintessence International 1992;23:257-70.
72. Magloire H., Bouvier M., Joffre A. Odontoblast response under carious lesions. Proceedings of the Finnish Dental Society 1992;88(1):257-74.
73. Lesot H., Begue-Kirn C., Kubler M.D., Meyer J.M., Smith A.J., Cassidy N., et al. Experimental induction of odontoblast differentiation and stimulation during reparative process. Cells & Materials 1993;3:201-07.
74. D'Souza R.N., Bachman T., Baumgardner K.R., Butler W.T., Litz M. Characterization of cellular responses involved in reparative dentinogenesis in rat molars. Journal of Dental Research 1995;74(2):702-09.
75. Tziafas D., Smith A.J., Lesot H. Designing new treatment strategies in vital pulp therapy. Journal of Dentistry 2000;28(2):77-92.
76. Linde A. Dentin matrix proteins: Composition and possible functions in calcification. The Anatomical Record 1989;224(2):154-66.
77. Ramachandran G.N., Kartha G. Structure of collagen. Nature 1954;174(4423):269-70.
78. Rich A., Crick F.H.C. The structure of collagen. Nature 1955;176(4489):915-16.
79. Gage J.P. Electrophoretic characterization of peptides from normal mature human dentin. Archives of Oral Biology 1984;29(8):575-80.
80. Lukinmaa P.L., Waltimo J. Immunohistochemical localization of types I, V, and VI collagen in human permanent teeth and periodontal ligament. Journal of Dental Research 1992;71(2):391-97.
81. Lowther D.A. Chemical aspects of collagen fibrillogenesis. International Review of Connective Tissue Research 1963;1:64–125.
82. Lukinmaa P.L., Vaahtokari A., Vainio S., Thesleff I. Expression of type I collagen pro-alpha 2 chain mRNA in adult human permanent teeth as revealed by in situ hybridization. Journal of Dental Research 1992;71:36-42.
83. Lees J.F., Tasab M., Bulleid N.J. Identification of the molecular recognition sequence which determines the type-specific assembly of procollagen. The EMBO Journal 1997;16(5):908-16.
84. Kielty C.M., Grant M.E. The collagen family: structure, assembly and organization in the extracellular matrix. Connective Tissue and its Heritable Diseases: molecular, genetic and medical aspects. New York: Wiley-Liss; 2002.
85. Parkinson J., Kadler K.E., Brass A. Simple physical model of collagen fibrillogenesis based on diffusion limited aggregation. Journal of Molecular Biology 1995;247(4):823-31.
86. De Coster P.J., Cornelissen M., De Paepe A., Martens L.C., Vral A. Abnormal dentin structure in two novel gene mutations [COL1A1, Arg134Cys] and [ADAMTS2, Trp795-to-ter] causing rare type I collagen disorders. Archives of Oral Biology 2007;52(2):101-09.

87. Sodek J., Mandell S.M. Collagen metabolism in rat incisor predentine in vivo: synthesis and maturation of type I, .alpha.1 (I) trimer, and type V collagens. Biochemistry 1982;21(9):2011-15.
88. Munksgaard E.C., Moe D. Types of collagen in an extract of odontoblasts and dentine from developing bovine teeth. Archives of Oral Biology 1980;25(7):485-89.
89. Shuttleworth C.A., Ward J.L., Hirschmann P.N. The presence of type III collagen in the developing tooth. Biochimica et Biophysica Acta (BBA) 1978;535:348-55.
90. van Amerongen J.P., Lemmens I.G., Tonino G.J.M. The concentration, extractability and characterization of collagen in human dental pulp. Archives of Oral Biology 1983;28(4):339-45.
91. Karjalainen S., Söderling E., Pelliniemi L., Foidart J.M. Immunohistochemical localization of types I and III collagen and fibronectin in the dentin of carious human teeth. Archives of Oral Biology 1986;31(12):801-06.
92. Becker J., Schuppan D., Benzian H., Bals T., Hahn E.G., C. C, et al. Immunohistochemical distribution of collagens types IV, V, and VI and of pro-collagens types I and III in human alveolar bone and dentin. Journal of Histochemistry and Cytochemistry 1986;34:1417-29.
93. Waltimo J., Risteli L., Risteli J., Lukinmaa P.L. Altered collagen expression in human dentin: increased reactivity of type III and presence of type VI in dentinogenesis imperfecta, as revealed by immunoelectron microscopy. Journal of Histochemistry and Cytochemistry 1994;42(12):1593-601.
94. Magloire H., Joffre A., Hartmann D.J. Localization and synthesis of type III collagen and fibronectin in human reparative dentin. Histochemistry 1988;88(2):141-49.
95. Fisher L.W., Torchia D.A., Fohr B., Young M.F., Fedarko N.S., . Flexible structures of SIBLING proteins, bone sialoprotein, and osteopontin. Biochemical and Biophysical Research Communications 2001;280(2):460-65.
96. Fisher L.W., Fedarko N.S. Six genes expressed in bones and teeth encode the current members of the SIBLING family of proteins. Connective Tissue Research 2003;44(Supp 1):33-40.
97. Denhardt D.T. The third international conference on osteopontin and related proteins. Calcified Tissue International 2002;74(3):213-19.
98. Qin C., Brunn J.C., Jones J., George A., Ramachandran A., Gorski J.P, et al. A comparative study of sialic acid-rich proteins in rat bone and dentin. European Journal of Oral Sciences 2001;109(2):133-41.
99. Ritchie H.H., Wang L.H. Sequence Determination of an Extremely Acidic Rat Dentin Phosphoprotein. Journal of Biological Chemistry 1996;271(36):21695–98.
100. Butler W.T. Dentin matrix proteins. European Journal of Oral Sciences 1998;106(Supp 1):204-10.
101. MacDougall M., Simmons D., Luan X., Nydegger J., Feng J., Gu T.T. Incorrect reference from scopus Dentin phosphoprotein and dentin sialoprotein are cleavage products expressed from a single transcript coded by a gene on human chromosome 4: Dentin phosphoprotein DNA sequence determination Journal of Biological Chemistry 1997;272(2):835-42.
102. Yamakoshi Y., Hu J.C., Fukae M., Zhang H., Simmer J.P. Dentin glycoprotein: the protein in the middle of the dentin sialophosphoprotein chimera. Journal of Biological Chemistry 2005;280(17):17472–79.

103. Ritchie H.H., Wang L. The presence of multiple rat DSP-PP transcripts. Biochimica et Biophysica Acta (BBA) - Gene Structure and Expression 2000;1493(1-2):27-32.
104. Leaver A.G., Shuttleworth C.A. The isolation from human dentine and ox bone of phosphate-containing peptides. Archives of Oral Biology 1966;11(11):1209-11.
105. Weinstock M., LeBlond C.P. Radioautographic visualization of the deposition of a phosphoprotein at the mineralization front in the dentin of the rat incisor. Journal of Cell Biology 1973;56(3):838-45.
106. Saito T., Arsenault A.L., Yamauchi M., Kuboki Y., Crenshaw M.A. Mineral induction by immobilized phosphoproteins. Bone 1997;21(4):305-11.
107. Saito T., Yamauchi M., Abiko Y., Matsuda K., Crenshaw M.A. In vitro apatite induction by phosphophoryn immobilized on modified collagen fibrils. Journal of Bone and Mineral Research 2000;15:1615-19.
108. Sreenath T., Thyagarajan T., Hall B., Longenecker G., D'Souza R., Hong S., et al. Dentin Sialophosphoprotein Knockout Mouse Teeth Display Widened Predentin Zone and Develop Defective Dentin Mineralization Similar to Human Dentinogenesis Imperfecta Type III. Journal of Biological Chemistry 2003;278(27):24874–80.
109. Gu K., Chang S., Ritchie H.H., Clarkson B.H., Rutherford R.B. Molecular cloning of a human dentin sialophosphoprotein gene. European journal of Oral Sciences 2000;108(1):35-42.
110. White S.N., Paine M.L., Ngan A.Y., Miklus V.G., Luo W., Wang H., et al. Ectopic expression of dentin sialoprotein during amelogenesis hardens bulk ename. Journal of Biological Chemistry 2007;282(8):5340–45.
111. Sugars R.V., Olsson M.L., Waddington R., Wendel M. Substitution of bovine dentine sialoprotein with chondroitin sulfate glycosaminoglycan chains. European Journal of Oral Sciences 2006;114(1):89-92.
112. George A., Sabsay B., Simonian P.A.L, Veis A. Characterization of a novel dentin matrix acidic phosphoprotein. Implications for induction of biomineralization. Journal of Biological Chemistry 1993;268(17):12624-30.
113. Thotakura S.R., Karthikeyan N., Smith T., Liu K., George A. Cloning and characterization of rat dentin matrix protein 1 (DMP1) gene and its 5'-upstream region. Journal of Biological Chemistry 2000;275(14):10272-77.
114. Ye L., MacDougall M., Zhang S., Xie Y., Zhang J., Li Z., et al. Deletion of Dentin Matrix Protein-1 Leads to a Partial Failure of Maturation of Predentin into Dentin, Hypomineralization, and Expanded Cavities of Pulp and Root Canal during Postnatal Tooth Development. Journal of Biological Chemistry 2004;279(18):19141-48.
115. Feng J.Q., Ward L.M., Liu S., Lu Y., Xie Y., Yuan B., et al. Loss of DMP1 causes rickets and osteomalacia and identifies a role for osteocytes in mineral metabolism. Nature Genetics 2006;38(11):1310-15.
116. Qin C., Brunn J.C., Cook R.G., Orkiszewski R.S., Malone J.P., Veis A., et al. Evidence for the proteolytic processing of dentin matrix protein 1. Identification and characterization of processed fragments and cleavage sites. Journal of Biological Chemistry 2003;278(36):34700-08.
117. Qin C., Huang B., Wygant J.N., McIntyre B.W., McDonald C.H., Cook R.G., et al. A chondroitin sulfate chain attached to the bone dentin matrix protein 1 NH2-terminal fragment. Journal of Biological Chemistry 2006;281(12):8034-40.

118. Gorski J.P., Kremer E.A., Chen Y., Ryan S., Fullenkamp C., Delviscio J., et al. Bone acidic glycoprotein-75 self-associates to form macromolecular complexes in vitro and in vivo with the potential to sequester phosphate ions. Journal of Cellular Biochemistry 1997;64(4):547-64.
119. Fujisawa R., Butler W.T., Brunn J.C., Zhou H.Y., Kuboki Y. Differences in composition of cell-attachment sialoproteins between dentine and bone. Journal of Dental Research 1993;72:1222–26.
120. Kasugai S., Todescan R. Jr., Nagata T., Yao K.-L., Butler W.T., Sodek J. Expression of bone matrix proteins associated with mineralized tissue formation by adult rat bone marrow cells in vitro: inductive effects of dexamethasone on osteoblastic phenotype. Journal Of Cellular Physiology 1991;147(1):111-20.
121. Stubbs III J.T., Mintz K.P., Eanes E.D., Torchia D.A., Fisher L.W. Characterization of native and recombinant bone sialoprotein: delineation of the mineral-binding and cell adhesion domains and structural analysis of the RGD domain. Journal of Bone and Mineral Research 1997;12(8):1210-22.
122. Ganss B., Kim R.H., Sodek J. Bone sialoprotein. Critical Reviews in Oral Biology & Medicine 1999;10:79-98.
123. Hunter G.K., Goldberg H.A. Nucleation of hydroxyapatite by bone sialoprotein. Proceedings of the National Academy of Sciences of the USA 1993;90(18):8562-65.
124. Chen J., McCulloch C.A.G., Sodek J. Bone sialoprotein in developing porcine dental tissues: cellular expression and comparison of tissue localization with osteopontin and osteonectin. Archives of Oral Biology 1993;38(3):241–49.
125. Helder M.N., Bronckers A.L.J.J., Woltgens J.H.M. Dissimilar expression patterns for the extracellular matrix proteins osteopontin (OPN) and collagen type I in dental tissues and alveolar bone of the neonatal rat. Matrix 1993;13(5):415-25.
126. Arana-Chavez V.E., Nanci A. High-resolution Immunocytochemistry of Noncollagenous Matrix Proteins in Rat Mandibles Processed with Microwave Irradiation. Journal of Histochemistry and Cytochemistry 2001;49(9):1099-110.
127. Boskey A.L., Spevak L., Paschalis E., Doty S.B., Mckee M.D. Osteopontin deficiency increases mineral content and mineral crystallinity in mouse bone. Calcified Tissue International 2002;71(2):145-54.
128. MacDougall M., Simmons D., Gu T.T., Dong J. MEPE/OF45, a new dentin/bone matrix protein and candidate gene for dentin diseases mapping to chromosome 4q21. Connective Tissue Research 2002;43(2-3):320-30.
129. Price P.A., Urist M.R., Otawara Y. Matrix Gla protein, a new γ-carboxyglutamic acid-containing protein which is associated with the organic matrix of bone. Biochemical and Biophysical Research Communications 1983;117(3):765-71.
130. Price P.A., Rice J.S., Williamson M.K. Conserved phosphorylation of serines in the Ser-X-Glu/Ser(P) sequences of the vitamin K-dependent matrix Gla protein from shark, lamb, rat, cow, and human. Protein Science 1994;3(5):822-30.
131. Luo G., Ducy P., McKee M.D., Pinero G.J., Loyer E., Behringer R.R., et al. Spontaneous calcification of arteries and cartilage in mice lacking MGP. Nature 1997;386(6620):78-81.

132. de Vries G.I., Quartier E., Boute P., Wisse E., Cosmans D. Immunocytochemical localization of OC in developing rat teeth. Journal of Dental Research 1987;66(3):784-90.
133. de Vries G.I., Coomans D., Wisse E. Immunocytochemical localization of OC in human and bovine teeth. Calcified Tissue International 1988;43(2):128-30.
134. Papagerakis P., Berdal A., Mesbah M., Peuchmaur M., Malaval L., Nydegger J., et al. Investigation of osteocalcin, osteonectin, and dentin sialophosphoprotein in developing human teeth. Bone 2002; 30(2):377–85.
135. Dulcy P., Desbois C., Boyce B., Pinero G., Story B., Dunstan C., et al. Increased bone formation in osteocalcin-deficient mice. Nature 1996;382(6590):448-52.
136. Boskey A.L., Wians F.H. Jr., Hauschka P.V. The effect of osteocalcin on in vitro lipid-induced hydroxyapatite formation and seeded hydroxyapatite growth. Calcified Tissue International 1985;37(1):57-62.
137. Jontell M., Linde A. Non-collagenous proteins of predentine from dentinogenically active bovine teeth. Biochemical Journal 1983;214(3):769-76.
138. Fujisawa R., Kuboki Y. Changes in the level of ON in bovine dentin during tooth development. Archives of Oral Biology 1989;34(2):89-92.
139. Lormee P., Septier D., Lecolle S., Baudoin C., Goldberg M. Dual incorporation of (35S)sulfate into dentin proteoglycans acting as mineralization promotors in rat molars and predentin proteoglycans. Calcified Tissue International 1996;58(5):368-75.
140. Jones I.L., Leaver A.G. Glycosaminoglycans of human dentine. Calcified Tissue Research 1974;16:37-44.
141. Embery G., Rees S., Hall R., Rose K., Waddington R., Shellis P. Calcium- and hydroxyapatite-binding properties of glucuronic acid-rich and iduronic acid-rich glycosaminoglycans and proteoglycans. European Journal of Oral Sciences 1998;106(Supp 1):267-73.
142. Jha M., Susheela A.K. In vivo chondrogenesis and histochemical appearance of dermatan sulphate in rabbit cancellous bone. Differentiation 1982;22(1-3):235-36.
143. Waddington R.J., Hall R.C., Embery G., Lloyd D.M. Changing profiles of proteoglycans in the transition of predentine to dentine. Matrix Biology 2003;22(2):153-61.
144. Hjerpe A., Antonopoulos C.A., Engfeldt B., Wikström B. Analysis of dentine glycosaminoglycans using high-performance liquid chromatography. Calcified Tissue International 1983;83(1):496-501.
145. Smith A.J., Lesot H. Induction and regulation of crown dentinogenesis: embryonic events as a template for dental tissue repair? Critical Reviews in Oral Biology & Medicine 2001;12(5):425-37.
146. Wozney J.M., Rosen V., Celeste A.J., Mitsock L.M., Whitters M.J., Kriz R.W., et al. Novel regulators of bone formation: molecular clones and activities. Science 1988;242(4885):1528-34.
147. Massague J. The transforming growth factor-beta family. Annual Review of Cell Biology 1990;6:597-641.
148. Risbridger G.P., Schmitt J.F., Robertson D.M. Activins and inhibins in endocrine and other tumors. Endocrine Reviews 2001;22:836-58.

149. Heikinheimo K., Salo T. Expression of basement membrane type IV collagen and type IV collagenases (MMP-2 and MMP-9) in human fetal teeth. Journal of Dental Research 1995;74(5):1226-34.
150. Nakashima M. Induction of dentin formation on canine amputated pulp by recombinant human bone morphogenetic proteins (BMP)-2 and -4. Journal of Dental Research 1994;73(9):1515-22.
151. Cassidy N., Fahey M., Prime S.S., Smith A.J. Comparative analysis of transforming growth factor-β isoforms 1–3 in human and rabbit dentine matrices. Archives of Oral Biology 1997;42(3):219-23.
152. Zhao S., Sloan A.J., Murray P.E., Lumley P.J., Smith A.J. Ultrastructural localisation of TGF-beta exposure in dentin by chemical treatment. The Histochemical Journal 2000;32(8):489-94.
153. Sloan A.J., Smith A.J. Stimulation of the dentin-pulp complex of rat incisor teeth by transforming growth factor-beta isoforms 1-3 in vitro. Archives of Oral Biology 1999;44(2):149-56.
154. Tziafas D. Basic mechanisms of cytodifferentiation and dentinogenesis during dental pulp repair. The international journal of developmental biology 1995;39(1):281-90.
155. Melin M., Joffre-Romeas A., Farges J.C., Couble M.L., Magloire H., Bleicher F. Effects of TGFbeta1 on dental pulp cells in cultured human tooth slices. Journal of Dental Research 2000;79:1689-96.
156. Smith A.J., Cassidy N., Perry H., Bègue-Kirn C., Ruch J.V., Lesot H. Reactionary dentinogenesis. The international journal of developmental biology 1995;39(1):273-80.
157. Shibata Y., Abiko Y., Moriya Y., Yoshida W., Takiguchi H. Effects of transforming growth factor-β on collagen gene expression and collagen synthesis level in mineralizing cultures of osteoblast-like cell line, MC3T3-E1. International Journal of Biochemistry 1993;25(2):239-45.
158. Ibbotson K.J., Orcutt C.M., Anglin A.M., D'Souza S.M. Effects of transforming growth factors β1 and β2 on a mouse clonal, osteoblastlike cell line MC3T3-E1. Journal of Bone and Mineral Research 1989;4:37-45.
159. Wozney J.M. The bone morphogenetic protein family and osteogenesis. Molecular Reproduction and Development 1992;32(2):160-67.
160. Centrella M., Horowitz M.C., Wozney J.M., McCarthy T.L. Transforming growth factor-β gene family members and bone. Endocrine Reviews 1994;15(1):27-39.
161. Bessho K., Tanaka N., Matsumoto J., Tagawa T., Murata M. Human dentin-matrix-derived bone morphogenetic protein. Journal of Dental Research 1991;70(3):171-75.
162. Celeste A.J., Iannazzi J.A., Taylor R.C., Hewick R.M., Rosen V., Wang E.A., et al. Identification of transforming growth factor beta family members present in bone-inductive protein purified from bovine bone. Proceedings of the National Academy of Sciences 1990;87:9843-47.
163. Celeste A.J., Ross J.L., Yamali N., Wozney J.M. The molecular cloning of human bone morphogenetic proteins-10, -11, and -12, three new members of the transforming growth factorbeta superfamily. Journal of Bone and Mineral Research 1995;10:S336.
164. Özkaynak E., Rueger D.C., Drier E.A., Corbett C., Ridge R.J., Sampath T.K., et al. OP-1 cDNA encodes an osteogenic protein in the TGF-beta family. The EMBO Journal 1990;9(7):2085-93.

165. Storm E.E., Huynh T.V., Copeland N.G., Jenkins N.A., Kingsley D.M., Lee S.J. Limb alterations in brachypodism mice due to mutations in a new member of the TGF β - superfamily. Nature 1994;368(6472):639-43.
166. Song J.J., Celeste A.J., Kong F.M., Jirtle R.L., Rosen V., Thies R.S. Bone morphogenetic protein-9 binds to liver cells and stimulates proliferation. Endocrinology 1995;136(10):4293-97.
167. Dube J.L., Wang P., Elvin J., Lyons K.M., Celeste A.J., Matzuk M.M. The Bone Morphogenetic Protein 15 Gene Is X-Linked and Expressed in Oocytes. Molecular Endocrinology 1998;12(12):1809-17.
168. Gu K., Smoke R.H., Rutherford R.B. Expression of genes for bone morphogenetic proteins and receptors in human dental pulp. Archives of Oral Biology 1996;41(10):919-23.
169. Calland J.W., Harris S.E., Carnes D.L.Jr. Human pulp cells respond to calcitonin gene-related peptide in vitro. Journal of Endodontics 1997;23(8):485-89.
170. Verstappen J., Von den Hoff J.W. Tissue Inhibitors of Metalloproteinases (TIMPs): Their Biological Functions and Involvement in Oral Desease. Journal of Dental Research 2006;85(12):1074-84.
171. Sahlberg C., Reponen P., Tryggvason K., Thesleff I. TIMP-1, -2 and -3 show coexpression with gelatinases A and B during mouse tooth morphogenesis. European Journal of Oral Sciences 1999;107(2):121-30.
172. Wilhelm S.M., Javed T., Miller R.L. Human gingival fibroblast collagenase: purification and properties of precursor and active forms. Collagen and Related Research 1984;4:129-52.
173. Grant G.A., Eisen A.Z., Marmer B.L., Roswit W.T., Goldberg G.I. The activation of human skin fibroblast procollagenase. Sequence identification of the major conversion products. Journal of Biological Chemistry 1987;262(12):5886-89.
174. Tjäderhane L., Salo T., Larjava H., Larmas M., Overall C.M. A novel organ culture method to study the function of human odontoblasts in vitro: gelatinase expression by odontoblasts is differentially regulated by TGF-β1. Journal of Dental Research 1998;77(7):1486-96.
175. Rifas L., Halstead L.R., Peck W.A., Avioli L.V., Welgus H.G. Human osteoblasts in vitro secrete tissue inhibitor of metalloproteinases and gelatinase but not interstitial collagenase as major cellular products. Journal of Clinical Investigation 1989;84(2):686-94.
176. Martin-De Las Heras S., Valenzuela A., Overall C.M. The matrix metalloproteinase gelatinase A in human dentin. Archives of Oral Biology 2000;45(9):757-65.
177. Tjäderhane L., Larjava H., Sorsa T., Uitto V.J., Larmas M., Salo T. The activation and function of host matrix metalloproteinases in dentin matrix breakdown in caries lesions. Journal of Dental Research 1998;77(8):1622-29.
178. Collier I.E., Wilhelm S.M., Eisen A.Z., Marmer B.L., Grant G.A., Seltzer J.L., et al. H-ras oncogene-transformed human bronchial epithelial cells (TBE-1) secrete a single metalloprotease capable of degrading basement membrane collagen Journal of Biological Chemistry 1988;263(14):6579–87.
179. Xu X., Wang Y., Lauer-Fields J.L., Fields G.B., Steffensen B. Contributions of the MMP-2 collagen binding domain to gelatin cleavage substrate binding via the collagen binding domain is required for hydrolysis of gelatin but not short peptides. Matrix Biology 2004;23(3):171-81.

180. Welgus H.G., Fliszar C.J., Seltzer J.L., Schmid T.M., Jeffrey J.J. Differential susceptibility of type X collagen to cleavage by two mammalian interstitial collagenases and 72-kDa type IV collagenase. Journal of Biological Chemistry 1990;265(23):13521-27.
181. Aimes R.T., Quigley J.P. Matrix metalloproteinase-2 is an interstitial collagenase. Inhibitorfree enzyme catalyzes the cleavage of collagen fibrils and soluble native type I collagen generating the specific 3/4- and 1/4-length fragments. Journal of Biological Chemistry 1995;270(11):5872-76.
182. Patterson M.L., Atkinson S.J., Knauper V., Murphy G. Specific collagenolysis by gelatinase A, MMP-2, is determined by the hemopexin domain and not the fibronectin-like domain. FEBS Letters 2001;503(2-3):158-62.
183. Okada Y., Morodomi T., Enghild J.J., Suzuki K., Yasui A., Nakanishi I., et al. Matrix metalloproteinase 2 from human rheumatoid synovial fibroblasts. Purification and activation of the precursor and enzymic properties. European Journal of Biochemistry 1990;194(3):721-30.
184. Ito A., Mukaiyama A., Itoh Y., Nagase H., Thogersen I.B., Enghild J.J., et al. Degradation of Interleukin 1beta by Matrix Metalloproteinases. Journal of Biological Chemistry 1996;271(25):14657-60.
185. Imai K., Hiramatsu A., Fukushima D., Pierschbacher M.D., Okada Y. Degradation of decorin by matrix metalloproteinases: identification of the cleavage sites, kinetic analyses and transforming growth factor-beta1 release. Biochemical Journal 1997;322(3):809-14.
186. Giannelli G., Falk-Marzillier J., Schiraldi O., Stetler-Stevenson W.G., Quaranta V. Induction of cell migration by matrix metalloprotease-2 cleavage of laminin-5. Science 1997;277:225-28.
187. Allan J.A., Docherty A.J., Barker P.J., Huskisson N.S., Reynolds J.J., Murphy G. Binding of gelatinases A and B to type-I collagen and other matrix components. Biochemical Journal 1995;309:299-306.
188. Ellerbroek S.M., Wu Y.I., Stack M.S. Type I collagen stabilization of matrix metalloproteinase-2. Archives of Biochemistry and Biophysics 2001;390(1):51-56.
189. Sato H., Takino T., Okada Y., Cao J., Shinagawa A., Yamamoto E., et al. A matrix metalloproteinase expressed on the surface of invasive tumour cells. Nature 1994;370(6484):61-65.
190. Llano E., Pendas A.M., Knauper V., Sorsa T., Salo T., Salido E., et al. Identification and structural and functional characterization of human enamelysin (MMP-20). Biochemistry 1997;36(49):15101-08.
191. Sulkala M., Larmas M., Sorsa T., Salo T., Tjäderhane L. The localization of matrix metalloproteinase-20 (MMP-20, enamelysin) in mature human teeth. Journal of Dental Research 2002;81(9):603-07.
192. Bartlett J.D., Simmer J.P., Xue J., Margolis H.C., Moreno E.C. Molecular cloning and mRNA tissue distribution of a novel matrix metalloproteinase isolated from porcine enamel organ. Gene 1996;183(1-2):123-28.
193. DenBesten P.K., Punzi J.S., Li W. Purification and sequencing of a 21 kDa and 25 kDa bovine enamel metalloproteinase. European journal of oral sciences 1998;106(S1):354-49.
194. Caterina J., Shi J., Krakora S., Bartlett J.D., Engler J.A., Kozak C.A., et al. Isolation, characterization, and chromosomal location of the mouse enamelysin gene. Genomics 1999;62(2):308-11.

195. Takata T., Zhao M., Uchida T., Wang T., Aoki T., Bartlett J.D., et al. Immunohistochemical detection and distribution of enamelysin (MMP-20) in human odontogenic tumors. Journal of Dental Research 2000;79(8):1608-13.
196. Väänänen A., Srinivas R., Parikka M., Palosaari H., Bartlett J.D., Iwata K., et al. Expression and regulation of MMP-20 in human tongue carcinoma cells. Journal of Dental Research 2001;80:1884-89.
197. Beniash E., Skobe Z., Bartlett J.D. Formation of the dentinoenamel interface in enamelysin (MMP-20)-deficient mouse incisors. European journal of Oral Sciences 2006;114(Supp 1):24-29.
198. Nakamura M., Bringas P. Jr., Nanci A., Zeichner-David M., Asdown B., Slavkin H.C. Translocation of enamel proteins from inner enamel epithelia to odontoblasts during mouse tooth development. Anatomical Record 1994;238(3):383-96.
199. Nebgen D.R., Inoue H., Sabsay B., Wei K., Ho C.-S., Veis A. Identification of the chondrogenic-inducing activity from bovine dentin (bCIA) as a low-molecular-mass amelogenin polypeptide. Journal of Dental Research 1999;78(9):1484-94.
200. Veis A., Tomkins K., Alvares K., Wei K.R., Wang L., Wang X.S. Specific amelogenin gene splice products have signaling effects on cells in culture and implants in vivo. Journal of Biological Chemistry 2000;275(52):41263-72.
201. Goldberg M., Septier D. Phospholipids in amelogenesis and dentinogenesis. Critical Reviews in Oral Biology & Medicine 2002;13(3):276-90.
202. Dunglas C., Septier D., Goldberg M., Qasba P., Sreenath T., Kulkarni A. Fabry mice display structural defects in teeth (abstract). Journal of Dental Research 2001;80(Spec Issue):216.
203. Kay M.I., Young R.A., Posner A.S. Crystal Structure of Hydroxyapatite. Nature 1964;204:1050.
204. Posner A.S., Betts F. Synthetic amorphous calcium phosphate and its relation to bone mineral structure. Accounts of Chemical Research 1975;8(8):273-81.
205. Nicolopoulos S., González-Calbet J.M., Alonso M.P., Gutierrez-Ríos M.T., de Frutos M.I., Vallet-Regí M. Characterization by TEM of Local Crystalline Changes during Irradiation Damage of Hydroxyapatite Compounds. Journal of Solid State Chemistry 1995;116(2):265.
206. Onuma K., Ito A. Cluster Growth Model for Hydroxyapatite. Chemistry of Materials 1998;10(11).
207. Dorozhkin S.V. A hierarchical structure for apatite crystals. Journal of Materials Science: Materials in Medicine 2007;18(2):363-66.
208. Cuisinier F.J.G., Voegel J.C., Yacaman J., Frank R.M. Structure of initial crystals formed during human amelogenesis. Journal of Crystal Growth 1992;116(3-4):314-18.
209. Onuma K., Ito A., Tateishi T., Kameyama T. Growth kinetics of hydroxyapatite crystal revealed by atomic force microscopy. Journal of Crystal Growth 1995;154(1-2):118-25.
210. Onuma K., Ito A., Tateishi T. Investigation of a growth unit of hydroxyapatite crystal from the measurements of step kinetics. Journal of Crystal Growth 1996;167(3-4):773-76.
211. Land T.A., Malkin A.J., Kuznetsov Y.G., McPherson A., DeYoreo J.J. Mechanisms of Protein Crystal Growth: An Atomic Force Microscopy Study of Canavalin Crystallization. Physical Review Letters 1995;75(14):2774-77.

212. Malkin A.J., Land T.A., Kuznetsov Y.G., McPherson A., DeYoreo J.J. Investigation of Virus Crystal Growth Mechanisms by In Situ Atomic Force Microscopy. Physical Review Letters 1995;75(14):2778-81.
213. Gilmore R.S., Katz J.L. Elastic properties of apatites. Journal of Materials Science 1982;17(4):1131–41.
214. Qin Q.-H., Swain M.V. A micro-mechanics model of dentin mechanical properties. Biomaterials 2004;25(20):5081-90.
215. Asai S., Sassa K.-s., Tahashi M. Crystal orientation of non-magnetic materials by imposing of a high magnetic field. Science and Technology of Advanced Materials 2003;4:455.
216. Bowen W.H. Do We Need To Be Concerned About Dental Caries In The Coming Millenium? Critical Reviews in Oral Biology & Medicine 2002;13(2):126-31.
217. Paes Leme A.F., Koo H., Bellato C.M., Bedi G., Cury J.A. The Role of Sucrose in Cariogenic Dental Biofilm Formation-New Insight. Journal of Dental Research 2006;85(10):878-87.
218. Hojo S., Takahashi N., Yamada T. Acid profile in carious dentin. Journal of Dental Research 1991;70(3):182-86.
219. Van Houte J. Role of micro-organisms in caries etiology. Journal of Dental Research 1994;73(3):672-81.
220. Venegas S.C., Palacios J.M., Apella M.C., Morando P.J., Blesa M.A., . Calcium Modulates Interactions between Bacteria and Hydroxyapatite. Journal of Dental Research 2006;85(12):1124-28.
221. Loesche W.J., Straffon L.H. Longitudinal investigation of the role of Streptococcus mutans in human fissure decay. Infection and Immunity 1979;26(2):498-507.
222. van Houte J., Lopman J., Kent R. The predominant cultivable flora of sound and carious human root surfaces. Journal of Dental Research 1994;73(11):1727-34.
223. Bjørndal L., Larsen T. Changes in the cultivable flora in deep carious lesions following a stepwise excavation procedure. Caries Research 2000;34(6):502-08.
224. Hoshino E. Predominant obligate anaerobes in human carious dentin. Journal of Dental Research 1985;64(10):1195-98.
225. Katz S., Park K.K., Palenik C.J. In-vitro root surface caries studies. Journal of Oral Medicine 1987;42(1):40-48.
226. van Strijp A.J., van Steenbergen T.J., ten Cate J.M. Bacterial colonization of mineralized and completely demineralized dentin in situ. Caries Research 1997;31(5):349.
227. Sulkala M., Wahlgren J., Larmas M., Sorsa T., Teronen O., Salo T., et al. The effects of MMP inhibitors on human salivary MMP activity and caries progression in rats. Journal of Dental Research 2001;80(6):1545-49.
228. Marshall Jr. G.W., Marshall S.J., Kinney J.H., Balooch M. The dentin substrate: structure and properties related to bonding. Journal of Dentistry 1997;25(6):441-58.
229. Fusayama T. A simple Pain-Free Adhesive Restorative System by Minimal Reduction and Total Etching. Tokyo: Ishiyaku EuroAmerica Inc.; 1993.
230. Arnold W.H., Kanopka S., Gaengler P. Qualitative and quantitative assessment of intratubular dentin formation in human natural carious lesions. Calcified Tissue International 2001;69(5):268-73.

231. Arnold W.H., Konopka S., Kriwalsky M.S., Gaengler P. Morphological analysis and chemical content of natural dentin carious lesion zones. Annals of Anatomy - Anatomischer Anzeiger 2003;185(5):419-24.

Chapter III. Experimental techniques

In the past four decades various characterisation techniques have been developed to reveal the ultrastructure of materials such as reflection high-energy electron diffraction [1] (RHEED), atomic force microscopy [2] (AFM), auger electron spectroscopy [3] (AES), X-ray photoelectron spectroscopy [3] (XPS), scanning electron microscopy [4] (SEM), scanning tunnelling microscopy [5] (STM), scanning tunnelling spectroscopy [6] (STS), atom probe tomography [7] (APT), X-ray diffraction [8] (XRD) etc. Among all these techniques the transmission electron microscopy [9] (TEM) is unsurpassed in its ability to provide the direct observational, imaging, diffraction and other related information about the material ultrastructure and composition for all scales down to the atomic resolution of $1\,\mathring{A}$.

TEM was the primary characterisation technique in this research work and therefore more attention was given to the description of the TEM than other techniques, which were also used in this study, i.e. SEM and micro XRD.

After a short introduction into various electron microscopy techniques a quick introduction into scanning electron microscopy was given, followed with a more detailed description of transmission electron microscopy techniques. Then a brief introduction into the XRD characterisation technique completed the description of the experimental methods used in this work. Finally specimen preparation techniques for electron microscopy and particularly for TEM deserved a special attention and the preparation techniques used in this research completed this chapter.

3.1 Electron microscopy

Electron microscopy is based on the analysis of elastically and inelastically scattered electrons after the interaction with the specimen. Figure 3.1 summarises (1) different scattering processes, (2) the related method of characterisation for each process and (3) the detected data from the specimen. While scanning electron microscopy (SEM) analyses the secondary and the backscattered electrons from the surface of the sample, transmission electron microscopy (TEM) characterises the transmitted electrons.

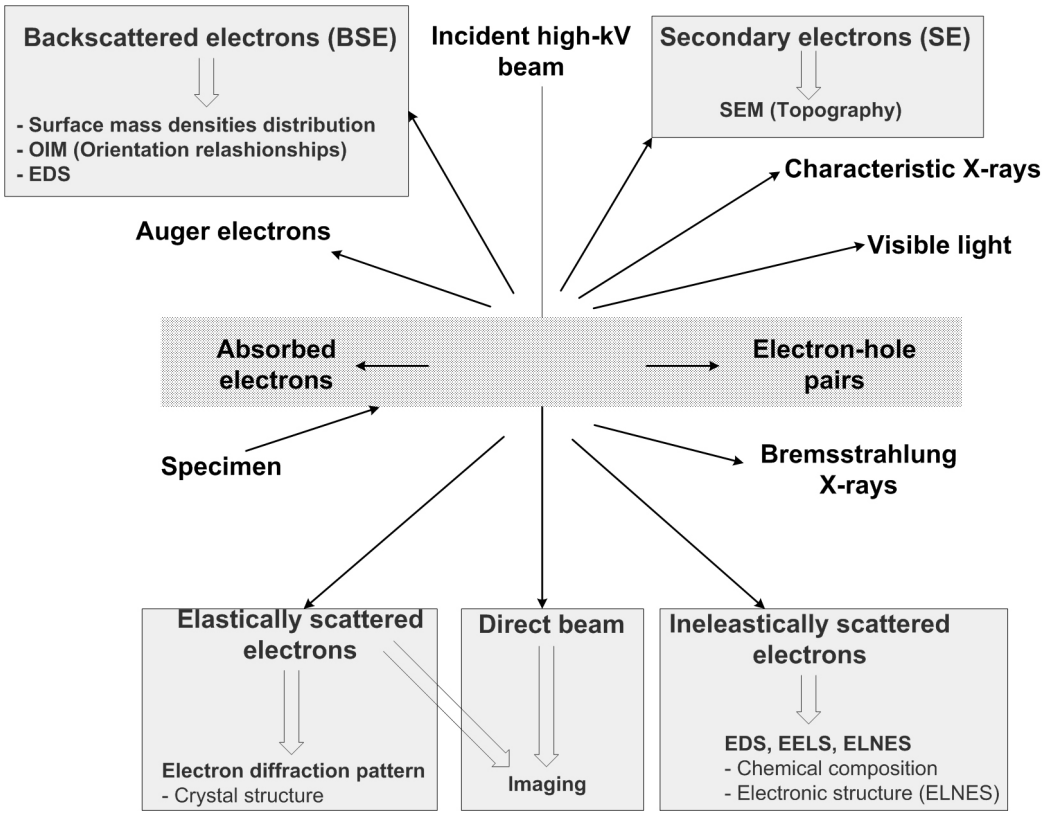

Figure 3.1 Types of interactions between incident beam and the specimen. The generated signals are registered by corresponding types of detectors mounted inside the specimen chamber inside an electron microscope. Processes enclosed in boxes were used in the presented work to characterize dentine. SEM was employed to analyse dentine specimens with SE and BSE. TEM was employed to analyse direct beam, elastically and inelastically electrons scattered on dentine structures.

3.2 Scanning electron microscopy (SEM)

Scanning Electron Microscopy is useful for the direct observation of surfaces because it offers better resolution and depth of field than optical microscope and allows direct observation of variability of mineral densities and mineral-to-organic ratios in calcified tissues, such as bone and dentine. The two major components of SEM are the electron column and control console [10]. The electron column consists of an electron gun and two or more electron lenses, which influence the path of electrons travelling down the evacuated tube. The control console consists of a cathode ray tube (CRT) viewing screen and computer to control the electron beam. The base of the column is connected with vacuum pumps that produce a vacuum of about 10^{-6} Torr. The purpose of the electron gun is to provide a stable beam of electrons. Usually tungsten or Lanthanum hexaboride (LaB_6) thermionic filaments are used as electron gun. The most common electron gun consists of three components: tungsten or LaB_6 wire filament serving as cathode, grid cap and anode. A filament is heated resistively by a current to a temperature of 2000 - 2700K. This results in an emission of thermionic electrons from the tip over an area of about 100 μm x 150 μm. The electron gun generates electrons and accelerates them to energy in the range 0.1 – 30.0 keV. The spot size from an electron hairpin gun is too large to produce a sharp image unless electron lenses are used to de-magnify it and place a much smaller focused electron spot onto the specimen. Most SEMs can produce an electron beam at the specimen with a spot size less than 10 nm that contains sufficient probe current to form an acceptable image. The beam arrives from the final lenses into the specimen chamber where it interacts with the specimen to a depth of approximately 1 μm and generates signals used to form an image. The scanned image is formed point by point. The deflection system causes the beam to move to a series of discrete locations along

a line and then along another line below the first one and so on until a rectangular 'raster' is generated on the specimen. Simultaneously, the same scan generator creates a similar raster on the viewing screen. Two pairs of the electromagnetic deflection coils (scan coils) are used to sweep the beam across the specimen. The first pair of the coils deflects the beam off the optical axis of the microscope and the second pair bends the beam back onto the axis at the pivot point of the scan [11].

Contrast in an image arises when the signal collected from the beam specimen interactions varies from one location to another. When the electron beam impinges on the specimen many types of signals are generated (Figure 3.1) and any of these can be displayed as an image. The two signals most often used to produce SEM images are secondary electrons (SE) and backscattered electrons (BSE). Most of the electrons are scattered at various angles between 0 and 180° when they interact with the positively charged nucleus. These elastically scattered electrons are called 'backscattered electrons' (BSE). BSE imaging is used to obtain a compositional contrast image, because the intensity of the BSE emission is related to the atomic number of the material. Regions that contain higher atomic number elements are brighter than those composed of lower atomic number elements. Some electrons scatter inelastically due to the loss in kinetic energy upon their interaction with orbital shell electrons. Due to electron bombardment phonons emerge in the specimen resulting in a heating of the specimen. Incident electrons may knock off loosely bound conduction electrons out of the sample. These are secondary electrons (SE) and they are widely used for SEM topographical imaging, SEM SE imaging. Both SE and BSE signals are collected when a positive voltage is applied to the collector screen in front of detector. When a negative voltage is applied on the collector screen only BSE signal is captured

because the low energy SEs are repelled. Electrons captured by the scintillator/photomultiplier are then amplified and used to form an image in the SEM.

If the electron beam knocks off an inner shell electron, the atom rearranges by dropping an outer shell electron to an inner one. This excited or ionized atom emits an electron commonly known as the Auger electron (Figure 3.1). Auger electron spectroscopy (AES) is useful to provide compositional information. Instead of excited atom releasing Auger electron, it can release a photon of electromagnetic radiation. If the amount of energy released is high, the photon will be an X-ray photon. These electrons are characteristic of the sample and can be used for qualitative chemical analysis of the specimen. This type of analysis is known as Energy Dispersive analysis of X-rays (EDAX).

The images collected with BSE detector allows to reveal levels of mineralization of the structure through the thickness of dentine from the DEJ towards the pulp and therefore reveal the carious zones of dentine, which were of interest, e.g. the transparent zone in this work.

3.3 Transmission electron microscopy (TEM)

TEM [9] is a method of producing images of a sample by illuminating the sample with electronic radiation under vacuum and detecting the electrons that are transmitted through the sample (Figure 3.1). After 35 years from the discovery of electron by J. J. Thompson in 1897, Max Knoll and Ernst Ruska found the way to accelerate electrons through a sample to create an image in a way remarkably similar to optical microscopy in order to create the first TEM [12]. In 1938 the first commercial TEM instruments began to be produced by Siemens-Halske Company in Berlin. TEM is similar to optical microscopy except that the photons are replaced by electrons.

Higher resolution can be achieved in TEM instruments because the electrons have a much smaller wavelength than visible light photons (Table 3.1).

Table 3.1 Comparison of light optical microscope (LOM) and TEM.

Characteristic of the instrument	LOM	TEM
Radiation	Light	Electrons
Lenses	Glass	Magnetic fields
Wavelength	$0.5\,\mu m$	$2\,pm$
Resolution	$0.5\,\mu m$	$0.1-0.2\,nm$
Sample thickness	$25-50\,\mu m$	$10-200\,nm$

TEM allows images to be obtained from the specimen at high resolution and magnification. Applying various types of TEM techniques, such as selected area diffraction (SAED), bright-field (BF) and dark-field (DF) imaging, high-resolution TEM (HRTEM) and high-angle annular dark field (HAADF, or Z-contrast) imaging, the crystallography and microstructure of the system can be investigated at the finest details.

TEM was the main experimental technique in the presented work. The measurements were performed on a Philips CM-12 conventional transmission electron microscope (CTEM), JEOL 3000F field emission gun high resolution TEM (FEG HRTEM) and an electron dispersive spectroscopy (EDS) was performed in a dedicated VGSTEM HB601 Scanning TEM (STEM).

3.3.1 Conventional TEM (CTEM)

The electron gun in CTEM usually consists of tungsten or Lanthanum hexaboride (LaB_6) wire filaments, which are bent into a hairpin ("V") shape and surrounded by a shield with a circular aperture (1-3 mm diameter) centred just below the filament tip. Electrons in the gun are accelerated across potential difference of the order of 10^5 volts between the cathode (at high negative potential) and anode (at ground potential). The function of the condenser lens is to focus the electron beam emerging from the electron gun onto the specimen to permit optimal illuminating conditions for visualizing and recording the image. The optical enlarging system of an electron microscope consists of an objective lens followed by one or more projector lenses (Figure 3.2). The objective lens determines resolution and contrast in the image and all subsequent lenses bring the final image to a convenient magnification for observation and recording. The objective lens is the most critical lens since it determines the resolving power of the instrument and performs the first stage of imaging. The specimen image generated by the objective lens is subsequently magnified in one or two more magnification stages by the intermediate and projector lens and projected onto a fluorescent screen or photographic plate.

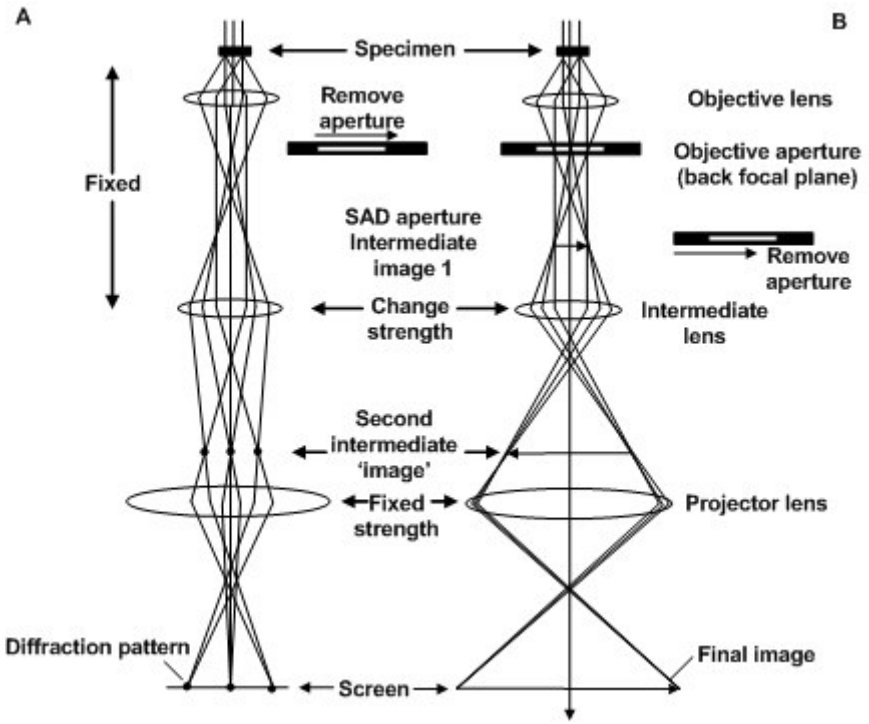

Figure 3.2 Ray diagram of a TEM operating in A. Bright-field imaging mode. B Diffraction mode (after [9]).

Two operation modes can be used, i.e. imaging mode (Figure 3.2A) and diffraction mode (Figure 3.2B). In the imaging mode an image is observed in the image plane, i.e. on the viewing screen, while in the diffraction mode a diffraction pattern is projected onto the viewing screen by changing the strength of intermediate lens. The contrast in conventional TEM is mainly due to diffraction/scattering contrast and mass-thickness contrast. These are based on the scattering cross-section of atoms in the specimen and the number of scattering atoms along the propagation of the electron beam. Stronger scattering regions of the specimen (heavy elements, large thickness) demonstrate darker contrast in the bright-field image than weaker scattering regions (light elements, thin specimen).

A diffraction pattern is formed in the back focal plane of the objective lens (Figure 3.2). The diffraction pattern of a polycrystalline specimen consists of diffuse rings and a crystalline specimen generates diffraction spots. These spots are formed

due to the constructive interference between the diffracted beams that fulfil the Bragg condition:

$$n\lambda = 2d_{hkl}\sin\Theta \tag{3.1}$$

where λ is the wave length of the electrons, Θ is the Bragg angle, d_{hkl} is the distance between the planes and n is an integer. The elastically diffracted electrons appear on the TEM screen as an array of bright spots (bright intensities) in a particular arrangement and distances depending on the structure of the sample under investigation. Since the direct beam is so intense that it may damage both the specimen and the viewing screen, an aperture (selected area electron diffraction aperture, SAED) is inserted into the back focal plane of the objective lens to reduce the illuminated area of the specimen. The image of this plane is then projected by the following lenses onto the viewing screen. Figure 3.3 demonstrates the electron diffraction pattern of hydroxyapatite oriented in the [001] direction.

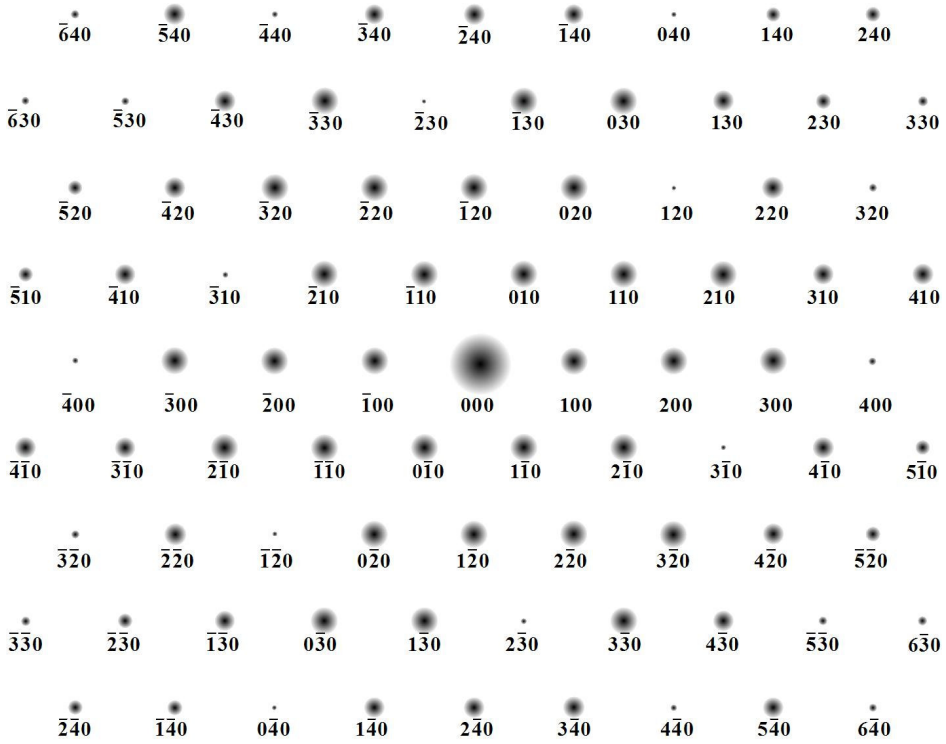

Figure 3.3 Electron diffraction pattern simulation of hydroxyapatite in [001] zone axis. Each spot is due to electron scattering by a specific (hkl) plane.

Electron diffraction patterns can be described in terms of the elastic scattering in the reciprocal space (Figure 3.4).

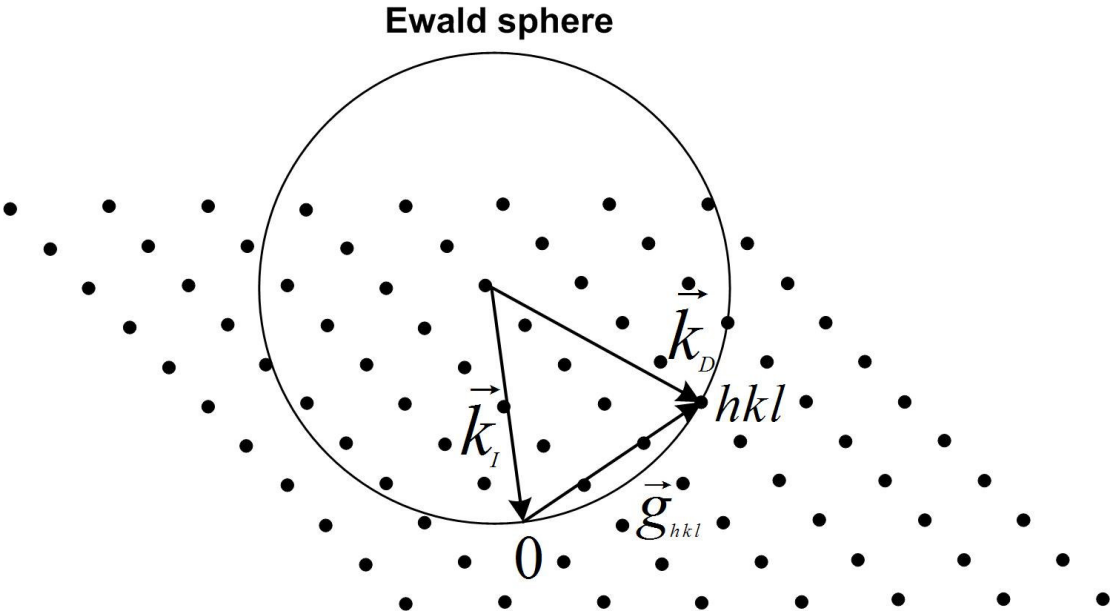

Figure 3.4 The intersection of the Ewald sphere of the radius $\vec{k}_I$ with the reciprocal lattice. The points of the reciprocal lattice, which lie on the Ewald sphere fulfil Laue condition.

In this space each set of parallel atomic (hkl) planes is represented by a single point located at a distance of $\frac{1}{d_{hkl}}$ from the lattice origin. The reciprocal lattice is formed by the collection of all (hkl) planes in the crystal. A reciprocal lattice vector $\vec{g}_{hkl}$ is assigned to each point in this space. The vector $\vec{g}_{hkl}$ is defined as a linear combination of the unit cell vectors $\vec{a}^*, \vec{b}^*, \vec{c}^*$ in reciprocal space:

$$\vec{g}_{hkl} = h\vec{a}^* + k\vec{b}^* + l\vec{c}^* \tag{3.2}$$

where h,k,l define (hkl) plane, $\vec{a}^* = \frac{\vec{b}\times\vec{c}}{\Omega}$, $\vec{b}^* = \frac{\vec{c}\times\vec{d}}{\Omega}$, $\vec{c}^* = \frac{\vec{a}\times\vec{b}}{\Omega}$ and $\Omega = \vec{a}\cdot(\vec{b}\times\vec{c})$ is the crystal unit cell volume.

The electron elastic scattering is described in reciprocal space by the condition:

$$\left|\vec{k}_I\right| = \left|\vec{k}_D\right| \tag{3.3}$$

where $\vec{k}_I$ and $\vec{k}_D$ denote wave vectors $\vec{k} = \frac{2\pi}{\lambda}\vec{e}_{beam}$ of the incident and diffracted electrons ($\vec{e}_{beam}$ is a unit vector in the direction of the corresponding beam). By construction of a sphere with radius $\left|\vec{k}_I\right|$ in reciprocal space (Ewald sphere) that passes through the origin of the reciprocal lattice, some of the reciprocal lattice points intersect the surface of the Ewald sphere. These lattice points satisfy the following condition (Figure 3.4):

$$\vec{g}_{hkl} = \vec{k}_D - \vec{k}_I \tag{3.4}$$

Equations 3.3 and 3.4 are known as Laue-condition. The reciprocal lattice points, which intersect the Ewald sphere fulfil the Laue-condition and give rise to diffraction with the characteristic scattering amplitude (A). Taking into account the curvature of the Ewald sphere, in the kinematics approximation the observed intensities (I_g is the intensity at $\vec{g}_{hkl}$) in the electron diffraction pattern for a thin foil [13]:

$$I_g = \left|A_g\right|^2 = \left|u_g\right|^2 \frac{\sin^2\left(\pi t s_g\right)}{{s_g}^2} \tag{3.5}$$

where u_g is proportional to the Fourier-coefficient of the electrostatic crystal potential $V(\vec{r})$ at $\vec{g}$, t is the thickness of the specimen and s_g is the excitation error: $s_g = \frac{1}{2}\left|\vec{g}\right|$. It is impossible to produce a perfectly parallel incident beam and therefore

the diffraction spots have a certain non zero diameter reflecting the convergence angle of the electron beam.

Depending on which diffraction spot contributes to the image formation, bright-field (BF) or dark-field (DF) images can be obtained. A BF image is formed when only the direct beam is selected by the objective aperture, which is inserted in the back focal plane of the objective lens (Figure 3.5).

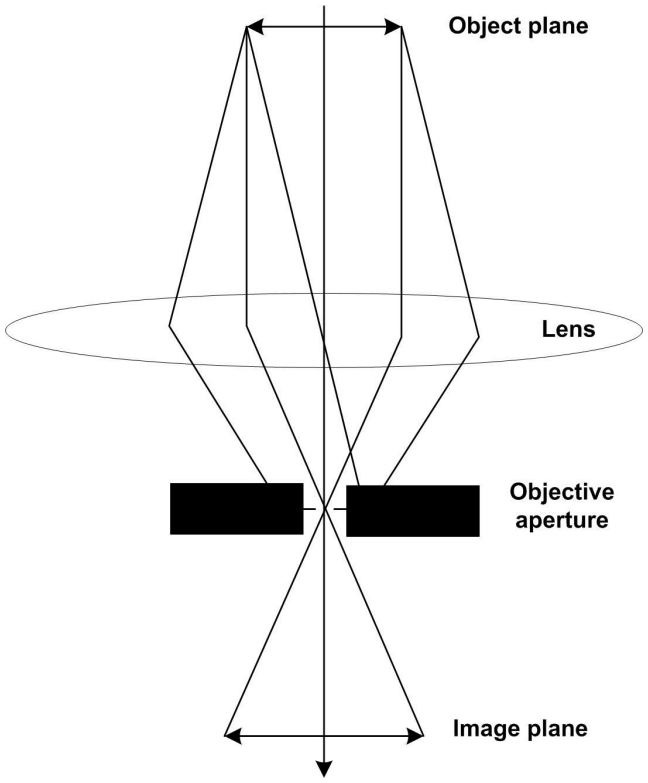

Figure 3.5 Bright-field (BF) image formation in TEM. Objective aperture stops all beams in the diffraction except the central beam, which is used for image formation.

For obtaining a DF image, the objective aperture is shifted in such a way that only one of the diffracted beams is contributing to the image formation (Figure 3.6).

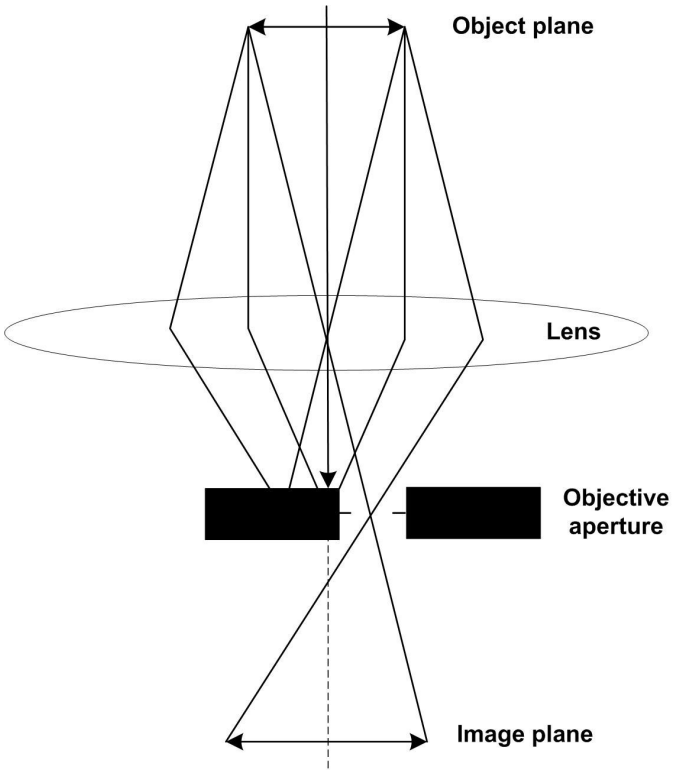

Figure 3.6 Dark-field (DF) image formation in TEM. Objective aperture stops all beams in the diffraction except the diffracted beam, which is used for image formation.

Since this beam runs off-axis its electrons suffer from the spherical aberration and astigmatism of the lenses more than the paraxially travelling electrons. Hence the incident beam should be tilted so that the scattered electrons used for imaging will travel parallel to the optic axis (angle corresponding to 2Θ with the optic axis). This method is called on-axis DF imaging.

BF and DF images are not images in Abbe's definition [14], since only one beam is used for imaging. The contrast in these images is in the case of a perfect crystal mostly due to the variation of thickness (thickness contours) or the variations in specimen orientation (bending contours). Lattice defects cause local bending of the crystallographic planes in their surrounding. This changes also the intensity of the beams that are selected for the image and a defect can be seen in the image. In

polycrystalline materials, intensity differences of the individual crystals can arise due to diffraction contrast and mass-thickness contrast.

The selected area electron diffraction (SAED) technique is used to obtain the diffraction pattern from a selected area of the specimen. To confine the diffraction pattern to the selected region of the specimen, a selected area aperture is used. The aperture is placed in the imaging plane of the objective lens, i.e. the plane where the first intermediate image is formed (Figure 3.2B). In this case, only beams (transmitted and diffracted) selected by the SAED aperture contribute to the final diffraction pattern, which is projected onto the viewing screen.

The micro-diffraction technique allows one to obtain a diffraction pattern from a small area of the specimen (of about 1 μm in the present work). This is done by focusing the incident beam on the specimen (i.e. focusing the condenser lens) while using the smallest condenser aperture. In this way, the regular diffraction from parallel illumination becomes convergent beam diffraction, and disks instead of spots are observed on the viewing screen.

In this work CTEM was employed for the study of inorganic phase of normal and carious dentine, i.e. characterisation of tubules, peritubular, intertubular and intratubular dentine in various zones and characterization of the dentine crystals in terms of the nature of the observed crystallites, texture (preferred orientation) and crystal sizes.

3.3.2 High Resolution TEM (HRTEM)

HRTEM can provide structural information with a spatial resolution of better than 0.2 nm [15]. If compared with CTEM, the HRTEM investigations reveal a magnified image of the specimen in projection up to finest details, i.e. atomic columns. Possible

applications for the HRTEM can be summarized as follows: distribution and structure of defects, interfaces and grain boundaries, nano-crystalline features in amorphous films, small particle analysis in heterogeneous catalysts, sub-micron morphological features, thermodynamic decomposition, diffusion and phase transformations. In this work it was employed for the ultrastructural investigation of caries induced intratubular dentine structural modifications.

In most crystalline materials including ceramics, semiconductors and metals, the position of individual atomic columns can be resolved at least in low-index zones [16]. When recorded under optimum conditions, electron micrographs can be directly interpreted in terms of the projected crystal potential. In other cases, image simulations are necessary to match proposed structures to image features [17]. At lower resolution, amplitude contrast images can be used to observe material features in the 0.5 - 1000 nm range.

HRTEM image formation can be described by Abbe's theory [14], which states that at least one diffracted beam and the direct beam have to be used to form an image. In order to resolve the fine details of the specimen, i.e. atomic columns, also large values of the $\vec{k}$ wave vector have to contribute to the image. The HRTEM image can be understood as a complex interference pattern of the various diffracted beams and the direct beam (Figure 3.7). This interference pattern depends on the imaging conditions and the thickness of the specimen.

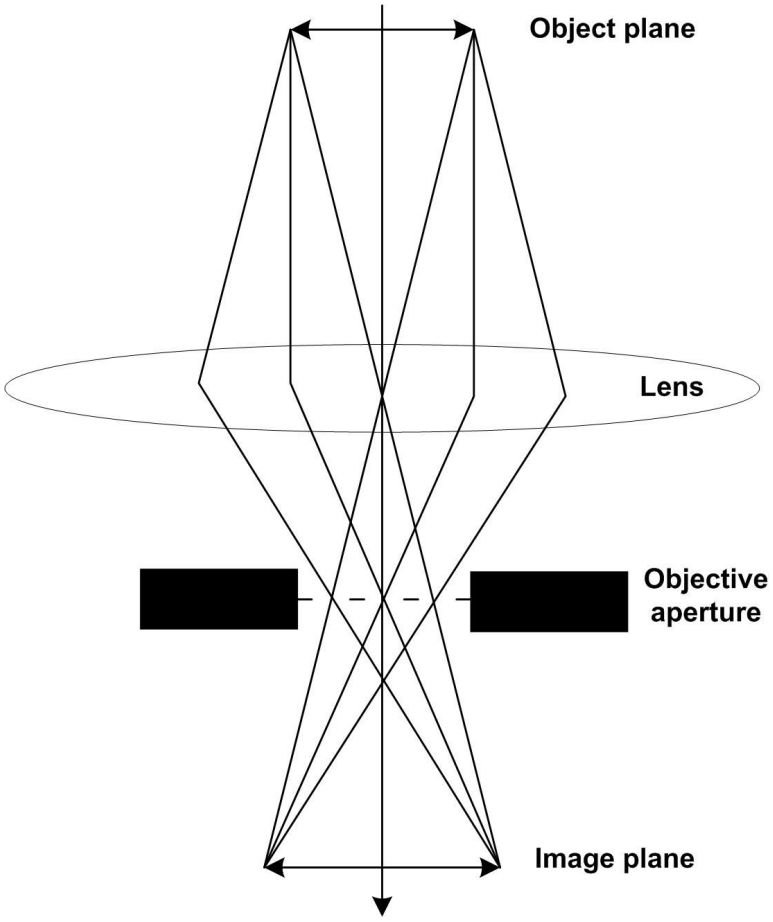

Figure 3.7. HRTEM makes use of a large objective aperture to form an image from many (or all) beams in the diffraction pattern. The resulting image is an interference image and the periodic features forming the image correspond to the planar spacings of the specimen. Each beam, which passes through the objective lens undergoes a certain phase shift, which depends on the path. Lens aberrations and defocus introduce additional phase shifts. The resolution of the microscope depends on these aberrations.

Direct interpretation of the obtained experimental HRTEM micrographs is often not possible. The main reasons for that are: (1) strong interactions between the electrons of the incoming electron wave with the Coulomb potentials of the atoms, which leads to dynamic effects such as multiple scattering even for small specimen thicknesses. Therefore the exit wave function cannot be easily related to the structure of the specimen. (2) Due to spherical aberration of the objective lens the electron rays from outer regions of the lens are bent more strongly compared to the electron rays passing the lens in the inner near-axis region. This leads to the formation of disks

rather than spots in the image plane. Due to the overlap of the disks the direct correlation between the image point and the object point gets lost.

These reasons often require HRTEM image simulations to retrieve the atomic structure of an unknown specimen. For that however, a model of the specimen structure has to be assumed. During the simulations the microscope parameters are used as an input and image intensity patterns are calculated. A digital comparison between simulated and experimental images is performed and the initial simulation parameters are varied until the best agreement is achieved. A more detailed description of the image simulation technique can be found in [9, 17].

In the presented work however, the resolved lattice planes of the crystallites were unambiguously linked to a particular calcium-phosphate phase. In this work the straightforward interpretation in terms of the object structure could be applied and therefore no further image simulation was necessary.

3.3.2.1 Image formation in HRTEM

Two main interactions contribute to the image formation: (i) the interaction of the incident plane wave with the electrostatic crystal potential and (ii) the interaction between the exit wave function and the microscope lens system (formation of the magnified image of the exit wave function).

The interaction of the incident wave function $\Psi_0(\vec{r})$ with the specimen becomes more complicated to calculate as soon as the specimen thickness increases, since dynamical effects (multiple electron scattering) have to be considered. For thin specimens the weak phase object approximation can be applied where the crystal potential modifies only the phase of the propagating electron wave but not the amplitude. Hence for the weak phase object the exit electron wave function $\Psi_e(\vec{r})$ is

'modulated' by the projected two-dimensional crystal potential. The exit wave function $\Psi_e(\vec{r})$ undergoes a Fourier transformation while travelling through the objective lens, i.e. a diffraction pattern is formed in the back focal plane (Figure 3.8):

$$\Psi_e(\vec{k}) = F(\Psi_e(\vec{r})) \tag{3.6}$$

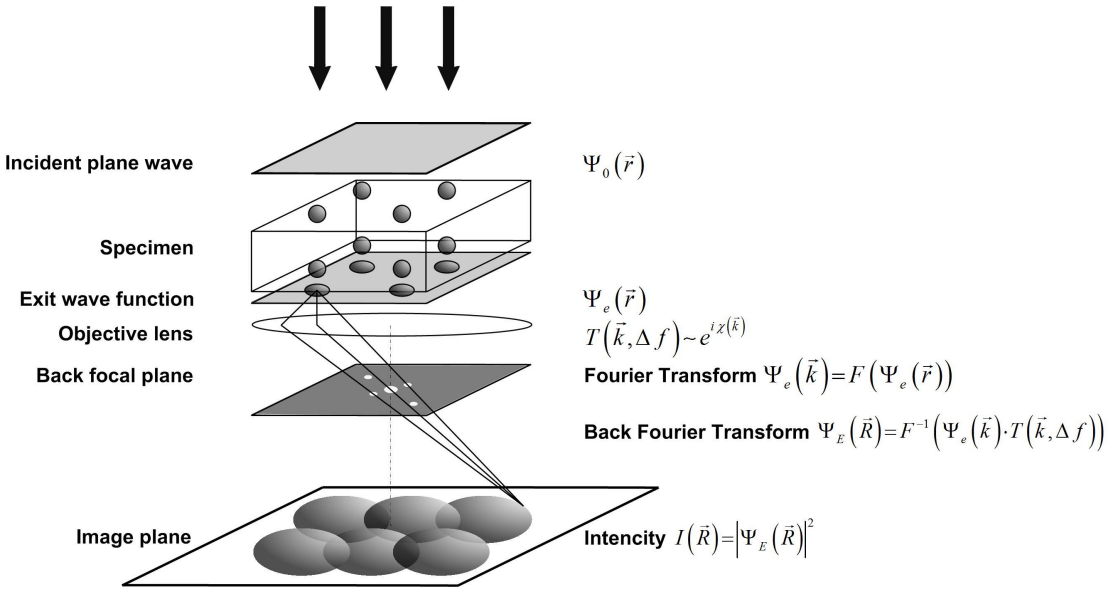

Figure 3.8 Image formation in HRTEM.

Electrons, emitted from the cathode have a certain energy spread, plus the instabilities of the high voltage also contribute to an energy spread. The energy spread together with the lens current instabilities and aberrations leads to differences in focal length and therefore to the formation of a disk rather than a point in the image plane (Figure 3.9).

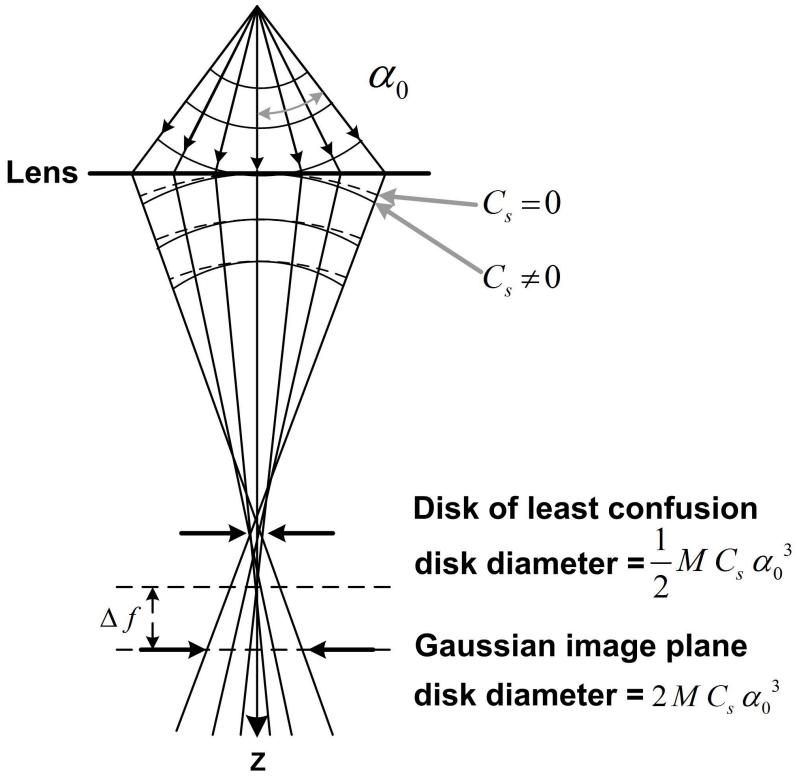

Figure 3.9 A ray diagram demonstrating the effect of spherical aberration: minimum contrast is obtained at the Gaussian image plane; the best imaging condition is achieved by defocusing the objective lens. M is the magnification, C_s is the spherical aberration and α_0 is the collection semi-angle of the lens.

The image plane in this case is defined as a plane where the paraxial beams are focused. The disk of least confusion is formed in the plane where the diameter of beams intersection is minimal.

The aberrations of the objective lens and the defocus (Table 3.2) are characterized by the aberration function:

$$\chi\left(\vec{k}\right) = \frac{\pi}{2} C_s \lambda^3 \left|\vec{k}\right|^4 - \pi \lambda \left|\vec{k}\right|^2 \Delta f \tag{3.7}$$

where C_s is the spherical aberration of the objective lens, Δf is the defocus, $\vec{k}$ is the wave vector and λ is the wave length. This aberration function is taken into account in the contrast transfer function (CTF) [9]:

$$T\left(\vec{k},\Delta f\right)=A\left(\vec{k}\right)E\left(\vec{k}\right)e^{i\chi\left(\vec{k}\right)} \tag{3.8}$$

where $A\left(\vec{k}\right)$ is the aperture function, $E\left(\vec{k}\right)$ an envelope function. CTF, $T\left(\vec{k},\Delta f\right)$, describes the transmitted wave vectors $\vec{k}$ (spatial frequences) and therefore, which atomic spacings are resolved.

Table 3.2 Lens aberrations and resolution.

Lens aberrations	Action	Influence of aberration	Correction
Spherical aberration	The strength of the lens increases with the angular deviation of the ray	$R_s \sim C_s\,\alpha_0^{\,3}$	Possible but still under development (very expensive)
Fraunhofer diffraction	Point images into a dot surrounded by concentric disks	$R_s = 0.61\frac{\lambda}{\sin\alpha_0}$ Adds up with spherical aberration	No
Defocus	Can be used to improve and optimize contrast	Counteracts with spherical aberration to give an optimum defocus (Scherzer defocus)	Unambiguous interpretation of the images to the resolution limit at Scherzer defocus
Chromatic aberration	The strength of the lens depends on the wavelength of the electrons	$\left(\frac{\Delta E}{E}\right)^2$ and $\left(\frac{\Delta I}{I}\right)^2$ Energy losses in thicker specimens	Only partly
Astigmatism	The strength of the lens is not cylindrically symmetric	Elongation and blurring of image details	Yes
Three-fold effects	Higher order lens errors	Deteriorates image details	Only partly

` The shape of CTF is controlled by changing and measuring of the defocus to the high precision. Compared with optical microscopes defocusing can actually increase the resolution and interpretability of the micrographs.

The aperture function $A\left(\vec{k}\right)$ cuts off beams scattered above certain critical angles that limit the resolution. However it is the envelope function $E\left(\vec{k}\right)$, which decreases the signal from the beams scattered at high angles and determines the maximum of the transmitted spatial frequency. This maximum determines the highest resolution achievable with a microscope and is known as the information limit. $E\left(\vec{k}\right)$ can be described as a product of single envelopes:

$$E\left(\vec{k}\right)=E_s\left(\vec{k}\right)E_c\left(\vec{k}\right)\cdot E_d\left(\vec{k}\right)E_v\left(\vec{k}\right)E_D\left(\vec{k}\right) \tag{3.9}$$

where $E_s\left(\vec{k}\right)$ is the angular spread of the source, $E_c\left(\vec{k}\right)$ is the chromatic aberration, $E_d\left(\vec{k}\right)$ is the specimen drift, $E_v\left(\vec{k}\right)$ is the specimen vibration and $E_D\left(\vec{k}\right)$ is the detector. Specimen drift and vibration can be minimized by proper engineering of the working environment of the microscope. The spherical aberration limits spatial coherency and defines $E_s\left(\vec{k}\right)$; the chromatic aberration, which includes current and voltage instabilities defines the temporal coherency in $E_c\left(\vec{k}\right)$. Together these two envelope functions determine the information limit.

If we consider the probe to have a Gaussian distribution of electron intensity, the spatial envelope function is given by [17]:

$$E_s\left(\vec{k}\right)=e^{-\left(\frac{\pi\alpha_0}{\lambda}\right)^2\left(C_s\lambda^3\left|\vec{k}\right|^3+\Delta f\lambda\left|\vec{k}\right|\right)^2} \tag{3.10}$$

The temporal envelope function, $E_c\left(\vec{k}\right)$, can be expressed as:

$$E_c\left(\vec{k}\right)=e^{-\frac{1}{2}(\pi\lambda\delta)^2\left|\vec{k}\right|^4} \tag{3.11}$$

where δ is the focus spread due to chromatic aberration:

$$\delta = C_c \sqrt{4\left(\frac{\Delta I_{obj}}{I_{obj}}\right)^2 + \left(\frac{\Delta V_{acc}}{V_{acc}}\right)^2 + \left(\frac{\Delta E}{V_{acc}}\right)^2} \tag{3.12}$$

where $\frac{\Delta I_{obj}}{I_{obj}}$ represents instabilities in the currents of the objective lens, $\frac{\Delta V_{acc}}{V_{acc}}$ is the instability in high voltage supply of the electron gun and $\frac{\Delta E}{V_{acc}}$ is the energy spread of electrons leaving the gun. More about the current state of technology in correcting spherical and chromatic aberrations and therefore pushing the information limit below $1\,\mathring{\mathrm{A}}$ can be found from [18] (achieved $0.5\,\mathring{\mathrm{A}}$ at present).

The CTF for Jeol 3000F FEG TEM is shown on Figure 3.10 at the 'extended' Scherzer defocus $\left(\Delta f_{s\mathrm{ch}} = -1.2\sqrt{\lambda C_s}\right)$ [19]. The value of Scherzer defocus is defined as the focus value where the pass-band in the CTF is the largest, i.e. where the first intersection of the CTF with the k - axis occurs (CTF = 0) at the highest frequencies. The hydroxyapatite spacing $d_{203} = 0.20\,nm$ lies just before the CTF intersection with the $k-$ axis, which is also called point-to-point resolution limit (Scherzer resolution $\delta = 0.66\left(C_s \lambda^3\right)^{\frac{1}{4}}$) [19].

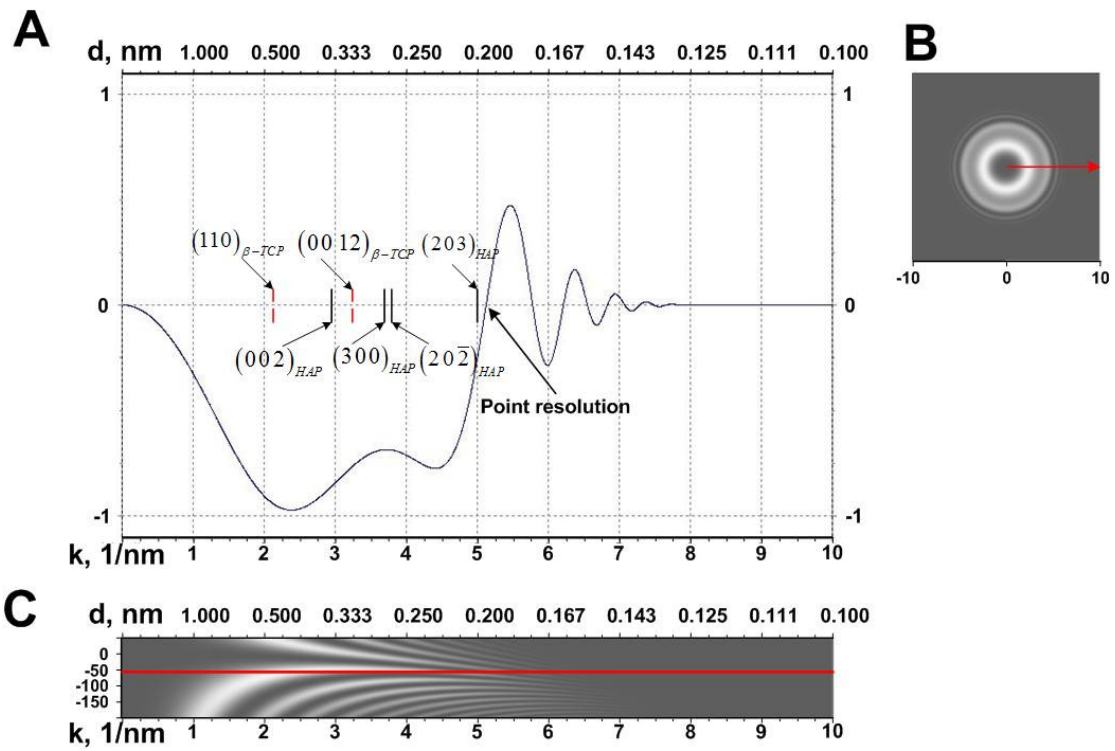

Figure 3.10 CTF of the Jeol 3000F FEG TEM at the 'extended' Scherzer defocus Δf_{sch} = -55.86 nm. Parameters: Voltage = 300 kV, C_s = 1.1 mm (spherical aberration), C_c = 1.8 mm(chromatic aberration), Energy Spread = 0.8 eV, HT ripple = 2 ppm, Objective Lens Instability = 1 ppm, Convergence = 1.5 mrad, Astigmatism and 3-fold Astigmatism = 0 nm. A. 1D CTF with HAP and β-TCP spacings used in the presented work. B. 2D CTF. The arrow demonstrates the direction in which the CTF was calculated. C. Defocus map of the Jeol 3000F FEGTEM (Spatial Frequency vs. Defocus vs. Intensity). The red line indicates the defocus for which 1D CTF was calculated.

The CTF multiplied with the Fourier transformed exit wave function $\Psi_e(\vec{r})$ describes the distribution of the amplitude in the back focal plane of the objective lens. Further wave propagation is described by the back Fourier transformation:

$$\Psi_E(\vec{R}) = F^{-1}\left(\Psi_e(\vec{k})\right) \cdot T(\vec{k}, \Delta f) \tag{3.13}$$

where $\Psi_E(\vec{R})$ represents the amplitude distribution in the image plane. Since an electron detector registers only the intensity $I(\vec{R})$ of interfered electron waves:

$$I(\vec{R}) = \Psi_E(\vec{R}) \cdot \Psi_E^*(\vec{R}) \tag{3.14}$$

and not the amplitude, the phase information is lost. Therefore, often it is not possible to reconstruct the object from the image in a straightforward manner and image simulations may be necessary.

Jeol 3000F FEG HRTEM operated at 300 kV was employed in this work to study a caries transparent zone of dentine.

3.3.3 Scanning transmission electron microscope (STEM)

In STEM the electrons pass through the specimen but in the same way as in SEM the electron optics focus the beam into a small spot, which is scanned over the specimen in a raster. The rastering of the beam across the sample makes these microscopes ideal for analysis techniques such as EDS, EELS and high-angle annular dark field imaging (HAADF). These signals can be obtained simultaneously, allowing direct correlation of image and quantitative data. By using STEM and a high-angle detector it is possible to form atomic resolution images where the contrast is directly related to the atomic number (Z-contrast) [20, 21]. This is a difference with the HRTEM technique, which uses phase-contrast and therefore often produces results, which may need interpretation by a simulation. Figure 3.11 presents a schematic drawing of such an instrument. The incident probe (0.15 – 0.20 nm for 100kV voltage STEM equipped with a field emission gun) is focused on the specimen. The electrons are scattered at different angles while passing through the specimen. The HAADF detector collects mainly the electrons that are scattered incoherently at relatively high angles (75 – 500 mrad). A background illumination is caused by thermal diffuse scattering.

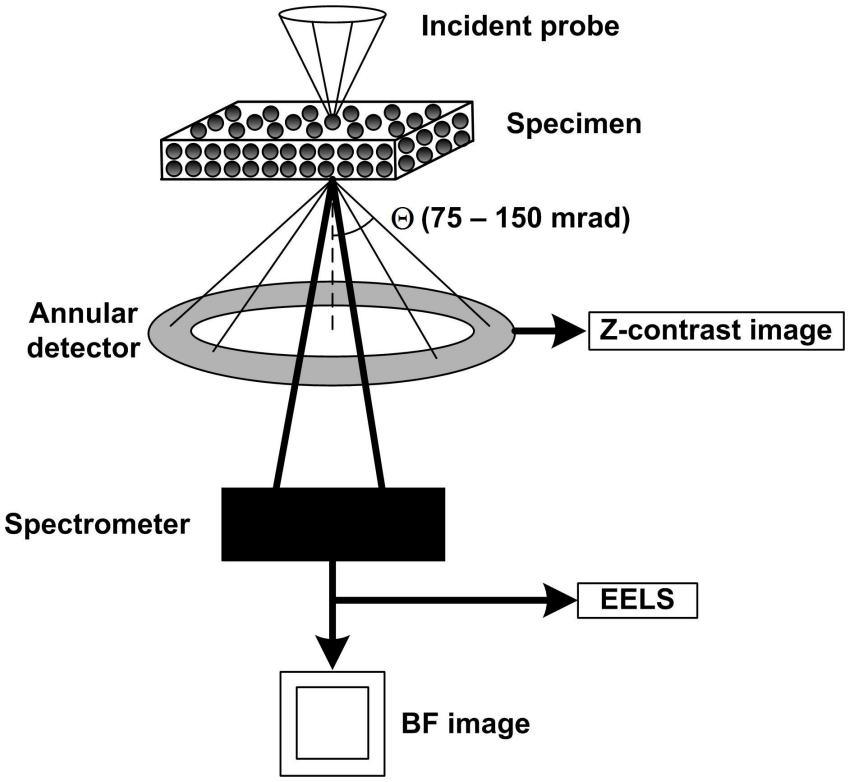

Figure 3.11 STEM – HAADF imaging system.

HAADF imaging can be described by Rutherford scattering, i.e. as a scattering by specimen atoms:

$$\frac{d\sigma}{d\Omega} = \frac{Z^2 e^4}{16 E^2 \sin^4 \Theta} \tag{3.15}$$

where σ is the scattering cross-section, Z is the atomic number, e is the elementary charge, Θ is the scattering angle and E is the energy of the scattered electron. Integrating Equation 3.15 we obtain $\sigma \sim Z^2$, i.e. the intensity in the image is proportional to the square of the atomic number of the scattering atom (Z-contrast technique). The image is formed by scanning of the electron beam across the specimen while simultaneously the HAADF signal is registered at each point.

VGSTEM HB601 Scanning TEM operated at 100kV and equipped with HAADF detector was employed in the present work for characterization of the intertubular and intratubular caries induced dentine in the transparent zone.

3.3.4 Electron Dispersive Spectroscopy (EDS)

Electron Dispersive Spectroscopy (EDS) is based on the interaction of incident electrons (electron beam) with inner-shell electrons of the specimen. The characteristic X-rays are produced when a material is bombarded with electrons in an electron beam instrument such as STEM.

During the ionization process (Figure 3.12) a high-energy electron ejects an electron from the inner-shell of the atom leaving a vacancy in the shell. The excited atom can return to its initial state filling the vacant place with an electron from an outer-shell (recombination). Because of the difference in bonding-energy the recombination process results in the emission of characteristic X-rays. The wavelength λ of the characteristic X-ray is given by:

$$\lambda = \frac{hc}{\Delta E} \tag{3.16}$$

where ΔE is the energy difference between two shells, h is the Planck's constant and c is the speed of light. The intensity and the wavelength of the X-ray yields quantitative and qualitative information on the elements present in the sample.

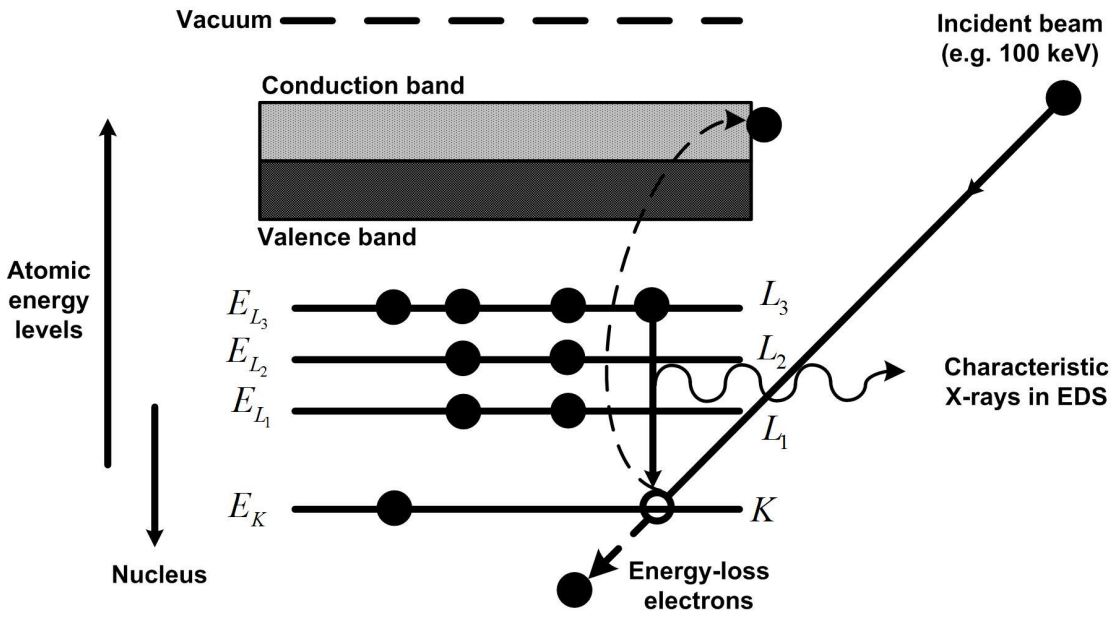

Figure 3.12 Interaction of an incident electron with an electron of the inner-shell. Characteristic X -ray (K_α line in this case) produced by an ionization process. The energy of this emission is unique for each atomic species forming the specimen.

EDS represents the intensity (photon counts) versus energy of the emitted X-rays. Peaks in the spectrum arise from the presence of certain elements in the sample. In the presented work EDS was performed on intratubular and intertubular carious dentine in a dedicated VGSTEM HB601 STEM.

3.4 X-ray diffraction (XRD)

Wilhelm Röntgen discovered X-rays in 1895 by demonstrating a new type of radiation, which was occurring inside a vacuum tube in his laboratory. He called this new type of radiation 'X radiation'. Also Röntgen was the first who took the X-ray image of his wife's hand and with that famous image he demonstrated the immense new possibilities in medical diagnosis. It was much later (1912 - 1913) when in the series of X-ray diffraction experiments the electromagnetic nature of the X-radiation was revealed and also the atomic structure of crystals was demonstrated with this new technique [22].

X-ray methods are suitable for investigating many scientific problems on length scales down to atomic dimensions: (1) the X-rays wavelength is at the atomic scale and therefore X-ray diffraction provides an information about the distances between atoms; (2) due to a small scattering cross-section the kinematical approximation is applicable, which makes the analysis straightforward; (3) generally X-rays based techniques are non-destructive; (4) modern X-rays techniques provide information of crystal properties of materials from 3D bulk down to extremely small quantities of atoms from the surface of a material when using a synchrotron light source, which provides a very high X-ray photon flux; (5) due to a small scattering cross section the penetration of the X-rays is relatively large and therefore suitable for studies of undersurface structures such as buried interfaces, e.g. solid-liquid interfaces.

The typical photon energies of the X-rays are in the range of 100 eV - 100 keV but for the diffraction applications only short wavelength X-rays in the range of a few angstroms down to 0.1 $\mathring{A}$ are used. X-rays are generated when a focused electron beam is accelerated across a high voltage field and bombards a stationary or rotating target. As electrons collide with atoms in the target and slow down, a continuous spectrum of X-rays are emitted, which are termed Bremsstrahlung radiation (Figure 3.1). The high-energy electrons also eject inner shell electrons in atoms through the ionization process. When a free electron fills the shell, X-ray photon with energy characteristic of the target material is emitted. Common targets used in X-ray tubes include Cu and Mo, which emits 8 keV and 14 keV X-rays with corresponding wavelengths of 1.54 $\mathring{A}$ and 0.8 $\mathring{A}$ respectively. X-rays primarily interact with electrons in atoms. When X-ray photons collide with electrons, some photons from the incident beam will be deflected away from the direction where they originally

travelled. If the wavelength of these scattered X-rays did not change (X-ray photons does not lose any energy) the process is called elastic scattering where only momentum was transferred in the scattering process. These are the X-rays measured in diffraction experiments.

The kinematical theory, which is the simple geometric representation of Bragg's law (Equation 3.1, where this time λ is the wave-length of the X-ray radiation), is sufficient to describe the measurements of crystal lattice spacings, i.e. the constructive interference is only observed if the path length difference between the incident beam and the reflected beam is equal to an integer number of wavelengths. In this approach absorption, extinction, refractive and multiple scattering effects are neglected. Only in special cases of almost perfect crystals (such as silica in some cases) kinematical approach is sometimes not sufficient and the so-called dynamic theory has to be applied, where all these neglected effects are considered. More often though, even in these special cases the Distorted Wave Born Approximation (DWBA) theory is sufficient, where only the refractive effects are considered and others are neglected. In this work the kinematical approach is adequate in describing scattering intensities from dentine and enamel inorganic phases.

3.4.1 Crystallites size

The physics behind the measurements of the size of the crystallites in the polycrystalline materials such as dentine and enamel can be easily understood taking into account the following considerations.

Lets consider the size of the crystal in the direction perpendicular to a certain (hkl) plane (Figure 3.13). The distance between these particular parallel lattice planes was d_{hkl}. Then the thickness of the crystallite in the direction perpendicular to (hkl)

was $t_{hkl} = m\,d_{hkl}$, where m was the number of parallel lattice planes through the thickness of the crystallite.

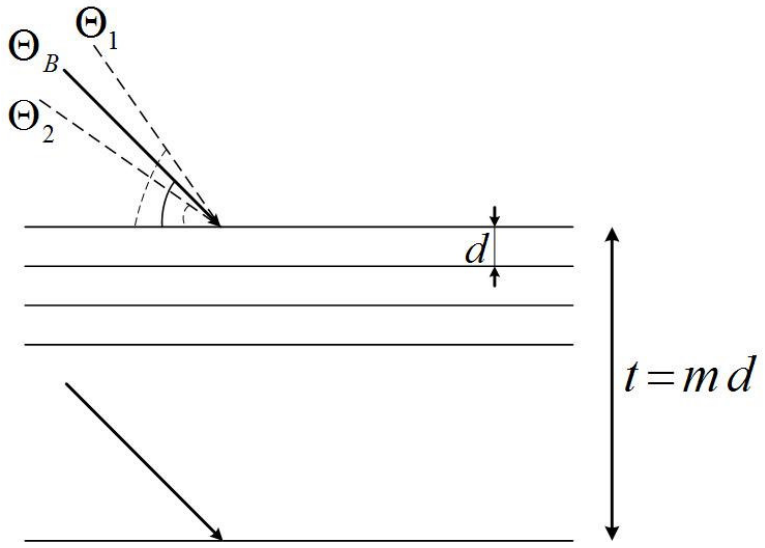

Figure 3.13 Schematic representation of the parallel (hkl) planes, which contribute to the constructive interference of the incident beams between $\Theta_{hkl}^{(1)}$ and $\Theta_{hkl}^{(2)}$ angles.

Taking into the consideration the kinematical approach let $\Theta_{hkl}^{(1)}$ be the highest angle (ray 1) of the incident beam and $\Theta_{hkl}^{(2)}$ be the lowest angle (ray 2) before the destructive interference occurs. Then the path lengths differences between X-rays scattered from the front and back planes of the crystallite are: $\delta_1 = \frac{2t_{hkl}}{\sin\Theta_{hkl}^{(1)}} - 2t_{hkl}\frac{\cos^2\Theta_{hkl}^{(1)}}{\sin\Theta_{hkl}^{(1)}} = 2t_{hkl}\sin\Theta_{hkl}^{(1)}$ and $\delta_2 = 2t_{hkl}\sin\Theta_{hkl}^{(2)}$. Taking into account that the path differences for rays 1 and 2 are $(m+1)\lambda$ and $(m-1)\lambda$ respectively we obtain the following system of equations:

$$\begin{cases} 2t_{hkl}\sin\Theta_{hkl}^{(1)} = (m+1)\lambda \\ 2t_{hkl}\sin\Theta_{hkl}^{(2)} = (m-1)\lambda \end{cases} \tag{3.17}$$

Using the approximation for small angles: $\sin\frac{\Theta_{hkl}^{(1)}-\Theta_{hkl}^{(2)}}{2}\approx\frac{\Theta_{hkl}^{(1)}-\Theta_{hkl}^{(2)}}{2}$, introducing $\Theta_{hkl}=\frac{\Theta_{hkl}^{(1)}+\Theta_{hkl}^{(2)}}{2}$ and approximating X-ray diffraction peak shape with a triangle (Figure 3.14) with a full-width at half-max (FWHM) $B_{hkl}=\frac{2\Theta_{hkl}^{(1)}-2\Theta_{hkl}^{(2)}}{2}$, the Equation 3.17 yields:

$$t_{hkl}=\frac{\lambda}{B_{hkl}\cos\Theta_{hkl}} \tag{3.18}$$

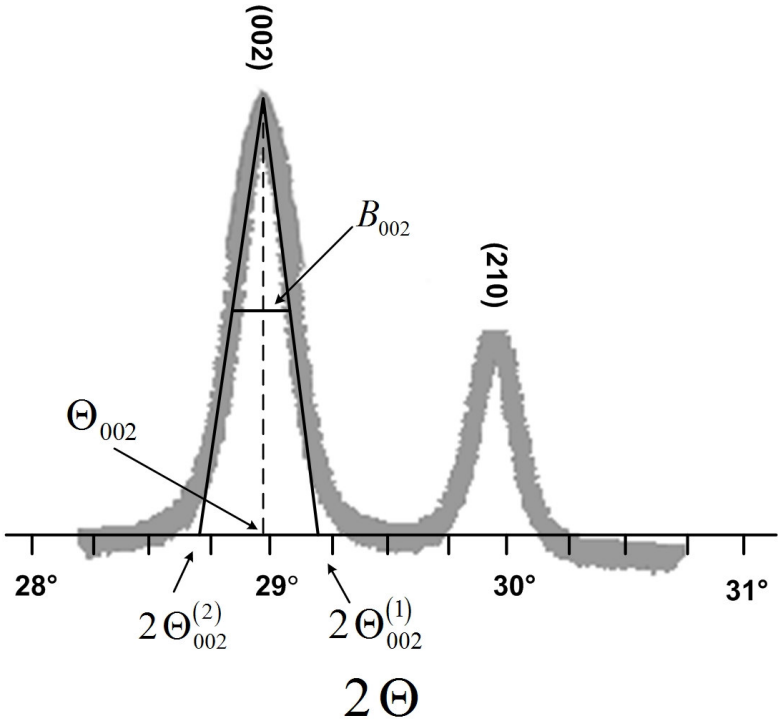

Figure 3.14 Fragment of the middle dentine X-ray diffraction profile. The shape of the peak corresponding to 002 reflections was approximated with a triangle.

A number of methods to extract the information about the grain size of the polycrystalline material from XRD data have been developed such as Scherrer method, Scherrer-Wilson etc. However, generally these methods are adjusting Equation 3.18 by various approximations of the X-ray diffraction peak shapes. For

example it was calculated that if X-ray diffraction peak shapes are approximated with a Gauss function (Scherrer's approximation), the Equation 3.18 should be adjusted:

$$t_{hkl} = K_G \frac{\lambda}{B_{hkl} \cos \Theta_{hkl}} \tag{3.19}$$

where $K_G = 2\sqrt{\frac{\ln 2}{\pi}} \approx 0.94$, t was interpreted as volume averaged crystalline dimension perpendicular to the reflecting planes and Θ_{hkl} was the centroid peak position [8].

Further adjustments to the Equation 3.18 were made following the consideration that peaks broadening is not only attributed to the finite size of a crystallite but also due to the presence of a non-uniform strain in the crystal. Then the separation of size and strain broadening can be performed based upon an explicit assumption of the shape of the broadening profile due to each effect. Since the experimental data suggested that the profiles should be some bell-shaped functions (Figure 3.14), two such functions were proposed: Lorentzian and Gaussian functions. One of the approaches suggests that both effects, which contribute to the broadening of the profile, can be approximated with Lorentzian functions. This approach is called Williamson-Hall method. However, considering the experimental results it was suggested that the effects of strain broadening could be more closely represented by a Gaussian function while the effects of small sizes of crystallites were represented by a Lorentzian function. Also it was demonstrated that though FWHM is a relatively simple parameter to interpret a measure of a peak width, integral breadth (area under the peak above the background divided by the peak height) was preferred in this type of work. Interpreting B_{hkl} as an integral breadth and further simplifying Lorentzian +

Gauss relationship to a parabolic expression we arrive to Scherrer-Wilson approximation [23]:

$$\frac{\Theta_{hkl}^2}{\tan^2\Theta_{hkl}} = \frac{1}{t_{hkl}} \frac{K_L \lambda B_{hkl}}{\tan\Theta_{hkl} \sin\Theta_{hkl}} + 16\sqrt{\left\langle \varepsilon_{hkl}^2 \right\rangle} \tag{3.20}$$

where $\sqrt{\left\langle \varepsilon^2{}_{hkl} \right\rangle}$ was the root-mean-square of the lattice strain and $B_{hkl} = \frac{1}{I_p}\int I(2\Theta)\, d\Theta$, where I_p was the peak intensity, $I(2\Theta)$ was the intensity at $2\Theta_{hkl}$ and $K_L \approx 0.9$.

Plotting $\frac{K_L \lambda B_{hkl}}{\tan\Theta_{hkl} \sin\Theta_{hkl}}$ vs. $\frac{\Theta_{hkl}^2}{\tan^2\Theta_{hkl}}$, the root-mean-square of the lattice strain can be extracted from the intercept with the ordinate and the crystallites size can be determined from the slope.

Another method of extracting crystallites properties from polycrystalline materials, which is worth mentioning is based on the assumption that the XRD line profile can be interpreted as Fourier transformation of the crystalline structure in the reciprocal space, i.e. that the Bragg-peak line profile can be expressed as a Fourier series. This approach is called Warren-Averbach method [23].

In this work however, Scherrer and Scherrer-Wilson methods were used to determine the size of the crystallites forming inorganic phase of dentine and enamel.

3.4.2 Texture

A material is considered ‘textured’ if the crystallites (grains) are aligned in a preferred orientation along certain lattice planes. One can view the textured state of a material as an intermediate state with properties between a randomly oriented polycrystalline powder and a completely oriented single crystal.

It is convenient to describe (hkl) planes orientation of a crystallite with Euler angles to the unit-vector normal to (hkl) [24], i.e. $\alpha \in [0, 2\pi]$ is the angle to the X-axis, $\beta \in [0, 2\pi]$ is the angle to the Y-axis and $\gamma \in [0, \pi]$ is the angle to the Z-axis, where Euler angles represent sample reference frame. Euler space (G) is then a set of (α, β, γ) angles associated with a unit-vector $\vec{g} = (\alpha, \beta, \gamma)$ (an (hkl) pole) and the (hkl) orientation distribution function (ODF) is $f(\vec{g}) = (\alpha, \beta, \gamma)$. Texture can be described as a volume fraction of crystallites, which (hkl) planes are orientated within $dg = \sin\gamma \, d\alpha \, d\beta \, d\gamma$:

$$\frac{dV(\vec{g})}{V} = \frac{1}{8\pi^2} f(\vec{g}) \, dg \tag{3.21}$$

where ODF is normalised $\frac{1}{8\pi^2} \int_G f(\vec{g}) \, dg = 1$.

In these terms ODF can be described as the density of (hkl) poles in a certain direction $P_{hkl} = \frac{1}{8\pi^2} f(\vec{g})$. The pole density distribution is obtained as a ratio of the reflected integral intensity to the intensity of the incident beam [25]:

$$\frac{I_{hkl}}{I_0} = k_{hkl} \, P_{hkl} \tag{3.22}$$

where k_{hkl} takes into account other intensity factors. In the kinematical approximation k_{hkl} is independent of sample orientation or the orientation of the crystallites in the sample and therefore Equation 3.22 can be simplified:

$$\frac{I_{hkl}}{I_0} = k \, P_{hkl} \tag{3.23}$$

Texture can now be measured by comparing the intensity peaks of the specimen, e.g. dentine or enamel, with the corresponding intensity peaks of a random

powder mixture of the same material as the specimen, e.g. hydroxyapatite random powder. A peak that is stronger than all other peaks from a random specimen identifies a direction of preferred crystallographic orientation that is normal to the diffracting planes for the peak. This approach was used in Chapter IV to calculate the preferred orientation (texture) indices in dentine and enamel.

Parallel beam XRD using poly-capillary collimating optics (micro XRD) can be used to enhance texture analysis of materials. Due to the insensitivity of parallel beam XRD to sample geometry and displacement errors, minimal sample preparation is required for texture analysis of samples. Furthermore, through use of a poly-capillary collimating optics, the parallel beam XRD system can be combined with a low power X-ray source, reducing instrument size and power requirements for *in situ* texture measurements.

3.4.3 Micro X-ray diffraction (μXRD)

Micro X-ray diffraction is a structural analysis technique, which allows for the examination of very small sample areas. Unlike conventional XRD technique, which has a typical spatial resolution ranging in diameter from several hundred micrometers up to several millimetres, μXRD uses X-ray optics to focus the excitation beam to a small spot on the sample surface (Figure 3.15) so that small features on the sample can be analysed.

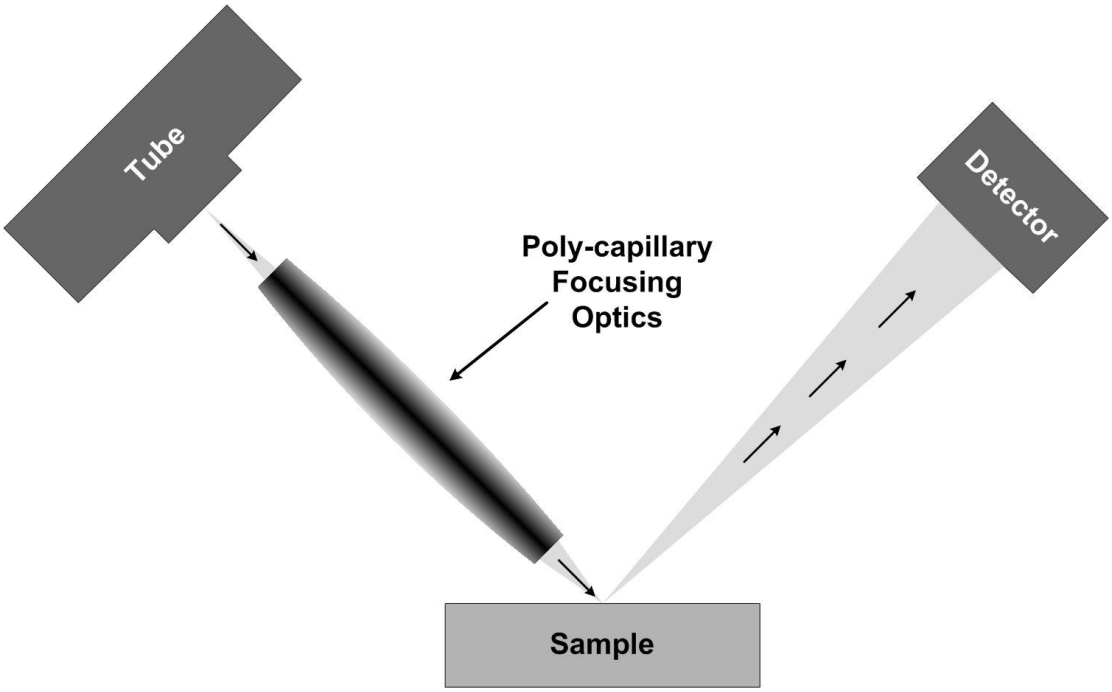

Figure 3.15 Schematic representation of the μXRD technique.

Poly-capillary focusing optics collects X-rays from the divergent X-ray source and directs them to a small focused beam at the sample surface with diameters as small as tens of micrometers. The resulting increased intensity delivered to the sample in a small focal spot allows for enhanced spatial resolution for small feature analysis and enhanced performance for diffraction measurement of small specimens.

μXRD experiments were performed on dentine and enamel using X-ray diffractometer D8 Discover with GADDS (general area detector diffraction solution) (Bruker AXS), which generated monochromatic and parallel X-ray beam using Cu target (CuKα line, λ = 1.5418Å). The poly-capillary optics focused X-ray beam to a 50 μm diameter spot. The sample to detector distance was 15.1 cm, 2Θ scanning angle range was from 8° to 102° with a step-size 0.02° and per step scan time was 1.15s, which was adequate to collect the reliable data due to the new generation of the state of the art detectors, 2D HI-STAR detector in this work, versus previous generation detectors, such as 1D Scinti (Figure 3.16).

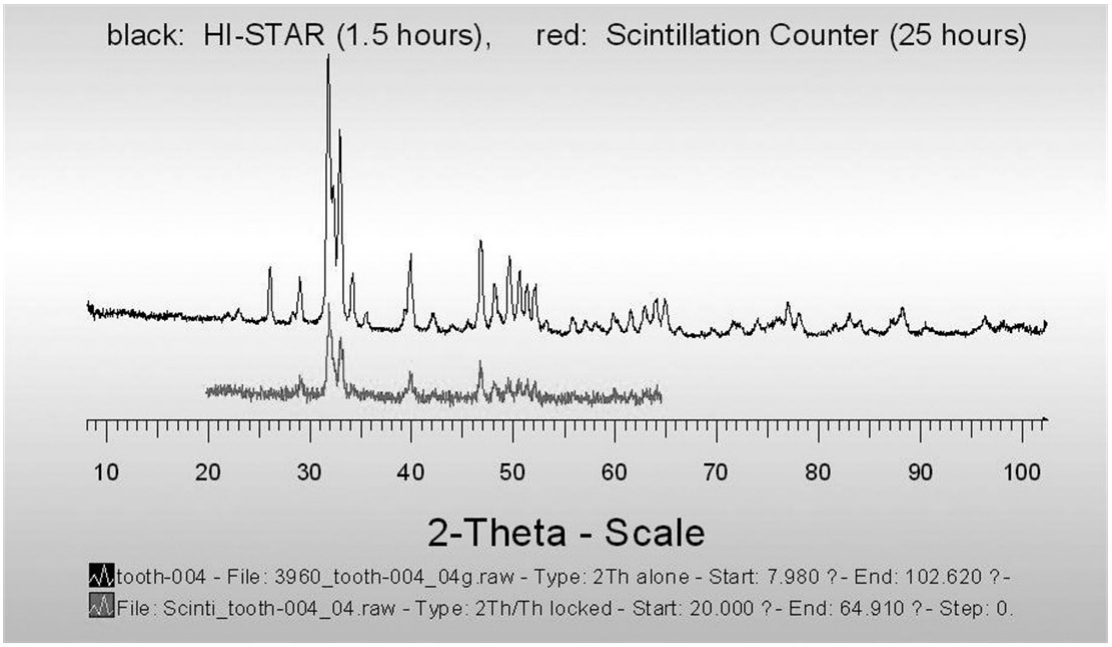

Figure 3.16 XRD profiles measured on enamel at 500 μm from the DEJ. Upper XRD profile was measured with the HI-STAR detector and lower profile was measured with Scinti, previous generation detector.

All measurements were performed at room temperature (290 ± 0.1 K). The analysis spots were determined using an optical microscope equipped with a laser marker.

3.5 Specimen preparation

The goal of the ultrastructural analysis in this work was to reveal the ultrastructure and constituents of the inorganic phase of carious dentine and compare the results with the ultrastructure of normal unaffected dentine. The specimen preparation technique was therefore very important because the ultrastructure and chemistry of the specimens may be obscured or altered by the use of a poor technique.

3.5.1 Specimen collection

Human molar teeth were extracted in Sydney Dental Hospital due to severe occlusal caries lesions with informed consent obtained prior the extraction from each subject and collected for this study according to the protocols approved by the Ethics Review Committee of Sydney South West Area Health Service, reference №X07-0217 & 07/RPAH/47 and by the Human Research Ethics Committee of the University of Sydney, reference №10541. Human molar non-carious teeth were also used in this study as reference specimens. These non-carious teeth were extracted in Sydney Dental Hospital from 12 – 17 years old subjects for orthodontic reasons.

3.5.2 Disinfection, fixation and embedding

Teeth surfaces were sterilised immediately upon extraction by placing in sodium hypochlorite 1% solution [26, 27] at 2° for 24 h and then further disinfected and fixed in paraformaldehyde containing solution [28, 29] (modified Karnovsky's fixative) at 2° for 24 h. If the specimen preparation procedure for the electron microscopy observation did not start immediately after the disinfection and initial fixation the specimens were placed into Hanks' balanced salts solution [30].

Since human teeth specimens were relatively small and difficult to handle for a precision sectioning it was necessary to embed specimens into a mounting material. A cold curing epoxy mounting medium was used in this work (Epofix, Struers, Copenhagen, Denmark). Carious lesions were sealed with adhesive (Bostik Blu-Tack) to prevent resin from penetrating into carious lesions. The resin was polymerised for 24 hours at the room temperature.

3.5.3 Sectioning

There are many ways of sectioning specimens, including blade sawing, wire sawing, abrasive cutting, fracturing, shearing, spark erosion, microtomy etc. If using a saw it is important not to damage a dentine specimen during the sawing operation by heating it so a water-cooled saw was used to cut all the specimens in this work. Also the surface of the specimens should be polished for observations in SEM so slow-speed diamond wheel cut-off saw was utilised to minimize the zone of deformation around the cut.

One-millimetre sections were prepared by sectioning the specimen along mesio-distal axis using a low-speed diamond saw (Isomet, Buehler Ltd., Lake Bluff, USA), equipped with a micrometer, and under constant water irrigation.

3.5.4 SEM specimen preparation

This part of the chapter covers the technique, which was used specifically for preparing teeth specimens for examination in the SEM.

3.5.4.1 Polishing

A graded sequence of abrasive materials was used to prepare the surface for microstructural observations in SEM. Specimens were mounted on a tripod and levelled. All grinding steps were carried out wet to prevent heating of the specimens and to promote a better surface finish. The first step involved coarse grinding using an abrasive of 320 – 400 grit. When the damage from sectioning operation was removed a sequence of finer abrasives was used, i.e. 600 and then 1200 grit abrasive papers. After the specimens were grounded to a 1200-mesh finish the specimens were

polished to produce a flat scratch-free surface. This was accomplished by polishing the specimens with diamond paper abrasives having particle sizes starting with 30 μm for coarse polishing and then 9 μm, 6 μm, 3 μm and 1 μm for a final surface finish. Each step of the polishing progress was checked with the aid of an optical microscope. The final result was a flat, scratch-free surface with a high reflectivity. Since backscatter electron imaging was used, no etching was needed to further prepare the surface of the specimens.

3.5.4.2 Cleaning and dehydration

The specimens were cleaned ultrasonically in deionised water for 20 seconds and then dehydrated in the series of ethanol up to absolute (100%) ethanol according to the following schedule (Table 3.3):

Table 3.3 Time-schedule for dehydration of dentine specimens in a graded ethanol.

Time, min	Ethanol concentration, %
15	50
15	50
15	95
15	95
10	100
10	100

2.5.4.3 Drying

For SEM investigations the specimens must be dried in order to prevent boiling water or ethanol, used to substitute water during the dehydration procedure, in the high vacuum conditions of the SEM chamber, which may damage the integrity of the

surface. There are several techniques available to dry specimens such as air-drying, freeze-drying and critical point drying (CPD).

Air-drying and CPD techniques were used in this work to dry carious and non-carious teeth specimens.

It was found that two days air-drying at room temperature in a dust free environment was sufficient for both carious and non-carious teeth specimens, however, more cracks seemed to develop when using this technique than using the CPD technique, perhaps due to a more extensive shrinkage of the specimens.

The procedure for the CPD technique was the following:

1. Fill the pre-chilled chamber of the critical point dryer with 100% ethanol.
2. Transfer the specimens into the chamber and seal the chamber.
3. Fill the chamber with liquid CO_2 and maintain 0°C temperature.
4. Change liquid CO_2 medium five times to displace ethanol.
5. Raise the temperature to the critical point, which is 31°C for CO_2 (at 5.55×10^4 Torr). After liquid CO_2 is converted into a gas phase, release pressure but maintain the higher temperature to prevent CO_2 condensation.
6. Remove specimens from the chamber.

3.5.4.4 Mounting on SEM stub

Two major types of adhesives available to fix specimens onto SEM aluminium stubs: liquid adhesives (silver- or carbon-doped conductive adhesives, quick-setting conductive epoxy cements, china cements and others) and various sticky tapes, such as double-sided carbon conductive tapes.

In this work specimens were mounted on stubs with either a double-sided carbon tape or silver-doped paint. Then the top surface edges and sides of each specimen were painted with carbon-doped paint to electrically ground the specimen to prevent the build up of a high voltage static charge from the electron beam in the SEM.

3.5.4.5 Coating

The final step before the specimens were examined in SEM was to coat the specimens and the surrounding mounting medium with a thin conductive layer. The thickness of the coating was very important. If the coating was too thin the specimens gave poor signal and were charging. If the coating was too thick then microscopic details of the specimen were buried under the deposited coating film. There are a variety of metal coatings available for SE SEM applications, e.g. gold, platinum, nickel, chromium etc. but they all mask signal from calcium atoms in both SEM BSE and EDAX applications so carbon coating in the order of 10 nm thickness was used in this work due to its good electrical conductivity, mechanical stability and low background signal. The specimens were carbon coated using sputtering technique and the thickness of the coating was controlled using colour-metric guides based on the carbon coating deposition on a white metal stub.

After this final step the specimens were observed in a Philips XL-30 scanning electron microscope (SEM) equipped with EDAX attachment.

3.5.5 TEM specimen preparation

TEM investigations require specimens, which are mechanically stable and are electron transparent. Typical specimen thicknesses in the regions of interest are lying in the range of 5 – 150 nm.

A TEM specimen of high quality should fulfil specific conditions such as small thickness and undisturbed crystalline and organic structure. Several techniques are available in order to obtain such specimens (ultramicrotomy, mechanical grinding, chemical etching, electrolytical thinning, dual FIB/SEM, ion-beam thinning techniques etc.). The preparation of electron transparent dentine specimens and dentine-enamel interfaces is a challenge for the TEM specimen preparation. These are complex hierarchical organic – inorganic composite structures, non-conductive, with high internal anisotropy and sharp variation of mechanical properties at the characteristic scales of 10 nm (crystallinity), 1 μm (dentinal tubules, peritubular-intertubular dentine interfaces), 10 μm (dentine-mantle dentine-enamel interfaces and other dentinal interfaces). Thus such composites and interfaces need special preparation techniques and approaches.

3.5.5.1 Ultramicrotomy

It is important to stabilize the structure of dentine specimen and protect the specimen from internal and external forces occur during the preparation of the specimen for TEM work by chemically fixing the specimen. The main internal factor, which can alter the structure of the specimen is related to osmotic alterations caused by movement of soluble ions. External factors are mainly the collapse of the structure during dehydration and exposure to the electron beam.

A mixture of glutaraldehyde and paraformaldehyde (Figure 3.17) (modified Karnovsky's fixative) was used as a primary fixative in this work.

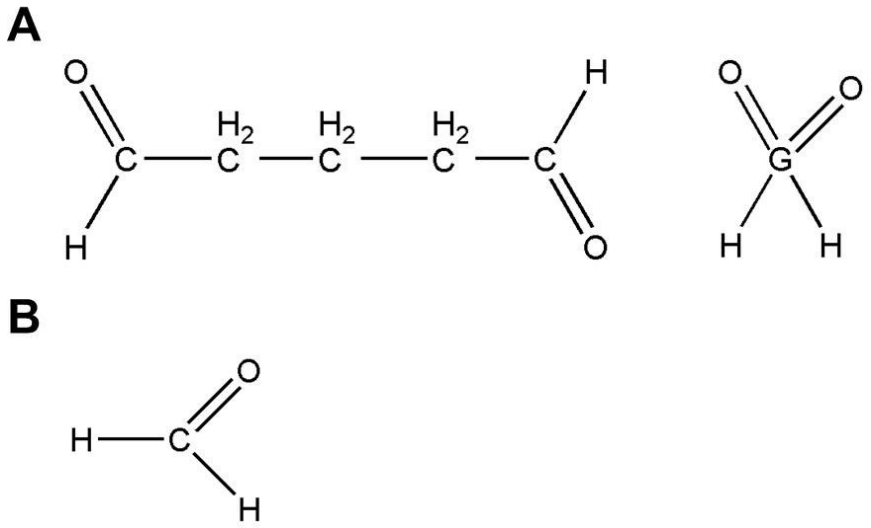

Figure 3.17 Chemical diagrams of Glutaraldehyde (A) and Paraformaldehyde (B).

The major function of glutaraldehyde is to crosslink proteins in the tissue and in the solution (Figure 3.18). These reactions are irreversible and the formed crosslinking gives the tissue structural strength and holds the components in place. Paraformaldehyde on the other hand is a much smaller molecule (Figure 3.17B) and lower molecule weight, which makes it one of the best penetrating agents of all the fixatives and therefore it is ideal for a use in fixation of resistant materials such as calcified structures. However, its reaction rate (crosslinking of proteins) is slower than glutaraldehyde and also reversible.

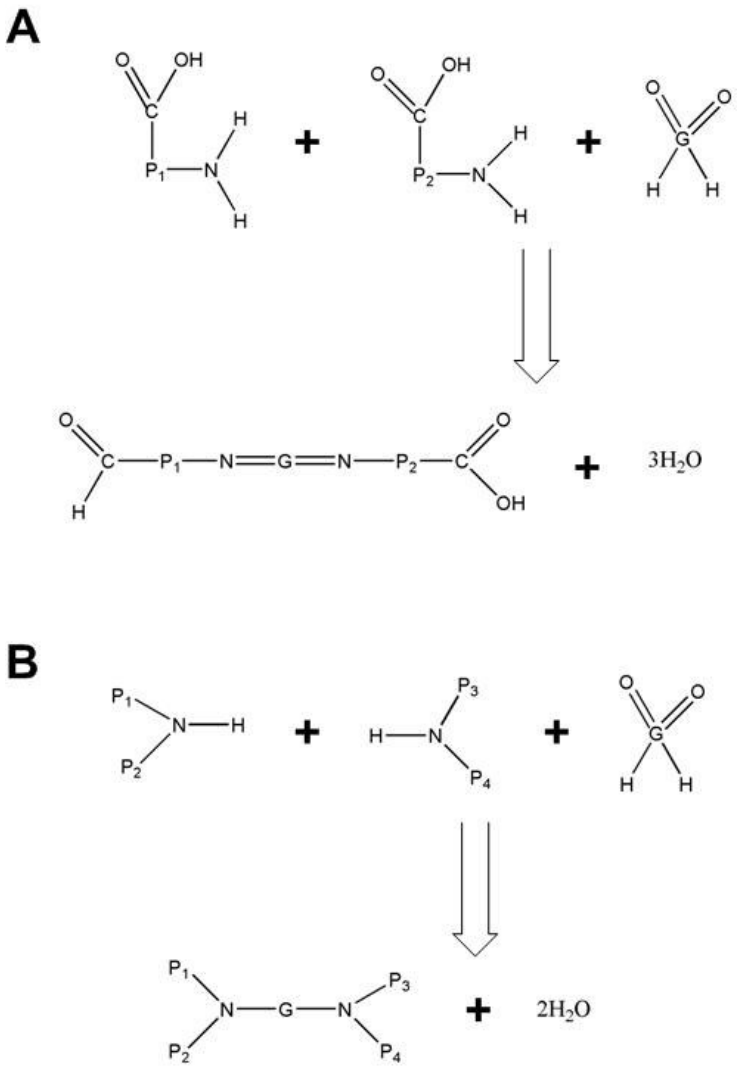

Figure 3.18 Crosslinking of proteins with glutaraldehyde. These reactions are not reversible. (A) Glutaraldehyde crosslinks proteins by their amino groups. (B) Two pair of proteins joined by peptide bonds, which crosslinks with glutaraldehyde to join all four proteins. (After [31])

Modified Karnovsky's fixative is formulated at half of the strength of the original Karnovsky's fixative recipe [32]. It reduces the tonicity of the solution and provides fixation that is better than that produced by the full strength mixture. Calcium chloride is withdrawn from the original recipe. Sorenson's sodium phosphate and cacodylate were used as buffers for this fixative in the presented work. Modified Karnovsky's recipe produces a fixative solution that contains 2% formaldehyde and 2.5% glutaraldehyde in phosphate (or cacodylate) buffer at pH 7.2 – 7.4:

1. Prepare 25 ml of 4% paraformaldehyde solution from paraformaldehyde powder:
    a. Dissolve 1.0 g of paraformaldehyde powder in 25 ml of distilled water heated to $60-70°C$
    b. Add 1 – 3 drops of 1N NaOH, stir until clear
    c. Cool to room temperature
    d. Filter the solution
2. Add 5 ml of 25% glutaraldehyde.
3. Add 0.2 M Sorenson's sodium phosphate (or cacodylate) buffer pH 7.2 – 7.4 to bring the final volume to 50 ml.

Modified Karnovsky's fixative was used on dentine specimens for 24 hours at $2°C$.

Sorenson's phosphate buffer and in some cases cacodylate buffer were used to maintain pH of 7.2 – 7.4 of the dentine specimens during fixation and post-fixation.

Osmium tetroxide was also often used in this work for post-fixation. Osmium is a strong oxidizer, which readily interacts with unsaturated bonds. There are a high number of unsaturated bonds in lipids and therefore osmium is widely used as a lipid fixative (Figure 3.19).

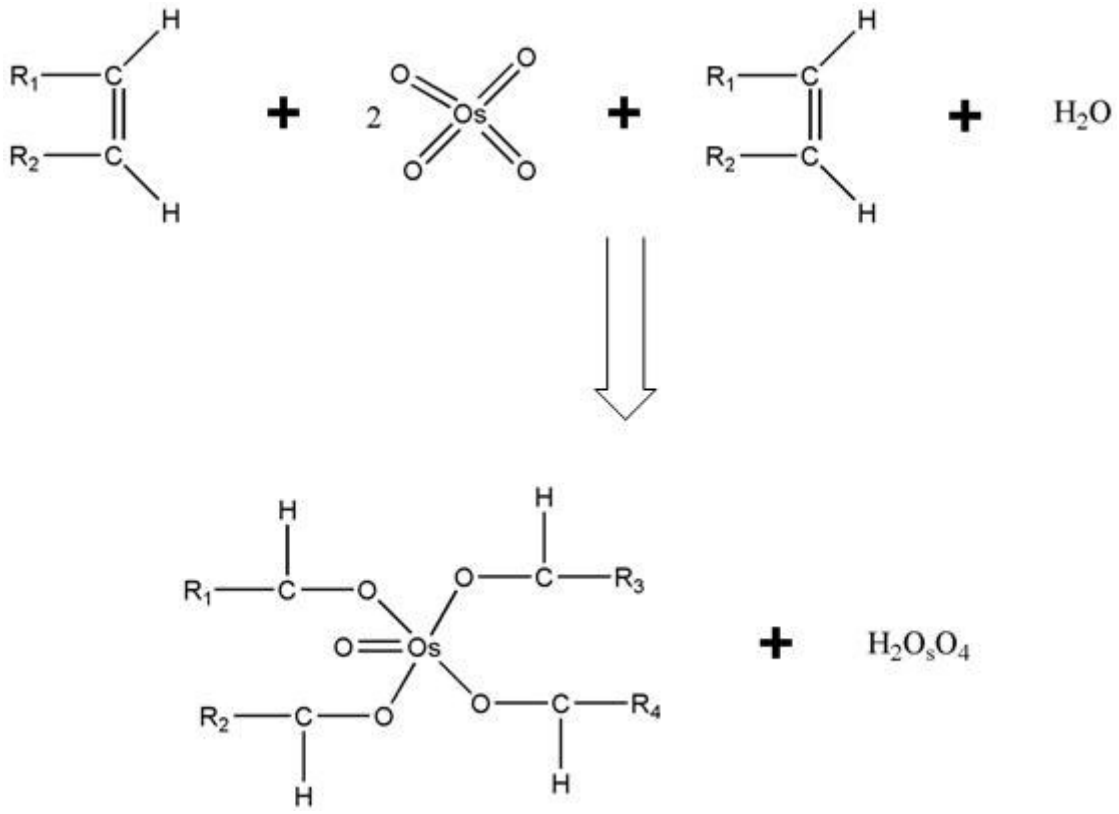

Figure 3.19 Crosslinking of unsaturated lipids by osmium tetroxide. The byproduct of the reaction is osmic acid, which may react with the tissue and further enhance contrast (After [31]).

When osmium oxidizes double bonds it is reduced to electron dense osmium blacks, which stop an electron beam at the site of the reduced osmium. Also osmium is soluble in non-polar media, e.g. saturated lipids, even though there will be no chemical reaction with the saturated lipids. Osmium dissolved in saturated lipids is reduced by ethanol during dehydration resulting in an osmium black at the site of the saturated lipids [33].

1% osmium tetroxide (mixture of 2 ml of 2% osmium stock with 2 ml of 0.2M Sorenson's sodium phosphate buffer in a pH 7.2 – 7.4 produces 1% osmium tetroxide in a pH 7.2 – 7.4, 0.1M sodium phosphate buffer) was used on dentine specimens for 2 hours at room temperature after primary fixation and rinsing in a phosphate buffer.

After a thorough rinse in a buffer the specimen must be completely dehydrated otherwise water remaining in the specimen will not allow embedding media to

infiltrate the specimen adequately. Specimens were dehydrated with graded ethanol (or acetone) in this work according to Table 3.4.

Table 3.4 Time-schedule for dehydration of dentine specimens in a graded dehydration agent.

Time, min	Ethanol or Acetone concentration, %
15	30
15	30
15	50
15	50
15	70
15	70
15	80
15	80
10	95
10	95
10	95
10	100
10	100
10	100

The infiltrating resin must be soluble and mix easily with a dehydrating agent, readily penetrate the tissue, remain uniform during the polymerization process. The polymerization process does not require very high temperature and does not cause shrinkage, similar density to the tissue embedded in it and is stable under the electron beam. Increasing concentration of Spurr's low-viscosity epoxy resin [34] was used to infiltrate dentine specimens in this work on rotators (Table 3.5).

Table 3.5 Resin infiltration schedule for dentine specimens.

Time, h	Volume parts of 100% resin / Volume parts of 100% dehydrating agent
24	1/2
24	1/1
24	2/1
24	3/1
24	1/0

Once the infiltration procedure is completed the specimen is then placed into a plastic mould, the mould filled with resin and polymerized for 24 hours at $60°C$. Then the plastic mould is cut off and the resin block is ready for trimming.

It is essential to trim the resin block before sectioning in ultra-microtome (Figure 3.20). The excess resin around the tissue at the tip of the block should be removed by trimming to the trapezoidal shape so that almost no part of the face would be without tissue. This reduces the variation of the density of the block face to minimum. The trapezoidal type of shape is supported much better during sectioning in the ultra-microtome – the longer bottom of the trapezoid pushes the shorter upper side away from the cutting edge and therefore the ribbon is formed more easily. The upper side of the face must be parallel to the lower side so that a block face comes in contact and leaves the cutting edge at the same time to obtain a straight unbroken ribbon (Figure 3.21). After a number of trials on dentine specimens it was established that the longest part of the trapezoid should not exceed 0.5 mm to obtain satisfactory sections on an ultra-microtome. The smaller the block face the less amount of compression produced thus the quality of the specimens was better.

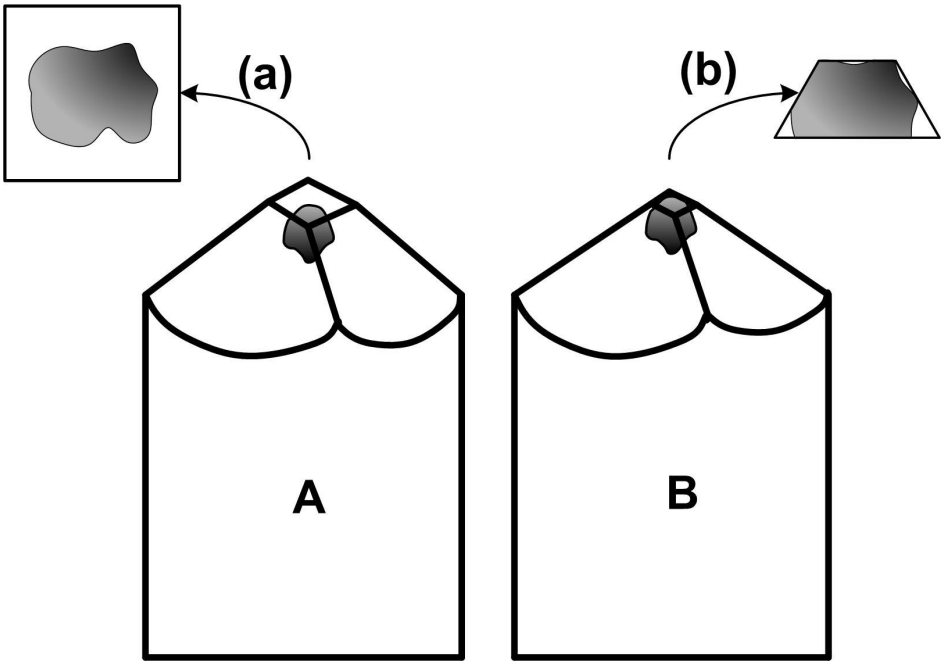

Figure 3.20 A. Untrimmed specimen resin block. The specimen is shown surrounded by resin just below the surface on the top of the block. Top view (a) demonstrates the square tip of the block and the specimen surrounded by resin. B. Trimmed specimen resin block. The specimen is shown on the top of the block. Top view (b) demonstrates trimmed tip of the resin block to a trapezoidal shape and the trimmed specimen.

Ultrathin sections (70 – 90 nm) were cut with Reichert-Leica Ultracut S ultra-microtome using glass knives and Diatome 45° diamond knives (Figure 3.21). Sections were collected onto copper 200 - 400 mesh grids with carbon coated (approximately 5 nm thickness) formwar film, dried for 24 hours at room temperature and observed in TEM without further staining.

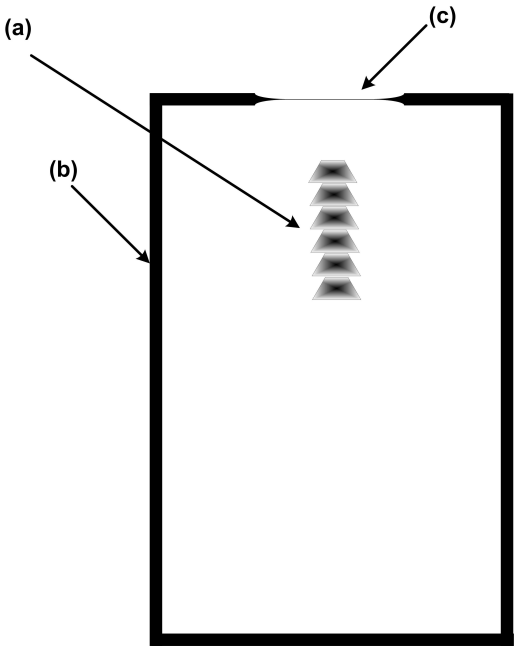

Figure 3.21 Specimens forming ribbon (a) are floating in the boat of the knife (b). Specimens were cut with a diamond blade (c).

3.5.5.2 Ion-beam thinning technique

Due to difficulties with cutting ultrathin sections from normal undecalcified dentine and enamel, ion-beam thinning technique was used to reduce the thickness to electron transparency in TEM. Pre-thinning was completed with tripod wedge polishing technique using diamond-impregnated plastic films grits of 30 μm, 9 μm, 6 μm, 3 μm and final polish was with 1 μm diamond film. Further thinning of the specimens was completed with ion-beam thinning using a cold stage (liquid N_2) to minimize damage to the specimens. During milling of the cross-sectional specimens (at DEJ) shields were used to protect the interface and to reduce the effect of different milling rates of enamel and dentine.

Inert gas (argon) is ionized and accelerated towards the specimen's surface [35]. Making use of momentum transfer the impinging ions sputter material from the specimen at a controlled rate (Figure 3.22).

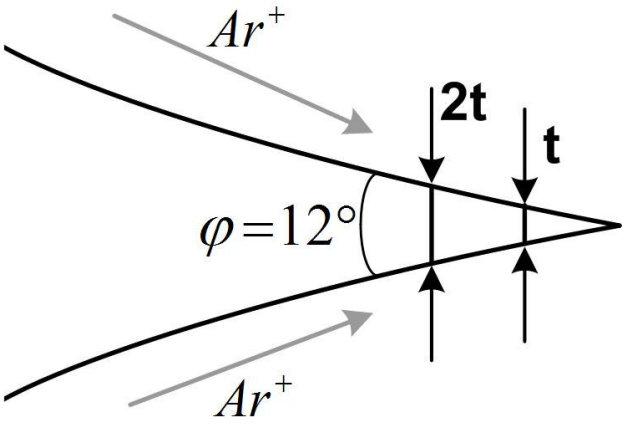

Figure 3.22 Single direction ion-beam thinning process. Fischione 3000 at $12°$, ion accelerating voltage 4 kV and ion source current 6 mA. The specimen is positioned on a cold stage at $-70°C$ to prevent heating and clamped with a molybdenum holder to prevent contamination. 360° rotation applied for homogenous thinning

The thicknesses of the areas adjacent to the specimen thinning edges were controlled in the reflection mode of an optical microscope by means of visible light interference pattern (Figure 3.23).

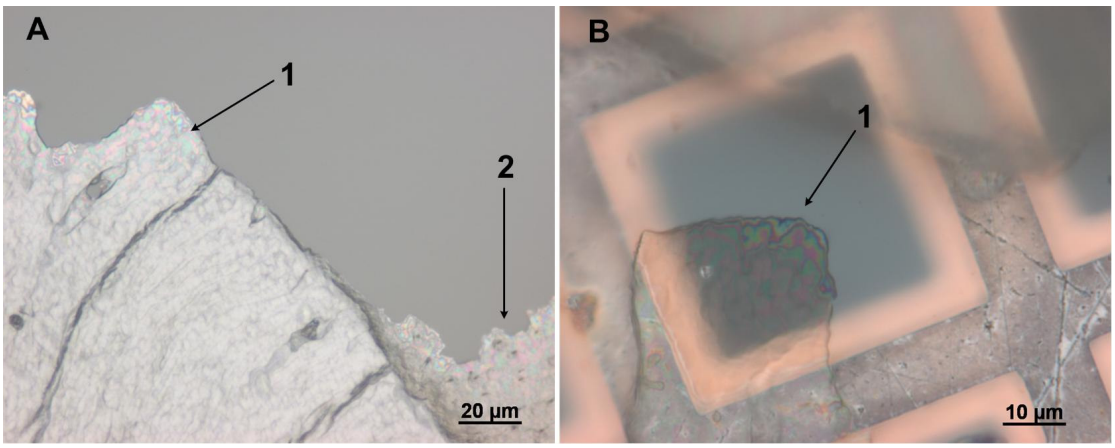

Figure 3.23 A. Ion-beam thinned areas of (1) enamel and (2) dentine at DEJ. Coloured fringes indicate that these areas are electron transparent for observations in TEM. B. Electron transparent thinned area of the enamel specimen (1) cut from the bulk specimen and placed on a copper mesh grid pre-coated with carbon-coated formwar support film for an observation under TEM.

Indeed, calculating optical path length difference (Figure 3.24) we obtain:

$$\delta = n(OA + AB) - OC \tag{3.24}$$

where n is the refractive index of the specimen (refractive index of air was taken as 1). Substitution of $OA=\frac{\cos\frac{\gamma}{2}}{\cos(\gamma-\beta)}t$, $AB=\frac{\cos\beta\cos\frac{\gamma}{2}}{\cos(2\gamma-\beta)\cos(\gamma-\beta)}t$ and $OC=2t\frac{\sin(\beta-\gamma)}{\cos(2\gamma-\beta)}\cos\frac{\gamma}{2}\sin\alpha=2tn\frac{\sin(\beta-\gamma)}{\cos(2\gamma-\beta)}\cos\frac{\gamma}{2}\sin\beta$ into Equation 3.24 yields:

$$\delta=nt\frac{\cos(2\gamma-\beta)+\cos\beta+\sin(2(\gamma-\beta))\sin\beta}{\cos(2\gamma-\beta)\cos(\gamma-\beta)}\cos\frac{\gamma}{2} \tag{3.25}$$

Then the condition for the constructive interference reads:

$$nt\frac{\cos(2\gamma-\beta)+\cos\beta+\sin(2(\gamma-\beta))\sin\beta}{\cos(2\gamma-\beta)\cos(\gamma-\beta)}\cos\frac{\gamma}{2}=\left(m+\frac{1}{2}\right)\lambda \tag{3.26}$$

where $m=0,1,2...$ is an integer and λ is the wavelength (phase of a light wave changes on π upon the reflection from the upper surface of the specimen because the refractive index of apatite is greater than the refractive index of air, no phase change occurs upon the reflection from the lower surface of the specimen).

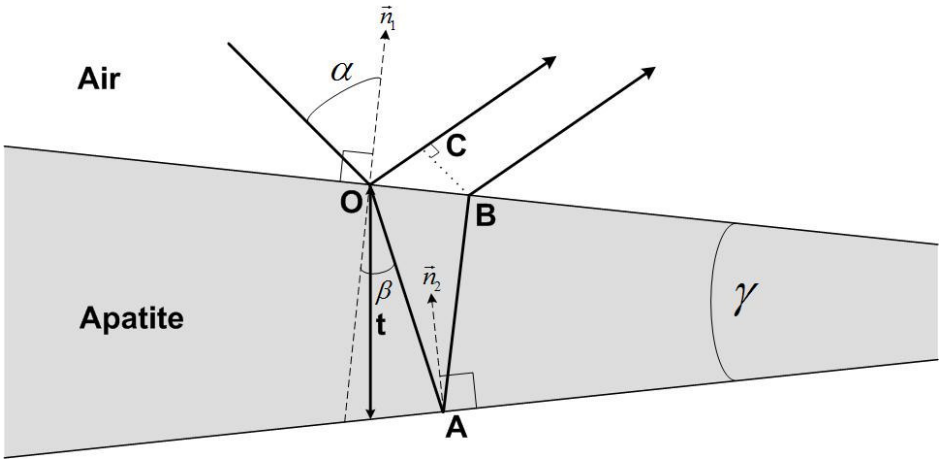

Figure 3.24 Visible light interference on a thin edge of the TEM specimen.

If the upper and lower surfaces of the specimen are parallel $(\gamma=0)$ Equation 3.26 is simplified:

$$2t\,n\cos\beta=\left(m+\frac{1}{2}\right)\lambda \tag{3.27}$$

Taking into account the refractive index of hydroxyapatite [36] $n=1.64$, spectrum of visible light, $m=0$ and that in the light microscope $\alpha=\frac{\gamma}{2}=6°$ (Figure 3.23A), using Equation 3.26 we can estimate the minimum thickness of the specimen (Table 3.6):

$$t=0.145\cdot\lambda \tag{3.28}$$

Table 3.6 Light optical microscope reference table of the minimum TEM specimen thickness (Figure 3.23).

Colour	Wavelength, nm	Specimen thickness, nm
Red	600 … 660	87.0 … 95.7
Yellow	560 … 580	81.2 … 84.1
Green	490 … 550	71.0 … 79.7
Blue	410 … 470	59.4 … 68.1

Due to charging of the TEM thinned edges of the specimens they were cut and placed on copper mesh grids with a carbon coated formwar support film (Figure 3.23B) and observed in TEM.

3.6 References

1. Ichimiya A., Cohen P.I. Reflection High Energy Electron Diffraction. 1st ed. Cambridge, U.K.: Cambridge University Press; 2004.
2. Humphris A.D.L., Miles M.J., Hobbs J.K. A mechanical microscope: High-speed atomic force microscopy. Applied Physics Letters 2005;86(034106):1-3.
3. Grant J.T., Briggs D. Surface Analysis by Auger and X-ray Photoelectron Spectroscopy. Chichester, U.K.: IM Publications; 2003.
4. Goldstein J., Newbury D.E., Joy D.C., Lyman C.E., Echlin P., Lifshin E., et al. Scanning Electron Microscopy and X-ray Microanalysis. 4th ed. New York: Springer; 2007.
5. Tersoff J., Hamann D.R. Theory of the scanning tunneling microscope. Physical Review B: Condensed Matter 1985;31(2):805-13.
6. Bonnell D.A. Scanning Probe Microscopy and Spectroscopy : Theory, Techniques, and Applications. 2nd ed. New York: Wiley-VCH Inc.; 2000.
7. Miller M.K. Atom Probe Tomography: Analysis at the Atomic Level. New York: Springer; 2000.
8. Klug H.P., Alexander L.E. X-ray Diffraction Procedures for Polycrystalline and Amorphous Materials. 2nd ed. New York: Wiley; 1974.
9. Williams D.B., Carter C.B. Transmission Electron Microscopy. New York: Plenum Press; 1996.
10. Lawes G. Scanning electron microscopy and X-ray microanalysis: Analytical chemistry by open learning: John Wiley & Sons; 1987.
11. Lyman C.E., Newbury D.E., Goldstein J.I., Williams D.B., Romig A.D. Jr., Armstrong J.T., et al. Scanning Electron Microscopy, X-Ray Microanalysis and Analytical Electron Microscopy: A Laboratory Workbook: Plenum Press; 1990.
12. Knoll M., Ruska E. Zeitschrift für Physics 1932;78:318-39.
13. Hirsch P., Howie A., Nichelson R. Electron Microscopy of Thin Crystal. Malabar, Florida: Kriger Publishing Co.; 1965.
14. Born M., Wolf E. Principles of optics. 7th ed: Cambridge University Press; 1999.
15. Smith D.J. The realization of atomic resolution with the electron microscope. Reports on Progress in Physics 1997;60(12):1513-80.
16. Buseck P.R., Cowley J.M., Eyring L. High-Resolution Transmission Electron Microscopy and Associated Techniques. New York: Oxford University Press; 1988.
17. Spence J.C.H. Experimental High-Resolution Electron Microscopy. Oxford: Clarendon Press; 2003.
18. The TEAM Project. http://ncem.lbl.gov/TEAM-project/.
19. Scherzer O. The Theoretical Resolution Limit of the Electron Microscope. Journal of Applied Physics 1949;20(1):20-29.
20. Pennycook S.J., Jesson D.E. High-resolution Z-contrast imaging of crystals. Ultramicroscopy 1991;37(1-4):14-38.

21. Browning N.D., Chrisholm M.F., Pennycook S.J. Atomic-resolution chemical analysis using a scanning transmission electron microscope. Nature 1993;366(6451):143-46.
22. Friedrich W., Knipping P., Laue M. Interferenzerscheinungen bei Röntgenstrahlen. Annalen der Physik 1913;41:971-88.
23. Zhang Z., Zhou F., Lavernia E.J. On the analysis of grain size in bulk nanocrystalline materials via X-ray diffraction. Metallurgical and Materials Transactions 2003;34A(6):1349-55.
24. Randle V., Engler O. Introduction to texture analysis: Macrotexture, Microtexture & Orientation Mapping. Amsterdam: Gordon and Breach Science Publishers; 2000.
25. Bunge H.J. Preferred Orientation Analysis in Textured Materials. In: Burrett C.S., Gilfrich J.V., Huang T.C., Jenkins R., McCarthy G.J., Predecki P.K., et al., editors. Advances in X-Ray Analysis. New York: Plenum Publishing Co.; 1992. p. 263-75.
26. Sjögren U., Figdor D., Spångberg L., Sundqvist G. The antimicrobial effect of calcium hydroxide as a short-term intracanal dressing. International Endodontic Journal 1991;24(3):119-25.
27. Zehnder M., Luder H.U., Schätzle M., Kerosuo E., Waltimo J. A comparative study on the disinfection potentials of bioactive glass S53P4 and calcium hydroxide in contra-lateral human premolars ex vivo. International Endodontic Journal 2006;39(12):952-58.
28. McGuckin R.S., Pashley D.H. The effect of disinfection/sterilization treatments on gluma-mediated dentin shear bond strengths. American Journal of Dentistry 1990;3:278-82.
29. Kumar M., Sequeira P.S., Peter S., Bhat G.K. Sterilisation of extracted human teeth for educational use. Indian Journal of Medical Microbiology 2005;23(4):256-58.
30. Habelitz S., Marshall G.W., Balooch M., Marshall S.J. Nanoindentation and storage of teeth. Journal of Biomechanics 2002;35(7):995-98.
31. Soon L., Simpson A. Biological Specimen Preparation: TEM & SEM (MCAN 5102B): The University of Sydney; 2004.
32. Karnovsky M.G. A formaldehyde-glutaraldehyde fixative of high osmolarity for use in electron microscopy. Journal of Cell Biology 1965;27(1):137A.
33. Dykstra M.J., Reuss L.E. Biological electron microscopy theory, techniques and troubleshooting. 2nd ed. New York ; London: Kluwer Academic/Plenum Publishers; 2003.
34. Spurr A.R. A low-viscosity epoxy resin embedding medium for electron microscopy. Journal of Ultrastructure Research 1969;26:31-43.
35. Strecker A., Salzberger U., Mayer J. Specimen preparation for transmission electron microscopy: reliable method for cross-sections and brittle materials. Praktische Metallographie 1993;30:482.
36. GIA Staff. Gem reference guide: Gemmological Institute of America; 1995.

Chapter IV. X-ray Microdiffraction and TEM Characterization of Human Dentine and Enamel

This chapter is based on the following submitted paper: Xue J., **Zavgorodniy A.V.**, Kennedy B.J., Wei L., Swain M.V. X-ray Microdiffraction and TEM Characterization of Human Dentine and Enamel. Biomaterials, In Review.

4.1 Abstract

Objective: The purpose of the present study was to investigate the crystal structure and texture of crown dentine and enamel through the thickness of healthy human molar teeth.

Methods: Transmission electron microscopy, electron diffraction and X-ray microdiffraction techniques were used to investigate the ultrastructure of the inorganic phase of healthy human teeth. The XRD data was analysed using the Le Bail profile fitting approach.

Results: The thickness of dentine crystallites was found to decrease towards the DEJ, while the thickness of the enamel crystallites increased from the DEJ towards the outer layers. It was demonstrated that enamel exhibited an increase of texture in 002 lattice planes from the DEJ towards the outer layers. In dentine the texture of 002 planes was also demonstrated. The values of the non-uniform microstrain in the dentine and enamel crystallites were low but a correlation between the width of the dentine and enamel crystals and microstrain was observed. The variation of lattice parameters as a function of the position within the thickness of dentine and enamel was also observed.

Conclusions: The increased preferred orientation and width of the enamel crystallites towards the outer surfaces of tooth suggested that such structure maybe evolutionary designed to resist wear, while the observed interprismatic cleavages may serve the purpose of resisting fracture. The variation of crystal sizes through the thickness of dentine towards the DEJ supports the concept that the outer 200 μm layer of dentine has a special role in damping stresses transferred from enamel. The correlation between the position within dentine and enamel layers and the variation of lattice parameters may be explained in termes of variation of chemical composition of the tooth mineral phase.

4.2 Introduction

Human teeth consist of two mineralised layers: highly mineralised enamel coat and the underlying softer dentine interior. Both of these layers protect the pulp. The principal mechanism of protection in teeth is by stress shielding, whereby the comparatively stiff enamel coat supports the bulk of occlusal loading in dental function. Dentine, by contrast, is tougher and resists the entry of cracks propagating through the enamel layer [1]. Considerable research has been carried out to model bi-layer systems that capture the essential macroscale characteristics of hard coating/soft substrate structures [2] as well as attempts to incorporate the role of specimen surface curvature (dome-shaped specimens) to take one step closer to real tooth geometry [3], which is of high interest for their relevance to dental crowns [4] and other biomechanical implant structures [5].

Enamel is a complex biomaterial, a composite of elongated mineral crystallites in the form of biological apatite (90%vol.) bonded by polymeric proteins and peptide chains (2%vol.) saturated with water (8%vol.) [6]. It has a hierarchical structure with

crystals of hexagonal cross section tightly packed into rods (prisms) (width ~ 5 μm) [7] and enclosed by polymeric sheaths (width 0.1 μm) [6]. The rods are highly aligned, approximately normal to the outer enamel surface but with some variation in emergent angle around the tooth surface [8]. Enamel is stiffer along the long axis of the rods and weaker between rods, where sliding and separation may occur. Also the decussation (crossing) of the rods is observed in human teeth in the region immediately adjacent to the dentine-enamel junction (DEJ), which is thought to confer toughness by inhibiting propagation of cracks [9].

Dentine is a mineralised connective tissue that constitutes the bulk of the tooth. It is intimately related to the dental pulp, with which it shares the same embryological origin from dental papilla [10]. Dentine forms the hard tissue portion of the dentine-pulp complex, whereas the dental pulp is the living, soft connective tissue that retains the vitality of dentine. Dentine is a hydrated structure, composed of a mineral phase in the form of needle- and plate-shaped biological calcium-deficient, carbon-rich apatite crystallites (48%vol.). The organic component is in the form of predominantly type I collagen and a minor presence of other proteins (29%vol.). Also dentine is hydrated with fluid to about 23% by volume, which is similar to plasma [11]. Dentine contains multiple closely packed dentinal tubules of up to 2 μm in diameter oriented radially between the pulp and dentine-enamel junction. Each tubule is surrounded by a cuff of highly mineralised peritubular dentine and intertubular dentine between them [12]. The main structural components of dentine are type I collagen fibrils impregnated and surrounded by mineral crystallites, which have c-axes aligned with the collagen fibril axis [13]. The interactions between collagen and nano-size mineral crystallites give rise to the stiffness of the dentine structure.

Both enamel and dentine demonstrate hierarchical structure at the nano- and microscales with organic and inorganic components organized in sub-structures optimized by evolution to withstand environmental stresses associated with their biological function [14]. Although dental restorative composite materials technology has succeeded in creating highly specialized, high performance materials, it is still far from being able to replicate the elegance of biological composites, such as enamel and dentine. Therefore dental restorative procedures are generally temporary with a lifespan of only few years before the restorative material or supporting tooth structure fails. From this perspective a new generation of synthetic restorative materials are needed better resembling the ultrastructure and mechanical properties of normal enamel and dentine. The prerequisite for producing such biomimetic materials with properties close to biological composites is to understand the influence of the geometry of the ultrastructural elements, such as size and preferred orientation (texture), of enamel and dentine nanocrystallites on the overall mechanical properties. Therefore a systematic investigation of tooth structures is needed to understand this correlation.

X-ray diffraction is one of the most powerful techniques to study the hierarchical structure of biological mineral composites such as teeth and bone. The traditional technique applied to study dental structures was powder XRD, which required a considerable amount of sample powder to generate diffraction patterns. This constraint makes the analysis of small specific areas of a specimen unachievable. Another important constraint, is that conventional powder X-ray diffraction is a destructive technique since the sample must be ground into a fine powder. This results in the loss of structural information such as heterogeneous distribution in composite, phases, stresses and texture [15]. Furthermore, powder XRD is insensitive to the

presence of amorphous materials and typically cannot be used to identify the presence of small quantities of secondary minerals (< 5%) [16]. Both enamel and dentine are heterogeneous structures and it has long been recognised that such structures should be investigated *in situ* by a high-resolution position-sensitive method in order to relate measurements to the exact position. With that goal in mind, micro beam diffraction techniques have been applied to study dental structures but the resolution of such instruments proved to be insufficient for reliable structural analysis, particularly when dealing with samples with relatively large grain sizes, inhomogeneous phase distribution and preferred orientation [17-20]. The development of μXRD instruments has overcome many of these constraints and it is now possible to apply this non-destructive technique to study selected areas of specimens down to 50 μm in diameter *in situ* [15, 17, 18].

The purpose of the present study was to investigate the crystal structure and texture of enamel and dentine through the thickness of the crown of human molar teeth with X-ray microdiffraction, TEM and electron diffraction techniques. Such ultrastructural characterisation may in turn provide insights into further improvements of dental restorative biomimetic materials.

4.3 Materials and Methods

Human molar non-carious teeth (4 specimens from 12 – 17 year old subjects) were extracted for orthodontic reasons and collected for this study according to the protocols approved by the Ethics Review Committee of Sydney South West Area Health Service, reference №X07-0217 & 07/RPAH/47 and by the Human Research Ethics Committee of the University of Sydney, reference №10541.

The specimens were fixed in Modified Karnovsky's fixative in 0.2 M Sorenson's buffer titrated to pH 7.2 for 24 hours at 2°C and then rinsed several times with 0.2 M Sorenson's buffer. The teeth were sectioned at the cementum-dentine junction to separate crowns and then 1 mm thick sectiones were prepared from the crowns along the mesio-distal axis using a low-speed diamond saw (Isomet, Buehler Ltd., Lake Bluff, USA) under constant water irrigation. A total of 6 points, forming a straight line, were selected for analysis: areas 1 – 3 were located within dentine (point 3 was at the dentine-enamel junction) and areas 4 – 6 were located within enamel (Figure 4.1).

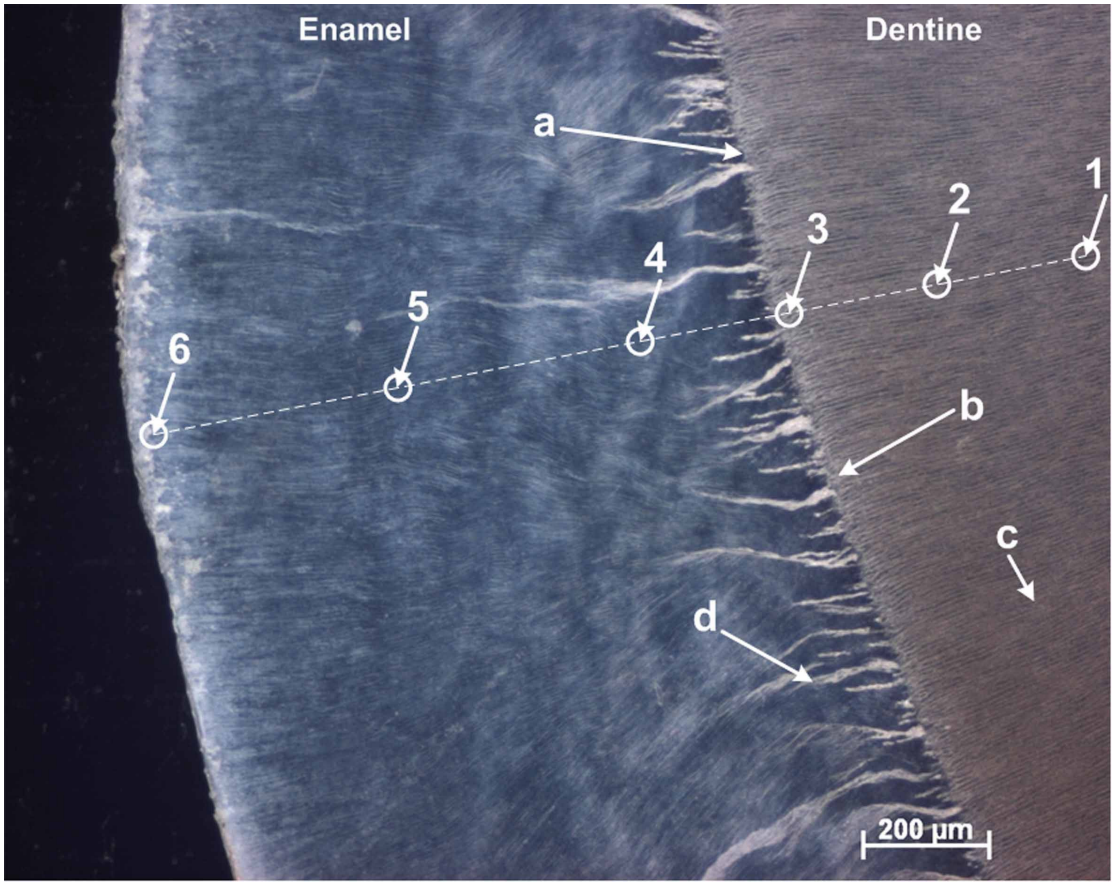

Figure 4.1 Dark field optical image of enamel, dentine-enamel junction (DEJ) (a), mantle (b) and circumpulpal dentine. The light contrast lines in dentine perpendicular DEJ are tubules (c). The light contrast thick lines protruding from DEJ into the thickness of enamel are tufts (d). The areas selected within dentine and enamel for µXRD and TEM experiments are schematically shown.

4.3.1 X-ray microdiffraction (μXRD)

The measurements were performed by real-time X-ray diffraction (Bruker AXS D8 Discover) equipped with the Eulerian 1/4 cradle HI-STAR (2D-Detector), fine collimator with 50 μm diameter exposed spot and GADDS (general area detector diffraction solution) software. The X-ray beam (CuKα line, λ=1.5418Å) was generated by 2.2 kW X-ray tube and Göbel mirror optics. The 2D position sensitive detector had 1024 × 1024 pixels with a 5 cm × 5 cm beryllium window. The tooth section was fixed to the sample holder. The sample to detector distance was 15.1 cm, 2Θ scanning angle range was from 8° to 102°, the step-size was 0.02° and the counting time was 1800 s. All measurements were performed at room temperature (290 ± 0.1 K). The analysis spots were determined using an optical microscope equipped with a laser marker. The instrumental peak broadening of the XRD instrument was determined by scanning a LaB_6 reference sample. Structural analysis of the X-ray diffraction patterns was undertaken using the Le Bail [19] method as implemented in the Rietica software package [20]. The XRD lines were identified by comparing the measured patterns to the JCPDS (Joint Committee on Powder Diffraction Standards) data cards [21].

The crystallite size was calculated from physical broadening of Bragg reflection peaks using Sherrer equation (peak shapes represented by a Gauss function) [22]:

$$t_{hkl} = K_G \frac{\lambda}{B_{hkl} \cos \Theta_{hkl}} \tag{4.1}$$

where t_{hkl} was the averaged crystalline dimension perpendicular to the reflecting planes, λ was the wave-length of the X-ray radiation, $K_G \approx 0.94$, broadening B_{hkl} was peak full-width at half-max (FWHM) and Θ_{hkl} was the centroid peak position. The

Scherrer-Wilson approximation was also employed to calculate grain size (represented by a Lorentzian function) and microstrain (Gaussian function) [23]:

$$\frac{\Theta_{hkl}^2}{\tan^2\Theta_{hkl}} = \frac{1}{t_{hkl}} \frac{K_L \lambda B_{hkl}}{\tan\Theta_{hkl} \sin\Theta_{hkl}} + 16\sqrt{\left\langle \varepsilon_{hkl}^2 \right\rangle} \tag{4.2}$$

where $\sqrt{\left\langle \varepsilon^2{}_{hkl} \right\rangle}$ was the root-mean-square of the lattice strain in the $\langle hkl \rangle$ direction and $B_{hkl} = \frac{1}{I_p}\int I(2\Theta)\, d\Theta$, where I_p was the peak intensity, $I(2\Theta)$ was the intensity at $2\Theta_{hkl}$ and $K_L \approx 0.9$. By plotting $\frac{K_L \lambda B_{hkl}}{\tan\Theta_{hkl} \sin\Theta_{hkl}}$ vs. $\frac{\Theta_{hkl}^2}{\tan^2\Theta_{hkl}}$, the root-mean-square of the lattice strain was extracted from the intercept with the ordinate and the crystallites size was determined from the slope.

It should be stressed that the sizes of the crystallites estimated from the analysis of the XRD profiles are the volume-averaged sizes of the crystalline domains and these need not be the same as the actual geometrical characteristics of the particles forming the mineral phases in dentine or enamel.

The crystallites preferred orientation (texture) indices (R_{hkl}) in dentine and enamel were calculated using the following intensity ratios:

$$R_{hkl} = k_{hkl} \frac{I_{211}}{I_{hkl}} \tag{4.3}$$

where the coefficient $k_{hkl} = \frac{I_{hkl}^{st}}{I_{211}^{st}}$ was calculated using intensities according to the JCPDS card 09-0432 [21] for a random hydroxyapatite powder mixture ($k_{002} = 0.42$ and $k_{300} = 0.55$), I_{211} intensity was corresponding to the observed 211 reflections and I_{hkl} were the intensities corresponding 002 and 300 reflections. For $R \approx 1$, the grains were considered randomly oriented. R values greater or lower than 1 indicated the

presence of preferred orientation of the crystallites in that crystallographic direction [24].

4.3.2 Transmission Electron Microscopy (TEM)

Using a low-speed diamond saw the dentine specimens were cut into smaller blocks of approximately 1×1×1 mm representing areas 1 and 2 (Figure 4.1) and then rinsed several times with 0.2 M Sorenson's buffer. The specimens were dehydrated in graded alcohols, infiltrated with the epoxy resin for 24 hours and then embedded into epoxy resin. Thin, 80-nm-thick, sections were cut with a diamond knife (Diatome, Bienne, Switzerland) and mounted onto 200 mesh copper grids.

To prepare ultrathin sections at the DEJ and from normal undecalcified enamel, ion-beam thinning technique was used to reduce the thickness to electron transparency in TEM (Figure 4.1, areas 3 – 6). Pre-thinning was completed with tripod wedge polishing technique using diamond-impregnated plastic film grits of 30 μm, 9 μm, 6 μm, 3 μm and final polish was with 1 μm diamond film. Further thinning of the specimens was completed with ion-beam thinning using a cold stage (liquid nitrogen) to minimize damage to the specimens. During milling of the cross-sectional specimens (Figure 4.1, area 3), shields were used to protect the interface and to reduce the effect of different milling rates of enamel and dentine.

The prepared specimens were then carbon coated and observed in a CM12 (Philips, Eindhoven, The Netherlands) TEM operated at 120 kV equipped with a nitrogen-cooled anti-contamination device.

The width of at least 40 crystallites was measured for each area from bright-field TEM images following the procedure described in [25]. The means and standard

deviations of these data were calculated. Statistical differences were examined using a two-tail unpaired t-test and the corresponding P values reported ($P < 0.05$ were considered statistically significant).

4.4 Results

Lattice parameters of the crystallites in dentine and enamel determined using a Le Bail analysis of the powder X-ray diffraction patterns [19] are presented in Table 4.1. It can be noticed from this table that the lattice parameters are sensitive to the position within the tooth structure.

Table 4.1 Refined structural parameters of dentine and enamel crystallites. Space group $P6_3/m$ (hexagonal), $\alpha = \beta = 90°$, $\gamma = 120°$. Cell parameters (a, c), cell volume (V), profile residues (Rp) and weighted profile residues (R_{wp}) are presented.

Test point №		a, Å	c, Å	V, Å^3	R_p, %	R_{wp}, %
Dentine	1	9.4377(9)	6.8830(8)	530.94(9)	5.63	7.34
	2	9.4139(14)	6.8593(10)	526.44(14)	5.23	6.78
	3	9.4269(14)	6.8642(11)	528.27(14)	7.52	10.02
Enamel	4	9.4313(5)	6.8671(4)	528.99(5)	6.00	8.46
	5	9.4285(4)	6.8697(3)	528.88(4)	5.45	7.54
	6	9.4359(5)	6.8699(5)	529.72(5)	5.41	7.12

The analysis of XRD profiles of dentine (Figure 4.2A) showed that the broadening of the 211 and 300 peaks decreased from the circumpulpal dentine towards the DEJ, which in turn suggested increased crystallinity of dentine towards DEJ. The relative intensity of the 002 reflections decreased towards the DEJ, while the intensity of the 211 peaks remained essentially constant. Depth profile 2-dimensional XRD GADDS frames of dentine (Figure 4.2, inset A1) showed Debye-Scherrer rings at lower 2Θ angles (8 - 42˚), which were continuous. In area 1 (Figure 4.1) the diffraction rings corresponding to 112, 211 and 300 planes were fused together and formed a broad intense ring, while in areas 2 and 3 (Figure 4.1) the

resolved rings from the 112, 211 and 300 planes were evident. The 210 rings became more intense towards the DEJ. At higher 2Θ angles (42 - 102˚) the contrast of the Debye-Scherrer rings was, as expected, weak.

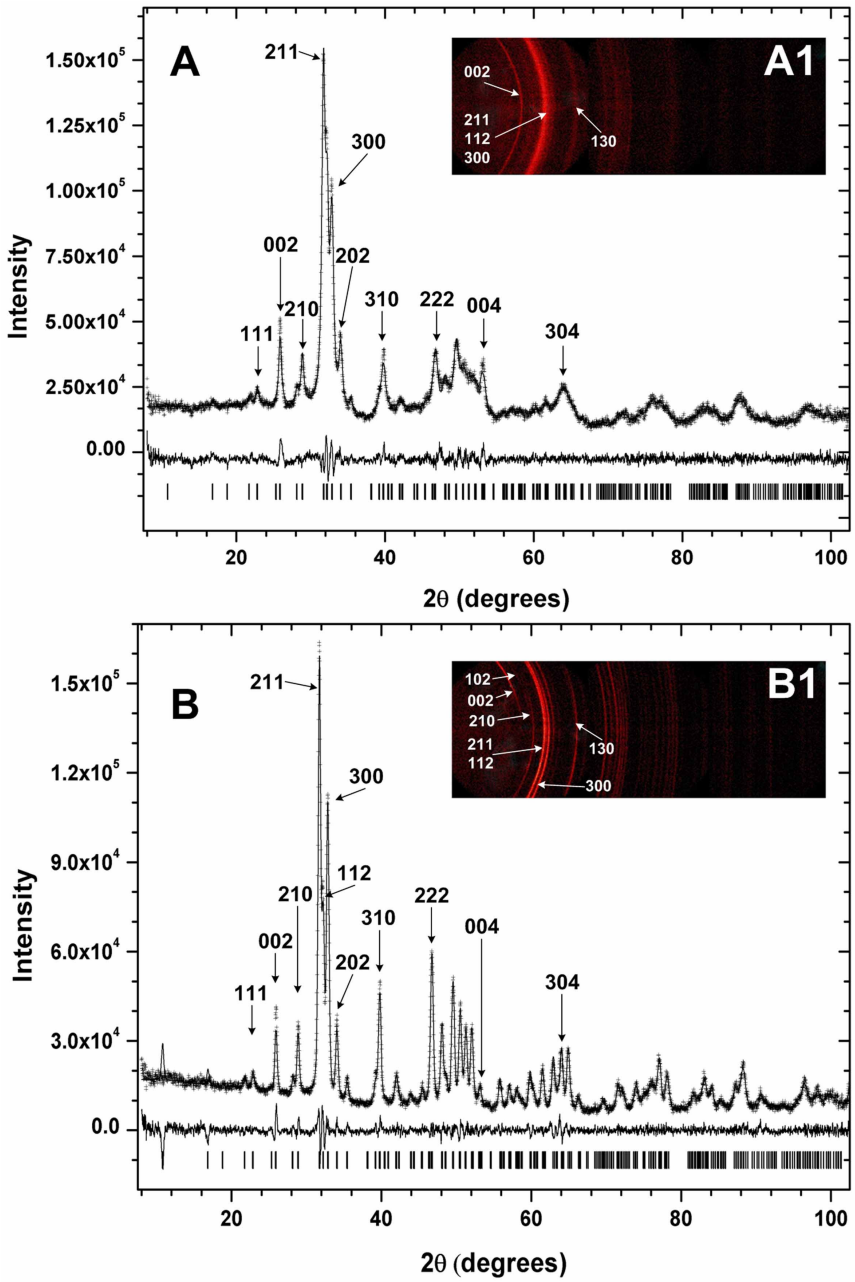

Figure 4.2 XRD profiles of dentine (A) and enamel (B). The observed data points are represented by the crosses and the calculated profile by the solid line. Below the profile is the difference plot and the vertical lines represent the peak position markers for hydroxyapatite phase. A. XRD profile of circumpulpal dentine (area 2, Figure 4.1). The corresponding Debye-Scherrer rings were shown in inset A1. B. XRD profile of enamel (area 4, Figure 4.1). The corresponding Debye-Scherrer rings were shown in inset B1.

The XRD peaks observed in the enamel (Figure 4.2B) were sharper than the corresponding peaks in dentine (Figure 4.2A). The line broadening of the 112, 211 and 300 peaks remained the same across the enamel, while the intensity of 112, 211 and 300 peaks was seen to decrease from inner enamel towards outer enamel. In enamel almost all of the Debye-Scherrer rings (Figure 4.2B, inset 2B) had better contrast than the corresponding rings observed in dentine. The intensity in the Debye-Scherrer rings from the 002 and 102 reflections was clearly inhomogenously distributed indicating the existence of preferred orientation. The most intense discontinuous rings were 002, while 102 rings appeared weak in areas 4 and 5 (Figure 4.1) and was not detected in the outer layer of enamel (area 6, Figure 4.1).

The mean sizes of the crystallites were calculated according to Eqs. 4.1 and 4.2 and measured through the direct observations in TEM following the procedure outlined in [25] (Table 4.2, Figure 4.3 and Table 4.3, Figure 4.4). Statistical difference of the width of the dentine and enamel crystallites is presented in Table 4.4.

Table 4.2 Mineral crystallite widths in dentine and enamel calculated from XRD data (200 reflections) and TEM.

Test point №		Sherrer equation, nm	Sherrer-Wilson equation, nm	TEM, nm	
				Mean	SD
Dentine	1	11.60	10.80	7.00	1.28
	2	19.05	16.20	6.52	1.34
	3	16.74	13.70	6.00	1.32
Enamel	4	21.51	18.20	27.01	5.86
	5	24.41	20.90	37.84	12.77
	6	22.83	20.90	41.42	9.20

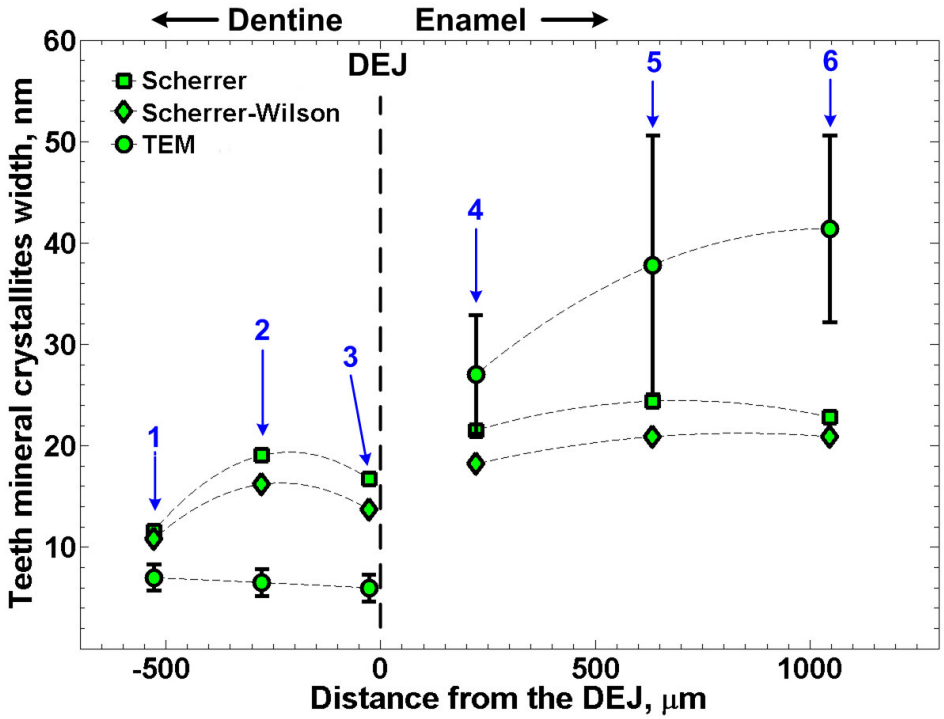

Figure 4.3 Mineral crystallite widths in dentine and enamel calculated from XRD data (200 reflections) and TEM. The connecting lines are the spline of the experimental data.

Tables 4.2 and 4.3 demonstrate the variability of the crystallites sizes through the thickness of dentine and enamel. In general the crystallites became thinner and longer from the middle circumpulpal dentine (areas 1 and 2, Figure 4.1) to the outer layer of circumpulpal dentine and further towards the DEJ (area 3, Figure 4.1). The lengths of the dentine crystallites near the DEJ calculated with Scherrer method (Eq. 4.1) appeared similar to the size of the crystals forming the outer layer of the circumpulpul dentine, while calculations based on Scherrer-Wilson equation (Eq. 4.2) showed a substantial increase in the length of grain particles embedded in the dentine crystallites at the DEJ, in comparison to the crystallites in the middle circumpulpal dentine.

Table 4.3 Grain size of mineral crystallite along the c-axis of crystallites in dentine and enamel calculated from XRD data (002 reflections).

Test point №		Sherrer equation, nm	Sherrer-Wilson equation, nm
Dentine	1	12.04	17.40
	2	19.03	50.20
	3	21.23	50.40
Enamel	4	21.86	22.20
	5	24.97	24.90
	6	23.11	21.30

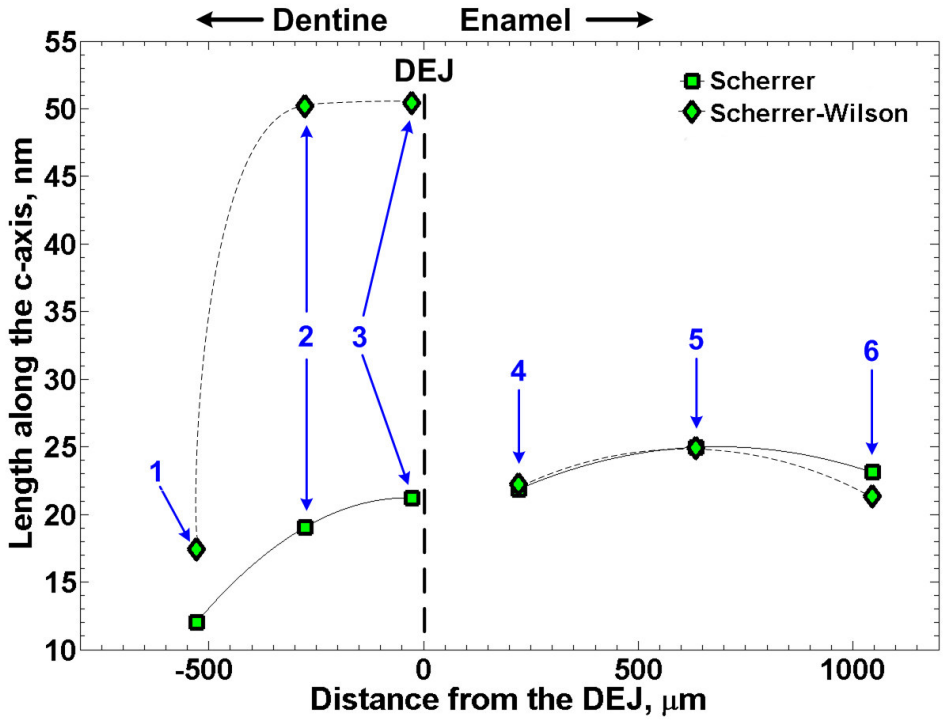

Figure 4.4 Grain size of mineral crystallite along the c-axis of crystallites in dentine and enamel calculated from XRD data (002 reflections). The connecting lines are the spline of the experimental data.

The average width of the enamel crystals substantially increased through the thickness of enamel towards the superficial layer (Table 4.2, Figure 4.3), while their length was increasing towards the outer layer of enamel (Table 4.3, Figure 4.4).

Table 4.4 Statistical comparison of the crystallites width in different areas of dentine and enamel.

		P-value
Dentine	Point 1 vs 2	0.071
	Point 1 vs 3	< 0.0001
	Point 2 vs 3	0.036
Enamel	Point 4 vs 5	0.007
	Point 4 vs 6	0.0001
	Point 5 vs 6	0.48

TEM was also employed to determine the width of dentine and enamel crystallites. The width of the crystallites forming the inorganic phase of dentine (Figure 4.1) was decreasing towards DEJ (Table 4.2, Figure 4.3). It could also be noticed that the crystallites in circumpulpul dentine (Figure 4.5A) demonstrated a decrease in length towards DEJ (Table 4.3, Figure 4.4), while mantle dentine (Figure 4.5B) showed a significant increase in the crystallites length in comparison with the circumpulpul dentine crystallites (Figure 4.5A).

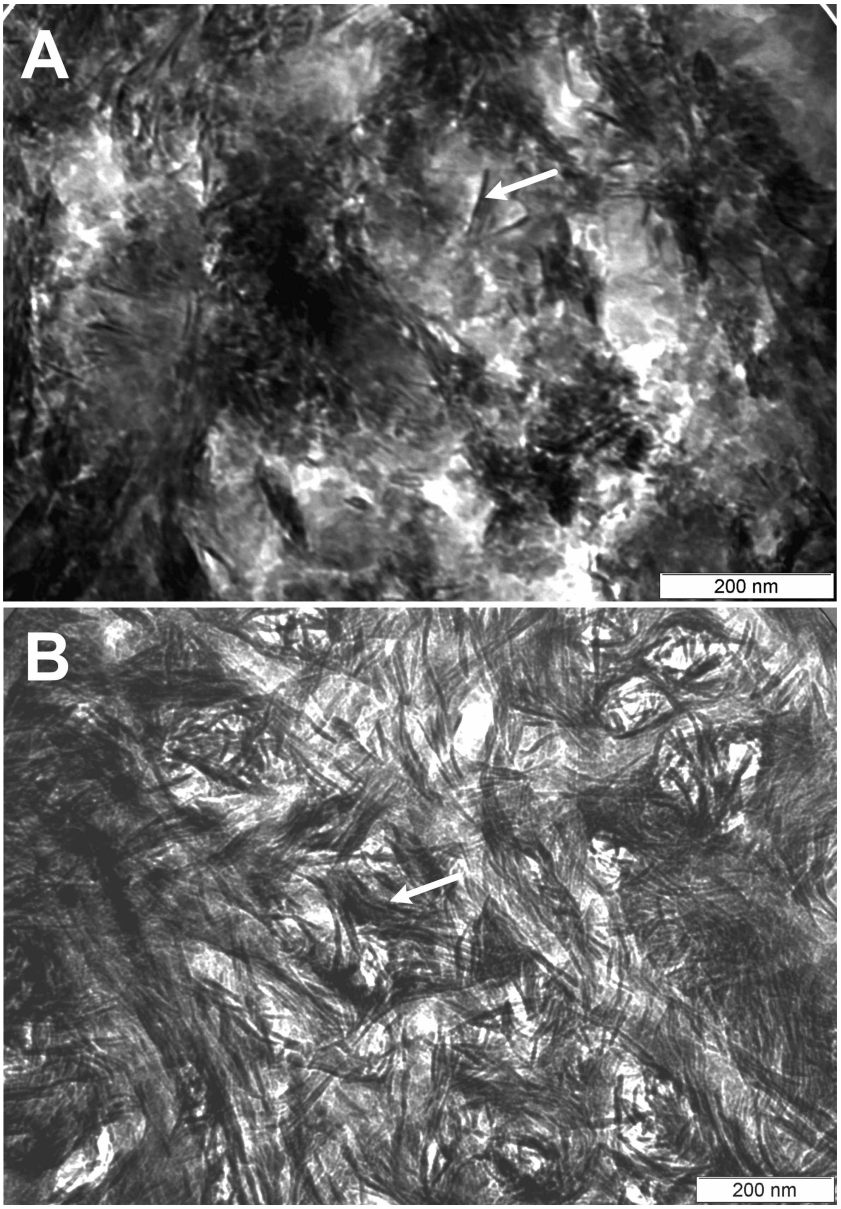

Figure 4.5 TEM images of circumpulpal (A) and mantle (B) dentine. Mineral crystallites were shown with arrows.

The mineral phase of mantle dentine located 4 μm underneath the DEJ observed in TEM appeared in the form of a porous reticulate texture (Figure 4.6) with numerous needle-like crystallites (Figure 4.5B), which were significantly longer than those observed in circumpulpal dentine. Indexing of the corresponding SAED pattern confirmed that the crystallites were apatite phase (Figure 4.6, inset A). The ring pattern of the SAED confirmed that dentine near DEJ was a polycrystalline material. The preferred orientation of the crystallites in the 002 planes was observed at the

characteristic scale of 1 μm. The preferred orientation at the scales greater than 1 μm appeared to be lost and the crystallites were oriented randomly in all directions. This texture was in contrast to the circumpulpal intertubular dentine found deeper in the crown (areas 1 and 2, Figure 4.1) where the preferred orientation of the crystallites was also random at the scales greater than 1 μm but not in all directions and only in the incremental growth planes orthogonal to the tubules. No peritubular dentine was observed in mantle dentine. Needle-like crystallites were tightly packed together forming dark contrast structures with lighter contrast material between them. Although the observed crystallites were predominantly straight, bending of the crystallites around the circumference of the voids was observed (Figures 4.5B and 4.6, arrows). Arrows indicated bending of crystallites around the voids. Indexing of the corresponding SAED pattern (Figure 4.6, inset A) confirmed the presence of hexagonal apatite and a highly polycrystalline structure.

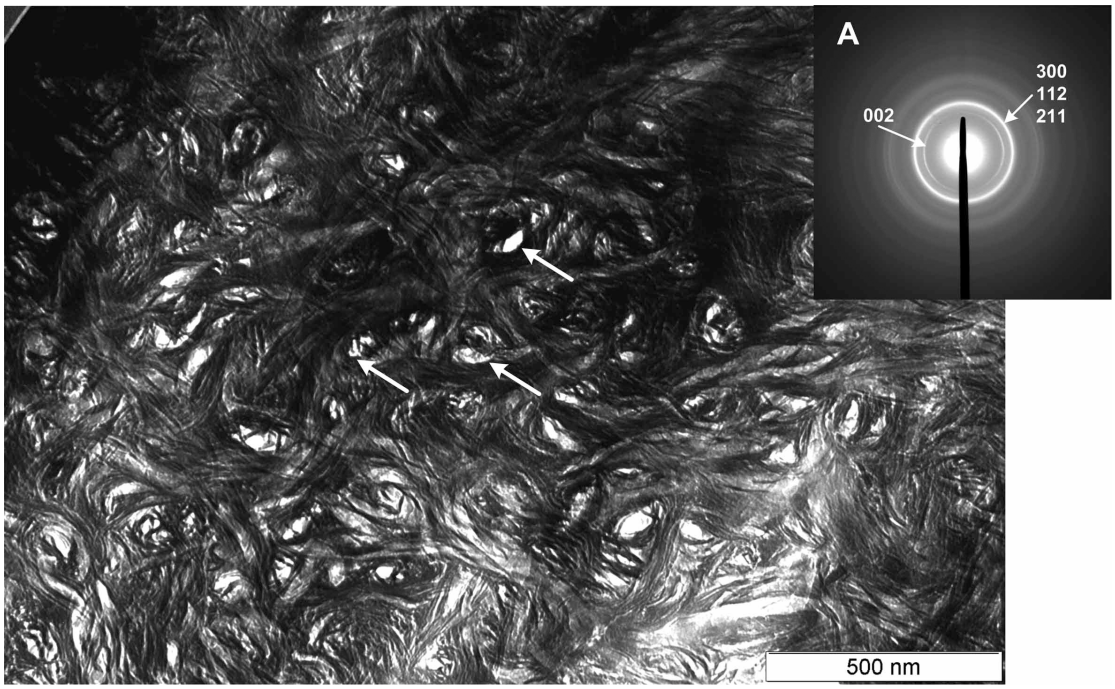

Figure 4.6 Transitional dentine at 4μm below DEJ. Arrows indicate bending of crystallites around the voids. Indexing of the corresponding SAED pattern (inset A) confirms the presence of apatite and a highly polycrystalline structure at the characteristic scale of 1 μm.

The underlying ultrastructure of enamel was revealed in the TEM observations (Figure 4.7). The enamel mineral phase consisted of needle-like crystals, which were tightly packed with gaps between them of less than 5 nm. Rings formed the selected area electron diffraction (SAED) pattern of enamel (Figure 4.7, inset A), which was consistent with its polycrystallinity. Indexing confirmed the apatetic nature of the observed crystallites. The enamel crystals preferred orientation was along the c-direction, the long axis of a needle-like apatite crystals (Figure 4.7), which was confirmed by the slightly spread spot structure of the enamel SAED pattern formed by 002 reflections (Figure 4.7, inset A).

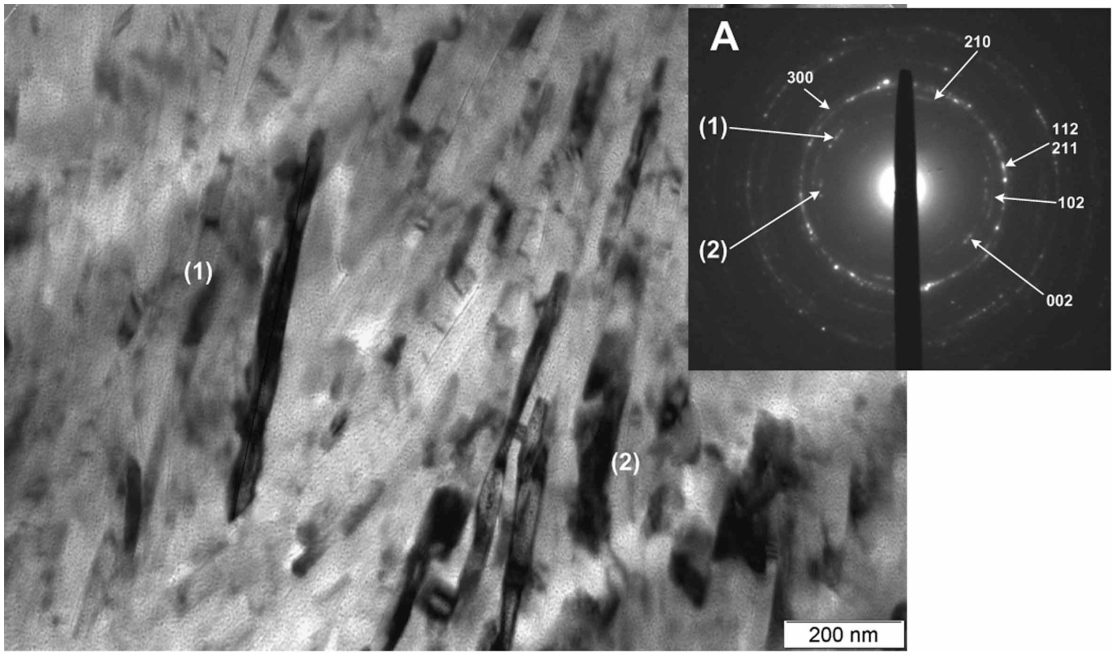

Figure 4.7 Enamel crystallites forming prisms (1) and (2) at the interprismatic junction and the corresponding SAED pattern (inset A) with indexing confirming the presence of apatite phase with preferred orientation in c-direction of the crystallites. The arrows point to the (002) reflections of the prisms (1) and (2).

The enamel crystals were oriented in nearly the same direction within the prism but demonstrated variation in the directions, when compared between the prisms. Figure 4.7 showed two enamel prisms and the interprismatic junction. The crystals in the enamel prism (1) were oriented at approximately 37° to the prism (2) (Figure 4.7).

The minor variation of the crystallites orientation within an enamel prism of less than 1.5° was due to a slight orientation mismatch of the crystallites near the boundaries of the enamel prisms. This orientation variation was clearly observed at the enamel SAED patterns, e.g. the slight spread of 002 reflections at (1) and (2) (Figure 4.7, inset A). The preferred orientation in 102 planes was also visible (Figure 4.7, inset A). The width of the enamel crystallites was increasing towards the superficial layer (Table 4.2).

Microstrain calculated from 002 and 200 reflexes of X-ray profiles (Eq. 4.2) was tensile for all crystallites in dentine and enamel. The strain within the cross section of the crystallites was significantly increasing from the middle circumpulpal dentine towards the DEJ (Table 4.5, Figure 4.8). The strain within the long axes of the crystallites changed relatively insignificantly from the middle curcumpulpal dentine (Table 4.5, Figure 4.8) towards the outer layer of curcumpulpal dentine but notably decreased in the mantle area of dentine at the DEJ (Table 4.5, Figure 4.8).

Table 4.5 Microstrain values in dentine and enamel mineral crystallites calculated from refined XRD profiles.

Test point №		Microstrain, %	
		Cross section	Long dimension
Dentine	1	9.12×10^{-6}	5.40×10^{-6}
	2	4.44×10^{-5}	7.76×10^{-6}
	3	3.92×10^{-5}	1.95×10^{-6}
Enamel	4	5.60×10^{-6}	1.40×10^{-6}
	5	7.83×10^{-6}	2.95×10^{-6}
	6	3.55×10^{-6}	1.69×10^{-6}

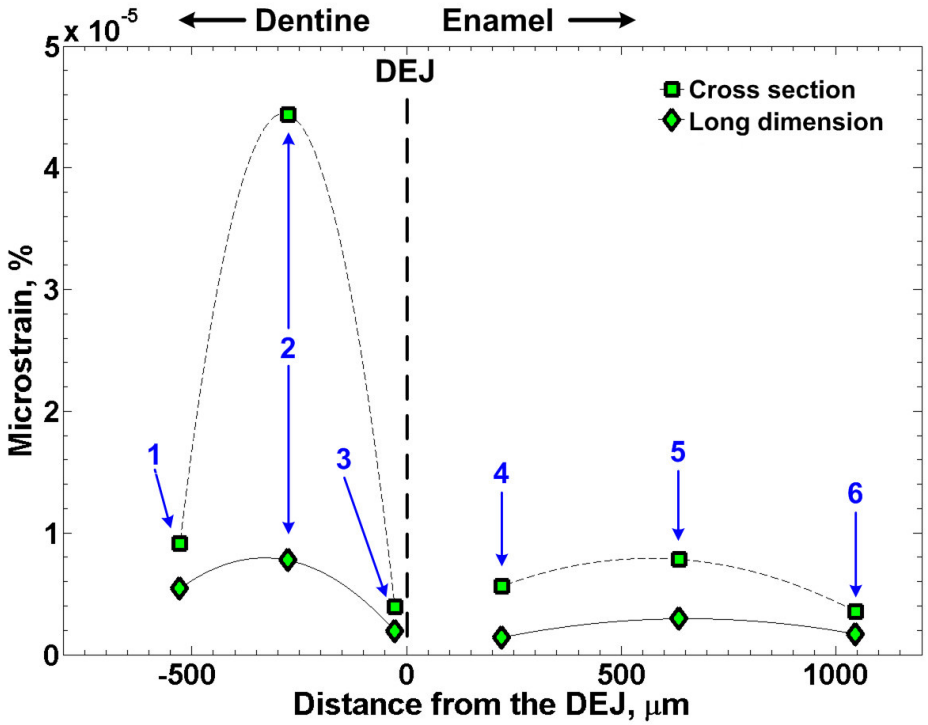

Figure 4.8 Microstrain values in dentine and enamel mineral crystallites calculated from refined XRD profiles. The connecting lines are the spline of the experimental data.

Microstrain within the cross-section of the enamel crystals remained similar through the thickness of the enamel layer (Table 4.5, Figure 4.8). The microstrain within the long axes of the enamel crystals (Table 4.5, Figure 4.8) also remained unchanged through the thickness of the enamel layer and were comparable to the values of dentine crystallites in the mantle layer of dentine (area 3, Figure 4.1).

Texture indices of dentine and enamel polycrystalline structures were calculated according to the Eq. 4.3 (Figure 4.9). Texture indices in enamel corresponding to the reflections 002 were significantly greater than 1, which indicated the preferred orientation of crystallites in these planes. Texture indices corresponding to the reflections 300 calculated for both dentine and enamel were close to 1, which indicated random orientation of crystallites in these planes.

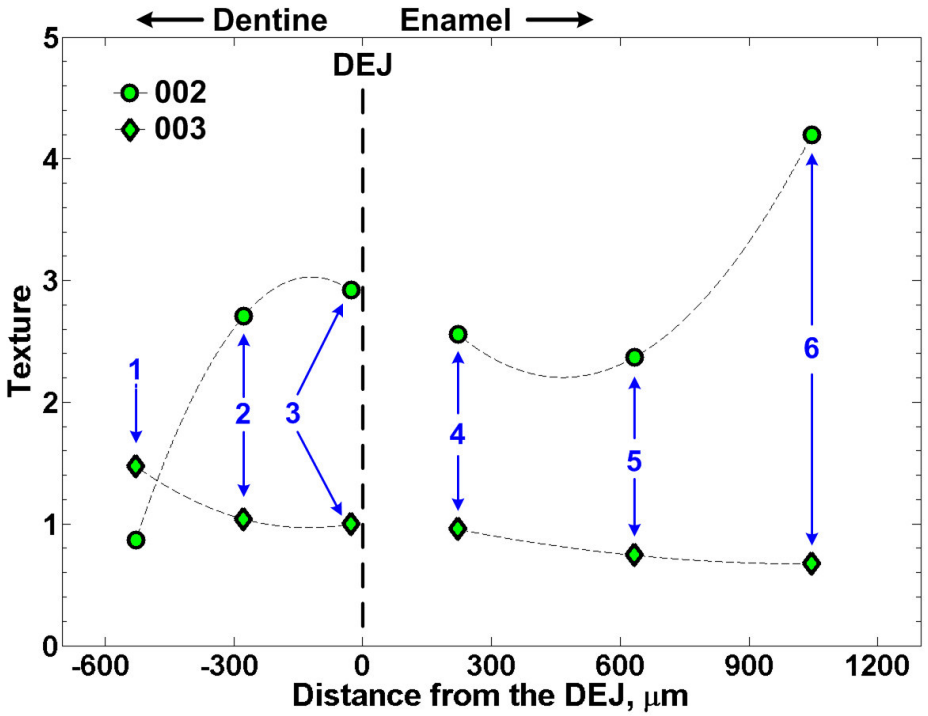

Figure 4.9 Texture index variation in dentine and enamel. Texture indices were calculated using 002 reflections, which correspond to the crystallites orientation along their long axis. Texture indices calculated using 003 reflections correspond to the crystallites orientation along their short axis. The connecting lines are the spline of the experimental data.

4.5 Discussion

The structure of enamel is designed to masticate nutrients placed in the oral cavity. To fulfil this function it must exhibit wear and fracture resistance [14]. It is reasonable from this perspective to argue that the observed increase in the preferred orientation and thickness of the crystal grains towards the outer surface of enamel (Figure 4.9), which are approximately perpendicular to the enamel surface [26], may be an evolutionary adaptation to reduce wear. Also the observed increasing degree of the thickness of the enamel crystallites agrees with previous observations of the increased mineralisation of enamel towards its superficial layer [27]. On the other hand, interprismatic cleavages (Figure 4.7) may not only limit crack propagation [28] but may also allow limited deformation [29]. The varying degrees of enamel anisotropy (Figure 4.9) may help to

direct stresses from the geometrically complex enamel occlusal surfaces to the resilient underlying dentine.

Using the integral line-breadth method [23], the coherently diffracting domain size averaged in the direction of the diffraction vector was determined for dentine and enamel crystallites (Table 4.2, Figure 4.3 and Table 4.3, Figure 4.4) as well as microstrain (Table 4.5, Figure 4.8). It has been discussed previously that in the bone-like samples not only the coherence size of the crystallites and microstrain influence the broadening of the X-ray diffraction lines, but also other parameters, which characterise biological crystallites, such as age, crystal disorders etc. [30]. Therefore caution should be applied when such calculated data is interpreted and these results should be treated as qualitative and identifying trends. With that in mind, it is apparent that while the volume averaged size of enamel crystallite grains remained unchanged through the thickness of the enamel layer, the geometrical width of enamel crystallites observed in TEM increased (almost doubled) towards the enamel occlusal surface (Table 4.2, Figure 4.3). It has been demonstrated that enamel apatite crystals are at least 100 μm long, which is inline with the suggestion that the crystallites are continuous from DEJ to the outer surface of the tooth [31]. Therefore the increased degree of the enamel hardness [32] towards the enamel occlusal surface is unlikely to be attributed to an increase in the number density of crystallites but to the observed increase in the width and volume fraction of the crystallites. Such increase in the enamel crystallites thickness can be attributed to the fusion of crystallites in the course of maturation process [31]. Another possibility arises from purely geometrical considerations taking into the account that the occlusal surface area of the enamel is larger than the DEJ surface, which implies that, particularly in the cusp areas of enamel, the gaps between the formed enamel crystallites are bigger than in the inner

portions of enamel and so at the end of the maturation process crystals are expected to be thicker at the surface area.

Due to the large surface-to-volume ratio in nano-size crystallites the influence of the surface energy on the bulk strain distribution fields increases with the reduction of the size of the crystallites [33] and therefore results in the presence of uniform [34] and non-uniform microstrains [35] in the nano-particles. Uniform microstrain is characterised by shifts in the crystal interplanar lattice spacings to the lower or higher side, which depends upon whether the strain is compressive or tensile. When the strain changes from one part of the grain to another as for instance with the bent crystallites (Figure 4.6), it is called non-uniform strain. This variation of the microstrain within one crystallite leads to the further increase in the broadening of the X-ray lines [23]. The microstrain of nano-size crystal grains depends on the surface-to-volume ratio of the crystallites, i.e. with the increase of the ratio the microstrain increases [34, 36]. The variation of microstrain was particularly significant in the dentine crystallites (Table 4.5, Figure 4.8) due to the substantial change of this ratio through the thickness of dentine towards the DEJ (Table 4.2, Figure 4.3). The substantial difference between the coherence size of the crystal domains in the areas 2 and 3 of dentine (Table 4.3, Figure 4.4) therefore maybe qualitatively explained by the substantial rise of microstrain (~ 5 times) in these areas (Table 4.5, Figure 4.8). Enamel crystals, on the other hand, indicated only an increasing trend of microstrain with the increase of the ratio probably due to the fact that the ratio change was significantly smaller than that observed in dentine. The values of the microstrain in all instances were relatively low corresponding to stresses of less than a few MPa.

The ultrastructural observations that dentine crystals became smaller towards the outer layers of circumpulpal dentine (Table 4.2, Figure 4.3) and then further

appeared thinner but longer in mantle dentine (Figure 4.5B) may possibly be attributed to the special role of the DEJ and outer layers of dentine in transferring mastication and other types of stresses from enamel into crown dentine below the sub-DEJ zone [37, 38]. Mechanical deformation and the in-plain strain distribution mapping of tooth slices by the Moiré fringe interferometry technique demonstrated that most strain was concentrated in this softer 200 μm dentine layer adjacent to the DEJ and it was suggested that this zone functions as a cushion, which allows enamel and dentine to work together [39]. This zone in coronal outer layer of dentine was described as a broad transition zone, or 'interphase', which also contributes to the bonding between enamel and dentine [38].

It was interesting to notice the dependence of a- and c-lattice parameters of the position of measurement through the thickness of dentine and enamel (Table 4.1). Such variation has been observed in dentine [18] and enamel [26]. These observations maybe interpreted in terms of the variation of the chemical composition of crystals through the thickness of dentine and enamel. It has been reported that biological apatite crystals in dental structures are calcium-deficient and carbon-rich hydroxyapatite [40] with substitution of $(CO_3)^{2-}$ for $(PO_4)^{3-}$ groups leading to a lower Ca/P ratio than that of stoichiometric hydroxyapatite [41]. This kind of substitution (B-substitution) leads to the change of both a- and c-lattice parameters. However, other compositional changes, including the ionic substitutions to maintain the charge balance for the carbonate-phosphate exchange [18, 41], may affect a- and c-lattice parameters.

4.6 Conclusions

TEM and X-ray microdiffraction (50 μm spot-size) are useful complementary techniques to study crystallography and microstructure of heterogeneous structures such as teeth. Using these techniques we demonstrated that: (1) the inorganic phase of human dentine and enamel was a polycrystalline structure mainly composed of biological apatite; (2) needle-like nanocrystallites formed the inorganic phase of human dentine and enamel; (3) the thickness of the dentine crystallites were decreasing from middle dentine towards the DEJ; (4) the crystallites in mantle dentine appeared longer than in circumpulpal dentine; (5) the enamel crystallites were increasing in thickness from the DEJ towards the outer layers; (6) non-uniform microstrain was insignificant in both dentine and enamel crystal grains; (7) preferred orientation existed in 002 direction but also observed in 102 planes in the enamel crystallites; (8) texture effect was increasing in 002 planes from the DEJ towards outer layers of enamel; (9) texture in dentine in 002 plains was demonstrated at the scale of 1 μm.

4.7 References

1. Imbeni V., Kruzic J.J., Marshall G.W., Marshall S.J., Ritchie R.O. The dentin-enamel junction and the fracture of human teeth. Nature Materials 2005;4(3):229-32.
2. Lawn B.R., Bhowmick S., Bush M.B., Qasim T., Rekow E.D., Zhang Y. Failure modes in ceramicbased layer structures: A basis for materials design of dental crowns. Journal of the American Ceramic Society 2007;90(6):1671-83.
3. Qasim T., Bush M.B., Hu X., Lawn B.R. Contact damage in brittle coating layers: Influence of surface curvature. Journal of Biomedical Materials Research Part B: Applied Biomaterials 2005;73(1):179-85.
4. Jung Y.G., Wuttiphan S., Peterson I.M., Lawn B.R. Damage modes in dental layer structures. Journal of Dental Research 1999;78(4):887-97.
5. Lawn B.R. Ceramic-based layer structures for biomechanical applications. Current Opinion in Solid State and Materials Science 2002;6(3):229-35.

6. Fincham A.G., Moradian-Oldak J., Simmer J.P. The structural biology of the developing dental enamel matrix. Journal of Structural Biology 1999;126(3):270-99.
7. Macho G.A., Jiang Y., Spears I.R. Enamel microstructure - a truly three dimensional structure. Journal of Human Evolution 2003;45(1):81-90.
8. Lawn B.R., Lee J. J.-W., Constantino P.J., Lucas P.W. Predicting failure in mammalian enamel. Journal of the Mechanical Behavior of Biomedical Materials 2009;2(1):33-42.
9. Lucas P., Constantino P., Wood B., Lawn B. Dental enamel as a dietary indicator in mammals. BioEssays 2008;30(4):374-85.
10. Arana-Chavez V.E., Massa L.F. Odontoblasts: the cells forming and maintaining dentine. The International Journal of Biochemistry & Cell Biology 2004;36(8):1367-73.
11. Nanci A. Ten Cate's Oral Histology: Development, Structure and Function. 7th ed. St Louis: Mosby; 2008.
12. Gotliv B.-A., Veis A. Peritubular Dentin, a Vertebrate Apatitic Mineralized Tissue without Collagen: Role of a Phospholipid-Proteolipid Complex. Calcified Tissue International 2007;81(3):191-205.
13. Linde A. Dentin matrix proteins: Composition and possible functions in calcification. The Anatomical Record 1989;224(2):154-66.
14. Xie Z., Swain M., Munroe P., Hoffman M. On the critical parameters that regulate the deformation behaviour of tooth enamel. Biomaterials 2008;29(17):2697-703.
15. He B.B. Microdiffraction using two-dimensional detectors. Powder Diffractometry 2004;19:110.
16. Flemming R.L., Salzsauler K.A., Sherriff B.L., Sidenko N.V. Identification of scorodite in fine-grained, high-sulfide, arsenopyrite mine-waste using micro x-ray diffraction micro xrd. The Canadian Mineralogist 2005;43:1243.
17. Friedel F., Winkler U., Holtz B., Seyrich R., Ullrich H.J. Material analysis with X-ray microdiffraction. Crystal Research and Technology 2005;40(1-2):182-87.
18. Zioupos P., Rogers K.D. Complementary Physical and Mechanical Techniques to Characterise Tooth: A Bone-like Tissue. Journal of Bionic Engineering 2006;3(1):19-31.
19. Le Bail A. Whole powder pattern decomposition methods and applications: A retrospection. Powder Diffraction 2005;20(4):316-26.
20. Hunter B. Rietica - A Visual Rietveld Program. International Union of Crystallography Commission on Powder Diffraction, Newsletter № 20, 1998.
21. International Centre for Diffraction Data. Powder Diffraction File 09-0432; 2005.
22. Zhang Z., Zhou F., Lavernia E.J. On the analysis of grain size in bulk nanocrystalline materials via X-ray diffraction. Metallurgical and Materials Transactions 2003;34A(6):1349-55.
23. Klug H.P., Alexander L.E. X-ray Diffraction Procedures for Polycrystalline and Amorphous Materials. 2nd ed. New York: Wiley; 1974.
24. Low I.-M. Depth-Profiling of Crystal Structure, Texture, and Microhardness in a Functionally Graded Tooth Enamel. Journal of the American Ceramic Society 2004;87(11):2125-31.
25. Zavgorodniy A.V., Rohanizadeh R., Swain M.V. Ultrastructure of Dentine Carious Lesions. Archives of Oral Biology 2008;53(2):124-32.

26. Al-Jawad M., Steuwer A., Kilcoyne S.H., Shore R.C., Cywinski R., Wood D.J. 2D mapping of texture and lattice parameters of dental enamel. Biomaterials 2007;28(18):2908-14.
27. Wong F.S.L., Anderson P., Fan H., Davis G.R. X-ray microtomographic study of mineral concentration distribution in deciduous enamel. Archives of Oral Biology 2004;49(11):937-44.
28. Lucas P.W. Dental Functional Morphology : How Teeth Work. Cambridge: Cambridge University Press; 2004.
29. He L.H., Swain M.V. Influence of environment on the mechanical behaviour of mature human enamel. Biomaterials 2007;28(30):4512-20.
30. Ziv V., Weiner S. Bone Crystal Sizes: A Comparison of Transmission Electron Microscopic and X-Ray Diffraction Line Width Broadening Techniques. Connective Tissue Research 1994;30(3):165-75.
31. Daculsi G., Menanteau J., Kerebel L. M., Mitre D. Length and shape of enamel crystals Calcified Tissue International 1984;36(1):550-55.
32. Cuy J.L., Mann A.B., Livi K.J., Teaford M.F., Weihs T.P. Nanoindentation mapping of the mechanical properties of human molar tooth enamel. Archives of Oral Biology 2002;47(4):281-91.
33. Sharma P., Ganti S., Bhate N. Effect of surfaces on the size-dependent elastic state of nano-inhomogeneities. Applied Physics Letters 2003;82(4):535-37.
34. Dingreville R., Qu J., Cherkaoui M. Surface free energy and its effect on the elastic behavior of nano-sized particles, wires and films. Journal of the Mechanics and Physics of Solids 2005;53(8):1827-54.
35. Dingreville R., Qu J. Interfacial excess energy, excess stress and excess strain in elastic solids: Planar interfaces. Journal of the Mechanics and Physics of Solids 2008;56(5):1944-54.
36. Lu H.M., Jiang Q. Size-Dependent Surface Energies of Nanocrystals. Journal of Physical Chemistry B 2004;108(18):5617-19.
37. Lin C.P., Douglas W.H. Structure-property relations and crack resistance at the bovine dentin-enamel junction. Journal of Dental Research 1994;73(5):1072-78.
38. Zaslansky P., Friesem A.A., Weiner S. Structure and mechanical properties of the soft zone separating bulk dentin and enamel in crowns of human teeth: Insight into tooth function. Journal of Structural Biology 2006;153(2):188-99.
39. Wang R. Z., Weiner S. Strain–structure relations in human teeth using Moiré fringes. Journal of Biomechanics 1997;31(2):135-41.
40. Marshall Jr. G.W., Marshall S.J., Kinney J.H., Balooch M. The dentin substrate: structure and properties related to bonding. Journal of Dentistry 1997;25(6):441-58.
41. Zavgorodniy A.V., Rohanizadeh R., Bulcock S., Swain M.V. Ultrastructural observations and growth of occluding crystals in carious dentine. Acta Biomaterialia 2008;4(5):1427-39.

Chapter V. Ultrastructure of Dentine Carious Lesions

This chapter is based on the following published paper:

Zavgorodniy A.V., Rohanizadeh R., Swain M.V. Ultrastructure of Dentine Carious Lesions. Archives of Oral Biology 2008;53(2):124-32.

5.1 Abstract

Objective: The aim of the present study was to investigate the ultrastructural changes within the different zones of carious dentine and compare those changes with sound dentine.

Methods: Transmission electron microscopy and electron diffraction techniques were used to investigate the effect of caries on the inorganic phase of dentine. Areas of interest were identified with optical and scanning electron microscopes.

Results: The results demonstrated that the intertubular mineral crystallites decrease in size as caries lesion progresses. In the transparent zone of carious lesion, both intratubular and intertubular dentine consisted of nano-size apatetic crystallites with smaller size in the former. The intratubular mineral phase in transparent zone was found to be chemically similar to the intertubular dentine.

Conclusions: The study suggested that a 'dissolution and precipitation' mechanism is important in understanding the process of formation of intratubular dentine within the transparent zone induced by caries attack. The observed partial demineralization of intertubular dentine in transparent zone is discussed in terms of dissolution of tubule microbranches and exposure of intertubular dentine to acids.

5.2 Introduction

Human dentine is a hard, elastic, avascular connective tissue forming the bulk of the tooth. It lies between the enamel and pulp chamber and serves as a resilient tissue, supporting very highly mineralized brittle enamel to withstand the forces of mastication without fracture [1]. Dentine is a complex hydrated composite of four main elements: (i) oriented tubules surrounded by (ii) a highly mineralized peritubular zone embedded in an intertubular matrix largely consisting of (iii) type I collagen with embedded biological apatite crystals and (iv) dentinal fluid. Overall, dentine is composed of about 50% volume mineral in the form of apatite crystals, 30% organic matter which is largely type I collagen and about 20% fluid which is similar to plasma. The tubules represent the tracks taken by the odontoblastic cells from the dentine-enamel junction (DEJ) or cementum to the pulp chamber. Dentinal tubules initiate at the predentine from the DEJ in the crown and from the cementum in the root. Tubule area and diameter vary from about 22% and 2.5 μm near the pulp to 1% and 0.8 μm near the DEJ. Intertubular matrix area reportedly varies from 12% at the predentine to 96% near the DEJ, while peritubular dentine decreases from over 60% to 2.9% close to the DEJ [2].

Mineralized collagen fibrils in normal dentine are arranged orthogonal to dentine tubules forming a planar felt-like intertubular dentine matrix that is entirely random [3]. Biological apatite minerals in dentine are in the form of calcium-deficient and carbonate-rich hydroxyapatite that are closely packed and incorporated within the gaps between the collagen fibrils where c-axes of apatetic structure is parallel with the fibrils [1]. It is thought there are two mechanisms involved in apatite crystals formation, (i) nucleation on vesicles and on (ii) non-collagenous proteins (NCP) with apatite crystals deposited in relation to the orientation of collagen fibrils [4]. Once an apatite

crystallite has nucleated the immediate environment influences crystal growth and determines the shape of the crystal. NCP are able to bind selectively to different surfaces of the forming crystal inhibiting growth in certain directions and therefore producing crystals of various shapes: needle-shaped crystal, plate-shaped crystal and in the absence of inhibition produces a block-shaped crystal [1, 5, 6]. The size of the apatite crystals in dentine is approximately 5 x 30 x 100 nm and have less calcium than stoichiometric hydroxyapatite and contain 4 to 5% carbonate [7]. Lower calcium content and higher carbonate content leads to higher acidic solubility of the dentine apatite crystals than stoichiometric apatite and therefore higher vulnerability to carious attack [8].

Demineralization of dentine (caries) is mainly caused by exposure to acidic solutions with pH less than critical [9] when the mineral tends to dissolve until the solution becomes saturated. Carious dentine is described in terms of two altered layers, an outer carious layer (or infected layer) and an inner carious layer (affected layer). Each layer is further divided into different zones [2].

Several studies have described the ultrastructure and chemical composition of different layers of carious lesion and investigated various defensive reactions by the dentine-pulp complex to carious attack [10-21]. The most common observed defence reaction is tubular sclerosis described as a gradual mineralization of the tubule lumens which can lead to complete obstruction of the tubules [22]. In addition to the presence of apatite crystals, large crystals of Mg-substituted β-TCP (whitlockite) were also observed in carious arrested zone of tubular sclerosis [14]. Some studies reported that Ca/P ratios in sound, demineralized, peritubular, and secondary dentine were close to that of hydroxyapatite, whereas in intratubular dentine this ratio did not confirm the presence of hydroxyapatite crystals [17]. In more recent studies [21, 23] the larger crystals

deposited in intratubular dentine were reported to be chemically and structurally similar to those in intertubular dentine and the authors suggested that these large grains were actually composed of nano-size apatetic crystallites.

Quantitative analysis of the mineral content across a carious lesion showed significant reduction in mineral content towards outer dentine where less than 10 wt.% of mineral phase was found, although in some instances a marked increase of mineral content was also recorded close to the cavity floor [24]. It has been shown that mechanical properties of dentine are correlated with its mineral content and both values of dentine hardness and elastic modulus decrease through the carious lesion towards the outer surface, although often an increase in hardness and elastic modulus of dentine is also observed close to the cavity floor [25].

Although the macroscopic structural changes in the carious region of dentine have been demonstrated by several studies [2, 17, 19], the ultrastructural modifications in carious dentine crystals still remain controversial and unknown. The aim of the present study is to investigate the ultrastructural changes within the different zones of carious dentine and compare those changes with sound dentine using Scanning and Transmission Electron Microscopy (SEM, TEM) and Electron Diffraction analytical methods.

5.3. Materials and methods

5.3.1 Sample preparation

A molar tooth was extracted due to severe occlusal caries lesions. It was sterilised by placing in sodium hypochlorite 1% solution (Milton's solution) for 24 h after extraction. The specimen was then placed into Hanks' balanced salts solution (Sigma-Aldricht Co., St.Louis, MO, USA, 9.8 g per 1L of deionized distilled water).

The specimen was prepared by embedding in epoxy resin (Epofix, Struers, Copenhagen, Denmark) while the lesion was sealed with adhesive (Bostik Blu-Tack) to prevent resin from penetrating into the carious lesion. The resin was polymerised over night and then two 1 mm sections were prepared by sectioning the specimen along mesio-distal axis using a low-speed diamond saw (Isomet, Buehler Ltd., Lake Bluff, USA) under constant water irrigation.

5.3.2 Scanning Electron Microscopy (SEM)

Backscattered electron (BSE) imaging has been shown to be a useful tool to visualise differences in degrees of mineralization of biological tissues [24]. Backscattered electron images were obtained from the first section with Scanning Electron Microscope (SEM) XL30 (Philips, Eindhoven, The Netherlands) equipped with a solid-state backscattered electron detector. The SEM was operated in pressure controlled mode at 1 mB in the chamber, 20 kV beam energy, 5 nm spot size and 30 mm working distance.

5.3.3 Transmission Electron Microscopy (TEM)

Using a low-speed diamond saw (Isomet, Buehler Ltd., Lake Bluff, USA), the second section of tooth was cut along the crown to pulp axis into four dentine bars each with 1 mm width (Figure 5.1). The zones of interest for TEM observation were identified at this stage. The active carious lesion (turbid zone) was brown-yellow in colour with soft rubbery consistency; transparent dentine – pale brown hard tissue and sound dentine was identified as white yellowish colour hard tissue. Smaller sections of approximately 1x1x1.2 mm were then cut from the dentine bars representing each of the mentioned zones of interest using a low-speed diamond saw equipped with a

micrometer. The blocks were then immediately fixed in Modified Karnovsky's fixative in 0.2 M Sorenson's buffer titrated to pH 7.2 for 24 hours at 2°C and then rinsed several times with 0.2 M Sorenson's buffer.

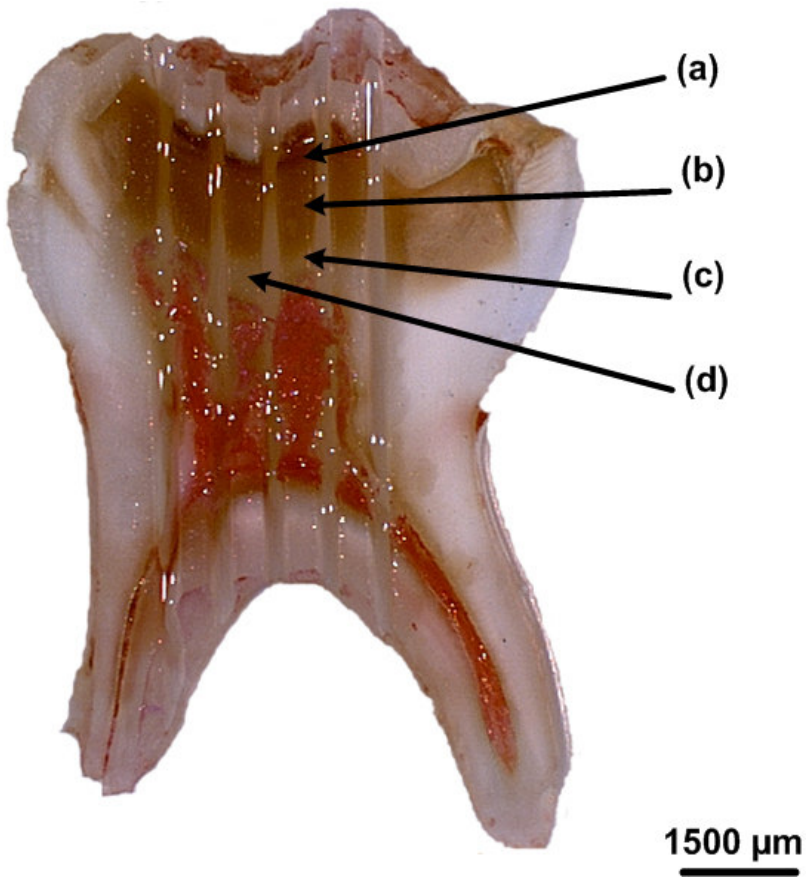

Figure 5.1 Optical image of the carious tooth cross-section cut into four 1 mm thick dentine bars. Visible caries zones are marked as (a) decomposed dentine, (b) demineralized dentine, (c) transparent zone and (d) sound dentine.

The specimens were dehydrated in increasing concentrations of ethanol (30%, 50%, 70% - twice 15 min each, 95% and 100% - twice 30 min each) and then infiltrated with the epoxy resin for 24 hours using 50% epoxy in ethanol and then 24 hours in 100% epoxy resin on rotators. The specimens were then embedded into 100% epoxy resin in the plastic moulds. The prepared resin blocks were cured for 48 hours at 65°C and 80-nm-thick sections were cut perpendicular to the dentine tubules using an ultramicrotome (Ultracut S, Reichert-Leica, Vienna, Austria) equipped with

45° diamond knife (Diatome, Bienne, Switzerland). The sections were collected from distilled water onto 200 mesh copper grids pre-coated with formwar film. After drying, the specimens were carbon coated, then observed using Transmission Electron Microscope (TEM) CM12 (Philips, Eindhoven, The Netherlands) operated at 120 kV and equipped with a nitrogen-cooled anti-contamination device.

5.3.4 Crystal size determination

In order to determine ultrastructural changes in primary dentine crystals due to carious attack, the plate width (short axis) and the length (long axis) of dentine crystals were measured. The measured lengths of the crystallites reflect the variability in the length of biological apatite crystallites rather than variability due to their orientation relative to the projection plane which as was estimated for uniform and Gaussian distributions (with assumption that 95% of the crystallites have the variation of small angle between c-axis of the crystal and the projection plane within 18°) was less than 1.46 nm (Appendix). The size of at least 55 crystallites was measured in each dentine zone. The means and standard deviations of these data were calculated. Statistical differences were examined using a two-tail unpaired t-test and the corresponding P values reported ($P < 0.05$) were considered statistically significant.

5.3.5 Electron diffraction

Corresponding selected area electron diffraction patterns were obtained to reveal the nature of the crystalline structure under observation. Crystals of gold were used as standard. The obtained d_{hkl} values were compared with those of the ASTM reference [26].

5.4 Results

Backscattered electron (BSE) imaging allows us to visualise and investigate the mineral distribution in the caries dentine across a tooth section due to different electron densities caused by acidic dissolution of the apatite mineral component [24]. The BSE image (Figure 5.2) of mesio-distal section of the tooth revealed carious affected layer of dentine, which appeared as a dark zone that graded to grey levels towards the cavity floor. The remnants of softened, decomposed dentine (Figure 5.2, arrow (a)) were still present and were visible as much lighter grey levels at the outer layer of dentine at the cavity floor sitting on top of the demineralized (turbid) dentine (Figure 5.2, arrow (b)). In the decomposed dentine loss of mineral in both peritubular and intertubular dentine were observed. Turbid zone was followed by transparent zone (Figure 5.2, arrow (c)) with extensive intratubular mineralization. Sound dentine (Figure 5.2, arrow (d)) appeared bright on the micrograph although a slight increase in grey levels was observed in dentine adjacent to the pulp chamber (Figure 5.2, arrow (e)), which indicates the mineralizing front of secondary dentine formed by the odontoblasts.

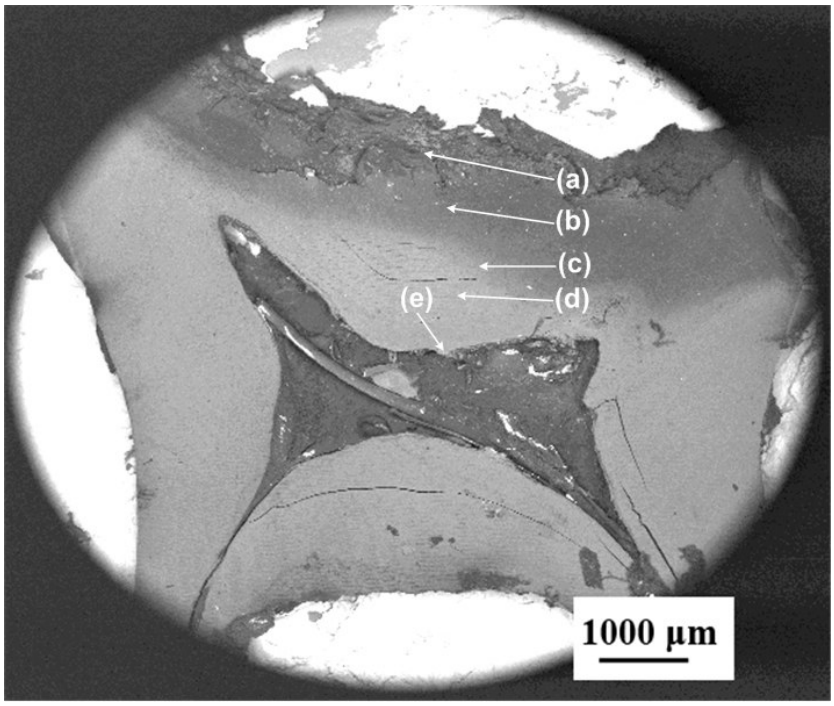

Figure 5.2 Backscattered SEM micrograph of mesio-distal section of the tooth specimen with deep and wide-spread carious lesion: (a) decomposed dentine, (b) demineralized dentine, (c) transparent dentine, (d) sound primary dentine and (e) secondary dentine.

5.4.1 Sound dentine

A cross-sectional image (Figure 5.3A) of the middle region of sound dentine was obtained using TEM. The basic structure of sound dentine, as observed with TEM, consists of tubules (Figure 5.3A, inset (a)) surrounded by thick peritubular structures (Figure 5.3A, arrow (b)) and intertubular area (Figure 5.3A, inset (c)). The tubules were closely packed and the mean value and standard deviation of the diameter of tubules in sound dentine was 2.19 ± 0.33 µm with numerical density of approximately 34000 tubules / mm^2 which is in accordance with values reported in another study [2] of the middle region between the pulp and DEJ in sound dentine.

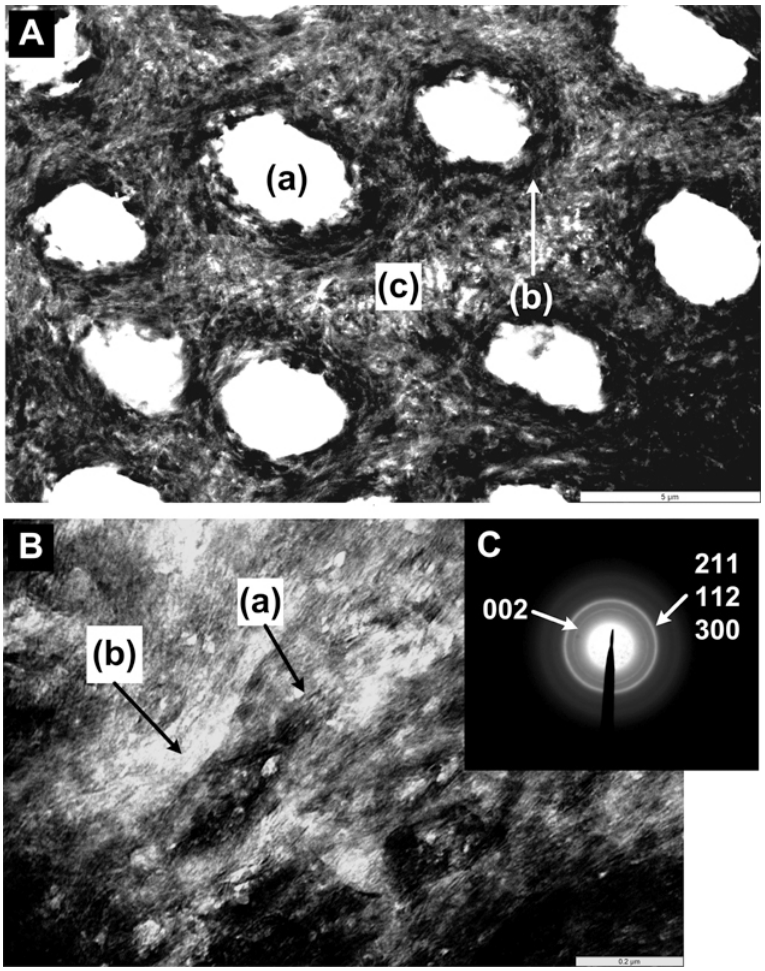

Figure 5.3 TEM micrographs of sound dentine. A. Low magnification TEM micrograph of sound dentine. Note well defined (a) tubules. The dark contrast around the tubules indicates peritubular dentine (b); lower density intertubular dentine is much brighter on the micrograph (c). B. Higher magnification TEM micrograph of intertubular sound dentine. Needle-shaped densely packed apatite crystals (a) with less mineral dense regions between them (b). C. SAED pattern of intertubular sound dentine with indexing confirming the presence of apatite phase.

In the TEM, given the thickness of dentine section is even in different areas of observation, the poorly mineralized regions appeared more electron-transparent than highly mineralized areas. Therefore the highly mineralized peritubular dentine was recognisable with dark rings (Figure 5.3A, arrow (b)) with an average thickness of 0.75 ± 0.20 μm surrounding each tubule. Intertubular dentine appeared as lighter matter which indicates intertubular dentine was less mineralized than peritubular dentine. Based on grey level contrast, in sound dentine the peritubular dentine appeared more mineralized than intertubular dentine.

The higher magnification TEM micrograph revealed underlying ultrastructure of the primary normal dentine (Figure 5.3B). The mineral phase consisted of needle-like apatite crystals (Figure 5.3B, arrow (a)), which were packed together forming structures with less mineral dense regions between them (Figure 5.3B, arrow (b)). The length and width of the sound dentine intertubular crystals was 109.6 ± 19.9 nm and 6.2 ± 1.2 nm respectively.

The higher magnification micrograph (Figure 5.3B, arrow (a)) also revealed that crystallites were aligned in dense dark contrast structures in planes perpendicular to the longer axis of the tubules with light contrast areas between them.

The selected area electron diffraction (SAED) pattern of sound intertubular dentine (Figure 5.3C) consisted of ring patterns. Measuring radii and indexing of the principal ring patterns, i.e. (002) ≈ 3.44Å and (300/112 and 211) rings where (112) ≈ 2.78Å, confirmed that the intertubular crystallites were apatite phase.

5.4.2 Transparent dentine

The structure of transparent dentine is shown in (Figure 5.4). The distinct feature of transparent dentine was that tubules were filled with mineral and partially occluded (tubular sclerosis) (Figure 5.4A, arrows (a)). Perforations in intratubular dentine are distinct (Figure 5.4A, arrows (a) and (b)). The intertubular dentine (Figure 5.4A, inset (c)) appeared less dense than in sound dentine, which also indicated partial demineralization of dentine tissue. Higher magnification TEM images (Figure 5.4B) revealed ultrastructure of intertubular transparent dentine. Needle-like crystals (Figure 5.4B, arrow (a)) with length of 51.6 ± 13.05 nm and width of 5.5 ± 1.2 nm were observed. The crystallites appeared less dense compared to those observed in sound dentine. Across the intertubular dentine in the transparent zone, the crystallites formed

dense but not homogenous structures (Figure 5.4B, arrow (b)) and voids were present between the denser areas (Figure 5.4B, arrows (c)).

Indexing of electron diffraction patterns obtained from transparent intertubular dentine (Figure 5.4C) confirmed that the bulk of the transparent intertubular dentine was formed with nano-size apatite crystallites. The rings in diffraction patterns were not totally continuous and consisted of separate diffraction spots.

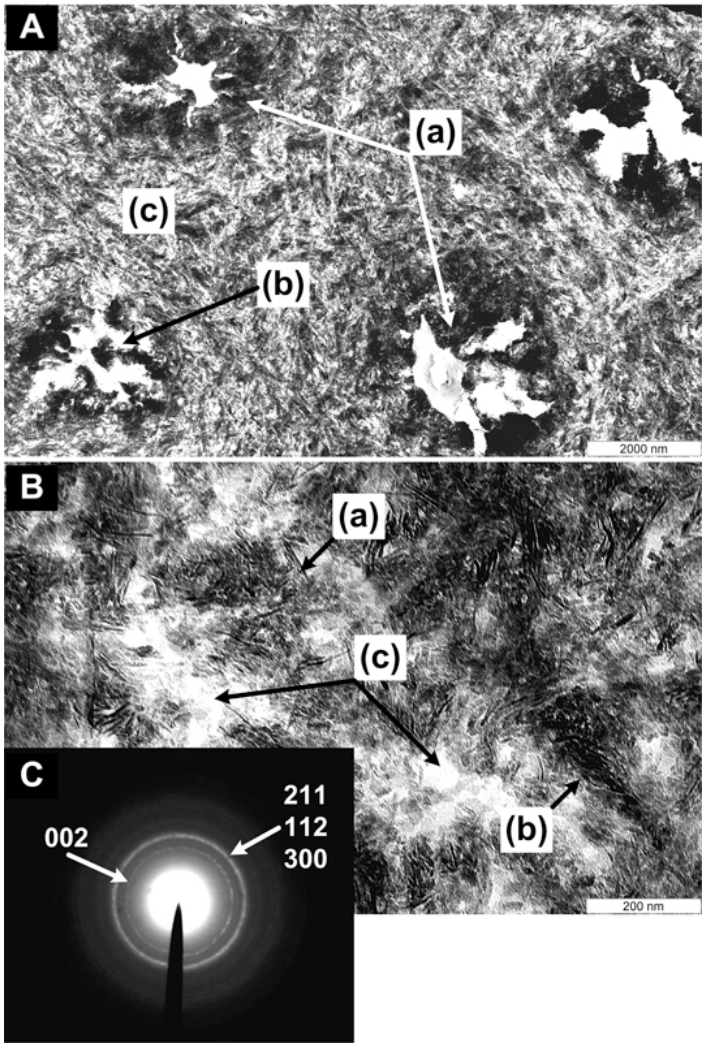

Figure 5.4 TEM micrographs of transparent dentine. A. Note partially occluded tubules (a) with intratubular dentine and perforations (b); (c) intertubular dentine surrounding tubules. B. TEM micrograph of transparent intertubular dentine at higher magnification. (a) Needle-like dentine crystals; (b) densely packed dentine crystallites were aligned along collagen fibril; (c) voids representing demineralized dentine in between collagen fibrils. C. SAED pattern of intertubular transparent dentine with indexing confirming the presence of apatite phase.

High magnification TEM micrograph of the intratubular dentine in the transparent zone is shown in Figure 5.5. Figure 5.5A reveals the presence of almost completely occluded tubules with perforations through the original peritubular cuff. Higher magnification images of the occluded mineral phase (Figure 5.5B) revealed two types of closely packed crystallites: plate-shaped (Figure 5.5B, arrow (a)) and needle-like (Figure 5.5B, arrow (b)). The bulk of the crystallites forming the intratubular dentine in the transparent zone were plate-shaped. The lengths of the needle-like crystallites measured 36.1 ± 9.2 nm and had a width of 4.8 ± 0.9 nm. The size of plate-shaped crystallites along the long axis was 9.1 ± 2.1 nm and along short axis was 5.3 ± 0.8 nm. In Figure 5.5C, SAED patterns of the deposited intratubular dentine within the lumen of the tubule confirmed the presence of an apatite phase. The semi-circles pattern shown in this SAED, corresponding to (002) crystal planes, indicates a preferred orientation of the deposited apatite crystals. Data corresponding to the size of crystals in different areas in dentine are summarised in (Table 5.1) and (Table 5.2).

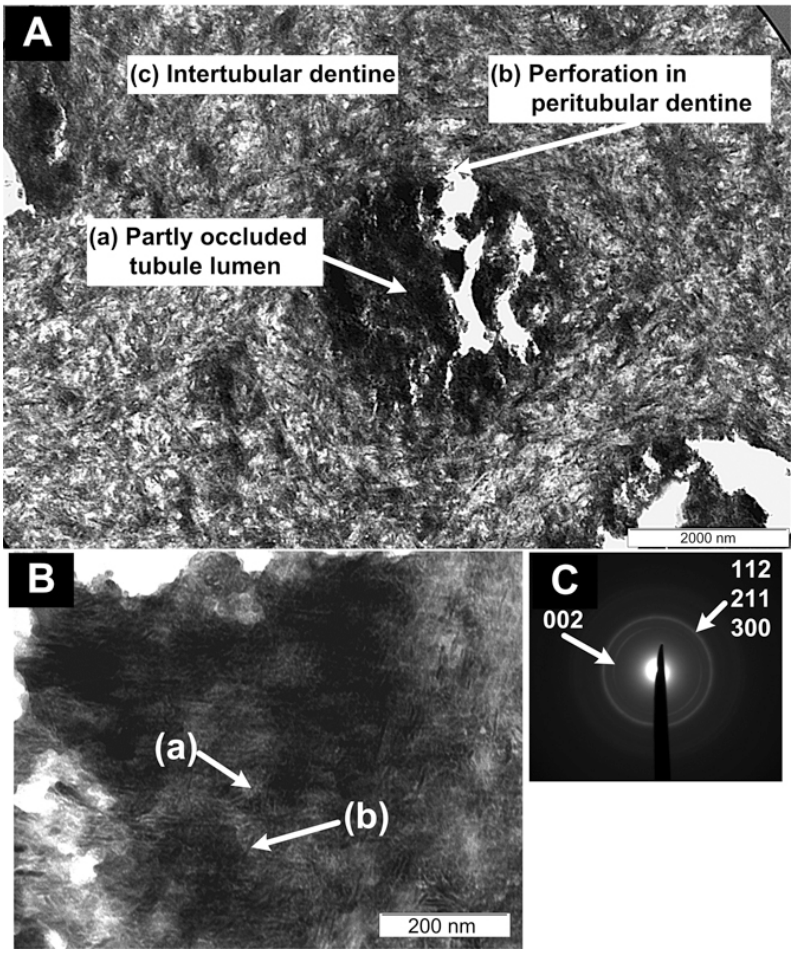

Figure 5.5 TEM micrograph of caries-induced intratubular transparent dentine. A. Note partially occluded tubule (a) with a perforation in peritubular dentine due to the demineralization of the mineral phase by acids produced by cariogenic bacteria (b). The tubules were surrounded by intertubular dentine (c). B. Higher magnification TEM image of intratubular dentine. The bulk of the mineral was formed with plate-shaped crystallites (a) with occasional presence of needle-shaped crystallites (b). C. SAED pattern of the enclosed area of intratubular dentine in the lumen of the tubule confirmed the presence of an apatite phase. The presence of semi-circles pattern corresponding to (002) crystal planes indicating a preferred orientation of apatite crystals.

Table 5.1 Mineral crystallite widths in sound, transparent and demineralized dentine.

Dentine type	Specimen location	Mean width, nm	S.D., nm
Sound	Middle dentine	6.2	1.2
Transparent	Middle dentine	5.5	1.2
Demineralised	Near DEJ	4.2	1.0

Table 5.2 Mineral crystallite lengths in sound, transparent and demineralized dentine.

Dentine type	Specimen location	Mean length, nm	S.D., nm
Sound	Middle dentine	109.6	19.9
Transparent	Middle dentine	51.6	13.0
Demineralised	Near DEJ	37.8	20.1

5.4.3 Demineralized (turbid) dentine

Figure 5.6 shows ultrastructural images of demineralized dentine (turbid zone). The peritubular cuffs, surrounding the tubules (Figure 5.6A, arrows (a)), were almost absent (Figure 5.6A, arrows (b)) and intertubular dentine (Figure 5.6A, inset (d)) was further demineralized. Although some remnants of mineral occluding the tubules lumens were still visible, the mineral which occluded the tubules in transparent dentine had almost disappeared in turbid dentine – probably due to dissolution (Figure 5.6A, arrows (c)). The tubules varied greatly in shape and diameter. The whole layer appeared to have lost a large amount of its mineral content. Higher magnification TEM images revealed needle-like crystallites (Figure 5.6B, arrow (a)), which were still present in some dense structures but the densities of the crystallites decreased substantially compared with intertubular transparent dentine (Figure 5.4B). The length and width of the intertubular dentine crystallites was 37.8 ± 20.1 nm and 4.2 ± 1.0 nm respectively.

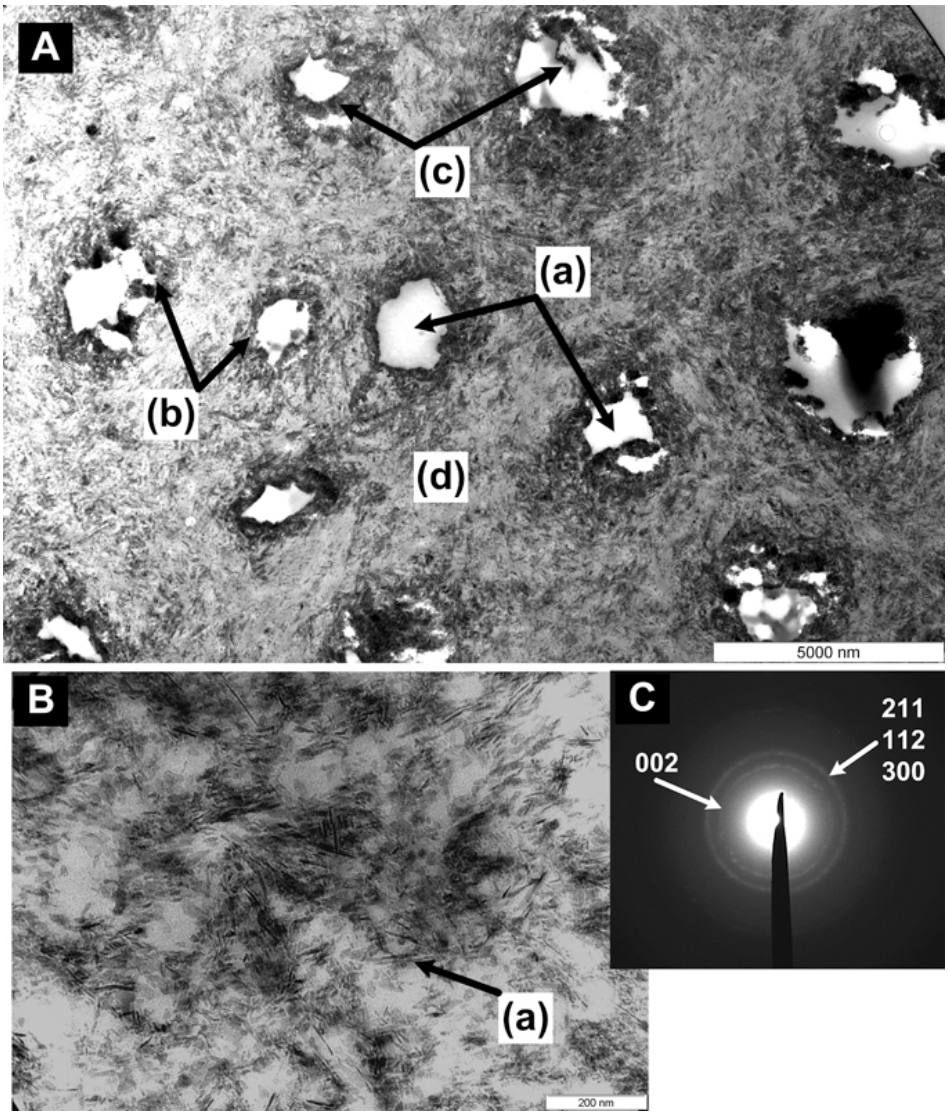

Figure 5.6 TEM micrographs of the demineralized dentine. A. (a) Tubules almost completely lost peritubular (b) and intratubular (c) dentine surrounded by intertubular dentine (d) which was significantly demineralized. B. Higher magnification TEM of the demineralized dentine. Mineral phase appeared as dark contrast needle-like crystals (a). C. SAED pattern of the intertubular demineralized dentine confirming the presence of apatite phase.

Due to the low density of crystals and being partially dissolved by the acidic conditions, it was difficult to obtain, analyse, and index diffraction patterns generated by crystals in demineralized dentine. Therefore very few crystals were available to scatter electrons to form clear diffraction patterns. A beam of electrons penetrated through the demineralized dentine without scattering forming large bright spot in the middle of the diffraction micrograph (Figure 5.6C), which almost completely

overshadowed diffraction spots. However, the brightest diffraction rings, which are unique to apatite crystal structures, were still distinguishable in the diffraction pattern obtained from demineralized dentine. It should be noted ring patterns that consisted of diffraction spots were observed in diffraction patterns obtain from demineralized areas. The predominant ring pattern corresponding to (002) planes appeared in form of two semi-circles instead of a continuous ring (Figure 5.6C), indicating the crystallites have preferred orientation in c-direction.

The crystallite width (Table 5.1) and length (Table 5.2) were determined from the TEM images in three locations corresponding to sound, transparent and demineralized (turbid) intertubular dentine. In all three regions qualitative and quantitative observations indicated a significant decrease (t-test, $P < 0.05$) in both length and width of the crystallite as a function of dentine transparency and demineralization. The mean crystallite length decreased by 53% and the width by 12% for transparent dentine and decreased by 65% and 32% respectively in demineralized intertubular dentine, which are in accordance with those reported in literature [23].

The crystallite sizes of intratubular dentine are listed in (Table 5.3). It can be noted the similarities in sizes of the intertubular dentine in the turbid layer and sizes of the needle-like crystallites observed in the intratubular transparent dentine in the areas just below the demineralized (turbid) dentine.

Table 5.3 Mineral crystallites size in intratubular transparent dentine.

Crystalline shape	Length, nm	S.D., nm	Width, nm	S.D., nm
Needle	36.1	9.2	4.8	0.9
Plate	9.1	2.1	5.3	0.8

5.5 Discussion

5.5.1 Sound dentine

Sound dentine is a highly mineralized tissue (Figure 5.3A) with inorganic phase of intertubular dentine confirmed to be apatite through indexing of the corresponding electron diffraction patterns (Figure 5.3C). The continuous rings of the diffraction pattern of sound dentine did not show preferred orientation of the crystallites, probably because of the high density of dentine crystals within the relatively large selected area for diffraction in the intertubular sound dentine as the crystallites within this area are more or less randomly oriented with their c-axes perpendicular to the electron beam. Diffraction patterns obtained at higher magnification revealed the local preferred orientation of crystallites in sound dentine probably with their c-axes along the collagen fibril (Figure 5.3B, arrow (a)).

5.5.2 Transparent dentine

One of the main characteristics of the transparent dentine is the occlusion of tubule lumens with mineral deposits referred as intratubular dentine (Figure 5.5A). Indexing of the corresponding electron diffraction patterns confirmed that the bulk of the intratubular dentine was apatitic phase (Figure 5.5C). Presence of large rhombohedral Mg-substituted β-TCP crystals (whitlockite) in the intratubular dentine in the transparent zone have been occasionally reported in the literature [11, 14]. However, there was no evidence of such crystals in the present work. Intratubular dentine appeared to be a dense structure formed of plate-shaped apatite crystallites with occasional presence of needle-like apatite crystallites (Table 5.3). The difference in crystalline structure between the carious- and aged-induced sclerosis was also noticeable. In the latter, large apatite crystals loosely filled up the tubules, producing

distinct electron diffraction spots [21]. In the present work, caries-induced intratubular mineral formed polycrystals densely filling the tubules, producing bright electron diffraction ring patterns implying a polycrystalline structure of the intratubular dentine.

Sclerosis of tubules by formation of mineral in intratubular spaces is the natural defence mechanism to caries attack, and thereby occlusion of the tubules, preventing acids and cariogenic bacteria penetrating deeper into the tooth [1]. This mechanism may be mediated by the carious-induced stimulated odontoblastic processes with a source of mineral being the pulpal blood supply.

A second mechanism which results in a partial mineralization of the tubule lumens may be due to the re-precipitation of the dissolved apatite from low supersaturated aqueous phase. The bulk of the observed mineral crystallites in intratubular dentine (Figure 5.5B) were plate shaped crystallites with occasional presence of needle-shaped crystallites. The observed crystallites were relatively small (Table 5.3) in size with low standard deviations in size, indicating the sizes of the crystallites were statistically similar within this section of the tubule lumen. The relatively limited variation in the dark contrast across the intratubular dentine (Figure 5.5B) indicates a homogenous density of intratubular crystallites across the tubule lumen. A uniformity in the size of crystallites within the intratubular zone shows that these crystallites nucleated approximately at the same time and under the same conditions through the volume of this section of tubule lumen and the precipitation did not gradually occur on the peritubular dentine surface. Minerals dissolved by bacterial acids in the affected demineralized layer can nucleate from carboxyl groups of non-collagenous proteins (NCP). These carboxyl groups have the proper orientation to nucleate crystals at the (001) crystal face thus orienting the c-axis of the

crystal in a controlled direction [27] which is in agreement with our observations of electron diffraction patterns of the intratubular dentine. Figure 5.5C shows the preferred c-direction orientation of the crystallites within this region. The growth and final shape of the crystals is also determined by NCP, which can bind to different surfaces of a crystal, inhibiting growth in that particular direction [1]. The bulk of crystallites observed in intratubular dentine were plate-shaped crystallites (Figure 5.5B) which indicates the presence of non-collagenous proteins (NCP) in the immediate environment of the growing crystallites. It is unlikely that saliva is the source of calcium and phosphate ions for the second mechanism of mineralization in intratubular spaces (re-precipitation process). The ionic absorption of calcium and phosphate from oral fluids was shown to be possible [28] and the rehardening of the soften demineralized dentine can occur at the cavity floor. However this less permeable remineralized hard layer of dentine limits oral fluids from remineralizing deeper layers of affected dentine as it has been shown *in vitro* [16].

The intertubular dentine in the transparent zone of carious dentine also appeared to be slightly demineralized (Figure 5.4A, inset (c)) in comparison with sound dentine (Figure 5.3A, inset (c)). High magnification TEM images of intertubular dentine (Figure 5.4B, arrow (a)) revealed that the size of dentine crystallites significantly decreased (t-test, $P < 0.05$) (Table 5.1) and (Table 5.2) compared with intertubular sound dentine which does indicate some demineralization of intertubular dentine in the transparent zone. Also at high magnification, the structure of crystallites in intertubular transparent dentine was less dense (Figure 5.4B) than in sound dentine (Figure 5.3B). Another study reported that mechanical properties (nano-hardness and elastic modulus measured with AFM) of intertubular dentine in carious transparent zone were statistically significantly lower than those of

intertubular sound dentine [29]. It has also been reported that a relatively high mineral content exists in deeper carious lesions [25]. These observations may be interpreted as the transparent zone having a higher mineral content but relatively low mechanical properties. However it has been shown that the mechanical properties are clearly correlated with inorganic mineral content: the deterioration of the mechanical properties is linked to a decrease in mineral content [25]. The higher mineral content may be attributed to the mineralization of the tubule lumens in the transparent zone as shown in (Figure 5.4A). The mechanical properties of transparent dentine, when observed as a composite, are lower in comparison with normal dentine because they are determined mainly by the mechanical properties of the intertubular dentine [30] and not by peritubular cuffs or intratubular dentine [29]. It has also been shown that bond strength to carious dentine is lower than bond strength to normal dentine [31] which also supports our observations of a slight demineralization of intetubular dentine in the transparent zone.

However, it is unlikely that such a homogenous partial demineralization of the intertubular dentine can be only attributed to the observed occasional perforations in peritubular dentine in the transparent zone. Not only tubules but also tubule branching network may represent sites for infiltration in dentine with acid substances in addition to the existing main tubules and therefore may play a role in progression of caries providing extra pathways and increasing permeability of the dentine. Three types of branches, major, fine and microbranches are described on the basis of size, direction and location. Microbranches, however, form the bulk of branches network within interubular middle dentine [32]. The diameter of the lumen varies from 50 to 100 nm [32] and the thickness of the peritubular cuff can also be estimated as 50 to 100 nm. Microbranches extend at approximately right angles from the dentinal tubules and are

found through out intertubular dentine [32]. From the micrographs presented in [32] it can be estimated the densities of microbranches in the middle sound dentine was about 10^6 per mm^2 while densities of the tubules are estimated as 34000 per mm^2. Simple calculations show that even though the space occupied by the lumens of microbranches per mm^2 is ~ 0.0093 mm^2 while the space occupied by the lumens of tubules per mm^2 can be estimated as ~ 0.065 mm^2 and therefore the space occupied by the lumens of the microbranches are only an order of magnitude less and indeed must be taken into account when demineralization induced by caries is interpreted. Acids can penetrate into those branches, dissolve the thin peritubular cuff and the intertubular dentine becomes readily exposed for further demineralization. The results from Marshall et al [18] showed that the etching rate of the peritubular dentine exposed to citric acid *in vitro* with pH = 2.5 was about 36 nm/sec, which means a peritubular cuff of a microbranch will simply disappear in less than 3 seconds if exposed to such acidic condition. Voids observed on higher magnification TEM micrographs (Figure 5.4B, arrows (c)) could be dissolved microbranches and therefore the intertubular dentine in the transparent zone is exposed to demineralization through the network of microbranches. This observation may explain observed partial demineralization of the intertubular dentine in the transparent zone and significant decrease of the size of the crystallites compared with intertubular sound dentine. These observations are also supported by the corresponding electron diffraction patterns of the intertubular dentine in the transparent zone (Figure 5.4C). It is evident that the diffraction rings are not continuous rings produced by intertubular normal dentine (Figure 5.3C) but instead individual spots were observed. These observations suggest that the density of intertubular crystallites between collagen fibrils was reduced as observed at high magnification (Figure 5.4B) and therefore the intensity of the diffused rings produced

by these randomly oriented crystallites dropped. On the other hand crystallites incorporated into collagen fibrils are less exposed to acids and also they are aligned along the collagen fibrils with their c-axes parallel to the fibril. Because of that, crystallites within the collagen fibrils contribute to diffraction pattern as spots due to their bigger size and high order of orientation than the crystallites between the collagen fibrils. Also due to relatively large areas of intertubular dentine selected for diffraction in the transparent zone fibrils appeared oriented in many (but not all) directions and therefore diffraction spots produced by crystallites can be distinguished and appear to be evenly distributed within the rings.

5.5.3 Demineralized dentine

Demineralized (turbid) dentine has lost its peritubular cuff and much of the intertubular mineral tubules (Figure 5.6A, arrows (a)). It is most likely that bacteria have penetrated into the region. The needle-like crystals of apatite phase could be still observed but they formed part of much less dense structures (Figure 5.6B, arrow (a)) than crystallites in intertubular transparent dentine (Figure 5.4B, arrow (a)). The crystallites in the intertubular demineralized zone were found to be significantly smaller in size than intertubular crystallites in the transparent zone (t-test, $P < 0.05$) (Table 5.1) and (Table 5.2) which is in agreement with qualitative observations by Shimizu et al [12]. The width of intertubular needle-like crystallites in turbid zone was statistically similar to the width of needle-like crystallites in intratubular dentine in transparent zone (t-test, $P > 0.10$), however their lengths were not statistically similar in these two zones (t-test, $P < 0.0.5$).

The diffraction spots which formed the ring diffraction patterns in the demineralized zone (Figure 5.6C) were clearly distinguishable and separated,

indicating lower density of crystals in this area, supporting the TEM observation of the crystallites in demineralized dentine (Figure 5.6B).

A new approach called 'minimum intervention' [33] has been recently introduced for cavity preparation prior to restoration of carious lesions in order to preserve tooth structure. This approach suggests that caries do not always need to be removed completely from deeper portions of the cavity: the outer carious dentine (turbid zone) must be removed, while the inner carious dentine should be preserved [34].

From this point of view the ultrastructure of turbid carious dentine is of a particular interest. Even though the tubules have almost completely lost peritubular dentine, the structure had not collapsed even when they happened to be significantly demineralized. The electron diffraction patterns of intertubular dentine in demineralized zone (Figure 5.6C) confirmed the presence of apatite phase with crystallites having preferred orientations. These findings suggest that the collagen matrix is still structured and crystallites are still aligned along collagen fibrils which is in agreement with the results by Frank [35] where cross-banded collagen fibrils were directly observed in infected demineralized zone of caries dentine.

5.6 Conclusions

Based on this ultrastructural study of mineral phase in different areas of a carious dentine, the following conclusions can be drawn:

1. Intertubular dentine crystallites in transparent zone were 53% smaller in length and 12% smaller in width than in sound intertubular dentine.
2. Intertubular dentine crystallites in demineralized (turbid) zone were 65% smaller in length and 32% smaller in width than in sound intertubular dentine.

3. The intratubular mineral crystals deposited within the lumens of the tubules in carious transparent zone were an apatite phase, nanometer size (<10 nm), plate-shaped, and chemically similar to intertubular dentine.
4. Ultrastrastructural observations of the intertubular dentine in the carious transparent zone demonstrated partial demineralization of the intertubular dentine through the dissolution of microbranches and exposure of the intertubular transparent dentine to acids.

5.7 References

1. Nanci A. Ten Cate's Oral Histology: Development, Structure and Function. 6th ed. St Louis: Mosby; 2003.
2. Marshall Jr. G.W., Marshall S.J., Kinney J.H., Balooch M. The dentin substrate: structure and properties related to bonding. Journal of Dentistry 1997;25(6):441-58.
3. Jones S.J., Boyde A. Ultrastructure of dentin and dentinogenesis. In: Linde A., editor. Dentin and Dentinogenesis. Boca Raton: CRC Press; 1984. p. 81-134.
4. Linde A. Calcification in biological systems. Boca Raton CRC Press; 2000.
5. Addadi L., Weiner S. Biomineralization : chemical and biochemical perspectives. New York: Weinheim; 1989.
6. Rohanizadeh R., Padrines M., Bouler J.M., Couchourel D., Fortun Y., Daculsi G. Apatite precipitation after incubation of biphasic calcium-phosphate ceramic in various solutions: Influence of seed species and proteins. Journal of Biomedical Material Research 1999;44:98-108.
7. Marshall Jr. G.W. Dentin: Microstructure and characterization. Quintessence International 1993;24(9):606-17.
8. LeGeros R.Z., Tung M.S. Chemical Stability of Carbonate- and Fluoride-Containing Apatites. Caries Research 1983;17:419.
9. Dawes C. What Is the Critical pH and Why Does a Tooth Dissolve in Acid. Journal of the Canadian Dental Association 2003;69(11):722-24.
10. Sarnat H., Massler M. Microstructure of Active and Arrested Dentinal Caries. Journal of Dental Research 1965;44(6):1389-401.
11. Frank R.M., Voegel J.C. Ultrastructure of the Human Odontoblast Process and Its Mineralisation during Dental Caries. Caries Research 1980;14:367-80.
12. Shimizu C., Yamashita Y., Ichijo T., Fusayama T. Carious change of dentin observed on longspan ultrathin sections. Journal of Dental Research 1981;60:1826-31.
13. Ogawa K., Yamashita Y., Ichijo T., Fusayama T. The ultrastructure and hardness of the transparent layer of human carious dentin. Journal of Dental Research 1983;62:7-10.

14. Daculsi G., LeGeros R.Z., Jean A., Kerebel B. Possible physico-chemical processes in human dentin caries. Journal of Dental Research 1987;66:1356-59.
15. Frank R.M. Ultrastructure of human dentine 40 years ago - progress and perspectives. Archives of Oral Biology 1999;44:979-84.
16. Kawasaki K., Ruben J., Tsuda H., Huysmans M.C.D.N.J.M., Takagi O. Relationship between mineral distributions in dentine lesions and subsequent remineralization in vitro. Caries Research 2000;34(5):395-403.
17. Arnold W.H., Kanopka S., Gaengler P. Qualitative and quantitative assessment of intratubular dentin formation in human natural carious lesions Calcified Tissue International 2001;69:268-73.
18. Marshall Jr. G.W., Chang Y.J., Gansky S.A., Marshall S.J. Demineralization of caries-affected transparent dentin by citric acid: an atomic force microscopy study. Dental Materials 2001;17(1):45-52.
19. Arnold W.H., Konopka S., Kriwalsky M.S., Gaengler P. Morphological analysis and chemical content of natural dentin carious lesion zones. Annals of Anatomy - Anatomischer Anzeiger 2003;185(5):419-24.
20. Nakornchai S., Atsawasuwan P., Kitamura E., Surarit R., Yamauchi M. Partial biochemical characterisation of collagen in carious dentin of human primary teeth. Archives of Oral Biology 2004;49:267-73.
21. Nalla R.K., Porter A.E., Daraio C, Minor A.M., Radmilovic V., Stach E.A., et al. Ultrastructural examination of dentin using focused ion-beam cross-sectioning and transmission electron microscopy. Micron 2005;36(7-8):672-80.
22. Silverstone L.M., Hicks M.J. The structure and ultrastructure of the carious lesion in human dentin. Gerodontics 1985;1:185-95.
23. Porter A.E., Nalla R.K., Minor A., Jinschek J.R., Kisielowski C., Radmilovic V., et al. A transmission electron microscopy study of mineralization in age-induced transparent dentin. Biomaterials 2005;26:7650-60.
24. Angker L., Nockolds C., Swain M.V., Kilpatrick N. Quantitative analysis of the mineral content of sound and carious primary dentine using BSE imaging. Archives of Oral Biology 2004;49(2):99-107.
25. Angker L., Nockolds C., Swain M.V., Kilpatrick N. Correlating the mechanical properties to the mineral content of carious dentine—a comparative study using an ultra-micro indentation system (UMIS) and SEM-BSE signals. Archives of Oral Biology 2004;49(5):369-78.
26. American Society for Testing Materials. X-ray powder diffraction file card. No. 9-432 and 4-0784. Philadelphia; 1967.
27. Fisher L.W., Termine J.D. Noncollagenous Proteins Influencing the Local Mechanisms of Calcification. Clinical Orthopaedics And Related Research 1985;200:362-85.
28. Pigman W., Kotwal K., Koulourides T. Calcifying ability of human body fluids. Archives of Oral Biology 1966;11(8):815-24.
29. Marshall G.W., Habelitz S., Gallagher R., Balooch M. Nanomechanical properties of hydrated carious human dentin. Journal of Dental Research 2001;80(8):1768-71.
30. Kinney J.H., Balooch M., Marshall G.W., Marshall S.J. A micromechanics model of the elastic properties of human dentine. Archives of Oral Biology 1999;44:813-22.

31. Nakajima M., Sano H., Burrow M.F., Tagami J., Yoshiyama M., Ebisu S., et al. Tensile bond strength and SEM evaluation of caries-affected dentin using dentin adhesives. Journal of Dental Research 1995;74:1679-88.
32. Mjör I.A., Nordahl I. The density and branching of dentinal tubules in human teeth. Archives of Oral Biology 1996;41(5):401-12.
33. Tyas M.J., Anusavice K.J., Frencken J.E., Mount G.J. Minimal intervention dentistry - a review. International Dental Journal 2000;50:1-12.
34. Fusayama T. Two Layers of Carious Dentin: Diagnosis and Treatment. Operational Dentistry 1979;4:63-70.
35. Frank R.M. Structural events in the caries process in enamel, cementum and dentin. Journal of Dental Research 1990;69(Special Issue):559-66.

Chapter VI. Ultrastructural Observations and Growth of Occluding Crystals in Carious Dentine

This chapter is based on the following published paper: **Zavgorodniy A.V.**, Rohanizadeh R., Bulcock S., Swain M.V. Ultrastructural observations and growth of occluding crystals in carious dentine. Acta Biomaterialia 2008;4(5):1427-39.

6.1 Abstract

Objective: The aim of the present study was to investigate the ultrastructural mechanisms involved in the formation of caries-induced intratubular dentine.

Methods: Conventional, high resolution and scanning transmission electron microscopy, electron diffraction and energy-dispersive X-ray spectroscopy techniques were used to study the ultrastructure of the inorganic phase in the transparent zone of carious dentine.

Results: The results demonstrated that the bulk of the inorganic phase in caries-induced intratubular dentine had an apatite crystal structure with the presence of additional Mg-substituted β-TCP (β-tricalcium phosphate) phase in the carious region. The apatite phase of the polycrystalline material forming intratubular dentine was highly oriented, while Mg-substituted β-TCP phase observed in intratubular dentine did not demonstrate texture.

Conclusions: The study suggested the regulated biomineralization process during the formation of the apatite mineral phase of the intratubular dentine in caries transparent layer, whereas Mg β-TCP crystals, which were observed in the intratubular dentine were presumably formed purely via 'dissolution/precipitation' mechanism. The study demonstrated the importance of 'dissolution/precipitation' process and the growth

kinetics of Mg-substituted β-TCP crystals in understanding the process of formation of calcium-phosphate crystallites in carious intratubular dentine.

6.2 Introduction

Under the environmental stimuli such as caries attack, dentine and pulp react simultaneously as one dentine-pulp functional complex [1]. Due to the sensitivity of dentine-pulp complex, a caries lesion progressing in enamel can be generally detected by odontoblasts lining the outer surface of the dental pulp ahead of the lesion front reaching the DEJ. Upon the detection of caries, the dentine tubules are gradually occluded forming intratubular dentine [2, 3], which will reduce the progress of caries when the lesion reaches dentine [4]. This layer of occluded dentine tubules occurs within the sound dentine in caries affected teeth and it is called the 'transparent' layer. This specific region of carious dentine is called 'transparent' region because the deposited minerals inside the dentinal tubules match the refractive indices of dentine, thereby producing a transparent appearance in this region under transmission light microscope [5]. Controversially, in spite of the fact that the dentinal tubules are filled with crystal deposition, it has been shown that the transparent region is not the hardest area of carious dentine and it is part of the softened carious dentine [6]. Scanning electron microscopy coupled with energy dispersive X-ray spectroscopy showed that Ca/P ratios in sound and caries intertubular and peritubular dentine were consistent with that of hydroxyapatite, whereas, carious intratubular dentine demonstrated a Ca/P ratio lower than that of hydroxyapatite [7]. In addition to the apatite crystals forming the bulk of the mineral component of the carious region in intratubular dentine, the presence of Mg-substituted β-tricalcium phosphate (β-TCP) crystals [8, 9], whitlockite, was occasionally reported in carious dentine [10]. However, the electron-

diffraction analysis on age-induced intratubular dentine demonstrated no evidence of the presence of Mg-substituted β-TCP and confirmed that the majority of the intratubular mineral in transparent dentine is indeed apatite [11, 12].

In order to preserve tooth structure during cavity preparation prior to restoration of carious lesions, a new approach called 'minimum intervention' [13] has been recently introduced. This approach suggests that the entire caries should not be removed completely from deeper portions of the cavity, and better restoration outcome may be achieved if only the outer carious dentine is removed and the inner carious dentine is left intact [14]. From this point of view the ultrastructure and the mechanism of the formation of intratubular dentine is of particular interest as it directly influences the bond strength of restorative materials to caries affected dentine in the transparent zone. While apatite is practically insoluble ($-\ln K_{sp} = 58.6$ at $37^{\circ} C$) at physiological pH [15], whitlockite mineral is much less stable, which in turn will weaken the bond strength between the restorative materials and dentine, and therefore its formation is undesirable.

Calcium phosphates, namely in the form of biological apatite, are the essential components of biomineralized tissue. The process of mineralization in hard dental tissues has been studied for decades but molecular quantitative analysis of mineral formation has not entirely been understood and investigated [16]. It is believed that the mineralization of the dentine is modulated by protein molecules and cell-derived microstructures, e.g. matrix vesicles, cell debris etc. [17]. It has also been shown that intertubular circumpulpal dentine mineralization is induced by extracellular matrix, which contains both collagenic and non-collagenic components such as collagens 1, phosphorylated proteins, non-phosphorylated dentine sialoprotein, proteoglycans, GLA-protein and phospholipids. On the other hand, the peritubular dentine

development has been shown to be induced by extracellular matrix containing only non-collagenous components such as glycoproteins, proteoglycans, lipids, and serum proteins [18]. Even less is known about the ultrastructure of caries-induced intratubular dentine and mechanisms of its formation. It has been shown that calcium concentration in dentinal fluid of carious tooth is higher than that of sound tooth, whereas the concentration of magnesium is only slightly increased [19]. Loosely aggregated unmineralized collagen bundles have been detected in sound dentine inside the dentinal tubules through the middle and inner dentine and separated loose collagen fibrils were observed near DEJ [20]. But whether the intratubular dentine formation is a biologically regulated process or purely the result of physico-chemical mechanism still remains unknown [7, 21]. In general, the theory of crystal growth from a solution includes three main steps: (i) nucleation, which is the process of forming a stable nuclei of a new phase greater than a certain critical size; (ii) growth kinetics of the newly formed crystal; and (iii) crystal-ambient phase equilibrium which determines size and shape of the newly formed crystals [22-24].

The aim of the present study was to investigate the ultrastructure and chemical content of the inorganic phase of the caries-induced intratubular dentine using transmission electron microscopy (TEM), electron diffraction analytical methods and energy-dispersive X-ray spectroscopy (EDS) and discuss the results in terms of the kinetics of crystal growth to gain more qualitative and quantitative information on the formation mechanisms of the caries-induced intratubular dentine.

6.3 Materials and Methods

Human molar teeth (5 teeth) were extracted due to severe occlusal caries lesions and collected for this study according to the protocols approved by the Ethics Review Committee of Sydney South West Area Health Service, reference №X07-0217 &

07/RPAH/47 and by the Human Research Ethics Committee of the University of Sydney, reference №10541.

6.3.1 Scanning Electron Microscopy (SEM)

Backscattered electron (BSE) imaging has been shown to be a useful tool to distinguish differences in the degree of mineralization of biological tissues [25]. Secondary electron (SE) imaging was used to observe surface morphology of the specimen. Backscattered and secondary electron images were obtained from the tooth section using SEM Philips XL30 equipped with a solid-state backscattered electron detector. The SEM was operated in vacuum at 10 kV, 5 nm spot size and 11 mm working distance.

6.3.2 Conventional TEM, High Resolution TEM and Scanning TEM

The specimens were fixed in Modified Karnovsky's fixative in 0.2 M Sorenson's buffer titrated to pH 7.2 for 24 hours at 2°C and then rinsed several times with 0.2 M Sorenson's buffer, dehydrated in graded alcohols, infiltrated with the epoxy resin for 24 hours and then embedded into epoxy resin according to the protocol described in [26]. Thin, 80-nm-thick, sections were cut with a diamond knife (Diatome, Bienne, Switzerland) and mounted onto 200 mesh copper grids.

Conventional Transmission Electron Microscopy (TEM) observations, bright-field imaging and selected-area electron diffraction (SAED) were performed using a Philips CM12 operated at 120kV. Higher magnification and atomic resolution lattice imaging were performed in a JEOL 3000F operated at 300kV. Electron dispersive spectroscopy (EDS) was performed in a dedicated VGSTEM HB601 Scanning TEM (STEM). EDS was performed on five tubules in carious transparent layer of the

dentine. For each tubule five X-ray spectra were collected from interubular dentine and ten spectra from intratubular dentine. The preliminary statistical analysis of each recorded spectrum was completed by EDS software (Gatan Digital Micrograph). The data was presented in terms of average value and standard deviation of the concentration of a chemical element. Statistical differences between elemental content recorded for each tubule were examined using a two-tail unpaired t-test and the corresponding P-values > 0.10 were considered statistically not significant.

6.4 Results

The composite secondary electron (SE) and backscattered electron (BSE) imaging allowed us to observe both the fine topographical structure and the mineral distribution across the caries lesion of the mesio-distal tooth section [27]. Figure 6.1 reveals a carious affected layer of dentine, which appeared as a dark zone with the grey levels decreasing towards the cavity floor. Enamel is clearly visible as a bright area at the top of the micrograph (Figure 6.1, arrow a) compared with the underlying sound dentine (Figure 6.1, arrow b), which appeared as a darker area than enamel. Carious affected highly mineralized dentine (Figure 6.1, arrow c) represents the so called “transparent zone” of the carious dentine and is characterised by the extensive intratubular mineralization of dentine tubules due to caries attack [7]. Beyond the transparent zone, the demineralized area closer to the cavity floor (Figure 6.1, arrow d) appeared as a darker contrast tissue due to substantial loss of intertubular and peritubular mineral in the carious lesion.

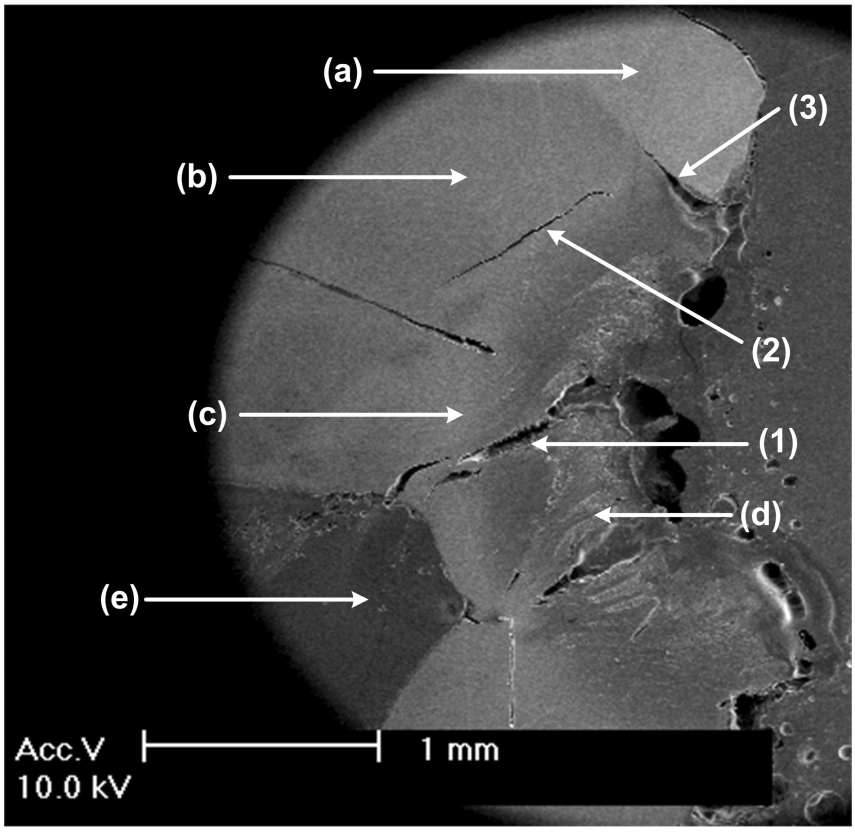

Figure 6.1 A composite (BSE + SE) SEM micrograph of a cross-section of a carious lesion of the tooth specimen. Enamel (a) looks brighter on the image due to higher mineral density than sound dentine (b). Higher mineralized transparent dentine (c) appeared as a light contrast tissue at the front of the dark contrast tissue representing demineralized carious dentine (d). (e) Pulp. (1), (2), (3) Cracks.

Cracks in dentine were clearly visible (Figure 6.1, arrows 1, 2 and 3) and appeared probably due to dehydration and collapse of the dentine tissue structure in the vacuum chamber of SEM. It should be noted that the observed cracks propagated either along the long axis of dentine tubules (Figure 6.1, arrow 1), or perpendicular to the demineralization front of the caries attack (Figure 6.1, arrow 2). The other visible crack propagated along the dentinal enamel junction (DEJ) (Figure 6.1, arrow 3).

Under TEM observation the dentine tubules were clearly identifiable when sections perpendicular to the long axis of the tubules were examined. Dentinal tubules (Figure 6.2A, arrow a) of $\sim 2\,\mu m$ diameter were partially occluded with intratubular mineral deposits (Figure 6.2A, arrow b). The mineral within the tubule lumens

(intratubular dentine) appeared to have darker contrast than that of the mineral between the tubules (intertubular dentine). It can also be noted that the intertubular dentine in the carious transparent zone has a highly inhomogeneous structure with dentine crystallites forming darker contrast lines clearly following the contour of tubules (Figure 6.2, arrows 1 and 2). Perforations in the intratubular dentine were visible and they are due to active caries attack [26] (Figure 6.2A, arrows c).

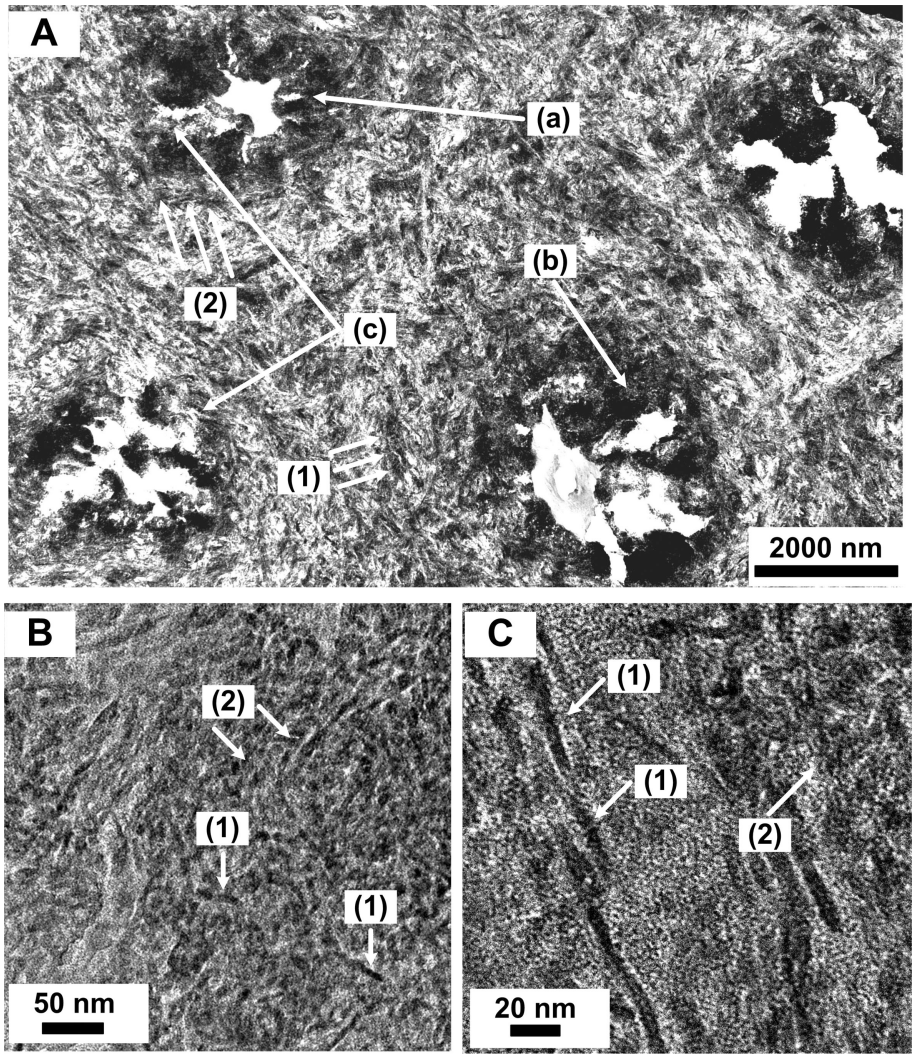

Figure 6.2 TEM micrographs of the transparent zone of carious dentine. A. Dentine tubules (a) filled with intratubular dentine (b) and surrounded by intertubular dentine. (c) Perforations in the intratubular dentine. B and C. Needle-like (1) and plate-like (2) crystallites.

Higher magnification HRTEM images of the intratubular dentine (Figures 6.2B and 6.2C) revealed two types of closely packed crystallite populations forming the bulk of the intratubular mineral: needle-like and plate-like crystallites. The size of the needle-like crystallites (Figures 6.2B and 6.2C, arrows 1) and plate-like crystallites (Figures 6.2B and 6.2C, arrows 2) were consistent with our previous observations [26] (Chapter 4). It should be noted that needle-like crystallites in intratubular dentine were highly oriented (Figure 6.2C, arrows 1).

High resolution TEM was performed on the intratubular dentine to investigate the ultrastructure of deposited minerals. Each focus series in HRTEM images (Figure 6.3) enabled differentiation of atomic columns within the crystals of the intratubular dentine in the transparent zone. It was clearly seen that the crystals comprised well defined single crystal grains sharing common direction and their lattice spacing (Figure 6.3, inserts a & b) matched those of hydroxyapatite [28]. The planes in both areas (a) and (b) (Figure 6.3) with $2.8\,\mathring{A}$ correspond to (211) and $2.7\,\mathring{A}$ correspond to (300) hydroxyapatite lattice planes, zone axis $\left[0\bar{1}1\right]$. The crystallites in the areas (a) and (b) in (Figure 6.3) were oriented in nearly the same direction with less than 7° orientation difference.

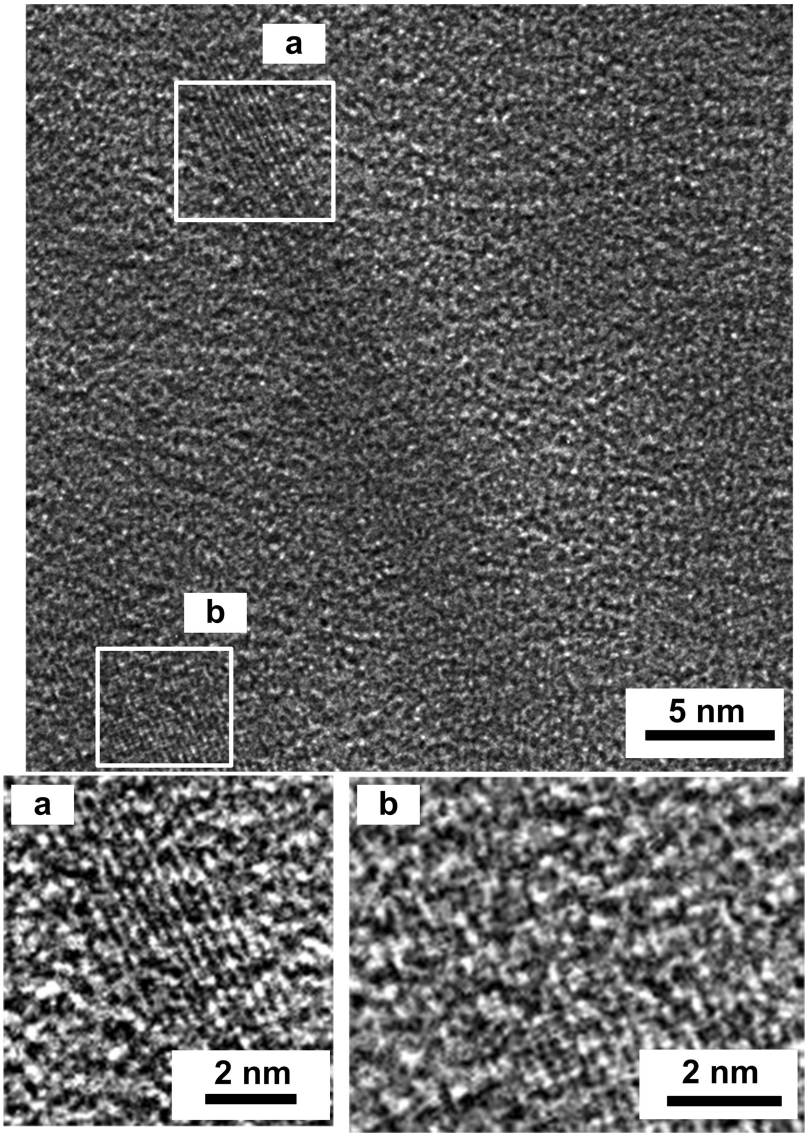

Figure 6.3 High-magnification HRTEM lattice micrographs of the intratubular mineral in the transparent zone. The enclosed regions (a) and (b) are magnified in the corresponding inserts (a) and (b). The regular periodic arrangement of the lattice fringes indicates that each mineral crystallite is oriented in the single direction.

Figure 6.4 shows HRTEM micrograph of intratubular dentine. Fast Fourier Transforms (FFTs) of the corresponding enclosed regions (a) and (b) demonstrated that the atomic spacings of $d_{002} = 3.4\,\mathring{A}$ in (Figure 6.4, enclosed region (a)) and $d_{300} = 2.7\,\mathring{A}$ in (Figure 6.4, enclosed region (b)) matched that of hydroxyapatite. Also the orientation of the patterns relative to each other is less than 1° and therefore the

crystallites in the Figure 6.4) (enclosed regions (a) and (b)) have the same orientation.

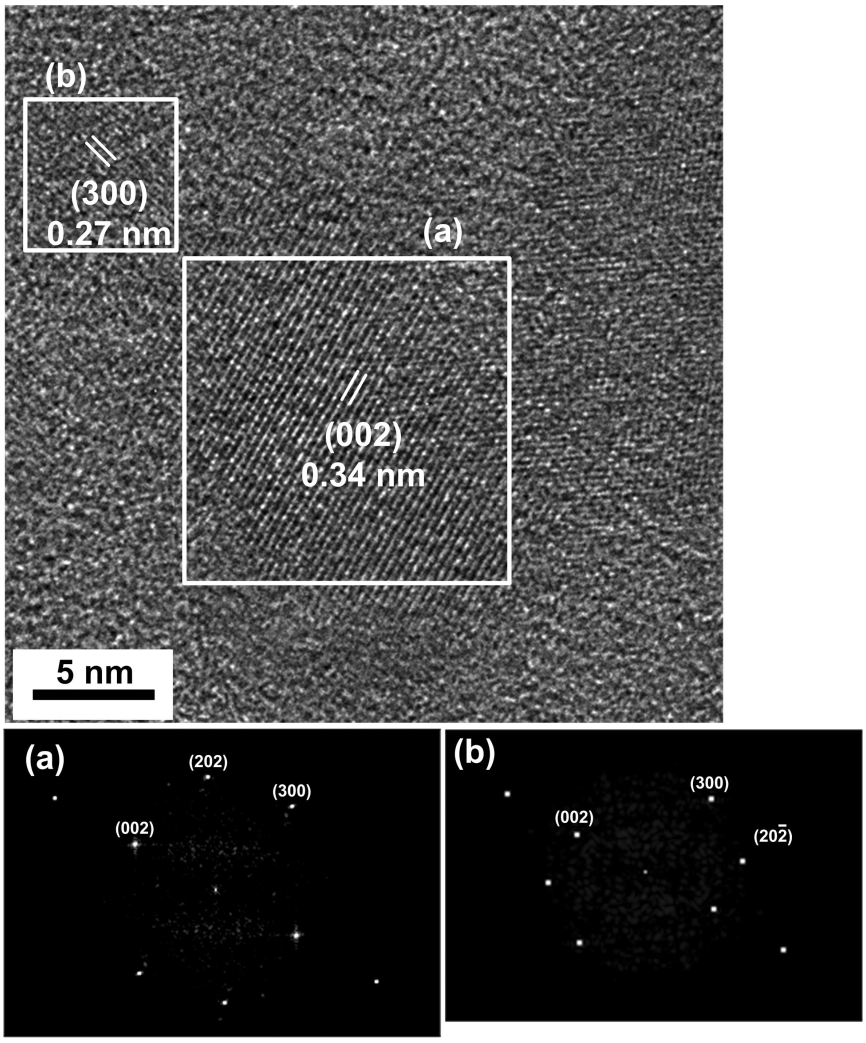

Figure 6.4 HRTEM image of the intratubular crystallites in the transparent zone showing nano-size single crystallite. FFTs of enclosed regions (a) and (b) show structure in [010] zone axis orientation.

Energy dispersive X-ray spectroscopy (EDS) was performed under STEM to compare the chemical composition of the intertubular and intratubular dentine in the carious transparent zone. The thickness of all specimens was about 80 nm so thin sample criterion was assumed (the effects of X-ray absorption and X-ray fluorescence were negligible).

Figure 6.5 shows EDS spectrum of the intratubular mineral in the transparent zone. The area selected for EDS analysis is clearly marked (Figure 6.5, rectangular

enclosed area (a) is magnified in insert (a)) and revealed individual needle-like and plate-like dentine crystallites forming the bulk of the intertubular dentine.

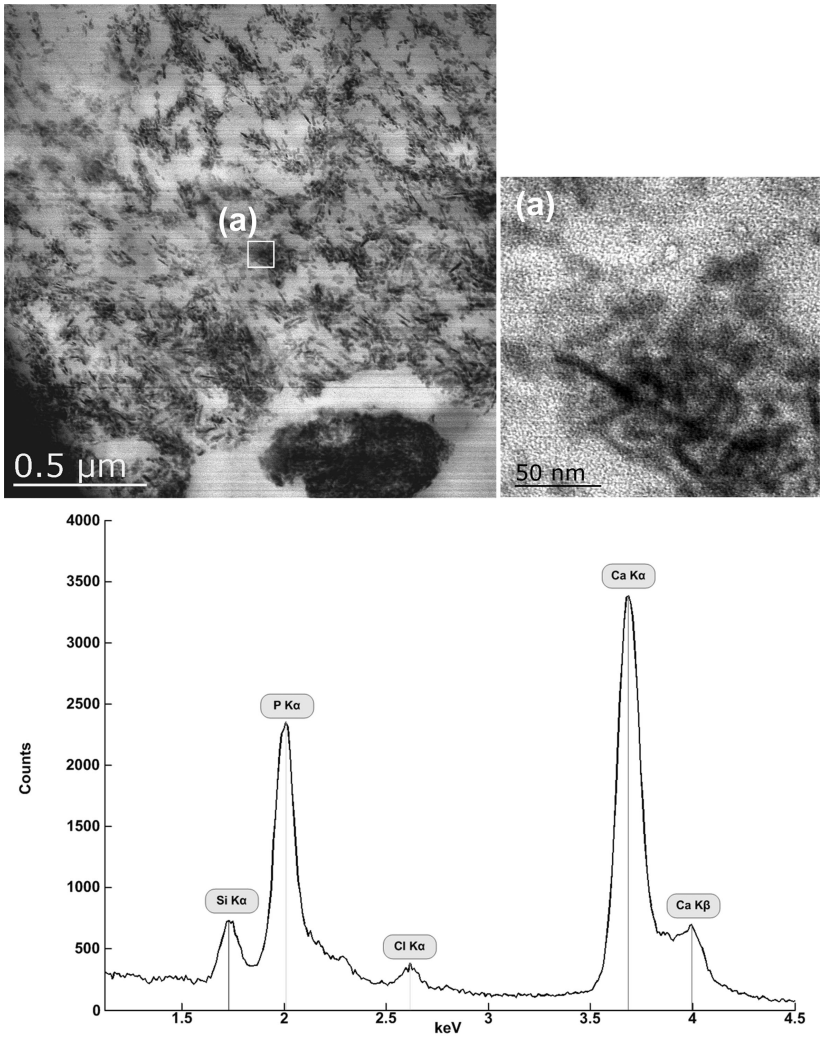

Figure 6.5 STEM micrograph of the intertubular crystallites in the carious transparent zone of dentine. Magnified enclosed region (a) shows the structure of intertubular dentine subject to EDS. (b) Voids in the structure of caries intertubular dentine.

X-ray spectrum of individual crystals forming intertubular dentine (Figure 6.5) revealed their chemical composition. Apart from the dominating Ca and P peaks, traces of Si and Cl were clearly detected. The results of these semi-quantitative measurements are summarised in (Table 6.1).

Table 6.1 Mean and standard deviations of elemental contents in intertubular and intratubular dentine in carious transparent zone. No statistical differences in elemental content were observed between the corresponding areas in the transparent layer of dentine (P > 0.10).

Element	Intertubular dentine in carious demineralised zone	Intratubular dentine in carious demineralised zone	
		Type 1	Type 2
	Mean ± SD	Mean ± SD	Mean ± SD
Ca, at%	52.57 ± 0.01	58.03 ± 0.01	52.19 ± 0.01
P, at%	37.27 ± 0.01	35.11 ± 0.01	41.66 ± 0.01
Mg, at%	0.00	4.19 ± 0.01	4.36 ± 0.01
Cl, at%	2.40 ± 0.01	0.28 ± 0.01	0.15 ± 0.01
Si, at%	7.77 ± 0.01	2.39 ± 0.01	1.65 ± 0.01
Ca/P	1.41	1.65	1.25
Ca/Mg	N/A	13.85	11.97
Mg/P	N/A	0.12	0.10

Observation of the intertubular dentine under STEM revealed that individual dentine crystallites in the transparent zone of carious dentine tended to align along their c-axis. These electron dense mineralized lines form a felt-like structure with the presence of large demineralized voids of about 200 nm in diameter (Figure 6.5, arrows (b)).

Figure 6.6A shows a dentine tubule surrounded by intertubular dentine. The line of dark contrast matter surrounding the perimeter of the tubule is the peritubular dentine. Perforations in the peritubular dentine were observed, which were likely due to carious acidic attack [26]. The tubules were partially occluded with light and dark contrast intratubular dentine, which reflects the different structure and composition between these two populations of crystals in intratubular dentine (Figure 6.6A, arrows (1) and (2)). Chemical elements of the light contrast crystals in intratubular dentine (Figure 6.6A, arrow (1)) were close to that of biological apatite (Table 6.1, Intratubular dentine: Type 1) while the chemical elements of the second population of crystals in intratubular dentine (Figure 6.6A, arrows (2)) was not apatitic (Table 6.1,

Intratubular dentine: Type 2) and therefore they are of particular interest. The approximate area selected for EDS analysis in the non-apatitic crystals (the second population of crystals) is marked with the arrow (a) in Figure 6.6A. That area is magnified (Figure 6.6B) and is shown as a rectangle marked with an arrow (a). Figure 6.6B revealed the presence of large individual rhombohedral dentine crystallites in intratubular dentine.

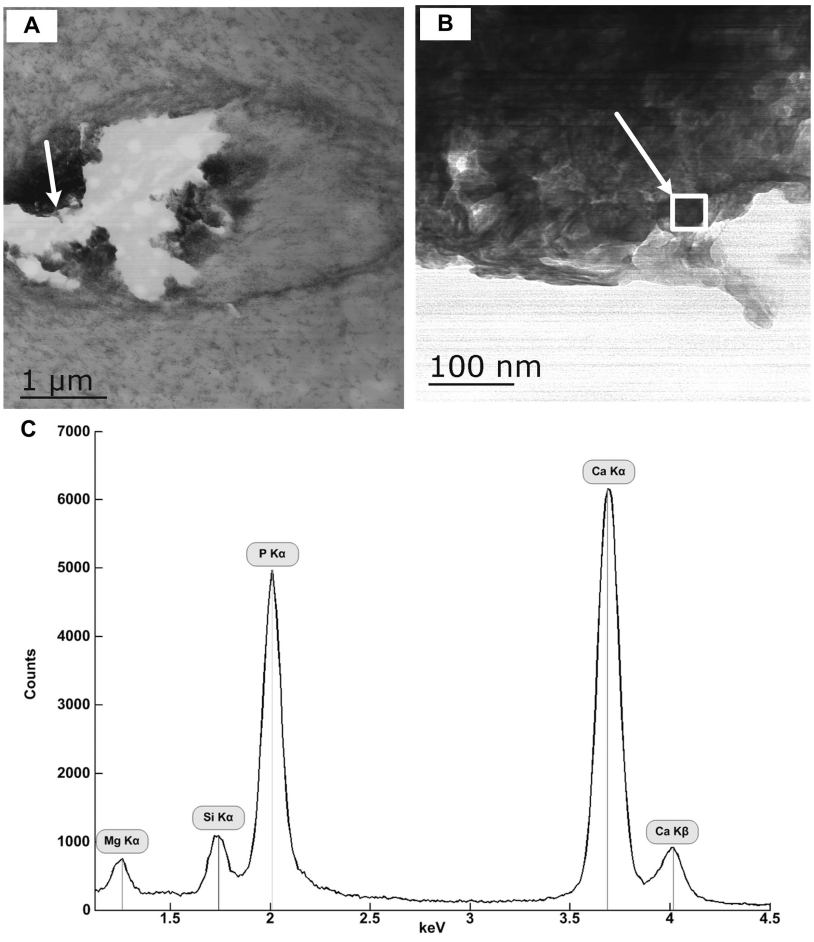

Figure 6.6 STEM micrograph of the intratubular dentine in the carious transparent zone. Magnified image of the area shown by the arrow (a), in micrograph (A), shows large closely packed crystals (B). Arrow (a) in the micrograph (B) points to enclosed region selected for EDS. EDS shows non-apatitic nature of the crystallites (C). (1) Type 1 crystallites and (2) type 2 crystallites.

X-ray spectrum of individual crystals forming the second population of crystals in intratubular dentine (Figure 6.6) revealed the chemical compositions of the

crystals. Apart from the dominant Ca and P peaks, traces of Mg and Si were clearly detected, and some evidence of Cl was also observed. The results of these semi-quantitative measurements are summarised in (Table 6.1).

The micrograph of carious dentine in transparent zone (Figure 6.7) shows a partly occluded tubule with intratubular deposits surrounded by demineralized intertubular dentine. Perforation in peritubular dentine was clearly visible. Figure 6.7 demonstrates three populations of dentine crystallites comprising intratubular dentine: needle-shaped, plate-shaped and large rhombohedral crystals deposited along the perimeter of the opening of the tubule. Selected area diffraction was performed to confirm the nature of the observed crystals.

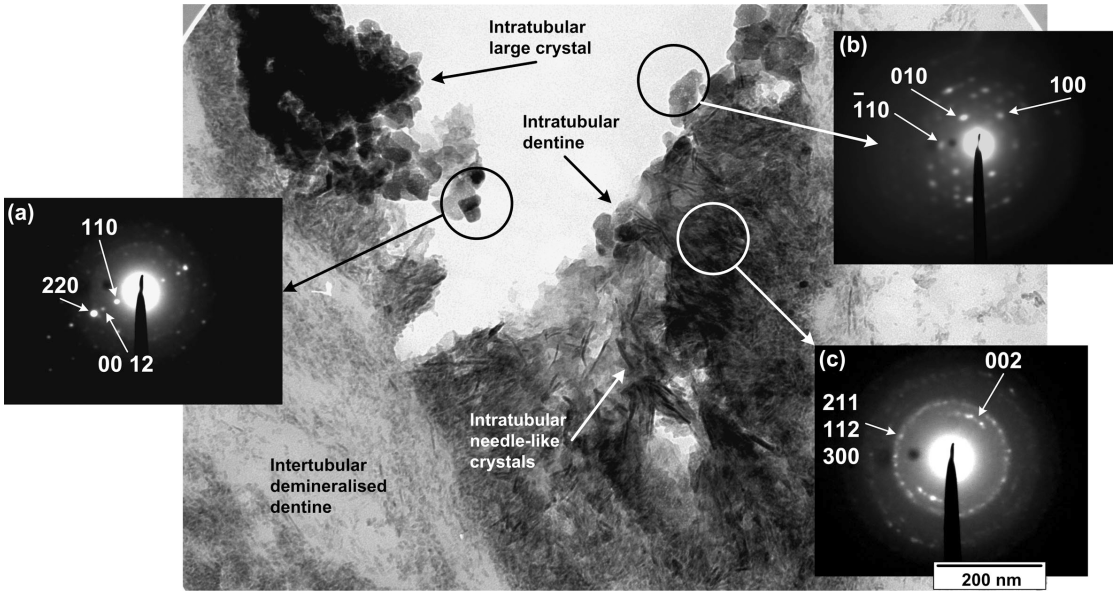

Figure 6.7 TEM micrograph of intratubular dentine in carious transparent zone. SAED spot patterns of large intratubular dentine crystals are shown in inserts (a) and (b) and correspond with Mg substituted biological whitlockite. SAED ring pattern of needle shaped crystallites in intratubular dentine correspond to biological apatite structure (c).

Inserts (a) and (b) in Figure 6.7 represent SAED patterns of the large

intratubular crystallites deposited at the perimeter of the tubule opening. The ring diffraction pattern indicated that the crystallites were oriented randomly forming a polycrystalline structure (Figure 6.7, insert (a)). SAED spot pattern presented in Figure 6.7 (insert (b)) was formed by superposition of several crystallites (encircled on this figure). The [001] zone axis of β phase of tricalcium phosphate (β-TCP) was identified for this diffraction pattern, corresponding to one of these crystallites. No evidence of preferred orientation of these crystallites has been detected. The distinct feature of the β-TCP diffraction pattern is that the interplanar space ratio between (00 12) and (220) crystal planes should be about 1.2 [29], which is the case for the obtained pattern (Figure 6.7, insert a). For β-TCP crystalline structure $(00\,12)=3.1\,\mathring{A}$ and $(220)=2.6\,\mathring{A}$.

In figure 6.7, insert c, SAED pattern of the intratubular needle- and plate-like crystallites deposited within the lumen of the tubule confirmed the presence of the apatite phase. The semi-circular pattern corresponding to (002) crystal planes indicate the preferred orientation of the apatite crystals in the intratubular caries induced dentine.

6.5 Discussion

6.5.1 Chemical elements of crystallites

SAED patterns of the intertubular dentine in the carious transparent zone demonstrated the apatitic nature of the crystalline structure in this region of dentine [30]. The analysis of the lattice parameters of the crystals in intratubular type 1 dentine (Figures 6.3 and 6.4) as well as SAED pattern of these crystals (Figure 6.7, insert (c)) demonstrated the apatitic nature of this population of crystals. Ca/P ratios obtained

from intertubular and intratubular type 1 crystals (Table 6.1) indicates the difference between chemical composition of these crystals and that of stoichiometric hydroxyapatite (HA) $Ca_{10}(PO_4)_6(OH)_2$. It has been reported that biological apatite crystals in intertubular dentine is calcium deficient and carbon rich HA [31] with substitution of $(CO_3)^{2-}$ for $(PO_4)^{3-}$ group leading to a lower Ca/P ratio than that of stoichiometric HA (1.67) [32] through the substitution of phosphate ions by silicate ($(SiO_4)^{4-}$ ions substituting $(PO_4)^{3-}$ yield the loss of OH^- ions) [33]. Si is another doping element, which is one of the essential trace elements associated with the properties of biological apatite and plays a role in the biochemistry of dentine [34] although this role has not yet been clearly understood [35]. It is believed however, that silicon is contributing to the architecture of the calcified tissues such as bone, enamel and dentine since it is a constituent element of some mucopolysaccharides [32]. Various hypotheses indicate that Si could be a cross-linking agent for acid mucopolysaccharides, collagen and elastin and therefore important for holding the organic matrix together in a structured way in connective tissues [32, 36, 37]. This indeed may be the reason that Si concentration detected in intertubular dentine is higher than in intratubular dentine and the presence of Si in intratubular dentine may be explained through diffusion of Si with acids from intertubular dentine through perforations in tubules walls and that Si may become free through breakdown of the collagen matrix in intertubular dentine during carious attack. It is however, a well established fact that Si can be introduced into HA structure through the substitution of phosphate ions by silicate ($(SiO_4)^{4-}$ ions substituting $(PO_4)^{3-}$ yielding the loss of OH^- ions) [36] in biological apatite, which cannot be ignored. And finally, ions of Cl^- replace OH^- ions forming chlorohydroxyapatite [32]. Therefore a general formula of the intertubular

dentine in caries transparent zone can be written as follows:

$$Ca_{10-\frac{x}{2}}\left(PO_4\right)_{6-x-y}\left(CO_3\right)_x\left(SiO_4\right)_y\left(OH\right)_{2-y-z}Cl_z \qquad (6.1)$$

Considering the percentages of the above chemical elements measured using EDS (Table 6.1) and assuming that all Ca, Si and Cl participate in the crystalline structure of apatite we can estimate the coefficients in the structural formula (6.1) of apatite: $Ca_{9.5}\left(PO_4\right)_{3.6}\left(CO_3\right)\left(SiO_4\right)_{1.4}\left(OH\right)_{0.2}Cl_{0.4}$. It should be noted that in this model only ~53% of P formed crystalline structure and the remaining ~47% may have come from organic structure of intertubular dentine and the assumption that 100% of Si participates in the crystalline structure may be arguable due to the possible participation of Si in the formation of the organic matrix of interubular dentine.

The results of our EDS analysis (Table 6.1) showed, in spite of the presence of Mg in the apatitic crystal population (type 1) of intratubular dentine, Ca/P ratio of these crystals was close to that of stoichiometric HA. Traces of Mg are always present in the dentinal fluid [19] and it can be incorporated into HA structure (Mg for Ca substitution). Mg is isoelectronic with Ca and it does not provoke any unbalance of charge in the related crystallographic site [34]. Given the noticeable amount of Si and some traces of Cl, the general formula of the intratubular dentine (type 1) can be written as follows:

$$Ca_{10-q}Mg_q\left(PO_4\right)_{6-y}\left(SiO_4\right)_y\left(OH\right)_{2-y-z}Cl_z \qquad (6.2)$$

Assuming that Ca, Mg, Si and Cl ions all participate in the crystalline structure of apatite, and given the percentage of these elements measured (Table 6.1), the structural formula of apatite in the type 1 intratubular dentine was in the form of $Ca_{9.33}Mg_{0.67}\left(PO_4\right)_{5.63}\left(SiO_4\right)_{0.37}\left(OH\right)_{1.59}Cl_{0.04}$.

The results of the elemental composition of the second population of crystals

in intratubular dentine (type 2) indicated that not only the percentage of Mg was slightly higher in these crystal population but also the Ca/P ratio was much lower than that of the pure HA (Table 6.1), revealing the difference in the nature of these crystals and that of the apatitic crystal population. Based on SAED patterns (Figure 6.7, inserts a and b), the observed crystallites should be Mg β-TCP $Ca_{3-q}Mg_q(PO_4)_2$ [9]. Considering the noticeable presence of Si and negligible amount of Cl, the general formula of the intratubular type 2 carious dentine in the transparent zone can be written as following:

$$Ca_{3-q}Mg_q(PO_4)_{2-\frac{4}{3}y}(SiO_4)_y \tag{6.3}$$

Assuming that 100% of Ca, Mg and Si are participating in the crystallite structure then based on the Ca/Mg stoichiometric ratio driven from Table 6.1 the second population of crystals in intertubular dentine was in the form of Mg β-TCP doped with traces of silicate: $Ca_{2.77}Mg_{0.23}(PO_4)_{1.88}(SiO_4)_{0.09}$. It should be noted that only ~85% of P formed crystallite structure and the remaining ~15% of P may have come from phosphate amorphous structure and organic molecules found in dentinal tubules, e.g. in the form of phosphoproteins [38].

6.5.2 Nucleation

Pathological caries-induced transparency in dentine was detected through the observation of the deposits in intratubular dentine obliterating dentinal tubules (Figure 6.2A), which is a natural defense mechanism against caries attack and serves the purpose of preventing toxins, acids and cariogenic bacteria from penetrating deeper into tooth and reaching pulp [39]. The bulk of the observed intratubular dentine was plate-like and needle-like crystallites (Figures 6.1B and 6.1C), similar to the apatite

crystallites found in bone [40]. The direct measurement of the atomic spacings of these crystallites confirmed that these crystals were apatite. The apatitic intratubular crystals were highly oriented not only at the nanoscale (Figures 6.3 and 6.4) but at the microscale as well (Figure 6.7, insert c), which indicates the biologically regulated mineral formation of the intratubular dentine. It has been shown that during biomineralization carboxyl groups of non-collagenous proteins (NCP) not only can serve the purpose of nucleation sites but also have the ability to nucleate crystals on the (001) crystal face thus orienting the c-axis of the crystal in a controlled direction [41-44]. NCPs can also modulate the growth and final shape of the apatitic crystals during the biomineralization process because of binding to the surfaces of the growing crystal and thus inhibiting the crystal growth in that particular direction producing apatite crystals of various shapes: needle- and plate-like crystals. It has been shown that when NCP is not present during the formation of apatite crystals, the final shape of mature crystals will be block-like instead of needle- or plate-like shapes [45, 46]. Preferred orientation of the crystals is not the sole indication of the bio-regulated mineralization in intratubular dentine. Direct observation of needle- and plate-like apatite crystallites suggested that these crystallites were indeed formed as part of the biologically regulated mineralization process activated as a part of the tooth defense mechanism against caries attack and not just part of a purely physicochemical reaction. EDTA- and HCl-soluble phosphoproteins were isolated in dentine [47-49] and it was shown that they could be the sites for initial nucleation of apatite crystals [50] (assisting nucleation from low supersaturated solution). From this perspective it was of particular interest to observe, not only the apatitic phase of the intratubular dentine (type 1 intratubular dentine), but also foreign (non-apatitic) type of crystallites (type 2 intratubular dentine), (Figures 6.6A and 6.7, inserts a and b), namely whitlockite.

Whitlockite (Mg β-TCP) however, can form directly from solutions or from gel-systems when the Mg/Ca stoichiometric ratio exceeds 0.1 with the more favorable formation in acidic conditions [51]. There is no evidence so far that whitlockite forms as part of bio-regulated mineralization. Our experimental results (Table 6.1) show that this ratio is just slightly below 0.1, which suggests that the growth of the Mg β-TCP crystals has finished and the size and the shape of the crystals formed from the solution is now in thermodynamic equilibrium with the ambient phase, which in turn can provide insight on the kinetics of the growth of these crystals.

6.5.3 Growth kinetics of Mg β-TCP crystals

The growth rate of a crystal depends on whether it occurs below or above the critical point called the 'roughening' temperature [52], T_R. At temperatures below the critical point the surface of the crystal is atomically smooth and above the critical point the surface transforms into atomically rough surface [53]. An analysis of this critical phenomena gives [54]:

$$T_R = \frac{2}{\pi}\frac{\alpha d^2}{k} \tag{6.4}$$

Where α is the specific energy of the step-riser per unit surface of the riser, d is the distance between the atomic planes parallel to the surface in question and k is the Boltzmann's constant. The lattice parameters for Mg β-TCP $Ca_{3-x}Mg_x(PO_4)_2$, $x=0.11$ is given [9] by $a=b=10.400\,\text{Å}$ and $c=37.315\,\text{Å}$. To estimate the lowest roughening temperature for the Mg β-TCP crystal faces we take the smallest lattice parameter of $10.400\,\text{Å}$ and TCP surface energy in water [55] $\alpha \approx 44.0\frac{\text{mJ}}{\text{m}^2}$. Then from

the Eq. (6.4) we get $T_R \approx 2195\,\mathrm{K}$ which is approximately the TCP melting point of 2073K [8]. Thus the surface of Mg β-TCP crystals in solutions must be atomically smooth and therefore grow by successive deposition of layers through two-dimensional nucleation.

Generally both volume and coupled surface types of diffusion contribute to the growth of a crystal by successive deposition of layers. However, it has been shown that for steps higher than a certain critical value the volume diffusion (direct integration of growth units from the mother phase) dominates the surface diffusion (indirect incorporation via the surface between steps). The criteria for the volume mechanism to dominate in crystal growth reads [56]:

$$h \geq a_0 \cdot e^{\frac{\Delta H_{se} - \Delta H_{ve}}{RT}} \tag{6.5}$$

Where h is the height of the step, a_0 is the surface diffusion jump distance, ΔH_{se} and ΔH_{ve} are activation enthalpies for growth units to enter the step edge from the surface and from the volume respectively, R is the gas constant.

Let's assume that the velocity of the fluid vanishes at the crystal surface forming a so-called stagnant layer. The thickness of a stagnant layer may be calculated [57]:

$$\delta \approx 5\sqrt{\frac{x\eta}{v\rho}} \tag{6.6}$$

Where, x, is the distance from the leading edge of the crystal, η, is the dynamic viscosity of the fluid, v, is the tangential velocity of the fluid relative to the surface of the crystal and ρ, is the density of the fluid. For aqueous solutions at body temperature $\eta = 10^{-3}\,\frac{\mathrm{kg}}{\mathrm{m}\cdot\mathrm{s}}$, $v = 0.4\,\frac{\mathrm{m}}{\mathrm{s}}$, $\rho = 10^{3}\,\frac{\mathrm{kg}}{\mathrm{m}^3}$ and $x \sim 10^{-8}\,\mathrm{m}$ as the sizes of the

crystals observed are of the order of 10 nm in all directions (Figure 6.7), then from the Eq. (6.6) the thickness of the stagnant layer is $\delta = 7.91 \cdot 10^{-7}$ m (Figure 6.8). Also we assume that the diffusion coefficient $D \sim 10^{-9} \frac{\text{m}^2}{\text{s}}$ and the rate of advance of a train of parallel steps on the crystal planes is much less than $\frac{D}{\delta} \sim 10^{-3} \frac{\text{m}}{\text{s}}$ and can be neglected.

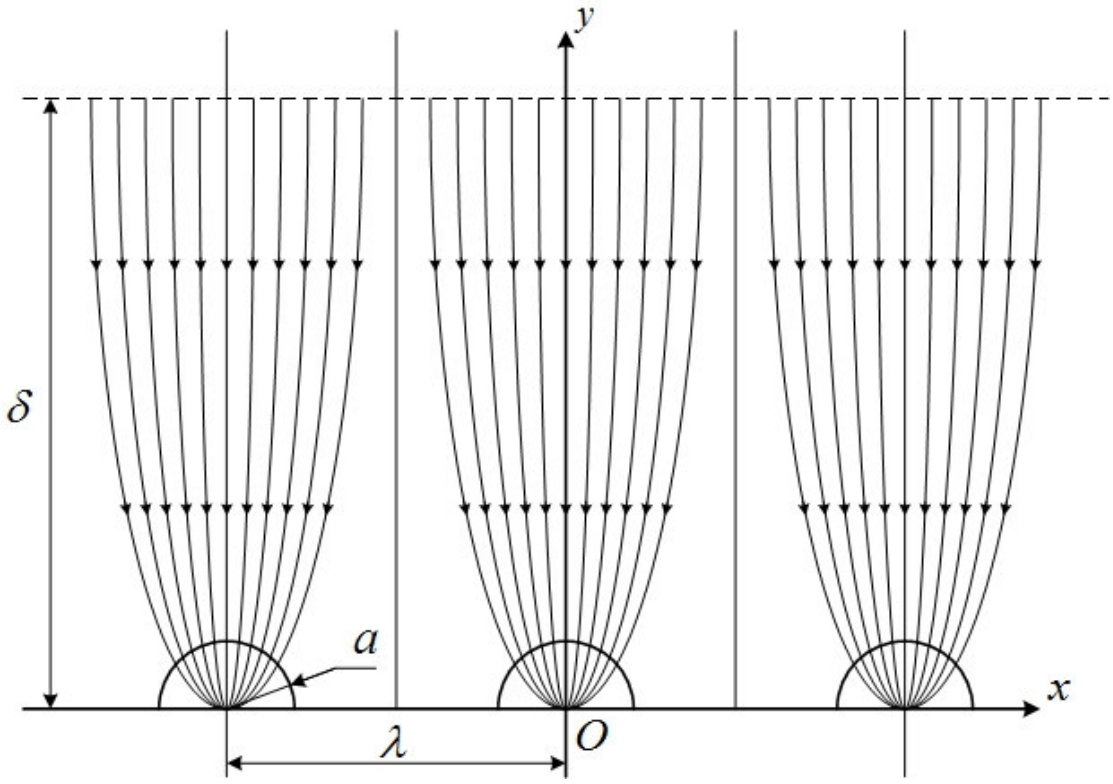

Figure 6.8 A net flux of growth units from solution through a diffusion boundary layer of thickness δ to the crystal surface is shown. A train of parallel steps approximated with semi-cylinders of radii a along the x direction are spaced at an average distance λ.

Then the concentration of the crystal building units in the solution obeys the system of equations [58]:

$$\begin{cases} \Delta c = 0, r > a \\ D\dfrac{\partial c}{\partial r} = \beta\left(c - c_{st}\right), r = a \end{cases} \tag{6.7}$$

Where Δ is the Laplace operator, c_{st} is the concentration at the step, and β is the kinetic coefficient, i.e. the rate of crystallization characterizing the exchange rate between the step and the solution.

The solution for the Eqs. (6.7) with boundary condition $c(0,\delta)=c_\delta, y=\delta$ for $-\frac{\lambda}{2}\le x\le\frac{\lambda}{2}$, $x^2+y^2\ge a^2$ and $y>0$ (Figure 6.8) was found in [58]. Then the rate of advance of the train of steps can be calculated $v=\pi\Omega\beta(c-c_e)$ and the growth rates of the crystal face:

$$V=\frac{a}{\lambda}v=\frac{\pi a\beta c_e kT}{19\alpha}\frac{\sigma^2}{1+\frac{\beta a}{D}\ln\frac{\sigma_c\delta}{\sigma a}\sinh\frac{\sigma}{\sigma_c}} \tag{6.8}$$

Where λ is the distance between two successive turns of the screw dislocation in crystal, $\lambda\cong 19\rho_c$ [59], ρ_c is the critical radius of the two dimensional nucleus on a crystal face, $\rho_c=\frac{\Omega\alpha}{kT\sigma}$ (calculated from Herring formula [60, 61] assuming that the specific free energy α is isotropic on the crystal face), Ω is the specific volume of one molecule in the crystal, $\sigma=\frac{c_\delta-c_e}{c_e}$ is the degree of supersaturation, and $\sigma_c=\frac{19\Omega\alpha}{\pi kT\delta}$ is the critical supersaturation condition. When the supersaturation is less than the critical supersaturation, the spiral steps are far enough from each other $(\pi\delta<<\lambda)$ and the diffusion concentration fields do not overlap. With the supersaturation close to and higher than the critical supersaturation, the diffusion concentration fields start to overlap slowing down the growth rate of the crystal face.

The empirical expression for the specific free surface energy of ionic crystals of electrolytes in aqueous solutions [62]:

$$\alpha = -18.3 \ln c_e + 34.5 \tag{6.9}$$

Where $c_e \left[\frac{\text{mol}}{\text{l}} \right]$ is the concentration of a saturated solution in equilibrium with the crystal and α is expressed in $\left[\frac{\text{mJ}}{\text{m}^2} \right]$. As discussed in [54] the empirical formula (6.9) does not take into account the anisotropy of surface energy and the empirical constants in the equation were calculated from the data on the heterogeneous nucleation of crystals in solutions, which leads to an underestimation of the free surface energy. However, we can use the Eq. (6.9) to estimate the average equilibrium concentration of a saturated solution above Mg β-TCP crystal faces and substituting $\alpha \approx 44.0 \frac{\text{mJ}}{\text{m}^2}$ [55], we obtain: $c_e \approx 6.59 \cdot e^{-\frac{\alpha}{18.3}} \approx 0.59 \frac{\text{mol}}{\text{l}} = 3.55 \cdot 10^{26}\ \text{m}^{-3}$.

The specific volume of one molecule $Ca_2 Mg\left(PO_4\right)_3$ (Figure 6.9) is estimated as $\Omega = 1.33 \cdot 10^{-28}\ \text{m}^3$ and taking $\alpha = 44 \frac{\text{mJ}}{\text{m}^2}$, $T = 310\,\text{K}$, $\delta = 7.91 \cdot 10^{-7}\ \text{m}$ and $\beta \cdot a \approx D = 10^{-7} \frac{\text{m}^2}{\text{s}}$ we obtain $\sigma_c = 1.05 \cdot 10^{-2}$ and with a maximum at approximately $\sigma = 2.3 \cdot 10^{-2}$ the theoretical maximum of the crystal growth rate is $V = 1.12 \cdot 10^{-7} \frac{\text{m}}{\text{s}}$ (Figure 6.10). With low supersaturation, $\sigma << \sigma_c$, $V \approx \frac{\pi}{19} \frac{\beta a c_e k T}{\alpha} \sigma^2$. The average growth rate for the values of $\sigma \le \sigma_c$ from the Eq. (6.8): $\langle V \rangle = 7.2 \cdot 10^{-8} \frac{\text{m}}{\text{s}}$. The size of the observed Mg β-TCP crystals (Figures 6.6B and 6.7) is approximately 20 x 40 nm and we can conclude that the crystals may have formed in the order of $10^{-1}\,\text{s}$.

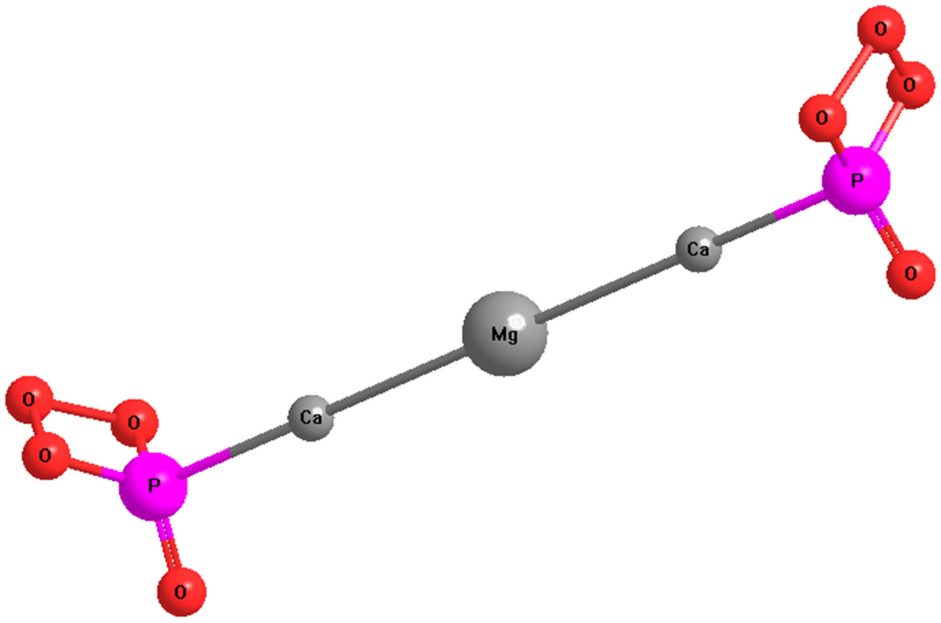

Figure 6.9 Model used to estimate the specific volume of one molecule of Mg β-TCP $Ca_2\,Mg\left(PO_4\right)_2$**. Mg-Ca links – 3.48** $\mathring{A}$**, Ca-P links – 2.83** $\mathring{A}$**, P=O links - 1.49** $\mathring{A}$**, P-O links – 2.18** $\mathring{A}$**, O-O links – 1.63** $\mathring{A}$**, Ca-P=O link -** 99.1°**, Ca-P-O$_3$ link –** 114.1°**.**

In this regard it is particularly interesting to note that the concentration of chlorine in the intertubular dentine was an order of magnitude higher than that in intratubular dentine (Table 6.1). Figure 6.5, arrows (b) demonstrated that intertubular dentine is a highly porous structure with pores of about 200 nm. This suggests that chlorine may have diffused into transparent dentine zone together with acids produced by bacteria through the cavity floor and outer dentine layer. Intertubular dentine is a much higher permeable media than intratubular dentine and as discussed previously in [30] this model can explain the reduced mechanical properties of caries-induced transparent dentine. The presence of traces of chlorine in the intratubular dentine suggests that small drops of acidic solution supersaturated with calcium phosphates penetrated through the perforations and dissolved lateral branches into the tubules from intertubular dentine and then came in contact with dentinal fluid (characterized

as being similar to human plasma [31]), which contains magnesium [63]. Such environment is favorable for nucleation and growth of Mg β-TCP crystals [51].

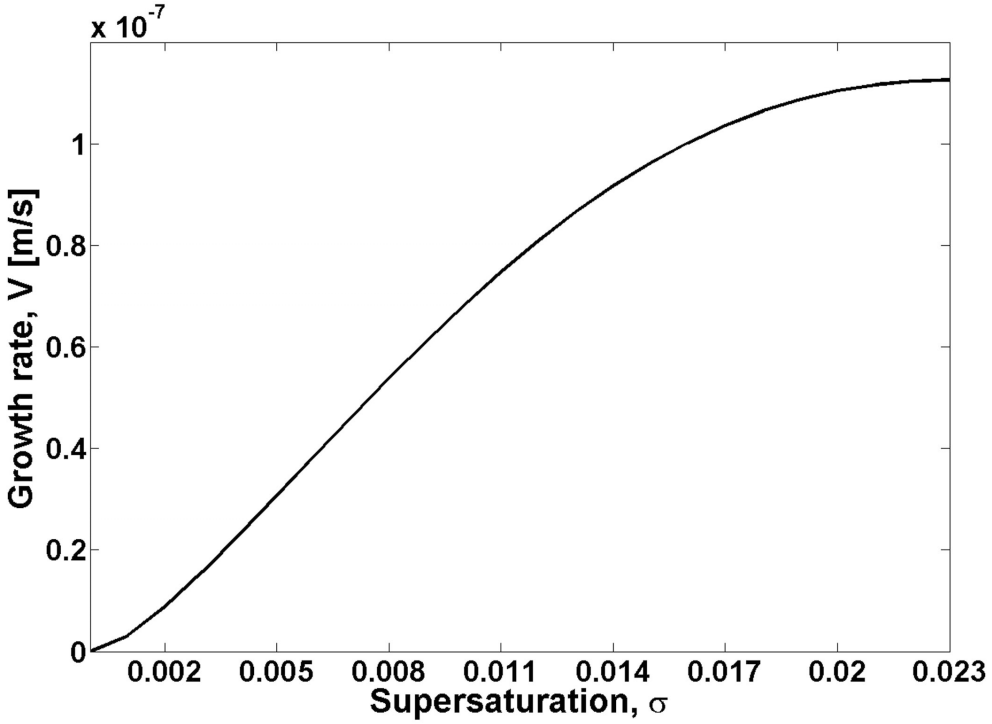

Figure 6.10 Growth rate of crystal face as a function of supersaturation. With low supersaturation $\sigma << \sigma_c$ the growth rate $V \sim \sigma^2$.

6.6 Conclusions

Based on the presented ultrastructural study of the mineral phase of caries induced transparent dentine, the following conclusions can be drawn:

1. The majority of the intratubular dentine crystals deposited within the lumens of the tubules in the carious transparent zone were needle- and plate-like apatite.
2. Highly orientated apatite crystallites in intratubular dentine suggested a bio-regulated mineralization process in the formation of intratubular dentine.

3. Minor presence of Mg-substituted β-TCP crystals (whitlockite) was observed in caries-induced intratubular dentine.
4. Polycrystalline nature of the Mg-substituted β-TCP crystals observed suggested that the formation of this mineral was purely due to the mechanism of dissolution of intertubular dentine followed by the precipitation of Mg-substituted β-TCP crystals within the tubule lumens in acidic conditions and in the presence of Mg. The presence of whitlockite and therefore the conditions that favor its formation may have a crucial role in caries decay. Whitlockite has a higher solubility than apatite, thus this type of calcium phosphate crystallites is less resistant than apatite to caries challenge.
5. Direct observation of the Mg-substituted β-TCP crystallites partly forming carious induced intratubular dentine coupled with volume diffusion mechanism and in conjunction with layer-spiral growth theory allowed us to calculate the growth kinetics of Mg β-TCP crystals. Rapid formation (within 1 second) of Mg β-TCP crystallites in the caries transparent zone was demonstrated.

6.7 References

1. Lee Y.-L., Liu J., Clarkson B.H., Lin C.-P., Godovikova V., Ritchie H.H. Dentin-Pulp Complex Responses to Carious Lesions. Caries Research 2006;40(3):256-64.
2. Bjørndal L., Thylstrup A. A structural analysis of approximal enamel caries lesions and subjacent dentin reactions. European journal of oral sciences 1995;103(1):25-31.
3. Johnson N.W., Taylor B.R., Berman D.S. The Response of Deciduous Dentine to Caries Studied by Correlated Light and Electron Microscopy. Caries Research 1969;3:348-68.
4. Bjørndal L., Mjör I.A. Pulp-dentin biology in restorative dentistry. Part 4: Dental caries – characteristics of lesions and pulpal reactions. Quintessence International 2001;32(9):717-36.

5. Weber D.F. Human dentine sclerosis: A microradiographic survey. Archives of Oral Biology 1974;19(2):163.
6. Ogawa K., Yamashita Y., Ichijo T., Fusayama T. The ultrastructure and hardness of the transparent layer of human carious dentin. Journal of Dental Research 1983;62:7-10.
7. Arnold W.H., Kanopka S., Gaengler P. Qualitative and quantitative assessment of intratubular dentin formation in human natural carious lesions. Calcified Tissue International 2001;69(5):268-73.
8. Dickens B., Schroeder L.W., Brown W.E. Crystallographic studies of the role of Mg as a stabilizing impurity in β-Ca3(PO4)2. The crystal structure of pure β-Ca3(PO4)2. Journal of Solid State Chemistry 1974;10(3):232.
9. Schroeder L.W., Dickens B., Brown W.E. Crystallographic studies of the role of Mg as a stabilizing impurity in β-Ca3(PO4)2. II. Refinement of Mg-containing β-Ca3(PO4)2. Journal of Solid State Chemistry 1977;22(3):253-62.
10. Daculsi G., LeGeros R.Z., Jean A., Kerebel B. Possible physico-chemical processes in human dentin caries. Journal of Dental Research 1987;66:1356-59.
11. Porter A.E., Nalla R.K., Minor A., Jinschek J.R., Kisielowski C., Radmilovic V., et al. A transmission electron microscopy study of mineralization in age-induced transparent dentin. Biomaterials 2005;26:7650-60.
12. Nalla R.K., Porter A.E., Daraio C, Minor A.M., Radmilovic V., Stach E.A., et al. Ultrastructural examination of dentin using focused ion-beam cross-sectioning and transmission electron microscopy. Micron 2005;36(7-8):672-80.
13. Tyas M.J., Anusavice K.J., Frencken J.E., Mount G.J. Minimal intervention dentistry - a review. International Dental Journal 2000;50:1-12.
14. Fusayama T. Two Layers of Carious Dentin: Diagnosis and Treatment. Operational Dentistry 1979;4:63-70.
15. Grover L.M., Gbureck U., Young A.M., Wright A.J., Barralet J.E. Temperature dependent setting kinetics and mechanical properties of β-TCP–pyrophosphoric acid bone cement. Journal of Materials Chemistry 2005;15:4955–62.
16. Chernov A.A., Rashkovich L.N., Vekilov P.G. Steps in solution growth: dynamics of kinks, bunching and turbulence. Journal of Crystal Growth 2005;275(1-2):1-18.
17. Arana-Chavez V.E., Massa L.F. Odontoblasts: the cells forming and maintaining dentine. The International Journal of Biochemistry & Cell Biology 2004;36(8):1367-73.
18. Goldberg M., Septier D., Lécolle S., Chardin H., Quintana M.A., Acevedo A.C., et al. Dental mineralization. International Journal of Developmental Biology 1995;39:93.
19. Larmas M. Odontoblast function seen as the response of dentinal tissue to dental caries. Advances in Dental Research 2001;15:68-71.
20. Dai X.F., Ten Cate A.R., Limeback H. The extent and distribution of intratubular collagen fibrils in human dentine. Archives of Oral Biology 1991;36(10):775-78.
21. Arnold W.H., Konopka S., Kriwalsky M.S., Gaengler P. Morphological analysis and chemical content of natural dentin carious lesion zones. Annals of Anatomy - Anatomischer Anzeiger 2003;185(5):419-24.

22. Markov I.V. Crystal Growth for Beginners. Singapore: World Scientific; 1995.
23. Landau L.D., Lifshitz E.M. Statistical Physics (Part 1). 3rd ed. Oxford: Butterworth-Heinenann Ltd; 1980.
24. Landau L.D., Lifshitz E.M. Physical Kinetics. Oxford: Butterworth-Heinenann Ltd; 1981.
25. Angker L., Nockolds C., Swain M.V., Kilpatrick N. Quantitative analysis of the mineral content of sound and carious primary dentine using BSE imaging. Archives of Oral Biology 2004;49(2):99-107.
26. Zavgorodniy A.V., Rohanizadeh R., Swain M.V. Ultrastructure of Dentine Carious Lesions. Archives of Oral Biology 2008;53:124-32.
27. Angker L., Nockolds C., Swain M.V., Kilpatrick N. Correlating the mechanical properties to the mineral content of carious dentine—a comparative study using an ultra-micro indentation system (UMIS) and SEM-BSE signals. Archives of Oral Biology 2004;49(5):369-78.
28. International Centre for Diffraction Data. Powder Diffraction File 09-0432; 2005.
29. International Centre for Diffraction Data. Powder Diffraction File 09-0169; 2005.
30. Zavgorodniy A.V., Rohanizadeh R., Swain M.V. Ultrastructure of Dentine Carious Lesions. Archives of Oral Biology 2007.
31. Marshall Jr. G.W., Marshall S.J., Kinney J.H., Balooch M. The dentin substrate: structure and properties related to bonding. Journal of Dentistry 1997;25(6):441-58.
32. Driessens F.C.M., Verbeek R.M.H. Biominerals. Boca Raton: CRC Press; 1990.
33. Gibson I.R., Best S.M., Bonfield W. Chemical characterization of silicon-substituted hydroxyapatite. Journal of Biomedical Materials Research 1999;44(4):422-28.
34. Sprio S., Tampieri A., Landi E., Sandri M., Martorana S., Celotti G., et al. Physico-chemical properties and solubility behaviour of multi-substituted hydroxyapatite powders containing silicon. Materials Science and Engineering: C 2006.
35. Saito T., Toyooka H, Ito S., Crenshaw M.A. In vitro Study of Remineralization of Dentin: Effects of Ions on Mineral Induction by Decalcified Dentin Matrix. Caries Research 2003;37(6):445-49.
36. Sprio S., Tampieri A., Landi E., Sandri M., Martorana S., Celotti G., et al. Physico-chemical properties and solubility behaviour of multi-substituted hydroxyapatite powders containing silicon. Materials Science and Engineering: C 2008;28(1):179-87.
37. Van Rensburg B.G.J. Oral Biology. Chicago: Quintessence Publishing Co, Inc; 1995.
38. Linde A. Noncollagenous Proteins and Proteoglycans in Dentinogenesis. In: Linde A., editor. Dentin and Dentinogenesis. Boca Raton, Fl: CRC Press, Inc.; 2000. p. 55-92.
39. Arnold W.H., Sonkol T., Zoellner A., Gaengler P. Comparative Study of In Vitro Caries-Like Lesions and Natural Caries Lesions at Crown Margins. Journal of Prosthodontics 2007;16(6):445-51.
40. Cuisinier F., Bres E.F., Hemmerle J., Voegel J.-C., Frank R.M. Transmission electron microscopy of lattice planes in human alveolar bone apatite crystals. Calcified Tissue International 1987;40(6):332-38.

41. Butler W.T., Ritchie H. The nature and functional significance of dentin extracellular matrix proteins. The international journal of developmental biology 1995;39:169-79.
42. He G., Dahl T., Veis A., George A. Dentin Matrix Protein 1 Initiates Hydroxyapatite Formation In Vitro. Connective Tissue Research 2003;44(1 Supplement 1):240-45.
43. He G., Dahl T., Veis A., George A. Nucleation of apatite crystals in vitro by self-assembled dentin matrix protein 1. Nature Materials 2003;2:552-58.
44. He G., Ramachandran A., Dahl T., George S., Schultz D., Cookson D., et al. Phosphorylation of Phosphophoryn Is Crucial for Its Function as a Mediator of Biomineralization. Journal of Biological Chemistry 2005;280(39):33109-14.
45. Addadi L., Weiner S. Biomineralization : chemical and biochemical perspectives. New York: Weinheim; 1989.
46. Rohanizadeh R., Padrines M., Bouler J.M., Couchourel D., Fortun Y., Daculsi G. Apatite precipitation after incubation of biphasic calcium-phosphate ceramic in various solutions: Influence of seed species and proteins. Journal of Biomedical Material Research 1998;42(4):530-39.
47. Veis A., Perry A. The Phosphoprotein of the Dentin Matrix. Biochemistry 1967;6(8):2409-16.
48. Butler W.T., Finch J.E. Jr., DeSteno C.V. Chemical character of proteins in rat incisors. Biochimica et Biophysica Acta (BBA) 1972;257(1):167-71.
49. Butler W.T., Hall W.T, Richardson W.S. Purification and some properties of the phosphoprotein from rat incisors. Biochimica et Biophysica Acta (BBA) 1976;427(1):262-67.
50. Glimcher M.J. Mechanism of calcification: Role of collagen fibrils and collagen-phosphoprotein complexes in vitro and in vivo. The Anatomical Record 1989;224(2):139-53.
51. LeGeros R.Z. Chemical and crystallographic events in the caries process. Journal of Dental Research 1990;69(Special Issue):567-74.
52. Chui S.T., Weeks J.D. Dynamics of the Roughening Transition. Physical Review Letters 1978;40(12):733-36.
53. Gilmer G.H., Weeks J.D. Statistical properties of steps on crystal surfaces. The Journal of Chemical Physics 1978;68(3):950-58.
54. Chernov A.A. Formation of crystals in solutions. Contemporary Physics 1989;30(4):251-76.
55. Harnett E.M., Alderman J., Wood T. The surface energy of various biomaterials coated with adhesion molecules used in cell culture. Colloids and Surfaces B: Biointerfaces 2007;55(1):90-97.
56. Van Der Eerden J.P. The advance velocity of steps under the influence of volume and surface diffusion, by direct and indirect incorporation of growth units. Journal of Crystal Growth 1982;56(1):174-88.
57. Schlichting H. Boundary Layer Theory: McGraw-Hill; 1968.
58. Chernov A.A. Layer-Spiral Growth of Crystals. Uspekhi Fizicheskikh Nauk 1961;83(2):277-331.
59. Cabrera N., Levine M.M. On the dislocation theory of evaporation of crystals. Philosophical Magazine 1956;1:450-58.
60. Herring C. Surface tension as a motivation for sintering. In: Kingston W.E., editor. The Physics of Powder Metallurgy. New York: McGraw-Hill; 1951. p. 143-79.

61. Herring C. The use of classical macroscopic concept in surface energy problems. In: Gomer R., Smith C.S., editors. Structure and Properties of Solid Surfaces. Chicago: University of Chicago Press; 1953. p. 5-72.
62. Söhnel O. Estimation of electrolyte-crystal-aqueous-solution interfacial tension. Journal of Crystal Growth 1983;63(1):174-76.
63. Walser M. Ion Association. VI. Interactions Between Calcium, Magnesium, Inorganic Phosphate, Citrate and Protein in Normal Human Plasma. The journal of clinical investigation 1961;40(4):731-42.

Chapter VII. Ultrastructure of Arrested Carious Dentine Lesions

This chapter is based on the following submitted paper: **Zavgorodniy A.V.**, Rohanizadeh R., Swain M.V. Ultrastructure of Arrested Carious Dentine Lesions. Journal of Dentistry, In Review.

7.1 Abstract

Objective: To characterise the ultrastructural properties of the inorganic phase of arrested dentinal carious lesions.

Methods: Transmission electron microscopy and electron diffraction analytical methods were used to investigate the ultrastructural characteristics of the inorganic phase of arrested carious lesions. Areas of interest were identified with an optical microscope and a dental explorer.

Results: Higher mineral density of intertubular dentine was observed in the region of the harder layer of dentine at the cavity floor. The dentinal tubules were filled with intratubular dentine. Dentine microtubules were filled with dense mineral apatite deposits. No preferred orientation of needle-like crystallites, which formed intertubular dentine, was observed in this region of carious dentine. Underlying soft carious dentine demonstrated demineralized intertubular dentine. Dentinal tubules retained peritubular dentine and were partially filled with intratubular dentine. Microtubules lost peritubular dentine and were not occluded with minerals. Needle-like crystallites in the intertubular dentine formed dense compact bands with the observed preferred orientation along the long axis of the bands.

Conclusions: The observed increased density of mineral deposits explained the reported increase of hardness at the cavity floor of the arrested dentine carious lesions.

Densely packed highly oriented needle-like crystallites, which formed intertubular dentine in the soft carious region, were indicative that the dentine collagen matrix was not degraded in this region. No preferred orientation of dentine crystallites within the harder layer at the cavity floor was interpreted on the basis of the collagen matrix near the cavity floor was degraded.

7.2 Introduction

Dentine is a tough mineralized layer, which supports the more highly mineralized and much stiffer enamel layer [1]. Dentine is softer than the enamel layer and it is structurally adapted to transfer and minimise stresses caused by the forces of mastication [2]. Together with enamel, dentine forms an integral protection system for the underlying pulp that is able to sustain a degree of damage from caries and impact loading. Dentine is composed of approximately 48 vol.% inorganic material in the form of carbon-rich and calcium-deficient hydroxyapatite mineral, 29 vol.% organic material, which is mostly collagenous fibres, and 23 vol.% water [3]. The structural units of dentine include mineralized intertubular matrix, higher mineralized peritubular dentine and the content of the dentinal tubules, which comprises soft tissue of the odontoblastic processes and the organic material in the periodontoblastic space. The unmineralized predentine lines the pulpal side of the dentine [4]. The intertubular dentine organic matrix provides the framework for biomineralization and primarily consists of fibrous type I collagens [5] and non-collagen proteins (NCPs), which include phosphorylated proteins (DPP [6], DSP [7] and other phosphorylated proteins [8]) and non-phosphorylated proteins (e.g. osteocalcin [9, 10]), proteoglycans (CS [11], KS [12]), growth factors (TGF-β1 [13, 14], BMPs [15, 16]), matrix metalloproteinases (MMPs) [17, 18] and other macromolecules, such as lipids [19].

Dental caries is one of the most prevalent diseases in the oral cavity [20], involving progressive demineralization and proteolytic degradation of organic matrices [21]. *In vitro*, previous studies demonstrated that caries-related bacteria can readily demineralize the matrix but fail to degrade the dentine organic matrix [22, 23]. It was suggested that host enzymes, MMPs, degrade the dentine matrix during or after demineralization by bacterial acids [24, 25]. The degree of the alteration of the dentine ultrastructure caused by caries progress through the thickness of dentine is characterized in terms of dentinal carious layers [26]. Though at present the operative radical intervention and removal of all carious affected dentine is widely accepted, an alternative cariologist view on dentinal caries treatment has started to emerge. It has been suggested that the progress of the caries front may be halted and that the softened dentine may be remineralized if the cariogenic environment is removed [27]. From this perspective, the investigation of the ultrastructure, mechanical properties and the conditions of the formation of the arrested carious dentine is of particular importance for the development of less invasive treatments of the dentinal caries via remineralization.

An arrested carious dentinal lesion differs from an active lesion by its darker pigmentation, higher values of mineral densities identified in the scanning electron microscope (SEM) using back-scattered electron (BSE) imaging [28] and higher values of hardness and elastic modulus measured on fully hydrated dentine specimens in the atomic force microscope (AFM) [29]. In addition, the arrested carious lesion demonstrates no tendency to progress further and to cavitate. The conditions under which the arrest of an active carious lesion occurs are being currently elucidated and it was proposed that the dentinal cavity floor exposed to saliva and higher fluoride content in the oral cavity may become remineralized and arrested [30].

Transmission electron microscopy (TEM) and electron diffraction techniques were used in this study to test the hypothesis that softened and arrested carious dentine lesions have distinctly different ultrastructure, which in turn can explain the reported increase of hardness and mineral densities at the cavity floor of arrested carious dentine lesions.

7.3 Materials and Methods

Human molar teeth extracted due to severe occlusal carious lesions with no prior history of restoration were immediately collected after extraction according to the protocols approved by the Ethics Review Committee of Sydney South West Area Health Service, reference № X07-0217 and 07/RPAH/47, and by the Human Research Ethics Committee of the University of Sydney, reference № 10541. Longitudinal 1 mm thick sections through the centre of the lesion were prepared using a low-speed water-cooled diamond saw (Isomet, Buehler Ltd., Lake Bluff, USA). In order to identify the presence of arrested (darkly pigmented brown or black with a harder consistency [31], thin layer, Figure 7.1, arrow c) and softened (slightly brownish yellow in colour, with a soft rubbery consistency [31], layer, Figure 7.1, arrow e) dentine carious lesions, both visual observations were performed under optical stereomicroscope (Leica MZ8) and the tactile response of carious dentine was probed with a dental explorer.

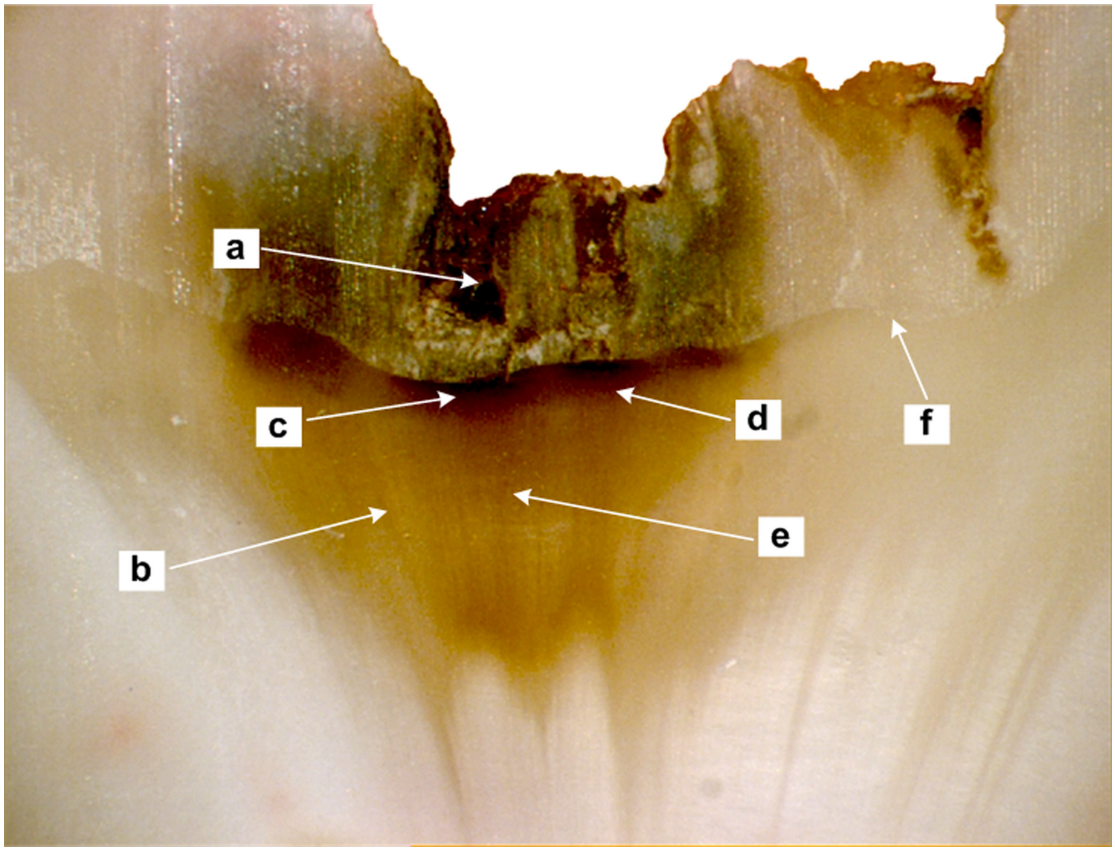

Figure 7.1 Optical images of the carious tooth cross-section. Carious cavitated enamel (a); dentine carious lesion (b); harder layer of caries dentine (c); layer of caries dentine (d) directly underneath the harder outer layer of caries dentine and softened inner caries dentine (e); dentine-enamel junction (f).

The selected sections were then treated in Modified Karnovsky's fixative in 0.2 M Sorenson's buffer titrated to pH 7.2 for 24 hours at 2°C, rinsed several times with 0.2 M Sorenson's buffer. 1x1x1 mm blocks were prepared from each section representing harder layer of carious dentine adjacent to the DEJ (Figure 7.1, arrow c), carious dentine directly underneath the identified outer harder layer of carious dentine (brownish layer, Figure 7.1, arrow d) and blocks representing softened dentine caries lesions (Figure 7.1, arrow e). The specimens were then dehydrated with the increasing concentration of ethanol and infiltrated with epoxy resin. The prepared resin blocks were cured for 48 h at 65°C and 80-nm-thick sections were cut using an ultramicrotome (Ultracut S, Reichert-Leica, Vienna, Austria) equipped with glass and 45° diamond knives (Diatome, Bienne, Switzerland). The sections were collected

from distilled water onto 200 mesh copper grids pre-coated with formwar film. After drying, the specimens were carbon coated and then observed using transmission electron microscope (TEM) CM12 (Philips, Eindhoven, The Netherlands) operated at 120 kV and equipped with a nitrogen-cooled anti-contamination device. Selected area electron diffraction (SAED) [32] was performed to reveal the nature of the crystalline structure of the inorganic phase of dentine samples.

7.4 Results

The TEM observations of soft carious lesions (Figure 7.1, arrow e) revealed the ultrastructure of the mineral phase of dentine in this region. Tubules were clearly identifiable (Figure 7.2, arrow a). The darker contrast peritubular dentine surrounding the tubule lumens was still partially present (Figure 7.2, arrow b), although this layer of dentine had lost a large amount of its mineral content. The perforations in the peritubular dentine were visible (Figure 7.2, arrow c). A prominent feature in all of the observed tubules was dark contrast material partially obliterating the tubules (Figure 7.2, arrow d). Rhombohedral crystals (Figure 7.2, inset A) formed this darker contrast intratubular dentine, which was consistent with our previous observations [33]. The remnants of the lighter contrast material were occasionally observed within the tubule lumens (Figure 7.2, arrow e).

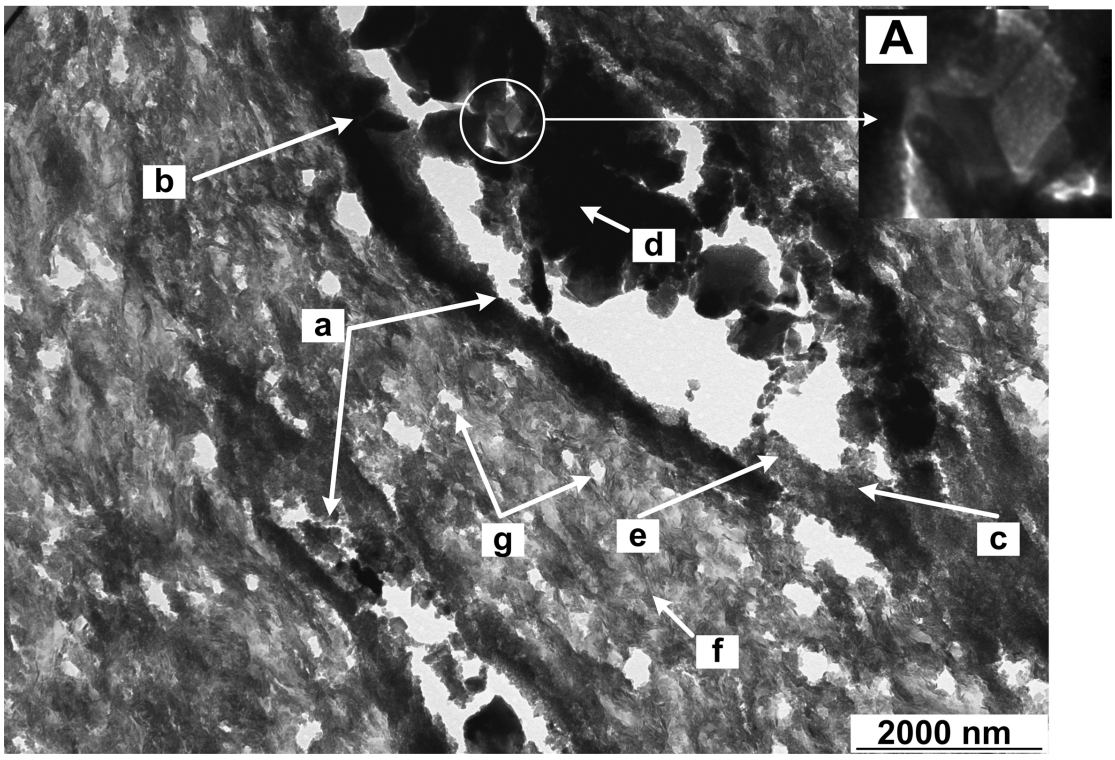

Figure 7.2 TEM micrograph of the soft carious layer of dentine. Dentinal tubules (a) were surrounded by peritubular dentine (b) with perforations (c). The tubules were partially filled with darker contrast large crystals (d) and a lighter contrast material (e). Intertubular dentine (f) was appeared perforated (g). The encircled region of intratubular dentine is magnified in inset A.

The intertubular dentine (Figure 7.2, arrow f) appeared as lighter contrast and therefore lower mineral density than intratubular or peritubular dentine (Figure 7.2). The presence of unmineralised voids (Figure 7.2, arrows g) was observed throughout the intertubular dentine in the softened carious layer.

The higher magnification TEM micrograph revealed the underlying ultrastructure of the intertubular dentine in the softened carious lesion (Figure 7.3). The mineral phase of dentine in this region consisted of needle-like crystallites (Figure 7.3, arrow a), which occasionally formed dense compact dark contrast bands (Figure 7.3, arrow b). The crystallites demonstrated texture (preferred orientation) within the bands with the needle-like crystallites parallel to the long axis of the bands.

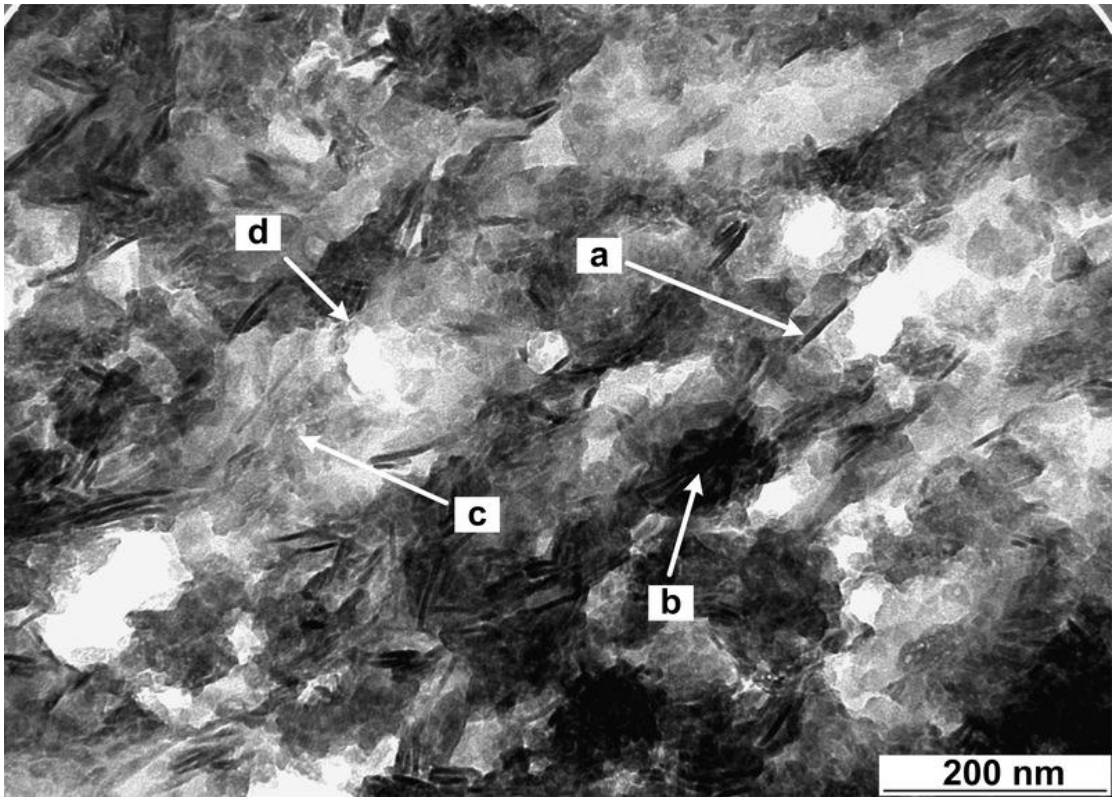

Figure 7.3 TEM micrograph of the intertubular dentine in the softened area of carious lesion. Needle-like dentine crystallites (a) formed darker contrast bands (b) and demonstrated preferred orientation within the bands. The intertubular dentine between the bands (c) appeared extensively demineralised especially around the voids (d).

The intertubular dentine between the darker contrast bands was a lighter contrast material (Figure 7.3, arrow c). The unmineralised voids (Figure 7.3, arrow d) were clearly visible. The mineral in the near vicinity around the voids appeared as a much lighter contrast material than further away from the voids.

The TEM observations of the dentine carious layer directly underneath the harder, outer layer of dentine (Figure 7.1, arrow d) revealed that the majority of the tubules in this layer had almost completely lost their peritubular and intratubular dentine (Figure 7.4, arrows a and b). The intertubular dentine between the tubules appeared to be a darker contrast material than the intertubular dentine near the edges of tubule openings (Figure 7.4, arrow c).

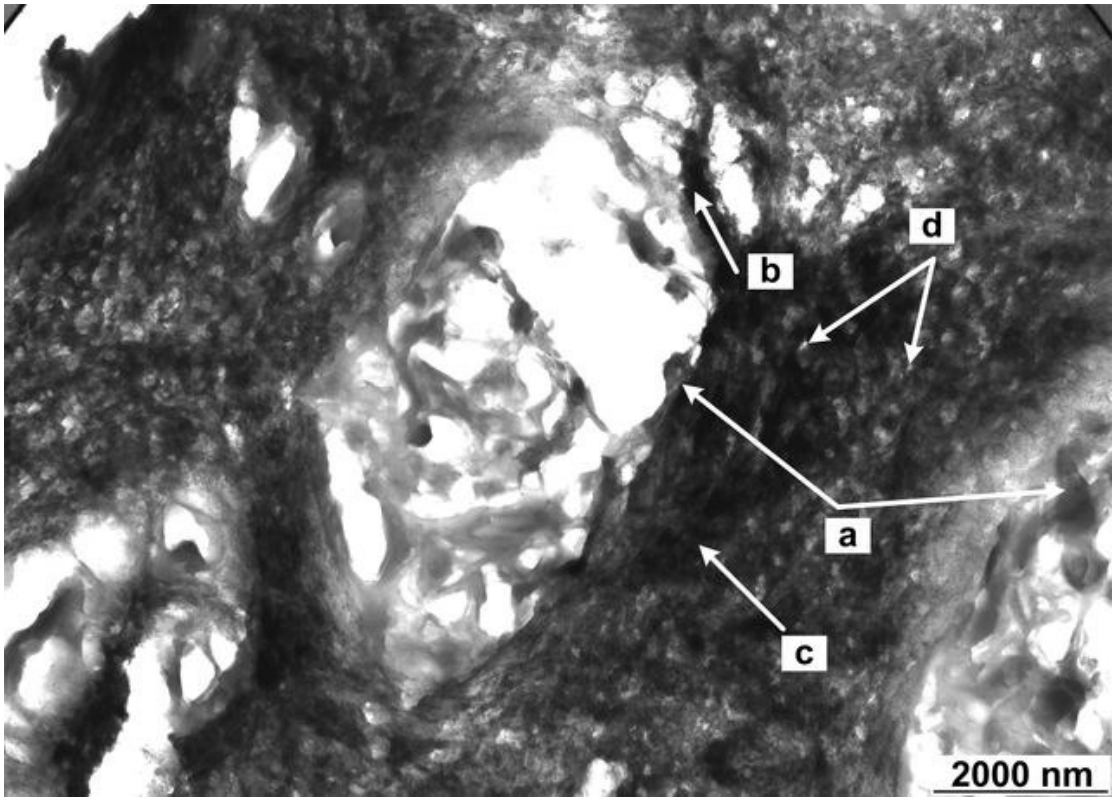

Figure 7.4 TEM micrograph of carious dentine in the region directly underneath the harder outer layer of dentine (Figure 7.1, arrow d). The dentinal tubules (a) lost peritubular and most of the intratubular dentine (b). The darker lines (c) within the intertubular dentine were visible as well as unmineralized voids (d).

It could also be noted that the demineralized voids within the intertubular dentine were less visible (Figure 7.4, arrow d) than in soft carious lesions (Figure 7.2). Although the darker contrast bands were still visible within the intertubular dentine (Figure 7.4, arrow c), they were not as clearly observed as in the soft carious lesions. This was because the difference in contrast level of the darker lines and the dentine between these darker lines in this region of carious dentine was much lower than that in soft carious lesions.

The higher magnification TEM micrograph (Figure 7.5) revealed the underlying ultrastructure of the intertubular dentine in the region directly underneath the harder, outer layer of dentine (Figure 7.1, arrow d). Needle-like crystallites were clearly visible (Figure 7.5, arrow a). Although these crystallites formed distinguishable darker contrast bundles (Figure 7.5, arrow b), they did not

demonstrate the preferred orientation similar to the texture observed in deeper layers of soft carious dentine (Figure 7.3, arrow b). Also the voids, which were observed in soft carious dentine (Figure 7.2, arrow g and Figure 7.3, arrow d), were generally enlarged (Figure 7.5, arrow c) in this region of dentine carious lesions.

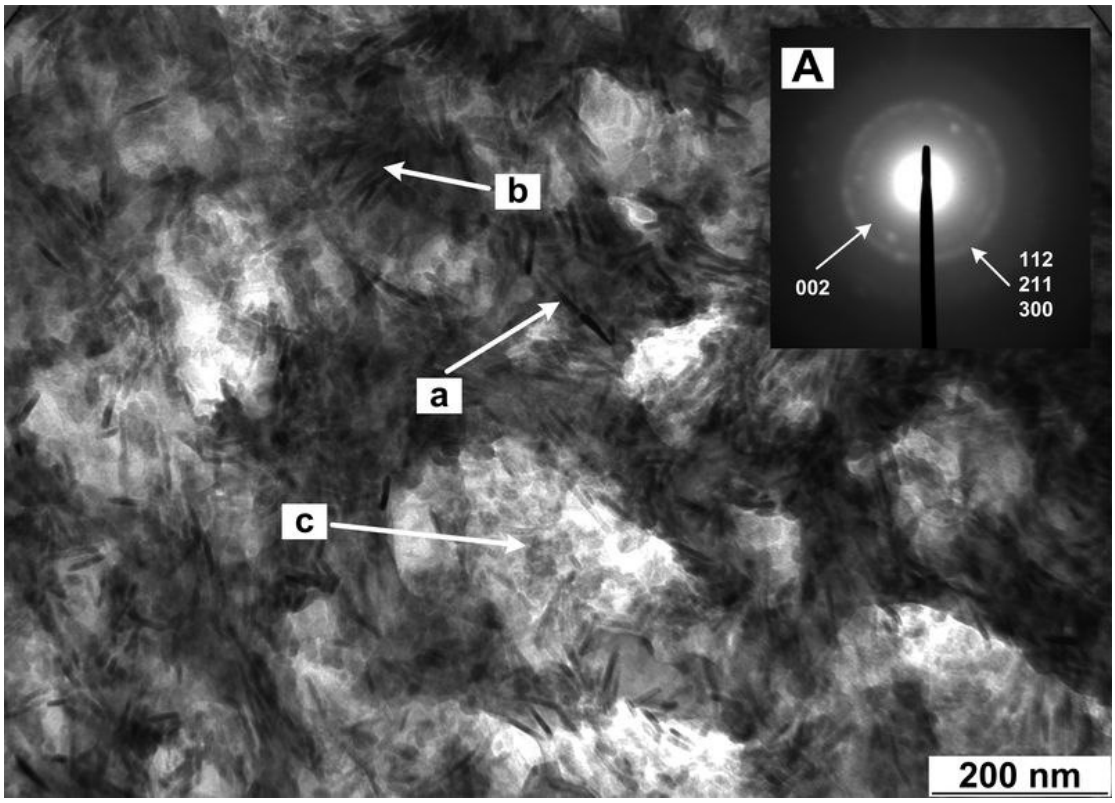

Figure 7.5 TEM micrograph of the intertubular carious dentine in the region directly underneath the harder outer layer of dentine. Needle-like crystallites (a) formed darker contrast bundles (b). The microtubles were filled with lighter contrast mineral deposits (c). The apatite nature of these mineral deposits was confirmed through the indexing of the corresponding selected area electron diffraction pattern (inset A).

The majority of the voids were filled with mineral deposits (Figure 7.5, arrow c), which made the appearance of the dentine structure in this layer more homogeneous than in soft dentine carious lesions (Figure 7.3) with less contrast variations, when viewed at lower magnifications (Figure 7.4). The nature of the mineral deposits within the voids (Figure 7.5, arrow c) was analysed using electron diffraction. Indexing of the electron diffraction patterns corresponding to the areas selected within the voids

(Figure 7.5, inset A) confirmed that the material inside the voids was the apatite polycrystalline phase [34].

Figure 7.6 demonstrates TEM micrograph of the outer harder layer of carious dentine. It was clearly seen that although the tubules had not collapsed (Figure 7.6, arrow a), they did not preserve their initial shape and demonstrated an irregular perimeter. No peritubular dentine was observed. The tubules were partially filled with dark contrast material (Figure 7.6, arrow b), which appeared to be much denser than the intertubular dentine (Figure 7.6, arrow c) and the remnants of the intratubular dentine observed in Figure 7.4 (arrow b).

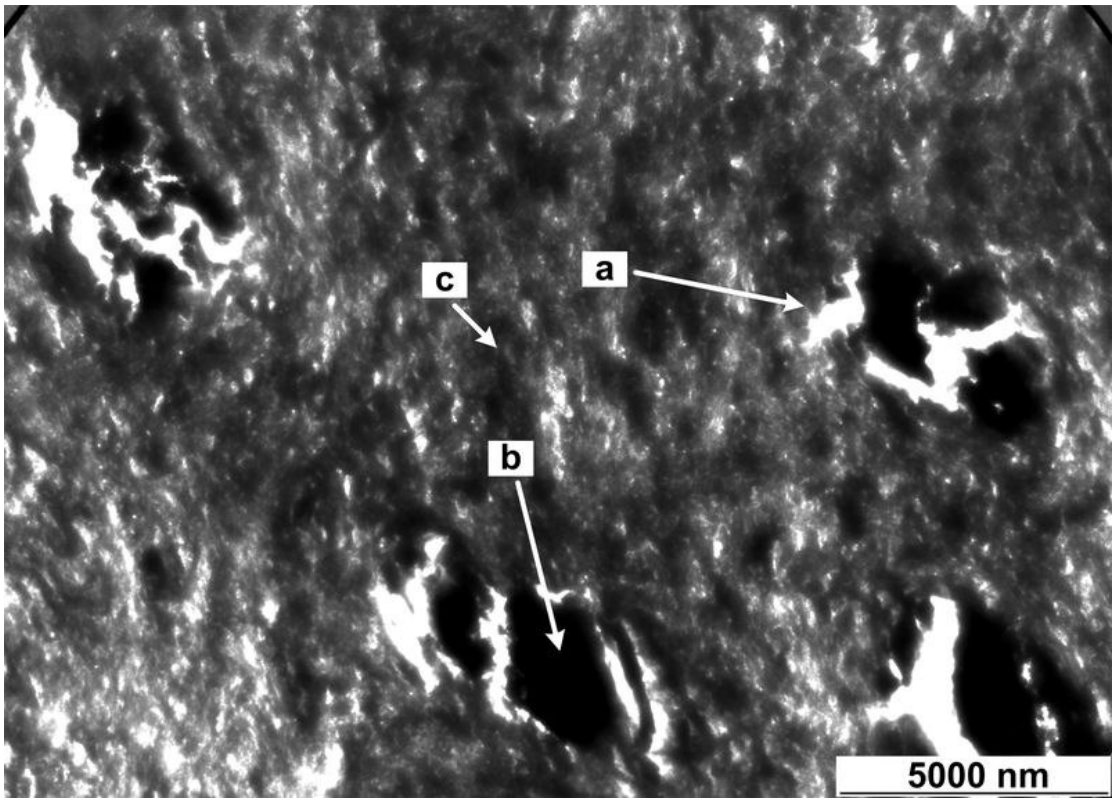

Figure 7.6 TEM micrograph of the harder outer layer of carious dentine. The tubules (a) demonstrated irregular perimeter and were partially filled with the intratubular mineral deposits (b). The intertubular dentine (c) demonstrated similar structure to the intertubular dentine directly underneath this harder outer layer of dentine.

The structure of the intertubular dentine in this region generally resembled the structure observed within the layer of dentine directly underneath this outer harder

layer of dentine (transition layer between demineralized, soft layer and the harder outer layer) (Figure 7.4, arrow c). The higher magnification TEM images of this harder outer layer of carious dentine revealed that the intratubular dentine appeared much denser (Figure 7.7, arrow a), than that observed in the transition layer (Figure 7.5, arrow c).

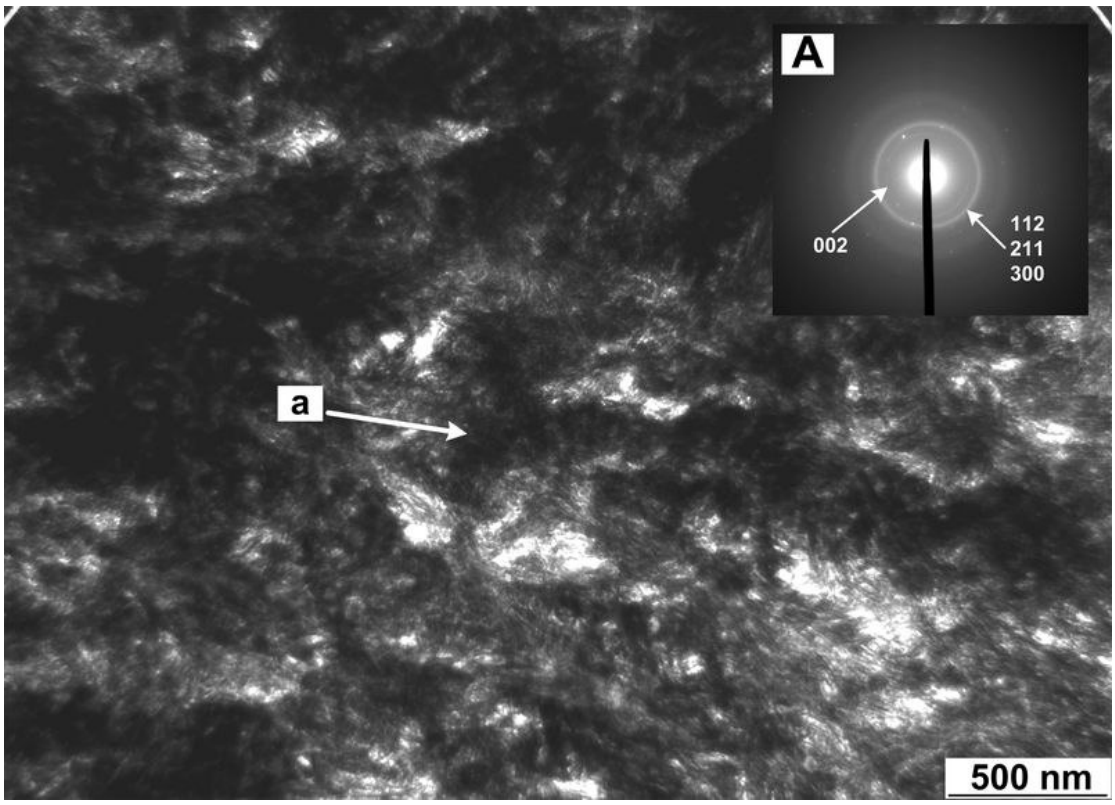

Figure 7.7 TEM micrograph of the ultrastructure of the outer harder region of carious dentine. The apatite nature of the mineral deposits (a) was confirmed by indexing of the corresponding selected area electron diffraction patterns (inset A).

The nature of dentine mineral, which was filling the voids, was confirmed to be apatite by indexing of the corresponding selected area electron diffraction (SAED) patterns (Figure 7.7, inset A) [34]. SAED patterns confirmed no preferred orientation of the apatite crystallites by observing the almost complete ring of the 002 reflections (Figure 7.7, inset A).

7.5 Discussion

The dentine-pulp complex forms a vital tissue containing odontoblasts and their processes. One of the functions of this tissue is its ability to defend itself by reacting to transmission of stimuli and insult from the oral cavity through nano-size pores in enamel [35] and to the release of signalling molecules such as growth factors present in dentine organic matrix [36]. The common defence reaction by the dentine-pulp complex is the deposition of mineral within the dentinal tubules (transparent dentine) [33] prior to the advancing caries demineralization front as it extends towards the dentine-enamel junction (DEJ). Once the enamel lesion comes into contact with the DEJ, a slightly brownish yellow discolouration of the dentine is seen, which indicates the onset of dentine demineralization. It was demonstrated that the progress of caries through the transparent layer of dentine includes dissolution of the peritubular dentine of the dentinal tubule lateral branches [26, 33]. The presence of an acidic environment in the dentinal tubules leads to dissolution of the intratubular dentine, which mainly consisted of carbonated apatite, followed by the precipitation of the Mg β-TCP crystals. Figure 7.2 demonstrates the advanced stage of this process in the soft layer of carious dentine. Perforations (Figure 7.2, arrow c) in otherwise still thick peritubular dentine (Figure 7.2, arrow b) were dissolved microbranches, through which acid diffused into the dentinal tubule. Although remnants of the initially deposited intratubular dentine [33] could still be seen (Figure 7.2, arrow e), the deposits of mineral formed in acidic conditions, Mg β-TCP, were evident (Figure 7.2, arrow d and inset A). Substantial loss of mineral in the intertubular dentine due to exposure to acid that had diffused into intertubular dentine through the dissolved walls of the microtubules was observed [26]. The larger mineral loss around the microtubule manifested itself as the lighter contrast material in close proximity to the perimeter of the microtubule,

while further away from the perimeter of the microtubule the mineral density gradually became denser.

The mechanical properties of carious dentine, such as hardness and elastic modulus, are single-valued functions (exponential and a power law respectively) of mineral density by wt.% (the lower the mineral density, the less the mechanical properties of dentine) [37]. The direct observations of the ultrastructure of the dentine soft carious lesions therefore confirmed the hypothesis that the lower values of the mechanical properties of soft caries lesion reported in [29] were because of the loss of mineral due to caries attack. The changes in the ultrastructure of the dentine carious lesion towards the harder layer at the cavity floor were prominent. As shown in Figure 7.4, it can be noticed that the mineral density variation of the intertubular dentine in the layer directly underneath the harder layer at the cavity floor was much less than the mineral density variation of the intertubular dentine in the soft carious layers of dentine (Figure 7.2). The darker contrast of the intertubular dentine near the cavity floor suggested that the mineral density increased, given that the specimens were prepared to the same thickness of about 80 nm. Higher magnification images (Figure 7.5) revealed that the contrast variation decreased due to the formation of mineral deposits inside the microtubules. Although microtubules were enlarged at the expense of the dissolved surrounding intertubular dentine, numerous new mineral crystallites were deposited within the opening of the microtubules and in the intertubular dentine.

These new block-shaped mineral deposited crystallites were much smaller in size than needle-shaped crystallites that had survived the surrounding acidic environment within the collagen fibrils (Figure 7.5, arrow b). The corresponding electron diffraction patterns (Figure 7.5, inset A) confirmed that these newly deposited crystallites were polycrystalline apatite. No texture (preferred orientation)

was observed, which suggested that these apatite crystallites precipitated without any associated biologically controlled mineralization process. The specimens observed from the harder carious layer of dentine at the surface of the cavity floor (Figure 7.6) reinforced our observations of the occurrences of remineralization. The mineral deposits observed in the arrested carious dentine were dense (Figure 7.7), almost completely occluding microtubules with polycrystalline deposits of apatite mineral with no preferred orientation (Figure 7.7, inset A). A dark pigmentation of the arrested caries dentine was linked to the high densities of the coalesced bodies of bacteria [38]. This implied that there were large remnants of organic structures in this area, which may generate inhomogeneous nucleation centres for the precipitation of apatite mineral [39].

Organic phase of dentine consists of type I collagen and non-collagenous proteins (NCPs), e.g. DPP, DMP1, BSP [40], which bind to type I collagen fibrils and serve as initiation sites for apatite crystal nucleation with a high degree of control over their location, orientation and shape. Collagen type I fibrils exhibit a banding pattern resulting from the alteration of gap regions and overlap regions. During mineralization, the initial mineral deposition occurs in the gap regions between collagen fibrils, which are bound by the non-triple-helical telopeptides of the collagen molecule. Intertubular dentine in soft layers of carious dentine demonstrated a high degree of demineralization but needle-like crystals deposited within collagen gap regions were partly protected from the acidic challenge (Figure 7.3, arrow a) and remained highly oriented in their c-direction with dense crystal bundles along the long axis of collagen fibrils (Figure 7.3, arrow b). This suggested that in soft carious lesions located below the harder layer of the arrested dentine carious lesions (Figure 7.1, arrow e) the structure of collagen fibrils had not been substantially affected.

However, during prolonged caries acidic challenge apatite crystallites impregnated through collagen fibrils lost their texture, which may be due to the degradation of the organic matrix of dentine. Though bacterial acids are the key factor in the process of demineralization of dentine, neither acids, nor proteolytic enzymes produced by cariogenic bacteria are capable of directly degrading of the organic matrix of dentine [24]. Although host matrix metalloproteinases (MMPs) are capable of degrading the organic matrix of dentine, they are secreted as latent proforms and require activation to be catalytically competent [41]. It was demonstrated previously that host MMPs could be released from the mineralized dentine matrix and they can be activated by low pH [24, 42]. This may cause degradation of the demineralized dentine matrix under different physiological [43] and pathological conditions [24]. MMP-8 was identified as a major collagenolytic enzyme in human dentine [44] but the presence of MMP-2, MMP-9 and MMP-20 has also been demonstrated in carious dentine lesions. The presence and activity of MMP-1, MMP-2, MMP-9 and cathepsin B in saliva was also reported but there was no evidence of a direct correlation between their activities and the degradation of dentine collagen [45]. Acid mechanism of MMPs activation of dentinal enzymes may also be involved in the degradation of collagen fibrils in the adhesive layer of dental composite restoration, being therefore partially responsible for restoration failures [43, 46].

In this study we demonstrated that the harder layer at the cavity floor of caries dentine lesions is partially remineralized dentine. The dentine organic matrix has been degraded in this region of carious dentine, which may significantly affect dentine elastic modulus. The reported value of the reduced elastic modulus of the arrested caries dentine measured using an AFM on fully hydrated specimens was 2.7 GPa [29], which was significantly lower than the values of the reduced elastic modulus of fully

hydrated intertubular intact dentine 22.8 – 24.5 GPa [47]. For the purposes of treatment of caries dentine via remineralization the presence of an intact biological scaffold in the form of collagen type I matrix is therefore important and the inhibition of MMPs with inhibitors, such as tissue inhibitors of metalloproteinases (TIMPs), at the early stages of caries treatment maybe essential. Dental caries is caused by strongly acidogenic and aciduric gram-positive facultative aerobes (e.g., mutans streptococci, lactobacilli and actinomyces). It was demonstrated that antibiotics were effective in inhibiting of such gram-positive microorganisms in rat models [48]. The present study of the phenomena of naturally occurring remineralization of caries-affected dentine may prove beneficial for the further development of caries-affected dentine remineralization techniques.

7.6 Conclusions

Based on this qualitative ultrastructural study of the mineral phase of arrested carious lesions, the following conclusions can be drawn:

1. In the arrested layer of dentinal carious lesions, the density of mineral content was higher than that of soft subsurface carious lesions.
2. The remineralization of carious dentine associated with the arrested carious lesions was due to the precipitation of apatite mineral. No preferred orientation of the apatite crystallites was observed, which may suggest that the process of mineralization of the arrested carious layer of dentine was not biologically controlled.
3. No degradation of collagen matrix in soft layers of carious dentine was detected, while the degradation of the collagen matrix near cavity floor maybe due to longer exposure to acidic challenge associated with caries and therefore activation of host MMPs in low pH conditions in demineralized dentine.

7.7 References

1. Imbeni V., Kruzic J.J., Marshall G.W., Marshall S.J., Ritchie R.O. The dentin-enamel junction and the fracture of human teeth. Nature Materials 2005;4(3):229-32.
2. Wang R. Z., Weiner S. Strain–structure relations in human teeth using Moiré fringes. Journal of Biomechanics 1998;31(2):135-41.
3. Nanci A. Ten Cate's Oral Histology: Development, Structure and Function. 7th ed. St Louis: Mosby; 2008.
4. Mjör I.A. Human coronal dentine: Structure and reactions. Oral Surgery, Oral Medicine, Oral Pathology 1972;33(5):810-23.
5. Lukinmaa P.L., Waltimo J. Immunohistochemical localization of types I, V, and VI collagen in human permanent teeth and periodontal ligament. Journal of Dental Research 1992;71(2):391-97.
6. Ritchie H.H., Wang L.H. Sequence Determination of an Extremely Acidic Rat Dentin Phosphoprotein. Journal of Biological Chemistry 1996;271(36):21695–98.
7. MacDougall M., Simmons D., Luan X., Nydegger J., Feng J., Gu T.T. Incorrect reference from scopus Dentin phosphoprotein and dentin sialoprotein are cleavage products expressed from a single transcript coded by a gene on human chromosome 4: Dentin phosphoprotein DNA sequence determination Journal of Biological Chemistry 1997;272(2):835-42.
8. Butler W.T. Dentin matrix proteins. European Journal of Oral Sciences 1998;106(Supp 1):204-10.
9. de Vries G.I., Quartier E., Boute P., Wisse E., Cosmans D. Immunocytochemical localization of OC in developing rat teeth. Journal of Dental Research 1987;66(3):784-90.
10. Papagerakis P., Berdal A., Mesbah M., Peuchmaur M., Malaval L., Nydegger J., et al. Investigation of osteocalcin, osteonectin, and dentin sialophosphoprotein in developing human teeth. Bone 2002; 30(2):377–85.
11. Jones I.L., Leaver A.G. Glycosaminoglycans of human dentine. Calcified Tissue Research 1974;16:37-44.
12. Waddington R.J., Hall R.C., Embery G., Lloyd D.M. Changing profiles of proteoglycans in the transition of predentine to dentine. Matrix Biology 2003;22(2):153-61.
13. Cassidy N., Fahey M., Prime S.S., Smith A.J. Comparative analysis of transforming growth factor-β isoforms 1–3 in human and rabbit dentine matrices. Archives of Oral Biology 1997;42(3):219-23.
14. Zhao S., Sloan A.J., Murray P.E., Lumley P.J., Smith A.J. Ultrastructural localisation of TGF-beta exposure in dentin by chemical treatment. The Histochemical Journal 2000;32(8):489-94.
15. Bessho K., Tanaka N., Matsumoto J., Tagawa T., Murata M. Human dentin-matrix-derived bone morphogenetic protein. Journal of Dental Research 1991;70(3):171-75.
16. Nakashima M. Induction of dentin formation on canine amputated pulp by recombinant human bone morphogenetic proteins (BMP)-2 and -4. Journal of Dental Research 1994;73(9):1515-22.

17. Martin-De Las Heras S., Valenzuela A., Overall C.M. The matrix metalloproteinase gelatinase A in human dentine. Archives of Oral Biology 2000;45(9):757-65.
18. Beniash E., Skobe Z., Bartlett J.D. Formation of the dentinoenamel interface in enamelysin (MMP-20)-deficient mouse incisors. European journal of Oral Sciences 2006;114(Supp 1):24-29.
19. Goldberg M., Septier D. Phospholipids in amelogenesis and dentinogenesis. Critical Reviews in Oral Biology & Medicine 2002;13(3):276-90.
20. Bowen W.H. Do We Need To Be Concerned About Dental Caries In The Coming Millenium? Critical Reviews in Oral Biology & Medicine 2002;13(2):126-31.
21. Nakornchai S., Atsawasuwan P., Kitamura E., Surarit R., Yamauchi M. Partial biochemical characterisation of collagen in carious dentin of human primary teeth. Archives of Oral Biology 2004;49:267-73.
22. Katz S., Park K.K., Palenik C.J. In-vitro root surface caries studies. Journal of Oral Medicine 1987;42(1):40-48.
23. van Strijp A.J., van Steenbergen T.J., ten Cate J.M. Bacterial colonization of mineralized and completely demineralized dentin in situ. Caries Research 1997;31(5):349.
24. Tjäderhane L., Larjava H., Sorsa T., Uitto V.J., Larmas M., Salo T. The activation and function of host matrix metalloproteinases in dentin matrix breakdown in caries lesions. Journal of Dental Research 1998;77(8):1622-29.
25. Sulkala M., Wahlgren J., Larmas M., Sorsa T., Teronen O., Salo T., et al. The effects of MMP inhibitors on human salivary MMP activity and caries progression in rats. Journal of Dental Research 2001;80(6):1545-49.
26. Zavgorodniy A.V., Rohanizadeh R., Swain M.V. Ultrastructure of Dentine Carious Lesions. Archives of Oral Biology 2008;53(2):124-32.
27. Bjørndal L. The Caries Process and Its Effect on the Pulp: The Science Is Changing and So Is Our Understanding. Journal of Endodontics 2008;34(7, Supplement 1):S2-S5.
28. Angker L., Nockolds C., Swain M.V., Kilpatrick N. Quantitative analysis of the mineral content of sound and carious primary dentine using BSE imaging. Archives of Oral Biology 2004;49(2):99-107.
29. Zheng L., Hilton J.F., Habelitz S., Marshall S.J., Marshall G.W. Dentin caries activity status related to hardness and elasticity. European Journal of Oral Sciences 2003;111(3):243-52.
30. Chu C.H., Lo E.C.M. Microhardness of dentine in primary teeth after topical fluoride applications. Journal of Dentistry 2008;36(6):387-91.
31. Iwami Y., Hayashi N., Takeshige F., Ebisu S. Relationship between the color of carious dentin with varying lesion activity, and bacterial detection. Journal of Dentistry 2008;36(2):143-51.
32. Fultz B., Howe J.M. Transmission Electrone Microscopy and Diffractometry of Materials. Second ed. Berlin: Springer-Verlag; 2002.
33. Zavgorodniy A.V., Rohanizadeh R., Bulcock S., Swain M.V. Ultrastructural observations and growth of occluding crystals in carious dentine. Acta Biomaterialia 2008;4(5):1427-39.
34. International Centre for Diffraction Data. Powder Diffraction File 09-0432; 2005.

35. Kidd E.A.M., Fejerskov O. What Constitutes Dental Caries? Histopathology of Carious Enamel and Dentin Related to the Action of Cariogenic Biofilms. Journal of Dental Research 2004;83(Special Issue C):C35-C38.
36. Smith A.J. Vitality of the dentin-pulp complex in health and disease: growth factors as key mediators. Journal of Dental Education 2003;67(6):678-89.
37. Angker L., Nockolds C., Swain M.V., Kilpatrick N. Correlating the mechanical properties to the mineral content of carious dentine—a comparative study using an ultra-micro indentation system (UMIS) and SEM-BSE signals. Archives of Oral Biology 2004;49(5):369-78.
38. Sarnat H., Massler M. Microstructure of Active and Arrested Dentinal Caries. Journal of Dental Research 1965;44(6):1389-401.
39. Bonucci E. Calcification in Biological Systems. Boca Raton, Florida: CRC Press; 1992.
40. Baht G.S., Hunter G.K., Goldberg H.A. Bone sialoprotein–collagen interaction promotes hydroxyapatite nucleation. Matrix Biology 2008;In Press.
41. Birkedal-Hansen H. Proteolytic remodeling of extracellular matrix. Current Opinion in Cell Biology 1995;7(5):728-35.
42. Vuotila T., Ylikontiola L., Sorsa T., Luoto H., Hanemaaijer R., Salo T., et al. The relationship between MMPs and pH in whole saliva of radiated head and neck cancer patients. Journal of Oral Pathology & Medicine 2002;31(6):329-38.
43. Pashley D.H., Tay F.R., Yiu C., Hashimoto M., Breschi L., Carvalho R.M., et al. Collagen Degradation by Host-derived Enzymes during Aging. Journal of Dental Research 2004;83(3):216-21.
44. Sulkala M., Tervahartiala T., Sorsa T., Larmas M., Salo T., Tjäderhane L. Matrix metalloproteinase-8 (MMP-8) is the major collagenase in human dentin. Archives of Oral Biology 2007;52(2):121-27.
45. van Strijp A.J.P., Jansen D.C., DeGroot J., ten Cate J.M., Everts V. Host-derived proteinases and degradation of dentine collagen in situ. Caries Research 2003;37(1):58-56.
46. Hashimoto M., Tay F.R., Ohno H., Sano H., Kaga M., Yiu C., et al. SEM and TEM analysis of water degradation of human dentinal collagen. Journal of Biomedical Materials Research Part B: Applied Biomaterials 2003;66B(1):287-98.
47. Habelitz S., Marshall G.W., Balooch M., Marshall S.J. Nanoindentation and storage of teeth. Journal of Biomechanics 2002;35(7):995-98.
48. Fitzgerald R.J. Inhibition of Experimental Dental Caries by Antibiotics. Antimicrobial Agents and Chemotherapy 1972;1(4):296-302.

Chapter VIII. Conclusions

For the overall well being of patients it is currently considered important to minimise dental restorative procedures (e.g. minimal invasive dentistry) [1, 2] when treating the dentinal caries. Such a less invasive restorative technique has to take into account that caries triggers a complex series of biological and physicochemical events, which lead to substantial structural changes of dentine.

Conventional, high resolution and scanning transmission electron microscopy, electron diffraction and energy-dispersive X-ray spectroscopy analytical techniques were used in this study to characterise the structure of carious dentine. But firstly sound dentine and enamel were investigated to establish the basis for the characterisation of the alterations of normal dentine, when affected by caries (Chapter 4).

8.1 X-ray Microdiffraction and TEM Characterization of Human Dentine and Enamel (Chapter 4)

Conventional TEM and μXRD techniques were used in this study to characterize ultra- and micro-structures of these natural hierarchical biocomposites at various locations through the thickness of dentine and enamel. The calculated profiles allowed us to establish the variation of a- and c-lattice parameters of the mineral forming dentine and enamel through the thickness of teeth. This observation implied that the chemical composition of sound dental structures is location dependent.

The analysis of the intensities of the obtained XRD profiles through the thickness of dentine and enamel and the comparison of the ratios of these intensities with that of a random hydroxyapatite powder mixture standard allowed us to conclude that the preferred orientation within dentine and enamel was location-dependent. It

was observed that the crystallinity of dentine increases towards the DEJ. It was also concluded that the crystallinity of enamel increases towards the occlusal surface. The ultrastructural TEM observations showed that dentine crystals became smaller towards the outer layers of circumpulpal dentine and then further appeared thinner but longer in mantle dentine. This result was correlated with the special role of the DEJ and outer layers of circumpulpal dentine in transferring mastication and other types of load from enamel into crown dentine below the sub-DEJ zone. The ultrastructural investigation of enamel established the increase of preferred orientation and thickness of the enamel crystal grains towards the outer surface of the tooth. The enamel crystallites were approximately perpendicular to the enamel surface and it was concluded that it was optimised by nature this way to reduce wear. Also the observed increase in thickness of enamel crystallites confirmed previous observations of the greater mineralization of enamel towards its superficial layer. Further ultrastructural investigation confirmed the presence of the interprismatic cleavages in enamel and it was concluded that such a structural feature may not only limit crack propagation but it could also allow a limited deformation under an external load. It was also concluded that the observed variation in the degree of enamel anisotropy may help to direct stresses from the geometrically complex enamel occlusal surface to the resilient underlying dentine. Using Scherrer-Wilson grain size-strain analysis, non-uniform microstrain was estimated for dentine and enamel crystallites. It was observed that the variation of microstrain was particularly significant in the dentine crystallites due to the substantial change of the crystallites surface-to-volume ratio through the thickness of dentine towards the DEJ. Enamel crystallites, on the other hand, indicated only a trend of the increase of microstrain with the increase of the grain surface-to-volume ratio probably due to the fact that the ratio change was significantly smaller than that

observed in dentine. The values of the microstrain in all instances were relatively low and were corresponding to stresses of less than a few MPa. This study offers an insight into the material nature of mineralized dental structures and provides a better understanding of the structure and physiology of dentine and enamel. Also such observations were instrumental to reveal the difference on the ultrastructural level between normal and carious affected dentine.

Another important implication of this study is related to the selection and development of novel dental materials for the restorative dentistry. Dental restorative materials are not ideal. Different thermal expansion and contraction behaviour between tooth structures and reparative materials, which are associated with differences in terms of chemical composition and crystal structure, prevent perfect adhesion. Thus, restorative fillings are generally only temporary and often require a replacement after a certain period of time. From this perspective, a new generation of synthetic restorative materials is needed to resemble the ultrastructure and mechanical properties of normal dentine and enamel. The prerequisite for producing such biomimetic materials with properties close to those of hard dental biological composites is to understand the influence of the ultrastructural properties, such as size and preferred orientation, of enamel and dentine nanocrystallites on the overall mechanical properties. Therefore the outcome of this work is anticipated to be beneficial for the development of the new generation of dental restorative materials.

Apart from the novel results in regards to the structure of sound and carious dentine and enamel, this work has important methodological outcomes through establishing an appropriate methodology to prepare electron transparent site-specific specimens of about 80 nm in thickness from hard undecalcified dentine, enamel and

dentine-enamel interfaces at the DEJ for an observation in TEM. This technique proved to be very successful and was used throughout this study.

8.2 Ultrastructure of Dentine Carious Lesions (Chapter 5)

Although the width of dentine crystallites was accurately evaluated through the thickness of coronal and mantle dentine in Chapter 4, the length of the crystallites was assessed only qualitatively. The quantitative structural investigation of carious layers of dentine required accurate measurement of the size of dentine crystallites. Such technique was developed in Chapter 5 and was successfully applied to investigate the mineral phase of both sound and carious affected dentine using conventional TEM and electron diffraction analytical techniques (Chapter 5). Firstly, electron diffraction patterns obtained from sound dentine revealed the local preferred orientation of crystallites with their c-axes along the collagen fibrils. TEM observations allowed us to accurately measure both widths and lenghts of dentine mineral crystallites. Secondly, the size of dentine crystallites was measured in dentine carious layers and it was demonstrated that in caries affected intertubular dentine the mineral crystallites became progressively smaller towards the DEJ.

Dentine is a vital tissue, which contains the odontoblastic processes and this tissue will react to transmission of stimuli from the oral cavity through the microporous enamel. One of the defensive reactions to such stimuli is the deposition of mineral within the dentinal tubules. Such dentine layer is called ‘transparent dentine’ because, when examined histologically, this tissue appears transparent in transmitted light. The analysis of the electron diffraction patterns confirmed that the bulk of the intertubular and intratubular dentine in the transparent zone of carious dentine was an apatite phase. Intratubular dentine appeared to be a dense structure formed of plate-shaped apatite crystallites with occasional presence of needle-like

apatite crystallites. The uniformity of the size of crystallites within the intratubular zone showed that these crystallites were nucleated at approximately the same time and under the same conditions through the volume of tubule lumens in the transparent zone and that the precipitation did not gradually occur on the surface of peritubular dentine (inner side of the walls of the dentinal tubules). It was proposed that the mechanism of the intratubular mineralization may be mediated by the carious stimulated odontoblastic processes with a source of mineral being the pulpal blood supply. Minerals dissolved by bacterial acids in the affected demineralized layer can nucleate on carboxyl groups of non-collagenous proteins (NCP) at the (001) crystal face, thus orienting the c-axis of the crystal in a controlled direction, which is in agreement with our observations of electron diffraction patterns of the intratubular dentine.

The outcomes of this work also established that not only tubules but the tubule branching network (specifically microbranches) lead to infiltration of dentine with acid substances in addition to the existing main tubules. It was demonstrated that this tubule branching network plays an important role in the progress of caries front increasing the permeability of dentine by providing extra pathways for acid substances.

A new approach called 'minimum intervention' [3] has been recently introduced for cavity preparation prior to restoration of carious lesions in order to preserve tooth structure. This approach suggests that caries do not always need to be removed completely from deeper portions of the cavity: the outer carious dentine (turbid zone) must be removed, while the inner carious dentine should be preserved. From this point of view, the ultrastructure of turbid carious dentine is of a particular interest. The electron diffraction patterns of intertubular dentine in demineralized zone confirmed

the presence of apatite phase with crystallites having preferred orientations. These findings suggested that the collagen matrix was still structured and crystallites were still aligned along collagen fibrils, which was in agreement with the results of previous researches who reported the observation of cross-banded collagen fibrils in the infected demineralized zone of caries dentine.

The presence of the apatite phase forming caries induced intratubular dentine was established in Chapter 5, however other studies also reported the presence of whitlockite within the dentinal tubules. Therefore further investigation was needed to study the phenomena of transparent layer of carious dentine in details, which was the focus of the study presented in Chapter 6.

8.3 Ultrastructural Observations and Growth of Occluding Crystals in Carious Dentine (Chapter 6)

Using SEM in the backscattered mode, the presence of the transparent layer was established. Firstly, the ultrastructure of the transparent layer of carious dentine was investigated with conventional and high-resolution TEM techniques, coupled with electron-diffraction analytical methods. Two phases of intratubular dentine were identified at this stage, the apatite phase and non-apatitic phase, the latter being a Mg-substituted β-tricalcium phosphate (β-TCP) mineral. These observations were further reinforced by the investigation of chemical composition of the individual nano-size crystallites occluding dentinal tubules using a complementary technique of the dedicated scanning TEM coupled with energy-dispersive X-ray spectroscopy. The presence of silicon was identified at this stage and the following structural composites were formulated: $Ca_{9.5}\left(PO_4\right)_{3.6}\left(CO_3\right)\left(SiO_4\right)_{1.4}\left(OH\right)_{0.2}Cl_{0.4}$ (apatite phase of intertubular dentine), $Ca_{9.33}Mg_{0.67}\left(PO_4\right)_{5.63}\left(SiO_4\right)_{0.37}\left(OH\right)_{1.59}Cl_{0.04}$ (apatite phase of

intratubular dentine) and $Ca_{2.77}Mg_{0.23}(PO_4)_{1.88}(SiO_4)_{0.09}$ (β-TCP phase of intratubular dentine).

Following from these compositional studies the growth kinetics of Mg-substituted β-TCP crystals was investigated and it was established that the formation of these crystals was governed by the volume diffusion mechanism. Applying layer-spiral crystal growth theory, the rapid growth of the whitlockite phase in the caries transparent zone was demonstrated. Based on the results of this study, it was concluded that the formation of the apatite mineral phase of the intratubular dentine in caries transparent zone is a regulated biomineralization process, whereas Mg β-TCP crystals, which were observed in the intratubular dentine, were formed via a 'dissolution/precipitation' mechanism. This study demonstrated the importance of the 'dissolution/precipitation' process and the growth kinetics of Mg-substituted β-TCP crystals to understand the process of formation of calcium-phosphate crystallites in carious intratubular dentine. The clinical implication is that Mg-substituted β-TCP is the unstable material at neutral pH and consequently bonding to such substrate is unreliable in the long term.

Studies presented in Chapters 4, 5 and 6 established the phenomenon of preferred orientation of dentine crystallites in different zones of active carious lesions in dentine, which was due to the presence of collagen matrix. The results of the investigation presented in Chapter 7, which established the differences between active and arrested carious lesions on the ultrastructural level, further facilitate treatment development of dentinal caries via remineralization.

8.4 Ultrastructure of Arrested Carious Dentine Lesions (Chapter 7)

Conventional TEM and electron diffraction analytical techniques were applied to investigate softened and arrested dentinal carious lesions as well as the transitional state between them (Chapter 7). It was demonstrated that the arrested layer of dentinal caries had a denser mineral content than that of inner layers of carious lesions. This observation confirmed the hypothesis that the reported increase of hardness in arrested carious lesions in comparison with soft carious lesions was due to increase in density of mineral deposits at the cavity floor. No degradation of collagen matrix in soft carious lesions was observed, while the degradation of the collagen matrix near the cavity floor was detected. How is it possible that acid-insoluble dentine collagen is destroyed? The results of the study suggested that collagen matrix degradation was due to the activation of host metalloproteinases in low pH conditions in demineralized carious dentine. For the purposes of reconstruction of the carious affected dentine structures, the presence of an intact biological scaffold in the form of collagen matrix is paramount, and the inhibition of MMPs with inhibitors, such as tissue inhibitors of metalloproteinases (TIMPs), at an early stages of caries treatment maybe essential. This study is the first step in the series of future studies to confirm the location and activity of different MMPs and TIMPs in the sound and carious affected dentine. Studies of other growth factors and cytokines are also essential to increase our knowledge and understanding of regulatory mechanisms in healthy and diseased dentine-pulp complex tissue.

8.5 References

1. Mertz-Fairhurst E.J., Curtis J.W. Jr., Ergle J.W., Rueggeberg F.A., Adair S.M., . Ultraconservative and Cariostatic Sealed Restorations: Results at Year 10. Journal of the American Dental Association 1998;129(1): 55-66.
2. Frencken J.E., Songpaisan Y., P. P, Pilot T. An atrauamatic treatment (ART) technique; evaluation after one year. International Dental Journal 1994;44:460-64.
3. Tyas M.J., Anusavice K.J., Frencken J.E., Mount G.J. Minimal intervention dentistry - a review. International Dental Journal 2000;50:1-12.

Appendix

Mineralized collagen fibrils in normal dentine are arranged orthogonal to dentine tubules forming a planar felt-like intertubular dentine matrix that is entirely random [1]. The mineral crystals in intertubular normal dentine are intimately associated with the collagenous matrix, in that they are arranged with their c-axes parallel with the collagen fibrils [2]. Therefore (i) we consider it was reasonable to assume that in ultrathin sections (~ 80 nm) of normal dentine cut approximately orthogonal to the dentine tubules, that the dentine crystals will lie parallel to the section with perhaps slight variability in the oblique angle relative to the projection plane, and (ii) the point regarding crystallites oriented more or less randomly largely applies to the random planar orientation of the crystals rather than orientation in 3D space.

The projection length of dentine needle-like crystal of length l is, $p = l\cos\theta$, where θ (on the basis of assumption (i) above) is the small angle between c-axis of the crystal and the projection plane such that $0 \le \theta \le \theta_{\max} << \frac{\pi}{2}$. In the worst scenario the random variable θ is distributed uniformly between 0 and $\theta_{\max}$, and hence the probability density function $f(\theta) = \frac{1}{\theta_{\max}}$. Since $dp = -l\sin\theta\, d\theta$ and the inverse function $\theta(p) = \arccos\frac{p}{l}$ is a single-valued function in the interval $0 \le p \le l$, the probability density function of random variable p can be found from the expression:

$$g(p) = f(\theta(p))\left|\frac{d\theta(p)}{dp}\right| = \frac{1}{\theta_{\max}}\frac{1}{l\sqrt{1-\left(\frac{p}{l}\right)^2}} \qquad \text{(A.1)}$$

Therefore the mean value:

$$< p >= \frac{1}{\theta_{\max} l} \int_{l\cos\theta_{\max}}^{l} \frac{p\,dp}{\sqrt{1-\left(\frac{p}{l}\right)^2}} = \frac{\sin\theta_{\max}}{\theta_{\max}} l \qquad \text{(A.2)}$$

Second moment:

$$< p^2 >= \frac{1}{\theta_{\max} l} \int_{l\cos\theta_{\max}}^{l} \frac{p^2\,dp}{\sqrt{1-\left(\frac{p}{l}\right)^2}} = \frac{1}{2}\left(1+\frac{\sin 2\theta_{\max}}{2\theta_{\max}}\right) l^2 \qquad \text{(A.3)}$$

Variance:

$$< p^2 > - < p >^2 = \left(\frac{1}{2} + \frac{\sin 2\theta_{\max}}{4\theta_{\max}} - \frac{\sin^2\theta_{\max}}{\theta_{\max}^2}\right) l^2 = \frac{\theta_{\max}^4}{45} l^2 - \frac{\theta_{\max}^6}{315} l^2 + O\left(\theta_{\max}^8\right) \qquad \text{(A.4)}$$

And standard deviation:

$$\sigma = \sqrt{< p^2 > - < p >^2} \approx \frac{\theta_{\max}^2 \sqrt{245 - 35\theta_{\max}^2}}{105} l = \frac{\sqrt{5}}{15}\theta_{\max}^2 l - \frac{\sqrt{5}}{210}\theta_{\max}^4 l + O\left(\theta_{\max}^6\right) \qquad \text{(A.5)}$$

Taking into account the Eqs. A.2 and A.5, and the assumption that $l = 100\,nm$ and $\theta_{\max} = \frac{\pi}{10} = 18^{\circ}$, the measured value would be $< p > \pm \sigma \approx 98.36 \pm 1.46\,nm$, which allowed to measure crystallites sizes directly from the obtained micrographs without further adjustments. The results for sound dentine for the measured length of dentine needle-shaped crystallites were $109.6 \pm 19.9\,nm$ (Table 5.2), which is in agreement with values published in the literature [3] and reflect the variability in the length of biological apatite crystallites rather than variability of their orientation relative to the projection plane.

It is more likely, however, that the distribution of the random variable θ can be fitted with the Gaussian distribution within the range of small angles $-\sigma \le \theta \le \sigma$,

where $0<\sigma<<\frac{\pi}{2}$ is the standard deviation. In this case the probability density function $f(\theta)=\frac{1}{\sqrt{2\pi}\sigma}e^{-\frac{\theta^2}{2\sigma^2}}$. Even without tedious calculations it is obvious that if similar to the case above for uniform distribution of the variable θ we assume that 95% of the crystallites are lying within the range $-\frac{\pi}{10}\leq\theta\leq\frac{\pi}{10}$, then $\sigma=\frac{\pi}{20}$ (according to '68-95-99.7' rule for normal distributions) and therefore measured length of 95% of the crystallites will be between 98.77 nm and 100 nm in the assumption of $l=100\,nm$, which, as expected, is much better result than for simply a uniform distribution considered above.

A.1 References

1. Jones S.J., Boyde A. Ultrastructure of dentin and dentinogenesis. In: Linde A., editor. Dentin and Dentinogenesis. Boca Raton: CRC Press; 1984. p. 81-134.
2. Linde A. Structure and calcification of dentin. In: Bonucci E., editor. Calcification in biological systems. Boca Raton, Florida: CRC Press; 1992. p. 269-311.
3. Marshall Jr. G.W., Marshall S.J., Kinney J.H., Balooch M. The dentin substrate: structure and properties related to bonding. Journal of Dentistry 1997;25(6):441-58.